CARBON NANOSTRUCTURES-DEVELOPMENT AND APPLICATION IN THE ANODE OF LI-ION BATTERY

A THESIS

Submitted in partial fulfilment of the requirements for the award of the degree
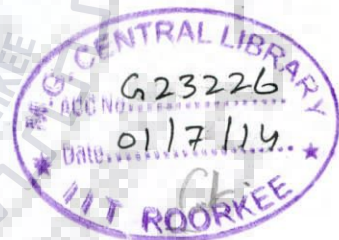
of

DOCTOR OF PHILOSOPHY

in

METALLURGICAL AND MATERIALS ENGINEERING

by

MALAY JANA

DEPARTMENT OF METALLURGICAL AND MATERIALS ENGINEERING

INDIAN INSTITUTE OF TECHNOLOGY ROORKEE

ROORKEE-247 667 (INDIA)

JULY, 2013

INDIAN INSTITUTE OF TECHNOLOGY ROORKEE
ROORKEE

CANDIDATE'S DECLARATION

I hereby certify that the work which is being presented in the thesis entitled **CARBON NANOSTRUCTURES-DEVELOPMENT AND APPLICATION IN THE ANODE OF LI-ION BATTERY** in partial fulfilment of the requirements for the award of the Degree of Doctor of Philosophy and submitted in the Department of Metallurgical and Materials Engineering of the Indian Institute of Technology Roorkee is an authentic record of my own work carried out during a period from July, 2009 to July, 2013 under the supervision of Dr. Anjan Sil, Professor and Dr. Subrata Ray, Professor, Department of Metallurgical and Materials Engineering, Indian Institute of Technology Roorkee, Roorkee.

The matter presented in the thesis has not been submitted by me for the award of any other degree of this or any other Institute.

(MALAY JANA)

This is to certify that the above statement made by the candidate is correct to the best of our knowledge.

(Subrata Ray)
Supervisor
Date: 5/7/2013

(Anjan Sil)
Supervisor

The Ph.D. Viva-Voice Examination of **Mr. MALAY JANA**, Research Scholar, has been held on _29.8.13._

Signature of Supervisors

Chairman, SRC

Signature of External Examiner

Head of the Dept. /Chairman, ODC

To my parents, brothers and friends whose support has been a continuous source of motivation

and

To my teachers, for giving me the opportunity to spend the best of my life playing with the fascinating material in the world

Abstract

Nanotechnology, although the term was coined by Norio Taniguchi in the 1970's, has witnessed its first breakthrough with the discovery of Buckeyballs (fullerene) in eighties and nanotubes in the nineties. The properties and applicability of carbon nanostructures in general have produced tremendous excitement and interest among scientists, engineers and technologists. The synthesis of carbon nanostructures has progressed significantly and now further advancement depends critically on better understanding of the steps involved in growth for each type of carbon nanostructures. The first segment of the present study aims to contribute to the understanding of the growth of carbon nanostructures in catalytic chemical vapour deposition method with particular emphasis on the conditions favouring the development of different morphologies viz. single walled carbon nanotube, multi walled carbon nanotube, carbon nanofiber and carbon nanotape around catalyst nanoparticles, so that the method may be adapted to large scale production of carbon nanostructures of a given morphology.

Since the commercial introduction of lithium-ion batteries by Sony Corporation in the early 1990, there is continuing global effort to develop lithium ion batteries with higher capacity and better stability in order to extend their application, particularly in mobile tools and automobiles. The battery performance solely depends upon the capacity of electrode materials to hold active species of lithium and discharge/charge reversibly. The currently used commercial anode of graphite has excellent stability and low cost but could be intercalated by the active species of lithium up to a maximum limit given by the chemical formula LiC_6, which leads to a theoretical limit of its specific charge capacity, 372 mAhg^{-1}. In order to overcome the limitation of charge capacity, attempts have been made to replace the existing graphite material with different nanostructures of carbon. The objective of the second segment of the present study is to understand the relationship between the morphology and the electrochemical properties of carbon nanostructures and further to examine their electrochemical performance in terms of capacity for practical application in rechargeable lithium ion batteries. The present work compares the electrochemical performance of different morphologies of carbon nanostructures viz., single walled carbon nanotube, double walled carbon nanotube, multi walled carbon nanotube and carbon nanofiber.

In the present study, catalytic chemical vapour deposition method has been used to grow carbon nanostructures at 640 °C by decomposition of acetylene gas using nanoparticles of cobalt and nickel oxides with and without doping by copper oxide. The oxide nanoparticles with various combinations of doping level and the particle size synthesised by sol-gel technique were dispersed on the substrate of porous anodic aluminium oxide obtained by two step anodization of pure aluminium. Teflon made electrochemical cells were assembled using the carbon nanostructure based electrode as the working electrode and lithium metal as the reference electrode for charge/discharge cycling using electrochemical analyzer.

It has been observed that there is melting or surface melting of oxide nanoparticles at the temperature prevailing during growth of carbon nanostructures. The melting/surface melting characteristics of the oxide nanoparticles having different sizes with and without doping have been extensively investigated and in a pioneering approach, the temperature at the start of melting has been taken as the characteristic parameter of melting to rationalise the observations on the growth morphology of carbon nanostructure. It has also been observed that there is reduction of oxide in the chamber of catalytic chemical vapour deposition set-up, which contains potent reducing agents like carbon and hydrogen. The surface melting of oxide perhaps helps in dissolution of carbon and relatively faster transport of the reducing agents inside the particles. Dissolution of carbon following deposition also helps to prevent the formation of thick deposit of carbon on the oxide nanoparticles, which results in the formation of nanobeads. The rate of flow of carbon bearing gas is therefore important as it controls the rate of decomposition and deposition of carbon over the nanoparticles.

The dissolution and diffusion of the reducing agents inside oxide nanoparticles may take place radially inside the oxide particles. Assuming a given temperature profile within the oxide particle, it may safely be presumed in general that the molten part of oxide at the surface remains molten even after reduction as metal has in general a lower melting point than its oxide. The thickness of the molten surface layer of metal may even be more than that of the molten layer of oxide before reduction. However, cobalt oxide, Co_3O_4, has a lower melting point than metallic cobalt and the thickness of the molten layer could be less than the thickness of molten layer in oxide. One may perceive that graphene may nucleate on the template of hexagonal close packed plane in the metal clusters created by reduction on the surface of solid oxide core. Once graphene has nucleated and grown around the particle there will be two direction of growth radially along the thickness and axially along the length. The flux of carbon entering the particle will have to be used for two purposes – (i) to cause

ii

reduction of oxide (along with hydrogen), and (ii) to provide carbon for axial growth as well as graphitic growth in thickness direction. Since growth in the thickness direction takes place by addition of more graphene layers and hence it is termed as graphitic growth, which may take place both outside and inside of the initially developed graphene tube. On the outside, this growth will take place provided there is molten layer or else there will be no graphitic growth and only loose carbon deposit may form as it has been commonly observed. The possibility of growing inside will depend on: (i) flux of carbon inside the graphene tube possibly through a dynamic process of dissolution and reformation of the graphene layer as the dissolved part of the layer will be reformed by flux of carbon arriving from outside, and (ii) progress of reduction and melting. Melting inside is required not only for part dissolution of graphene and high flux of carbon inside but also for squeezing out the melt along the axial hole of the tube to make room for the graphitic growth inside. This could be the explanation for the shape change of catalyst particles as it has been observed inside carbon nanostructure. If the entire core melts due to reduction it will pave a way for the growth of carbon nanofiber and partial melting will lead to multi walled carbon nanotube. When the oxide particle is very small and there is not enough thickness in the liquid layer for radial graphitic growth either inside or outside, single walled carbon nanotube is expected to grow only by axial growth. The core melting in the reaction chamber of catalytic chemical vapour deposition depends both on the melting characteristics of the oxide nanoparticle, indicated by the temperature at the start of surface melting, T_s, which in turn depends on the chemical constitution as modified by doping and the size of the oxide particle. When the temperature at the start of melting is normalized with respect to the growth temperature, T_g, of carbon nanostructure as $\Delta = (T_s - T_g)/T_s$ and Δ is plotted with the minimum size of the oxide nanoparticle used in an experiment for the growth of carbon nanostructure, it was observed that there is clustering of the experimental points representing the carbon nanostructure with the same morphology irrespective of the type of catalyst used.

The anode based on carbon nanostructures shows superior electrochemical properties and better coulombic efficiency as compared to graphite. Depending on the type of nanostructure, reversible capacity obtained lies in the range from 450 to 600 mAhg^{-1} and the coulombic efficiency beyond the third cycle is within the range from 85 to 98%.

The content of the thesis has been presented in six chapters which are outlined below:

Chapter 1 presents a brief introduction describing the importance of present study.

Chapter 2 presents an overview of different types of carbon nanostructures, their structural difference, properties and method of production. The current state of growth mechanism and selective synthesis processes, have been reviewed. Application of carbon based materials for energy storage application with a special emphasis on their use in the anode of lithium-ion battery system has been highlighted. The present state of knowledge available in the area has been discussed in order to identify the gap towards which the present investigation has been directed.

Chapter 3 describes the details of the experimental work carried out in the present study.

Chapter 4 presents results and discussion on oxide nanoparticle synthesis, nanoporous substrate preparation and synthesis of carbon nanostructure using nanoparticles of cobalt and nickel oxides with and without doping by copper oxide, having different size distribution and melting characteristics.

Chapter 5 presents electrochemical characterization of the different types of carbon nanostructure based anode materials to determine their suitability as anode materials for lithium ion batteries.

Chapter 6 summarizes the major conclusions.
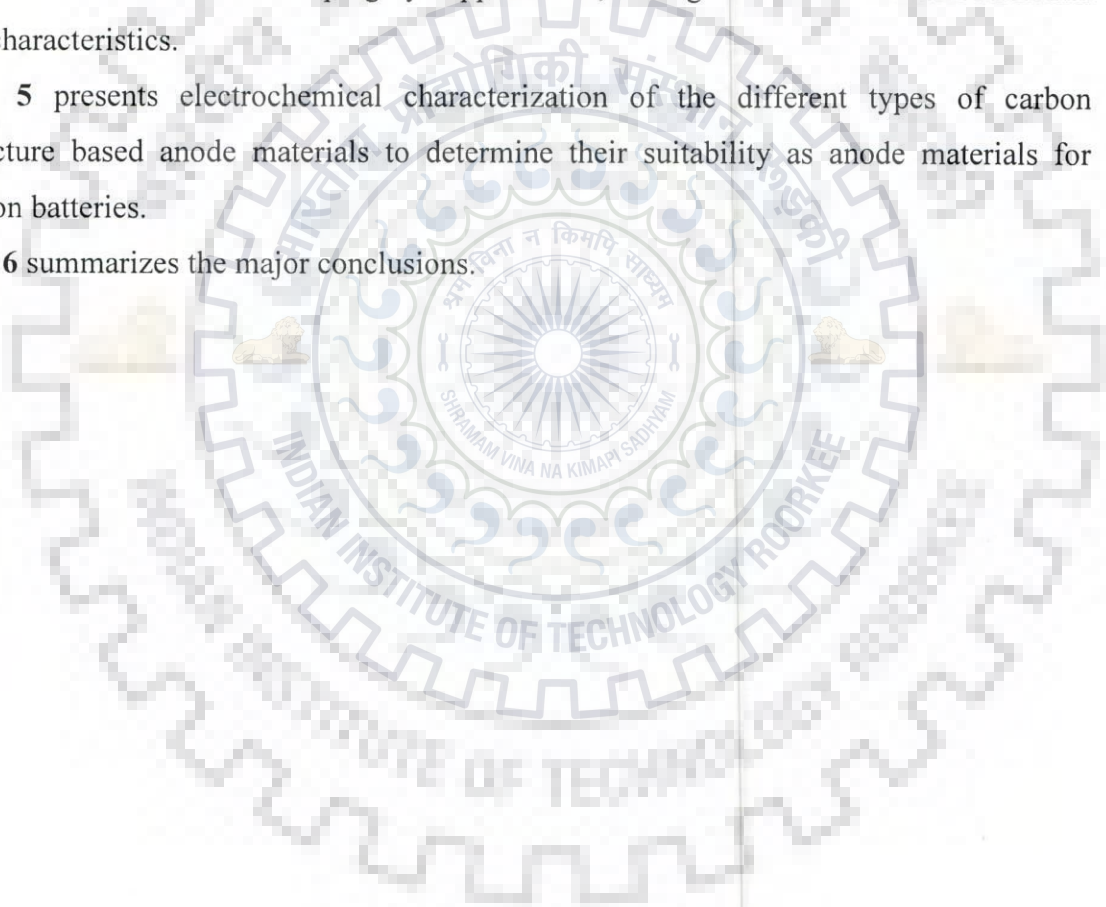
List of Publications

Book Chapter:

[1] S. Ray, M. Jana, A. Sil. "Handbook of Graphene Science", CRC Press, Taylor & Francis, In press.

Peer Reviewed Journals:

[1] M. Jana, A. Sil and S. Ray. "Tailoring of surface melting of oxide based catalyst particles by doping to influence the growth of multi-walled carbon nano-structures". Carbon, 49 (2011) 5142-5149 (Archived in NRC-CISTI: Discover).

[2] M. Jana, A. Sil and S. Ray. "Influence of melting of transition metal oxides on the morphology of carbon nanostructures". Advanced Materials Research, 585 (2012) 159-163.

[3] M. Jana, A. Sil and S. Ray. "Growth of carbon nanostructures in catalytic chemical vapour deposition method". The Banaras Metallurgist, 17 (2012) 1-16.

[4] M. Jana, A. Sil and S. Ray. "Morphology of carbon nanostructures and their electrochemical performance for lithium ion battery". Journal of Physics and Chemistry of Solids, Communicated.

[5] M. Jana, A. Sil and S. Ray. "Growth and morphology of carbon nanostructures on nickel oxide nanoparticles in catalytic chemical vapour deposition". Communicated.

Conference Proceedings/Symposium:

[6] M. Jana, A. Sil and S. Ray. "Doping and growth of carbon nano-structures". International Conference on Indian Metals Industry-Shaping the Next Decade. Feb. 12-14, 2011; IIM News Letter, New Delhi, XXXX (40), p.7.

[7] A. Sil, S. Ray and M. Jana. "Carbon nano-composite materials for energy storage application". 4th International Symposium on Advancing the Chemical Sciences-Challenges in Renewable Energy. July 05-08, 2011; MIT, Boston, United States of America.

[8] M. Jana, A. Sil and S. Ray. "Selective growth of carbon nanostructures: Role of surface melting". International Conference on Advances in Materials and Materials Processing. Dec. 9-11, 2011; IIT Kharagpur, India.

[9] M. Jana, A. Sil and S. Ray. "Surface melting and growth of carbon nanostructures". National Symposium Nano biotechnology (NSNT)-2012. June 1-2, 2012; IIT Mandi, India.

[10] M. Jana, A. Sil and S. Ray. "Influence of melting of transition metal oxides on the morphology of carbon nanostructures". Advances in Materials and Processing Challenges and Opportunities. Nov. 2-4, 2012; IIT Roorkee, India.

[11] M. Jana, A. Sil and S. Ray. "Fabrication of carbon nanostructures by CCVD using nano-porous alumina template". 4th International & 25th All India Maufacturing Technology, Design and Research Conference (AIMTDR). Dec. 14-16, 2012; Jadavpur University, Kolkata. India.

[12] M. Jana, A. Sil and S. Ray. "Carbon nanostructure based hybrid nanocomposites as electrode material for rechargeable Li-ion batteries". 4th International Conference on Recent Advances in Composite Materials (ICRACM). Feb. 18-21, 2013; Goa, India.

[13] A. Sil, M. Jana and S. Ray. "Chemical and structural changes of catalysts affecting growth of carbon nanostructures". International Conference on Materials Science and Chemical Engineering (MSCE 2013), Feb. 20-21, 2013; Singapore.

[14] M. Jana, A. Sil and S. Ray. "Growth of Carbon Nanostructures - Effect of Chemical and Structural Changes of Catalysts". 8th International Conference on Surfaces, Coatings and Nanostructured Materials (NANOSMAT). Sep. 22-25, 2013; Granada, Spain, Accepted.

Acknowledgements

Animesh, Bappa (Sudip), Biswanath all of them are equally supported me from my school life. Few others from my M.Tech I want to mention here are Suman, Abhijit and many more, whose support makes me stronger and gives me confidence.

During the tenure of this thesis work, I was accompanied and supported by many people and it will not be possible for me to conclude the acknowledgements. So, I would like to express my gratitude to all those who helped me in completing my thesis.

(MALAY JANA)

Contents

List of Abbreviations

CNT	Carbon Nanotube
SWCNT	Single Walled Carbon Nanotube
DWCNT	Double Walled Carbon Nanotube
MWCNT	Multi Walled Carbon Nanotube
CNF	Carbon Nanofiber
CNS	Carbon Nanostructures
CCVD	Catalytic Chemical Vapour Deposition
EV	Electrical Vehicle
HEV	Hybrid Electrical Vehicle
SEI	Surface Electrolyte Interphase
C_{60}	Buckminsterfullerene/ Buckyball
HOPG	Highly Oriented Pyrolytic Graphite
GNR	Graphene Nanoribbon
DOS	Density of States
RT	Room Temperature
YAG	Yttrium-Aluminum-Garnet
CVD	Chemical Vapour Deposition
HRTEM	High Resolution Transmission Electron Microscope
ETEM	Environmental Transmission Electron Microscope
XPS	X-ray Photoelectron Spectroscopy
VLS	Vapour-Liquid-Solid
DSC	Differential Scanning Calorimetry
XRD	X-ray Diffraction
SAD	Selected Area Diffraction
TEM	Transmission Electron Microscope
HM	Homogeneous Melting
LNG	Liquid Nucleation and Growth
LSM	Liquid Skin Melting
CNR	Carbon Nanoribbons
PC	Propylene Carbonate
EC	Ethylene Carbonate
DEC	Diethyl Carbonate

DMC	Dimethyl Carbonate
GIC	Graphite Intercalation Compound
MCMB	Mesocarbon Microbeads
PPy	PolyPyrrole
FED	Field Emission Displays
EDLC	Electric Double Layer Capacitor
STM	Scanning Tunneling Microscope
AFM	Atomic Force Microscope
AAO	Anodized Aluminium Oxide
FESEM	Field Emission Scanning Electron Microscope
EDAX	Energy Dispersive X-ray Analysis
DTA	Differential Thermal Analysis
DLS	Dynamic Light Scattering
BET	Brunauer, Emmett and Teller
TGA	Thermogravimetric Analysis
WAXS	Wide Angle X-ray Scattering
SAXS	Small Angle X-ray Scattering
SE	Secondary Electron
BS	Backscattering
SEM	Scanning Electron Microscopy
EDS	Energy Dispersive Spectroscopy
SPM	Scanning Probe Microscopy
CCD	Charge Coupled Device
SDT	Simultaneous DTA and TGA
RBM	Radial Breathing Mode
CB	Carbon Black
PVDF	Polyvinylidene Fluoride
NMP	N-Methyl-2-Pyrrolidinone
PAAO	Porous Anodized Alumina Oxide
FWHM	Full Width at Half Maximum
STEM	Scanning Transmission Electron Microscopy
CNB	Carbon Nanobeads

List of Figures

List of Tables

Introduction

Chapter 1

Introduction

Nearly twenty years have passed since the discovery of carbon nanotubes (CNT) was made in the year 1991 (Iijima, 1991) but researchers are still exploring the potential applications of CNT due to their unusual structural and electronic properties. Tubular carbon nanostructures may be conceived as graphene sheets with hexagonal arrangement of carbon atoms, rolled up to form a seamless tube with diameter in the nanometer range but having large length to diameter ratio. There are a variety of morphology of one dimensional nanostructures such as (i) single walled carbon nanotube (SWCNT), which may be conceived as a rolled-up single graphene sheet containing hexagonal array of carbon atoms forming single wall, (ii) double walled carbon nanotube (DWCNT) or multi walled carbon nanotube (MWCNT), which are rolled up co-axial assembly of two or more graphene sheets like a Russian doll one inside the other, with separation between the co-axial tubes similar to that between the layers in natural graphite and (iii) the solid carbon nanofiber (CNF) or nanotape, which are all referred in this study by the generic name of carbon nanostructures (CNS). Catalytic chemical vapour deposition (CCVD) is one of the methods which involve catalyst assisted thermal decomposition of hydrocarbons leading to nucleation and growth of these nanostructures and it is the most popular method of producing CNS because of its low-cost and scalability for mass production. The formation of CNS is triggered by the release of carbon from a source material, generally carbon bearing gas like acetylene, methane, ethane or benzene vapour in presence of nanoparticles of catalyst, which is either a transition metal like iron, cobalt, nickel or their oxides (Dupuis, 2005).

Experiments show that the type of CNS, i.e. morphology and the diameter distribution depend on the size, shape and composition of the catalyst besides other prevailing growth conditions including the growth temperature. The properties of carbon nanostructures are directly related to the structure in terms of the atomic arrangement resulting from the manner of folding of graphene sheet characterizing its chirality and also to the size and the number of walls. The structure and the type of CNS growing need to be understood and controlled in order to get reproducible product commercially. A thorough understanding of the mechanisms of nucleation and growth of CNS is, therefore, of crucial importance. Despite significant progress in this field of research over the years, there are several questions which are to be

3

answered before we could control synthesis of CNS and the present investigation aims to address some of these questions.

The study reported in the thesis is divided into two segments. In the first segment the growth of oxide nanoparticles by sol-gel process for the synthesis of carbon nanostructures by CCVD method has been discussed. The steps involved in the CCVD process beginning from oxide nanoparticles have been explored and understood by performing supplementary experiments like the study of the melting behaviour of oxide nanoparticles and the chemical change of the oxides in the CCVD chamber. In the second segment of this investigation, the electrochemical performance of the different carbon nanostructures have been determined and correlated to their morphology in order to assess the possibility of the application of the nanostructures in high charge capacity anodes in lithium ion battery replacing the presently used graphite.

Cobalt and nickel as well as their oxides have been extensively used to grow CNS by CCVD method. The present study plans to use these oxides as these could be obtained in nano-size inexpensively by sol-gel method. Further, it may be interesting to dope these oxides with other oxides e.g. copper oxide that are not very effective in promoting CNS and study the effect of this doping, which has not been investigated so far. The particle size of these oxides are important in deciding the type of CNS forming as it has been widely observed but it is not known as to how doping will affect the processes involved in CCVD. For commercial exploitation of CNS, it is necessary to grow CNS of a specific morphology by controlling the catalyst and appropriate growth conditions in CCVD method. To attain this ability one has to understand the detailed mechanism of growth of different morphologies of CNS in this method.

Modern life requires steady and reliable energy supplies, which, in the present days, should be clean and renewable so as to ensure sustainability. Though fossil fuels have been and are still the major energy resources, but future availability and limitation of emission of green house gases and other pollutants are worrying aspects of the current energy scenario. Unless alternatives emerge, global warming enhanced by green house gases may eventually threaten our existence. There is an extensive exploration of alternate ways of generating energy and also the feasibility of their storage, which is required as the peaks in generation and utilization of energy may be at different times. Also, the storage of energy is required for mobile power sources as in non-polluting electric vehicles and mobile tools. The lithium ion batteries, in particular, are at the forefront amongst the contenders for high power applications because of their higher energy density and being light in weight, making it superior to either lead acid,

4

nickel cadmium or nickel metal hydride battery systems. There is significant success of lithium ion battery in consumer electronics. However, the current commercial lithium-ion batteries may still be improved considerably in respect of specific energy density to provide power for electric vehicle (EV) and hybrid electric vehicle (HEV). Thus, there is continuing search for lithium-ion batteries with higher energy density, higher power density and better cyclic stability. A lithium-ion battery, just like any other type of battery, consists of three major components-an anode, a cathode and the electrolyte between the electrodes and works by converting chemical potential to electrical energy through electrochemical reactions, which include the heterogeneous charge transfer process occurring at the surface of an electrode.

The 'standard' anode for a lithium ion battery is a carbonaceous compound, either graphite or coke (Megahed and Scrosati, 1994). The main motivations to choose these materials are their low cost, more negative redox potential and the low operational voltage. The carbonaceous anode is coupled with a high voltage cathode, in order to obtain a battery operating in the range of ~ 4 V. The mechanism of lithium intercalation in the so-called 'soft' anodes, i.e. graphite or graphitizable carbons, is well known. It develops through well-identified, reversible stages, corresponding to progressive intercalation within discrete graphene layers, to reach the chemical formula LiC_6, with a maximum theoretical capacity of 372 mAhg^{-1}, which limits the energy density of the battery (Kambe et al, 1979). For each lithium ion working as active species in the battery, one has to tolerate the weight of six carbon atoms, which increases the weight of the anode to reduce its specific charge density and capacity. Thus, new anode materials with high theoretical charge capacity, low cost, enhanced safety and long cycle life, have to be explored to meet the demands for improved energy storage capacity, rate capability and cycling stability of electrodes along with reduced detrimental effects of large volume change and solid electrolyte interphase (SEI) formation.

The lithium ion battery may benefit from the introduction of nanostructures in the electrodes and particularly, carbon nanostructure in the anode. The application of nanostructured electrodes has significantly improved the lithium ion intercalation capability in terms of storage capacity, intercalation rate and cyclic stability (Bruce et al, 2008). Considering the liquid/solid interface reaction characteristic of lithium ion intercalation, followed by diffusion into the electrode, it is reasonable to expect that a large surface area and short lithium ion diffusion path can facilitate the diffusion into the electrode. Porous materials in the electrodes by virtue of large pore surface area and numerous pores, offer many advantages including the buffering of the large volume changes, which may be caused by cyclic intercalation and de-

5

intercalation. Thus, it is possible that porous nanostructured materials may show improved reversible capacity, enhanced cycling performance and elevated rate capability.

The primary purpose of choosing CNS based electrode material is to provide the large surface area resulting from the side walls and inside pores, which may provide enhanced intercalation by lithium ions and buffer the large volume changes to preserve the integrity of the electrodes maintaining the electronic contact between the active particles and the conductive phase. The nanomaterials with porous structures of carbon could be the best way to achieve breakthroughs in the energy storage field, especially for the lithium-ion battery. Nanostructures of carbon are also endowed with unusual mechanical, electrical and thermal properties by confining the dimensions of such materials. It is known that the performance of lithium ion batteries depends strongly on the method of production and morphology of the carbon materials used (Endo et al, 1996). The present study, therefore, undertakes systematic investigation to improve the electrochemical performance of electrodes by incorporating different types of nanostructures of carbon like SWCNT, DWCNT, MWCNT and CNF in order to understand the role of morphological features and defects in the context of their commercial application in the anode of lithium ion batteries.

The present study aims to enhance understanding of the growth of one dimensional carbon nanostructures by CCVD method so that one may grow a specific morphology, which may be more suitable for application in the anode of lithium ion battery in terms of electrochemical performance and cost. In order to convince industries to adopt nanostructured materials for the anode preparation to attain higher energy density in a battery may require reliable production technology for these materials as well as reproducible performance, which may happen at the culmination of many such studies.

Literature Review

Chapter 2

Literature Review

Carbon is a nonmetallic element abundantly available in nature. From prehistoric times, it has been used in smelting of ores leading to the emergence of the Bronze Age and later the Iron Age. The name of this element is derived from the Latin name "carbo" for burnt wood. There are several allotropes of carbon of which the best known are graphite, diamond, and fullerenes/carbon nanotubes or in general carbon nanostructures (CNS). Apart from fullerene, CNS now includes hollow tube, fiber, ribbon and tape. The physical properties of carbon vary widely with the allotropic form. Elemental carbon atoms bonded by sp^2 hybridization form a variety of amazing structures. The story of CNS started with fullerenes or buckministerfullerene, C_{60} (popularly called buckyballs), which is a new class of carbon material of spherical molecules about 1 nm in diameter, comprising 60 carbon atoms arranged as 20 hexagons and 12 pentagons in the configuration of a football. Buckminsterfullerene (C_{60}) was discovered by Smalley for which he got Noble Prize in 1996 (Kroto et al, 1985). Graphene sheet is the hexagonal atomic arrangement of carbon atoms, which is stacked to form hexagonal close packed structure of graphite. Tubular carbon nanostructures may be considered as graphene sheets rolled up to form a seamless tube of diameter in nanometers but having large length to diameter ratio. The axial direction, around which the sheet is rolled into tube, with respect to hexagonal arrangement of atoms in the graphene sheet results in three types of helical structures - the armchair, the zigzag and the chiral carbon nanotube (CNT) (Dresselhaus et al, 1995). When a single sheet of graphene is rolled up it forms single walled carbon nanotube (SWCNT), which was discovered in 1992 (Ajayan and Iijima, 1992). A multiwall carbon nanotube (MWCNT) which is a coaxial assembly of cylinders of SWCNT, like a Russian doll, one within another was also discovered by Iijima (Iijima, 1991) in 1991. The separation between the individual tubes is similar to that between the layers in natural graphite. There could be a few walls (two or more) in MWCNT as reported by Iijima and other researchers (Iijima, 1991). Carbon products in tubular form were first observed soon after introduction of electron microscope in 1950 (Davis et al, 1953). Gibson (Gibson, 1992) in a letter to "Nature" indicated that similar structures had been prepared in 1953. In 2006 Reibold et al. (Reibold et al, 2006) observed that Damascus sabre steel from the seventeenth

9

century, contains carbon nanotubes as well as cementite nanowires under high-resolution transmission electron microscopy. Nanotechnology is expected to exploit the unusual and interesting properties in nano regime due to their large surface-to-volume ratio, quantum-confinement and atomic disorder effects (Mukherjee et al, 2006).

Nanotubes are, therefore, one-dimensional objects with a well-defined direction along the nanotube axis that is analogous to the in-plane directions of graphite. There are other kinds of nontubular filled structures, known as carbon nanofiber (CNF) in general. The first graphite fiber was reported by Hughes and Chambers in 1889 (Hughes and Chambers, 1889). The others include fishbone/herringbone (Zhu et al, 2005), platelet and straight/helical (coiled) shape (Baker et al, 1972; Hughes and Chambers, 1889; Ding et al, 2003).

2.1 The Structure of Carbon Nantubes

The properties of nanostructures of carbon are a direct result of their structural inheritance from graphene, a single sheet of graphite. Most of its properties arise from its plane honeycomb structure which precisely provides the basic skeleton of the nanotube (Bernier and Lefrant, 1997). Properties specific to the nanotube stem from the perturbations to this plane due to curvature and the reduction in dimensionality. The properties of the nanotube thus arise by adapting the properties of graphite to the conditions imposed by rolling up the graphene sheets and these may be classified into electrical, mechanical, thermal and chemical properties. Actually, for polyaromatic solids that consist of stacked graphenes, the bond strength varies significantly depending on whether the in-plane direction is considered (characterized by very strong covalent and therefore having very short bond length of 0.142 nm) or the direction perpendicular to it (characterized by very weak van der Waals bond and having relatively large bond length of 0.34 nm). Such heterogeneity is not found in single (isolated) SWCNT. However, the heterogeneity returns, along with the related consequences, when SWCNT associate into bundles. Therefore, the properties and applicability of SWCNT may also change depending on whether single or bundles of SWCNT are involved. Therefore, the physics of graphene and the nano tubes are related and so this section begins with a subsection on graphene.

2.1.1 Graphene

Graphite is well known layered hexagonal close packed structure containing layers of graphene sheet, where each carbon is covalently bonded to three other carbon atoms through sp^2 hybridization. Andre Geim and Konstantin Novoselov were awarded Nobel Prize in 2010 for obtaining graphene sheet by mechanical exfoliation of highly oriented pyrolytic graphite

(HOPG) with an adhesive tape (Geim and Novoselov, 2007). It was believed that 2D crystals in general cannot be found in free state. Graphene can be quite easily manipulated, and can be deposited on a SiO₂ layer grown over a doped silicon substrate. It was further observed that when SiO₂ is grown over doped silicon to a thickness typically about 300 nm, Si substrate acts as a gate inducing surface charge density in graphene, related to applied gate voltage. The gate induced charge is like chemical doping of a semiconductor but once chemical doping is done it cannot be changed. But in this case one may tune in positive or negative gate voltage to make the graphene n- or p- type of semiconductor. Typical carrier mobility in graphene is 15,000 $cm^2V^{-1}s^{-1}$ and may attain an astounding value of 200,000 $cm^2V^{-1}s^{-1}$ in suspended graphene for a charge carrier concentration (n) = 4 × 10⁹ cm^{-2} (Dragoman and Dragoman, 2009). The room temperature mean free path for ballistic transport is 200-300 nm. The mobility does not depend significantly on doping or temperature. The anomalous charge transport properties of finite conductivity when the charge carrier density (hence gate voltage) is zero, is because of the electron and hole states are correlated by charge conjugation symmetry and their transport is described by Dirac like equation for massless particles. Both the electrons and holes have linear dispersion relations for small energy E as (Dragoman and Dragoman, 2009)

$$E = \pm \frac{h}{2\pi}|k|v_F \qquad (2.1)$$

Where $\vec{k} = i\vec{k_x} + j\vec{k_y}$ is the wave number of the charged state and v_F is the Fermi velocity. The sign + is for electrons and − is for holes. Thus, graphene is a semiconductor with no energy gap, the valence and conduction bands touching each other at one point, which is termed as Dirac point as shown in Fig. 2.1.
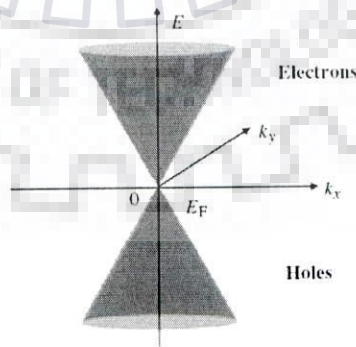
Fig. 2.1: Dispersion relation in graphene (Dragoman and Dragoman, 2009).

One may resort to band gap engineering. A graphene sheet contacted between electrodes may be etched to narrow strips which are called graphene nanoribbons (GNR) and the width (*w*) of

the strip (typically of 1 to 2 nm) decides the energy gap E_g that opens up at the Dirac point. Experimentally it has been observed that,

$$E_g = \frac{\alpha}{w - w^*} \qquad (2.2)$$

Where $\alpha = 0.2$ eV and $w^* = 16$ nm. The properties of graphene summarized in Table-2.1 are given below.

Table-2.1: Properties of graphene (Dragoman and Dragoman, 2009).

Parameter	Value and units	Observations
Mobility	40,000 cm^2 V^{-1} s^{-1}	At room temperature (intrinsic mobility 200,000 cm^2 V^{-1} s^{-1})
Mean free path (ballistic transport)	> 400 nm	At room temperature
Fermi velocity	$c/300 = 1,000,000$ m/s	At room temperature
Electron effective mass	$0.06 m_0$	At room temperature
Hole effective mass	$0.03 m_0$	At room temperature
Thermal conductivity	5000 W/mK	Better thermal conductivity than in most crystals
Young modulus	1.5 TPa	Ten times greater than in steel

The electronic band structure of graphene may be considered in terms of two bands – valence band p and conduction band p*. The tight binding model using nearest neighbour Hamiltonian related to carrier hopping between two bands may be written as (Dragoman and Dragoman, 2009)

$$H = \begin{pmatrix} E_{2p} & -\gamma_0 g(k) \\ -\gamma_0 g^*(k) & E_{2p} \end{pmatrix} \qquad (2.3)$$

Where, E_{2p} is the site energy of the 2p atomic orbital, γ_0 (> 0) is the carbon–carbon energy, and

$$g(k) = \exp\left[\frac{ik_x a}{\sqrt{3}}\right] + 2 \exp\left[\frac{-i\left(\frac{k_x a}{2}\right)}{\sqrt{3}}\right]\cos\left[\frac{k_y a}{2}\right] \qquad (2.4)$$

Where, k = (k_x, k_y) is the reciprocal lattice vector of the graphene lattice and $a = |a_1| = |a_2| = 3a_{c-c}$. If s is the overlap of the electronic wave function over adjacent atomic sites in the graphene honeycomb lattice, the overlap matrix is expressed as

$$S_0 = \begin{pmatrix} 1 & sg(k) \\ sg^*(k) & 1 \end{pmatrix} \qquad (2.5)$$

The graphene band structure E(k) may now be obtained from

$$det|H - ES| = 0 \qquad (2.6)$$

and it has a two branch solution as

$$E^\pm(k) = \frac{E_{2p} \pm \gamma_0 w(k)}{1 \mp sw(k)} \qquad (2.7)$$

where, $w(k) = |g(k)|^{1/2} = [1 + 4\cos\left(\frac{3^{\frac{1}{2}}k_x a}{2}\right)\cos\left(\frac{k_y a}{2}\right) + 4\cos^2\left(\frac{k_y a}{2}\right)]^{1/2}$
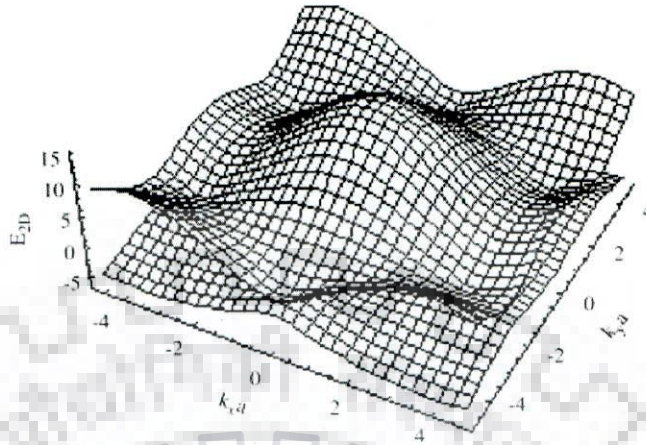
Fig. 2.2: Band structure of graphene (Dragoman and Dragoman, 2009).

Fig. 2.2 shows the band structure of graphene obtained by Dragoman and Dragoman (Dragoman and Dragoman, 2009) by superimposing the two branches of the dispersion relation, E^+ and E^-. These two branches actually touch each other at six points, called Fermi points situated at Fermi level, denoted by K and K′ in Fig. 2.3, showing a hexagon that represents the limit of the Brillouin zone in graphene. The Fermi energy level at the K points is considered as a reference, $E = 0$. Graphene is thus a zero-band gap semiconductor, as its density of states (DOS) is zero at the Fermi level as it has been stated earlier in the beginning of the subsection.
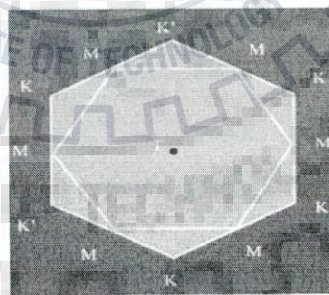
Fig. 2.3: Brillouin zone of graphene showing Fermi points K and K′ (Dragoman and Dragoman, 2009).

2.1.2 Carbon Nanotube

The structures of carbon nanotubes are clearly related to graphene sheet, which rolls up to form a cylinder as shown in Fig. 2.4. In the case of naotubes with closed end geometry, the end corresponds to the closure of a half-space which is achieved by introducing 6 pentagons

13

into the hexagonal lattice. The topology of the end depends on the distribution of these pentagons.
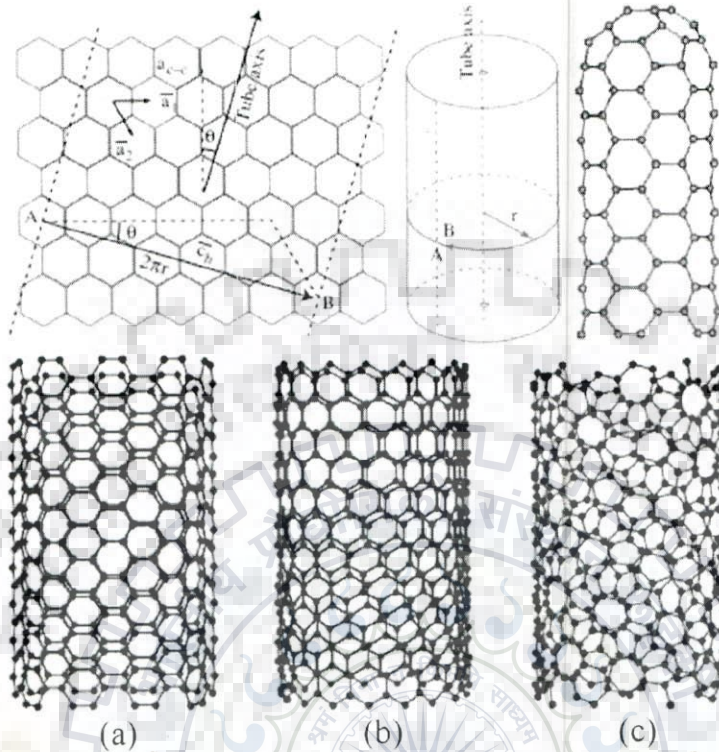
Fig. 2.4: Construction of a nanotube by rolling up a graphene sheet. The three tubes in the lower part of the figure result from rolling up the sheet at different angles θ. (a) $\theta = 30°$, armchair configuration, (b) $\theta = 0°$, zigzag configuration, (c) $\theta \neq 0°$ or $30°$, chiral configuration (Bourgoin, 2007).

To give a complete description of the nanotube structure, one must examine the way the graphene sheet is rolled up. This operation amounts to superposing two hexagons A and B of the lattice as shown in Fig. 2.4 and the choice of these two hexagons entirely and uniquely fixes the diameter of the nanotube and the angle, θ, known as the chiral angle or helicity, which specifies the axial direction of the sheet. To determine the chiral angle θ one requires choosing one side of a hexagon in the graphene sheet as the reference direction. This angle varies between 0 and $30°$, given the symmetry of the hexagonal lattice, and allows a complete classification of all possible configurations into three categories called the armchair, zigzag and chiral configurations. Zigzag and armchair tubes have chiral angle equal to 0 and $30°$, respectively. Their names refer to the arrangement of carbon atoms on the rim of an open tube (Fig. 2.4). In these two types of tubes, the hexagons in the upper part of the tube have the same orientation with respect to the axis as those in the lower part. Such tubes are said to be achiral. This property is not satisfied in tubes with chiral angle θ different from either $0°$ or

14

30°, which belong to the third category. The chiral vector or roll-up vector $\vec{C} = n\vec{a}_1 + m\vec{a}_2$, where n and m are integer numbers ($n, m \in N$), and $\vec{a}_1$, $\vec{a}_2$ are unit vectors of the graphene lattice as shown in Fig. 2.4. The structure of the three types of nanotubes illustrated in the Fig. 2.4 could be characterized by the pair of integers (n, m); the armchair tube characterised by pair (n, n), has n equal to m, the zigzag tube characterized by pair $(n, 0)$, has $m = 0$ while the chiral tube characterized by pair (n, m) could have any integer value of m and n excluding those for zigzag and armchair configurations.

The electronic properties of nanotubes are directly dependent on the chiral vector. The set of numbers (n, m) determines entirely the semiconducting or the metallic character of the CNT. The CNT is semiconducting when $n - m \neq 3i$ and it displays a small band gap (as semi-metallic behaviour) if $n - m = 3i$, where i = 1, 2, 3,.... But it is metallic if $n = m$ (Ouyang et al, 2001). The semiconducting CNT characterized by $(n, 0)$, are called zigzag CNT, and the (n, n) metallic CNT, are armchair CNT (Dresselhaus and Avouris, 2001). However, this rule has exceptions, because curvature effects in small diameter carbon nanotubes can strongly influence electrical properties. Thus, a (5, 0) SWCNT that should be semiconducting, in fact, is metallic according to the calculations. Likewise, vice versa zigzag and chiral SWCNT with small diameters that should be metallic have finite gap (armchair nanotubes remain metallic) (Lu and Chen, 2005). In theory, metallic nanotubes can carry an electric current density of 4×10^9 Acm^{-2}, which is more than 1,000 times greater than those of metals such as copper (Hong and Myung, 2007). The connection between the set (n, m) and the diameter d of the CNT can be expressed as (Dragoman and Dragoman, 2009)

$$d = a_{C-C}\,[3(m^2 + mn + n^2)]^{1/2}/\pi = |C|/\pi \qquad (2.8)$$

Where $|C|$ is the length of the chiral vector, and a_{C-C} is the length of carbon to carbon bond (1.42 Å). Equation 2.8 indicates that the modulus of the chiral vector is the circumference of CNT. The chiral angle, θ, is defined as

$$\theta = tan^{-1}\left[\frac{\sqrt{3}n}{2m+n}\right] \qquad (2.9)$$

The band structure of the CNT follows from that of graphene when rolled into tube, confines the charge carriers in the circumferential direction of the tube. If the vector k = (k_c, k_a) in the context of tube where subscript a indicates axial component and c indicates circumferential component, the confinement in the circumferential direction will lead to quantization as

$$k_c C = 2\pi n \qquad (2.10)$$

where k_c is the circumferential component of k and n = 1, 2,...N where N is the number of hexagon in the unit cell of CNT. The impact of this quantization may be reflected by slicing

the band structure of graphene in one dimensional section, particularly in the vicinity of Fermi points as shown in Fig. 2.5.
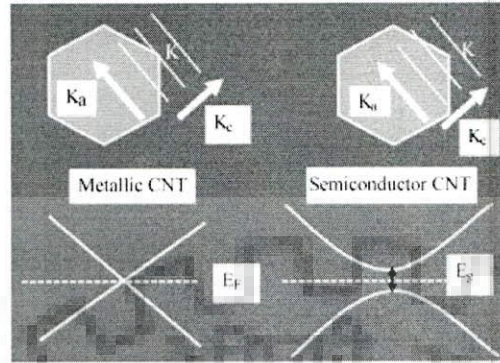
Fig. 2.5: Brillouin zones and band structure of metallic and semiconductor CNT (Dragoman and Dragoman, 2009).

The band structure around Fermi point in metallic CNT consists of two energy bands intersecting at K and having linear dispersion relations. The semi-conductor CNT will have a band gap, Eg, opening between two energy bands as

$$E_g = \frac{4v_F}{3d}$$

(2.11)

and its numerical value is $E_g(eV) = 0.9/d(nm)$ when $v_F = 8 \times 10^7$ ms^{-1}.

The energy gap decreases for larger tube diameter. In these respects, the electronic property of CNT is unique and is not found in any other one-dimensional system. The semiconducting properties of nanotubes have been used to develop electronic components. Nanotubes can carry quite remarkable current densities, of the order of 10^{10} Acm^{-2}, at least two orders of magnitude greater than that of metals.

Probably the most unusual property of nanotubes is the sensitivity of their bandstructure to geometry (Hamada et al, 1992). MWCNT are more complex objects than the SWCNT as each of its carbon shells can be metallic or semiconducting with different chiralities. The complex structure of MWCNT has discouraged their detailed study and use. However, based on a low temperature study of the Aharonov-Bohm effect in MWCNT (Bachtold et al, 1999), it has been concluded that in MWCNT only the outer shell contributes to electrical transport (Schonenberger et al, 1999). These systems show 1D or 2D characteristics, depending on their diameter and the nature of the property. The band-gap is inversely proportional to the tube diameter, so only small diameter MWCNT is expected to exemplify semiconducting outer shell. These shells may interact and the transport characteristics of a MWCNT at ambient temperature reflect the contributions of more than the outer shell. This is particularly observed

16

for large diameter tubes, i.e. for small energy gap (Avouris, 2002). According to Collins and Avouris (Collins and Avouris, 2002) the individual shells interact weakly, in the same way that graphene sheets are weakly coupled in graphite and MWCNT can be modeled as a complex bundle of parallel conductors, each having a different band structure. For example, since each carbon shell has a different bandstructure with slightly different allowed momenta, transport mechanisms which are rigorously momentum conserving should completely exclude contributions from inner shells (Collins and Avouris, 2002). A typical value determined for the resistivity ρ is 10^{-3} Ωcm (Fischer et al, 1997). Using the measured resistance and the knowledge that the electric current flows through the outermost cylinder of the MWCNT, Schonenberger et al. (Schonenberger et al, 1999) estimated $\rho \sim 10^{-6}$ Ωcm. This large difference is probably due to the low volume fraction of conducting nanotubes in thin-film samples. For all measured MWCNT they found a resistance of the order 10 kΩ at low temperature and a temperature dependence in which the resistance increases by a factor of 2-3 times if the temperature is lowered from room temperature (RT) to a few degree celcius.

2.2 Physical and Mechanical Properties of Carbon Nanostructures

Carbon nanotubes are the strongest and stiffest materials yet discovered in terms of tensile strength and elastic modulus respectively. This strength results from the covalent sp^2 bonds formed between the individual carbon atoms. Due to its structural anisotropy, graphite has a very high elastic modulus (measuring its resistance to deformation) in the hexagonal plane, reaching values of about 10^{12} Pa or 1 TPa, but much lower values out of the plane, at 4×10^9 Pa. The nanotube inherits the mechanical capacities of graphene, and even enhances them, since elastic moduli of 1 TPa have been calculated and measured (Smalley and Yakobson, 1998). It combines this resistance to deformation with a high level of flexibility, due to the partial sp^2-sp^3 hybridisation of the C–C bond which is stronger than in diamond (sp^3 hybridisation), as revealed by the difference in C–C bond lengths (0.142 vs. 0.154 nm for graphene and diamond respectively). The bulk modulus of superhard phase nanotubes is 462 to 546 GPa, even higher than that of diamond (Popov et al, 2002). Various experiments have shown that the nanotube has an incredible ability to bend to considerable angles, and also to deform and twist about its axis (Smalley and Yakobson, 1998). MWCNT with larger diameter are found to have properties similar to other forms of regular, polyaromatic solids. Tensile strength values as high as $\sim$ 150 GPa have actually been measured for perfect MWCNT made from an electric arc (Demczyk et al, 2002). In 2000, a multi walled carbon nanotube was tested to have a tensile strength of 63 GPa (Yu et al, 2000a). Further studies, revealed that

17

individual CNT shells have strengths of up to ~ 100 GPa, which is in good agreement with quantum/atomistic models (Peng et al, 2008). However, these elastic properties, which have indeed been confirmed experimentally for individual SWCNT, are considerably downgraded in MWCNT, and all the more so as the number of walls increases. Very high tensile strength values are also expected for defect-free MWCNT. Since carbon nanotubes have a low density for a solid of 1.3 to 1.4 gcm^{-3} (Collins and Avouris, 2000) its specific strength of up to 48,000 $kNmkg^{-1}$ is the best of known materials, compared to high-carbon steel 154 $kNmkg^{-1}$. Although the strength of individual CNT shells is extremely high, weak shear interactions between adjacent shells and tubes leads to significant reductions in the effective strength of multi walled carbon nanotubes and carbon nanotube bundles down to the order of GPa (Filleter et al, 2011).

Phonons denote the quantized normal-mode vibrations that strongly affect many processes in condensed-matter systems, including thermal (Singh et al, 2010), transport and mechanical properties. Phonons play an important role as carriers of thermal energy in thermal conduction processes and in thermodynamic properties, such as the heat capacity, and in scattering processes for bringing electrons into equilibrium with the lattice in various electron transport phenomena, such as electrical conductivity, magneto-transport phenomena and thermoelectricity. The thermal properties of CNS, including their specific heat, thermal conductivity and thermopower display a wide range of behaviours which stem from both their relation to a 2D graphene layer and their unique structure and tiny size (Dresselhaus et al, 2004). The specific heat of individual nanotubes should be similar to that of 2D graphene at high temperatures, with the effects of phonon quantization becoming apparent at lower temperatures for SWCNT of small diameter. To study the intrinsic thermal conductivity and thermoelectric power of nanotubes, measurements must be made at the single-nanotube level. Such measurements are technically very difficult to make. All nanotubes are expected to be very good thermal conductors along the tube, exhibiting a property known as "ballistic conduction", but good insulators laterally to the tube axis. Measurements show that a SWCNT has a room-temperature thermal conductivity along its axis of about 3500 $Wm^{-1}K^{-1}$ (Pop et al, 2006) compared to copper, a metal well known for its good thermal conductivity, which transmits ~ 385 $Wm^{-1}K^{-1}$. Measurements of thermal conductivity $\kappa(T)$ for an individual MWCNT show very high values of $\kappa(T)$ (over 3000 $Wm^{-1}K^{-1}$) and a maximum in $\kappa(T)$, which is indicative of significant phonon-phonon scattering at high T (Kim et al, 2001). A SWCNT has a room temperature thermal conductivity across its axis of about 1.52 $Wm^{-1}K^{-1}$ (Sinha et al, 2005) which is about as thermally conductive as soil. The temperature stability of

carbon nanotubes is estimated to be up to 2800 °C in vacuum and about 750 °C in air (Thostenson et al, 2005). The thermal expansion of an SWCNT bundle has been measured using X-ray diffraction techniques (Maniwa et al, 2001), and the results are consistent with expectations based on graphite, which has an exceedingly small in-plane thermal expansion coefficient, but a large inter-planar expansion coefficient. The measurements show almost no thermal expansion along the direction of the nanotube axis ($(-0.15 \pm 0.20) \times 10^{-5}$ K^{-1}), but a value of $(0.75 \pm 0.25) \times 10^{-5}$ K^{-1} is found for the expansion in the range 28–678 °C along the direction of the diameter.

The surface area may go upto few thousand m^{2}g^{-1}, depending on the number of walls, the diameter and the number of nanostructures in a bundle (Peigney et al, 2001) for which they can be used for any adsorption based application. Various studies dealing with the adsorption of nitrogen onto MWCNT and SWCNT have highlighted the porous nature of these materials (Yang et al, 2001). Magnetic field is also found to have strong effects on the structure and properties of CNT and for which Lu (Lu, 1995) predicted field-induced metal-insulator transition.

2.3 Synthesis of Carbon Nanostructures

There are various methods which are used to produce carbon nanostructures. They all have in general three common ingredients: (i) a carbon source, (ii) catalyst nanoparticles, and (iii) an energy input. The industrial application of CNS requires the development of techniques for large-scale production of defect-free nanostructures.

The optimal conditions for nanotube generation using arc-discharge technique involve the passage of a direct current through two high-purity graphite electrodes separated by about 1-2 mm, in a He atmosphere (500 torr) (Ebbesen and Ajayan, 1992). The arc-discharge method was used to discover MWCNT by Iijima (Iijima, 1991). This method has been used long before that in the production of carbon fibers and fullerenes. Large-scale synthesis of MWCNT by a variant of the standard arc-discharge technique was reported by Ebbesen and Ajayan (Ebbesen and Ajayan, 1992). The yield of nanotubes was maximal of 75% relative to the starting graphitic material. Later Iijima and Ichihashi (Iijima and Ichihashi, 1993) and Bethune et al. (Bethune et al, 1993) synthesize SWCNT by use of metal catalysts in the arc-discharge method in 1993. The lower electrode, the cathode, had a shallow dip to hold a small piece of iron during the evaporation. In the arc-discharge synthesis of nanotubes, Bethune et al. (Bethune et al, 1993) used anodes with bored holes which were filled with a mixture of pure powdered metals (Fe, Ni or Co) and graphite. The arc method usually involves high-

19

purity graphite electrodes, catalyst powders and high-purity He and Ar gases; thus the costs associated with the production of CNS are high. Although the crystallinity of the material is also high, there is no control over dimensions (length and diameter) of the tubes. Unfortunately, by-products such as polyhedral graphite particles, encapsulated metal particles and amorphous carbon are also formed.

In 1996, Thess et al. (Thess et al, 1996) produced high yields (>70%) of SWCNT by laser-ablation of graphite rods with small amounts of Ni and Co at 1200 $^\circ$C. High power laser vapourization (YAG type) of pure graphite targets inside a furnace at 1200 $^\circ$C, in an Ar atmosphere is capable of generating MWCNT (Guo et al, 1995). The nanotube growth using this technique has been explained in terms of the attachment of incoming carbon species at the edges of adjacent growing graphene tubules, responsible for prolonging the lifetime of the open structure (e.g., lip-lip interactions), which finally results in a multilayered tube. Dillon and co-workers (Dillon et al, 2000) noticed that the diameter of the tubes depends upon the laser power. In other words, as the laser pulse power is increased, the diameter of the tubes gets reduced. Unfortunately, the laser technique is not economically advantageous because the process involves high-purity graphite rods, the laser powers required are high, and the amount of nanotubes that can be produced per day is not as high as some of the methods discussed in this section.

Both arc-discharge and laser-ablation techniques involve sublimation of graphite in an atmosphere of rare gases. The furnace has been brought to temperatures above 3200 $^\circ$C, and then the rapid condensation of carbon atoms in a chamber which has a strong temperature gradient. Both these methods have the advantage of highly graphitized CNS product and the drawback that (i) they rely on evaporation of carbon atoms from solid targets at temperatures > 3000 $^\circ$C, and (ii) the nanotubes are very much tangled which makes difficult the purification and application of the samples. These methods are now less used mainly because of the lack of control over growth conditions.

2.3.1 Catalytic Chemical Vapour Deposition

When the cost of CNS production comes into account, the first consideration is the synthesis method. Almost every type of carbon nanostructures have been produced since 1960 by catalytic chemical vapour deposition (CCVD) of hydrocarbons in the presence of a catalyst because of their low cost and scalability for mass production (Amelinckx et al, 1994). Generally, the chemical vapour deposition (CVD) process includes catalyst assisted decomposition of carbon bearing gas, in a tube reactor at a sufficiently high temperature and

growth of carbon nanostructures over the catalyst (Fig. 2.6). The history of CVD for the synthesis of CNS dates back to nineteenth century. In 1890, French scientists observed the formation of carbon filaments during experiments involving the passage of cyanogens over red-hot porcelain (Schultzenberger and Schultzenberger, 1890). By mid-twentieth century, CVD was an established method for producing carbon fibers utilizing thermal decomposition of hydrocarbons in the presence of metal catalysts. In 1952 Radushkevich and Lukyanovich published a range of electron micrographs clearly exhibiting tubular carbon filaments of 50-100 nm diameters grown from thermal decomposition of carbon monoxide on iron catalyst at 600 $^{\circ}$C (Radushkevich and Lukyanovich, 1952). In the same year, another Russian group, Tesner and Echeistova, also reported similar carbon threads on lampblack particles exposed to methane, benzene or cyclohexane atmospheres at temperatures above 977 $^{\circ}$C (Bacon, 1960). In 1953, Davis et al. (Davis et al, 1953) published an article on carbon nanofibers grown from the reaction of CO and Fe_2O_4 at 450 $^{\circ}$C in blast furnace. In the 1970s extensive works were carried out independently by Baker and others to synthesize and understand tubular nanofibers of multi-layered carbon (Baker et al, 1972; Baker et al, 1973). A similar approach was used by Amelinckx and co-workers and others (Amelinckx et al, 1994) to grow MWCNT. It is also possible to generate SWCNT via pyrolytic methods. In this context, Dai et al. (Dai et al, 1996) reported the generation of SWCNT via thermolytic processes involving Mo particles in conjunction with CO at 1200 $^{\circ}$C. This technique resulted in the production of large quantities of SWCNT bundles when Kong et al. (Kong et al, 1998a) pyrolyzed methane in the presence of iron oxide at 1000 $^{\circ}$C over amorphous silica particles. Following these achievements, several groups exploited the CVD process to generate large amounts of SWCNT. Large-scale synthesis of aligned carbon nanotubes was achieved by the CVD technique and iron as catalyst by Li et al. (Li et al, 1996). High-quality SWCNT have been grown on patterned silicon wafers by the use of catalysts by the CVD technique by Kong et al. (Kong et al, 1998b). Thus, today's most popular technique, the CVD, may probably be the most-ancient technique of growing CNS in the name of filaments and fibers.
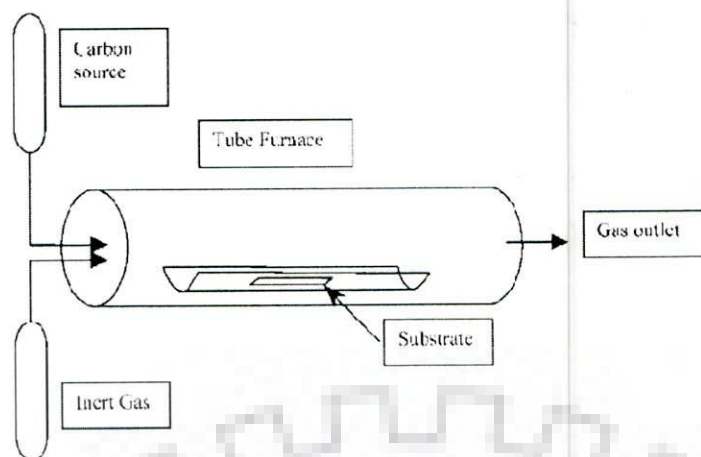
Fig. 2.6: Schematic diagram of a typical CCVD set-up (Oncel and Yurum, 2006).

The parameters which can be changed to obtain different morphologies of CNS and degrees of graphitization by this method are e.g. type of catalysts, growth temperature, particle size, source of hydrocarbon, substrates etc.

One may have variety of choices for catalyst from transition metals and their mixtures to even semiconductors in the form of metallic or their oxides (Dupuis, 2005; Takagi et al, 2006; Liu et al, 2009). The yield and crystallinity of nanotubes have been observed to be improved by the use of catalyst in the form of solid solution such as Co–Fe or Co–Ni (Dupuis, 2005). The catalyst can be deposited (i) from a suspension of nanoparticles (Cheung et al, 2002), (ii) in thin film by sputtering (Liu et al, 2009) or vacuum evaporation (Takagi et al 2006), (iii) by impregnation or spin coating with a solution of a metal salt or organometallic compound (Fujiwara et al, 2005; Jeong et al, 2005) or (iv) by loosely dispersing sol gel derived powder (Rana et al, 2010).

The most commonly used substrates are graphite (Baker et al, 1972), quartz (Kumar and Ando, 2003), silicon (Hata et al, 2004), silicon carbide (Ding et al, 2003), silica (Kitiyanan et al, 2000), alumina (Hongo et al, 2002), $CaCO_3$ (Couteau et al, 2003), magnesium oxide (Ward et al, 2003), zeolite (Kumar and Ando, 2005), porous alumina (Hu et al, 2001, Sarkar et al, 2007) etc. Substrate material, its surface morphology, texture and catalyst-substrate interaction greatly affect the yield and quality of the resulting CNS.

The growth temperatures are typically in the range of 500-1000 $^{\circ}$C and there is a temperature above which CNS forms (Cui et al, 2003) for a particular size and composition of a catalyst. Similarly, by varying growth temperature the morphology of the CNS can also change for a similar composition of catalyst (Iyuke et al, 2009). It should also be noted that different catalyst composition would have their optimum catalytic activity at different temperatures.

22

Beside growth temperature, the size of the catalyst is also an important factor in deciding the morphology of the CNS. On particles of size less than 5 nm, Gohier et al. (Gohier et al, 2008) have observed growth of SWCNT at 700 ^{o}C, while on particles of sizes more than 15 nm MWCNT grows for cobalt catalyst. MWCNT have been found to grow on particles having size even less than 8 nm (Huh et al, 2003) to several hundreds of nanometers at temperature lying in the range between 750-950 ^{o}C (Jang et al, 2003; Terrones et al, 1997). Carbon fibers have been grown on cobalt oxide catalyst of relatively smaller sizes of 10-70 nm as well as larger sizes of 200-350 nm at 700 ^{o}C (Manafi and Badiee, 2003) whereas for nickel oxide catalyst, CNF grows on catalysts of size 16 nm at 600-750 ^{o}C (Kvande et al, 2006).

The carbon precursor is typically a gaseous hydrocarbon such as methane (Kong et al, 1998a), ethylene (Fan et al, 1999), acetylene (Li et al, 1996), benzene (Sen et al, 1997), xylene (Wei et al, 2002), carbon monoxide (Nikolaev et al, 1999) etc. that is sometimes diluted in a carrier gas (e.g. nitrogen, helium or argon). The total pressure usually lies in the range from a few Pa to atmospheric pressure. The molecular structure of the precursor affects the morphology of the CNS grown (Shaikjee and Coville, 2012). Baker and Harris (Baker and Harris, 1978) reported that unsaturated hydrocarbons such as C_2H_2 had much higher yields and higher deposition rates than saturated gases (e.g. C_2H_4). They also observed that saturated carbon gases tended to produce highly graphitized filaments with fewer walls compared with unsaturated gases. Thus, hydrocarbons such as methane and carbon monoxide are commonly used for SWCNT growth (Kong et al, 1998a; Nikolaev et al, 1999), whereas hydrocarbons such as acetylene and benzene, which are unsaturated and thus have high carbon content, are typically used for MWCNT growth (Dai et al, 1999; Piedigrosso et al, 2000; Endo et al, 1993). Commonly efficient precursors of MWCNT (viz. acetylene, benzene, etc.) are unstable at higher temperature and lead to the deposition of large amounts of carbonaceous compounds other than the nanostructures. Methane is commonly used as the carbon source for SWCNT growth because it is a kinetically stable hydrocarbon and undergoes the least pyrolytic decomposition at high temperatures, typically 900 ^{o}C (Kong et al, 1998a; Dai et al, 1996). It may be recalled that high temperature is favoured for less defective and well crystallized nanotubes, and hence it is important to select a hydrocarbon which does not thermally decompose to form unwanted amorphous carbon at high temperatures. Similarly, CO has been used to grow SWCNT at elevated temperatures (Nikolaev et al, 1999).

As compared to arc-discharge and laser-ablation methods, CCVD is a simple and economic technique for synthesizing CNS at low temperature and ambient pressure and therefore less

amount of energy is consumed though sometimes in crystallinity, arc- and laser-grown CNS are superior to the CCVD grown ones. However, in yield and purity, CCVD beats the arc and laser methods, and when it comes to structure control or architecture, CCVD is perhaps the only technique to be used. CCVD is versatile in the sense that it offers harnessing plenty of hydrocarbons in any state (solid, liquid or gas), enables the use of various substrates, and allows CNS growth in a variety of forms, such as powder, film, aligned or entangled, straight or coiled nanotubes, or a desired architecture of nanotubes on predefined sites of a patterned substrate. It also offers better control on the growth parameters.

There are few other methods of producing carbon nanostructures. Among the later introduced techniques two efficient methods are plasma enhanced chemical vapour deposition and laser assisted catalytic chemical vapour deposition. Plasma-assisted methods are especially attractive for the growth of carbon nanotubes on temperature-sensitive substrates and devices. The plasma enhanced CVD method generates a glow discharge in a chamber or a reaction furnace by a high frequency power applied to both electrodes. In the later case, the energy input is partially or entirely provided by the photo-thermal effect induced by a laser beam. There also exist some methods like electrolysis which involves a liquid phase process and is able to produce MWCNT (Hsu et al, 1996). The process involves graphite electrodes immersed in molten LiCl under an Ar atmosphere, with a dc voltage applied between the electrodes. It was proposed that at temperatures above 600 $^{\circ}$C, graphite dissolves in molten Li in order to yield Li_2C_2 suggesting a key step in cathode dissolution and subsequent nanostructure formation (Hsu et al, 1996). The liquid-phase electrolytic method has not been widely used probably because the nanotube yield is difficult to control and the technique has not been able to produce SWCNT. In addition to high-energy lasers, arc-discharge and thermal routes, solar energy offer an alternative route to produce CNS. Laplaze et al. (Laplaze et al, 1998) have managed to produce CNS, when solar energy is focused on a carbon-metal target in an inert atmosphere. Solar energy is capable of vaporizing graphite-metal targets because the average incident solar flux in such experiments is close to 500 Wcm^{-2} and can reach a front temperature of 2528 $^{\circ}$C (Guillard et al, 1999). Recently, it has been proved that it is possible to generate a more powerful solar furnace (1000 kW) that results in temperatures close to 3128 $^{\circ}$C, which can increase significantly the yields of fullerenes and nanotubes (Alvarez et al, 1999).

2.3.2 Growth of Carbon Nanostructures by CCVD

It is evident that for various applications CNS of different morphologies are required. Despite significant progress in CNS research over the years, we are still unable to control the synthesis of CNS so as to obtain well-defined reproducible properties in a batch of large quantities by a cost-effective process. It has been claimed that the catalytic growth of carbon nanostructures takes place by dissolution of carbon and their precipitation on a moving catalytic particle surface (Oberlin et al, 1976). The morphology and the diameter distribution of CNS depend on the size, shape and composition of the catalyst, the growth temperature and other growth conditions. In a recent investigation Zhu et al. (Zhu et al, 2008) used high resolution transmission electron microscope (HRTEM) images to show a correlation between the chirality of the nanotube and the structure of the catalytic nanoparticle. CNS growth mechanism has been debatable right from its discovery. Based on the reaction conditions and post deposition product analyses, several groups have proposed different possibilities which are often contradictory and there is no unanimity on CNS growth mechanism till date.

A hydrocarbon vapour when comes in contact with the 'hot' metal nanoparticles, first decomposes into carbon and hydrogen species and carbon gets dissolved into the metallic catalysts. During in-situ growth of CNT on iron nanoparticle in environmental transmission electron microscope (ETEM) it has been observed by Hoffman et al. (Hofmann et al, 2007) by X-ray photoelectron spectroscopy (XPS) that initially there is extensive formation of carbon-iron bonds as indicated by XPS peaks at ~ 282.6 eV but this peak is replaced by C-C peak ($\sim$ 284.5 eV) corresponding to sp^2 bonded graphitic carbon. In between, there is a transitory presence of carbidic carbon (~ 283.4 eV) before graphitic carbon forms. These authors felt that initially C-Fe bond forms due to chemisorptions.

Yoshida et al. (Yoshida et al, 2008), while observing in-situ growth of CNT in ETEM, noted significant change in shape of nanoparticles of catalyst during growth of both SWCNT and MWCNT respectively on relatively smaller and larger size catalyst particles. Hoffman et al. (Hofmann et al, 2007) have also observed 'dynamic reshaping' of the nickel catalyst nanoparticles during growth of CNS for which there is no plausible explanation. It appears that there is surface melting of metallic catalyst nanoparticles and the surface liquid moves under the action of capillary forces during growth of CNS. If there is surface melting then the decomposed carbon may get dissolved in the molten surface layer to show extensive formation of C-Fe bonds.

Gomez-Gualdron et al. (Gomez-Gualdron et al, 2012) has carried out molecular dynamic simulation studies and observed that carbon precipitates at the interface of the metal catalyst to form carbon rings as demonstrated in Fig. 2.7. According to this study, the growth of CNS takes place in following steps: (1) carbon dissolution into the metal catalyst nanoparticle, (2) carbon segregation to the nanoparticle surface, (3) formation of CNS on the metal surface identified as chains, isolated rings (usually branched) and concatenated rings (usually branched), (4) "merging" of carbon nanostructures to form a nanotube cap, (5) lifting-off of the nanotube cap and (6) incorporation of carbon to the nanotube rim at the nanoparticle surface for increasing the length of the tube. It has been claimed that growth terminates when the catalyst particle gets poisoned by impurities or after the formation of a stable metal carbide (Schunemann et al, 2011; Dresselhaus and Avouris, 2001).
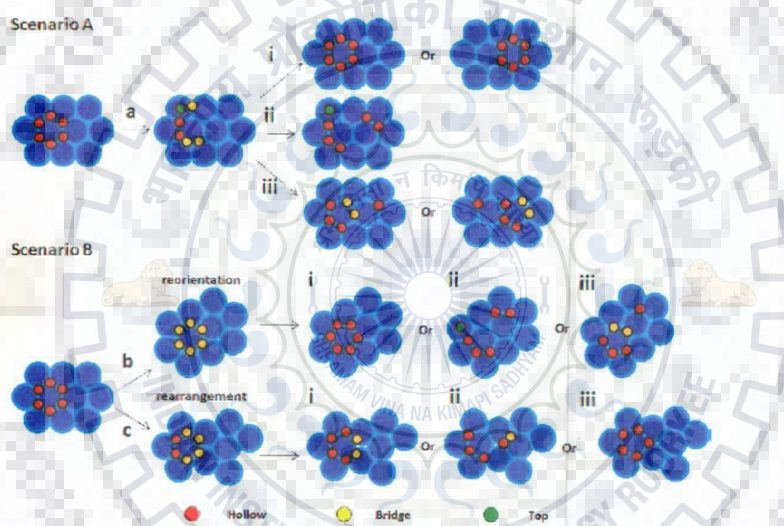
Fig. 2.7: Schematics scenario of the surface region of nanoparticle catalyst, showing early formation of carbon rings. In scenario A (top), within a time interval Δt, the surface pattern of stable ring breaks down in (a). In scenario B (bottom), within a time interval Δt, the surface pattern of stable ring undergoes either a reorientation in (b) or a rearrangement in (c). Hollow positions are stable valley positions over hexagons of spheres, bridge positions are on the periphery of the sphere along the boundary while top positions are directly over the top of the sphere (Gomez-Gualdron et al, 2012).

There are two specific circumstances of strong and weak interaction between the catalyst and the supporting substrate, which have been identified (Fig. 2.8) and it has been claimed that this interaction is important in deciding the modes of CNS growth. When the catalyst-substrate interaction is weak (metal has an acute contact angle with the substrate),

hydrocarbon decomposes on the top surface of the metal, carbon diffuses down through the metal, and CNS precipitates out across the metal bottom, pushing the whole metal particle up detaching it from the substrate (Fig. 2.8(a)). As long as there is no cap formation at the top of the metal catalyst nanoparticle and it is open for fresh hydrocarbon decomposition, the concentration gradient exists in the metal allowing carbon diffusion and CNS continues to grow longer. This is known as "tip-growth model". When the catalyst-substrate interaction is strong (metal has an obtuse contact angle with the substrate), initial hydrocarbon decomposition and carbon diffusion take place similar to that in the tip-growth case, but the CNS precipitation fails to push the metal particle up because of strong interaction with the substrate and carbon precipitates out as a hemispherical dome (the most favorable closed-carbon network on a spherical nanoparticle) which then extends up in the form of seamless graphitic cylinder. Subsequent hydrocarbon decomposition takes place on the lower peripheral surface of the metal nanoparticle and as-dissolved carbon diffuses upward. Thus, CNS grows up with the catalyst particle rooted on its base; hence, this is known as "base-growth model". However, molecular dynamic simulation results (Charlier et al, 2007) demonstrated a cap formation to be a necessary step for nanotube growth which is contradicting the tip growth mechanism proposed. Raty et al. (Raty et al, 2005) also have observed formation of a sp^2 bonded cap on iron nanoparticle catalyst by diffusion of C atoms and due to weak adhesion with the particle, the cap detaches and floats for SWCNT to grow from the root. Charlier et al. (Charlier et al, 1997) have shown through atomistic calculations that only MWCNT may grow with an open end. Gualdron et al. (Gomez-Gualdron et al, 2012) have investigated the effect of metal/support interaction strengths for nanoparticles of Ni and observed that the direction of growth on a given facet of the catalyst depends on this interaction. Also, it was observed that for strong interaction between the substrate and the particle, the stretching of the catalyst particle due to capillary action results in easier lifting of the cap. However, the study could not decide whether the facet of nanoparticle is acting as a template for the nascent nanotube or the emerging nanotube conditions the structure of the surface of the nanoparticle adjacent to it due to higher strength of C-C bonds compared to those of M-M bonds (Gomez-Gualdron et al, 2012) in the prevailing context of melting point depression of metallic nanoparticles (Qi, 2005).
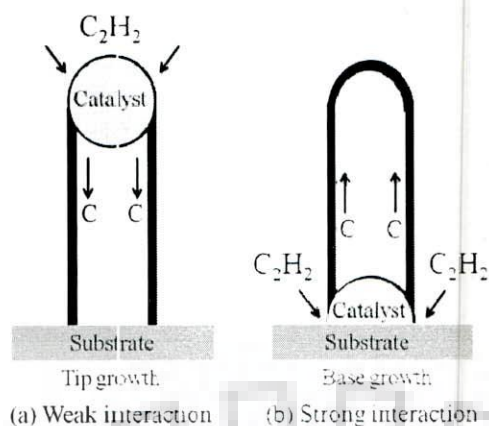
Fig. 2.8: Catalytic growth model for CNS for (a) weak interaction (tip-growth), and (b) strong interaction (base-growth).

A large number of investigations have been carried out to establish a concrete mechanism of tip or base growth of CNS. Table-2.2 summarizes some of the results of tip and base-growth mode.

Table-2.2: Results summarizing tip and base-growth of SWCNT, MWCNT and other CNS.

Catalyst	Size (nm) **	Temp. (°C)	Type of catalyst	Type of CNS	Mode of growth
Fe (Rummeli et al, 2007)	<5p (from image)	800	Balled up catalyst on oxide substrate	MWCNT	Tip and Base/Root
Fe (Lee and Park, 2001a)	100f	550-950	Film thermally deposited on silicon oxide and balled up at 750-950 °C	Bamboo-like CNT	Tip
Fe-Pt (Schuneman et al, 2011)	1.6 and 3.6p	590-890	Deposited on substrate of thermally oxidized silicon with an additional Al_2O_3 layer	MWCNT	Base
Al/Fe (Matthews et al, 2006)	2/1, 4/1 and 6/1f	700-800	Metal films deposited by plasma sputtering on Au and Mo	MWCNT	Tip (favoured on Au substrates enhancing MWCNT)
		750-900		SWCNT	Base (preferred on Mo promoting SWCNT)
Fe, Co, Ni (Gohier et al, 2008)	<5p and	700	Film deposited onto SiO_2 and annealed at 700 °C	SWCNT	<5 nm: Base-growth (SWCNT)
	>15p			MWCNT	>15 nm: Tip-growth (MWCNT)

28

Catalyst	Size	Temp (°C)	Description	CNT type	Base/Tip
Co (Lee and Park, 2001b)	200f	950	Balled up film on SiO$_2$ substrate	Baboo like CNT	Base
Ni (Abdi et al, 2006)	10-50p	550-650	Balled up from thin layer of catalyst on SiO$_2$	MWCNT	Tip
Ni (Lin et al, 2007)	<6p 7-30p	650-700	Film deposited on a SiO$_2$-coated Si(100) substrate supported on MgO and balled up at 700 °C	SWCNT Bamboo-like MWCNT	Base (for SWCNT) Tip (for MWCNT)
Ni (Horibe et al, 2004)	Ni/Ti: 30/50f Ni/TiO$_x$: 10/50f	540	Ni film on Ti or TiO$_x$ deposited by rf magnetron sputtering	MWCNT	Base (For Ti substrate) Tip (for TiO$_x$ substrate)
Ni, Ni-Au (Sharma et al, 2011)	2f	520	Deposited by physical vapour deposition of metals on perforated SiO$_2$ films	MWCNT CNF	Base Tip
Ni/Cu (Saavedra et al, 2012)	2 nm of Ni p and 8 nm of Cu p	511	Sputtered Bi-metallic layer (Ni/Cu)	Carbon octopi	Tip
Iron oxide (Li et al, 2001a)	1-2 and 3-5p	900	Iron film deposited in air on SiO$_2$ substrate	SWCNT	Base
Fe/Mo oxide (Cassell et al, 1999)	~1p	900	Catalyst made by impregnating silica-alumina support	SWCNT	Base
Ni after reduction from NiO (Helveg et al, 2004)	5-20p	500-540	Nickel nanocrystals in the metallic state formed by reduction of the NiO precursor supported on MgAl$_2$O$_4$.	CNF (larger nano-cluster) MWCNT (smaller nano-cluster)	Tip
Initially oxidized Fe and Ni (Hofmann et al, 2007)	5p	480-700 615	SiO$_x$ supported balled up Ni and Fe catalyst films (thermally evaporated)	CNF SWCNT	Tip (at lower press. and lower temp. for CNF) Base/Root (at higher press. and higher temp. for SWCNT)

**p: particles and f: film

Most of the investigators have used oxide substrate and it is expected that there should be weak adhesion between the catalyst and the substrate. But it is observed that SWCNT grows

by base growth in general while MWCNT grows by tip growth as observed in Table-2.2. Thus, it is apparent that the understanding about the mode of growth is still not clear. It is also observed that the smaller size of catalyst particles promotes the formation of SWCNT while MWCNT grows around relatively larger catalyst particles. However, both MWCNT and SWCNT grow over similar temperature range.

There are still more unresolved issues regarding (i) the presence of liquid phase in the catalyst during growth, and (ii) the diffusion path of carbon in the catalyst to deliver carbon during growth of CNS. There is substantial shape change of the catalyst during growth of CNS and if it is claimed that this is due to deformation in solid catalyst particle, (Hofmann et al, 2007; Yoshida et al, 2008) one will have to identify a significant force responsible for it and explain its origin. It cannot be just broadly attributed to high mobility of atoms in the surface layer. The observed metal carbon bonds are being explained by chemisorption of carbon atoms on nanocatalysts (Hofmann et al, 2007) but these bonds could also be indicative of solution of carbon in liquid phase of the catalyst. Yeshchenko and co-workers (Yeshchenko et al, 2007) have shown that the surface melting of nanoparticles starts at a temperature far below the bulk melting point. Baker et al. (Baker et al, 1972) in their experiments with nickel catalyst and acetylene gas at 600 °C, have observed the change in shape of the catalyst during the growth of CNF and attributed it to vapour-liquid-solid (VLS) mechanism of growth. Their estimate of activation energy for growth has been similar to the activation energy of carbon diffusion in liquid nickel and fiber growth is observed to be diffusion controlled. In the VLS growth, carbon resulting from decomposition of the carbon bearing gas or vapour, gets dissolved in the liquid phase of the catalyst and diffuses to the growing CNS. Tibbetts (Tibbetts, 1984) has claimed that the bending of graphene sheet to tubular growth is energetically favourable due to large anisotropy in surface energy, i.e. high surface energy of other planes of graphite compared to the basal plane. However, the energy of bending is relatively more as the diameter is smaller and beyond some smaller inner radius, formation of the layer may not be energetically favourable for growth due to 'weak maximum' of the difference of chemical potential. This may explain the growth of SWCNT on smaller catalyst particles while MWCNT grows on relatively larger ones. However, he has presumed surface diffusion of carbon through the surface of the catalyst, on the basis the activation energy being similar to that of bulk diffusion of carbon in iron (Baker et al, 1973). However the surface and the bulk diffusion should have distinctly different activation energies.

The uneasiness in assuming the presence of liquid phase in the catalyst particles of Fe, Co, Ni arise possibly from relatively high bulk melting temperatures of these elements compared to the range of growth temperatures of 600-1000 ^{o}C, commonly prevailing during growth of CNS in CCVD. It is now fairly well known that the melting point of particles falls abruptly when the size decreases to the range of nanometers. In the experimental work reported by Takagi (Takagi, 1954), halos in the diffraction pattern indicating melting of thin films of Pb, Sn and Bi of thickness in the range of 1-100 nm were observed by electron diffraction respectively at 287, 203 and 249 ^{o}C. In another experiment, Shin et al. (Shin et al, 2007) observed melting of tin nanowires of radius ranging from 7-30 nm at 214 ^{o}C using differential scanning calorimetry (DSC) and their fragmentation due to Rayleigh instability. Peters et al. (Peters et al, 1997) investigated surface melting of small particles (50 nm diameter) of lead in-situ using X-ray diffraction (XRD) as shown in Fig. 2.9.
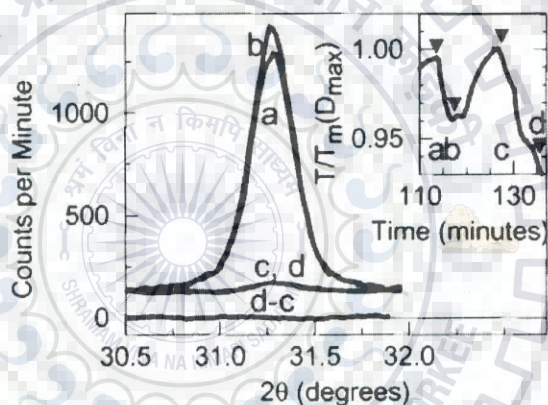
Fig. 2.9: X-ray peak of (111) plane of lead for four time and temperatures indicated by a, b, c and d shown in the time-temperature plot (inset) (Peters et al, 1997).

Between positions a and b below bulk melting temperature, the difference in intensity is attributed to surface melting of 0.5 nm skin at b enveloping the 52 nm crystallites while the bulk melting takes place at c and the peak has almost vanished and it remains in this state till d, indicating presence of supercooled liquid. Buffet and Borel (Buffat and Borel, 1976) first measured the melting point of small gold nanoparticles using a scanning electron-diffraction technique. Their experimental results are quantitatively in good agreement with two phenomenological models where they found that the melting temperature drops to 328 ^{o}C for particles of size 20 Å compared to the bulk melting of Au. It is known that bulk melting is preceded by surface melting due to the weakened state of bonding at the surface as determined even in large crystals by ion backscattering (Dash, 2002). Wang et al. (Wang et al, 1998a) have observed under in-situ transmission electron microscope (TEM), dramatic

transformation of platinum nanocrystals into spherical-like shapes when the temperature was raised above 500 ^{o}C, demonstrating surface melting. Surface melting became obvious also due to coalescence of the surfaces of neighbouring nanoparticles leading to aggregation to a smaller volume of the assembled nanoparticles. Selected area diffraction (SAD) pattern also indicates this change by diffuse rings. The surface melting results in a few atomic layers deep liquid around the still solid core of the nanoparticle. This temperature was much lower than the melting point of bulk metallic platinum.

Yu and Duxbury (Yu and Duxbury, 1995) by their molecular-dynamics simulations for gold clusters, have also observed that for nanoclusters the surface atoms start to diffuse well below the melting point resulting in shape change. Theoretical investigations on thermodynamic model of size-dependent melting of nanoparticles have been reviewed by Nanda et al. (Nanda, 2009) and three different models proposed are – (a) homogeneous melting (HM), (b) liquid nucleation at the surface and its growth to consume the solid core (LNG) and (c) liquid skin melting (LSM). The prediction of LSM model matches better for the experimental results on tin nanoparticles (Lai et al, 1996). The surface melting temperature decreases with size and the driving force for the surface melting is the reduction in surface energy. Thus, the shapes of nanoparticles and the support or substrate, which affect the surface energy, are expected to influence surface melting of nanoparticles. Qi et al. (Qi et al, 2001) have carried out molecular dynamic investigation on melting of mesoscale nanocrystals through surface processes and found start of surface melting of Ni nanocrystals at ~ 708 ^{o}C ($T_{m, 336 atoms}$) compared to bulk melting at ~ 1488 ^{o}C ($T_{m, bulk}$). A quasiliquid skin forms on the surface below the bulk melting temperature ($T_{m, bulk}$), and it thickens as the temperature increases, leading finally to the melting of the entire nanocrystal. The bulk melting temperature has been defined as the temperature at which the thickness of the "skin" diverges to infinity and thus they characterized the mesoscale regime by surface melting. The simulation results show that the order of atoms starts to destroy from the surface and spreads inside to vanish above certain temperature.

It may be remembered that for VLS growth mechanism to operate the entire particle need not be melted. Surface melting of the nanoparticle will be adequate for VLS growth. If the start of CNS growth takes place through formation of rings as shown in Fig. 2.7, it is not yet clear whether it will require the template of solid catalyst. Then, surface melting may provide more appropriate scenario. But the liquid phase also has short range order of atoms and may provide arrangement of atoms as shown in Fig. 2.7. It may be important to note that Hoffman

32

et al. (Hofmann et al, 2007) have reported that there are some catalyst particles, which could not nucleate CNS. This could be due to absence of liquid phase due to their size or may be due to the absence of specific crystallographic plane on the surface which may act as the template for CNS growth.

It has been claimed by some researchers that metal as such does not catalyze the formation of CNS, and there is need for metal carbide formation. The growth of CNS is by decomposition of carbide and the addition of resulting carbon to the growing nanostructure. Ni et al. (Ni et al, 2009) have claimed that formation of CNT by the catalytic decomposition of CH_4 over metallic catalysts of Co, Ni or Fe on MgO substrate requires growth temperatures higher than the decomposition temperature of the respective metal carbides as carbon in the CNT originates from the decomposition of metal carbides to graphitic carbon on the catalyst surface. They have reported a direct relationship between CNT formation and metal carbide decomposition temperature for Ni, Co, and Fe catalysts. It has been claimed that metal carbide formation precedes the CNT or CNF nucleation and may be an intermediate step (Ni et al, 2009). However, the catalytic activity of these metal carbides for hydrocarbon dissociation has not been confirmed. Wirth and others (Wirth et al, 2009) proposed that pure metal is the active catalyst, while metal carbides have sometimes been detected in experiments involving iron catalyst nanoparticles (Oberlin et al, 1976). Hoffman et al. (Hofmann et al, 2007) also have observed transitory presence of carbidic carbon before the appearance of graphitic carbon. Similarly, the formation of iron carbide (Fe_3C) during CNT synthesis from Fe catalyst nanoparticles has also been reported (Sharma et al, 2009). In 2008, Yoshida et al. (Yoshida et al, 2008) performed atomic-scale in-situ observation of acetylene decomposition on Fe catalyst at 600 °C. Electron diffraction analysis of the metal clusters in each frame was reported to match with that of iron carbide corresponding to cementite (Fe_3C). Accordingly, the authors concluded that the active catalyst was in 'fluctuating solid state' of 'iron carbide'. Sharma et al. (Sharma et al, 2011) believe that metastable phase of carbide may form under a dynamic equilibrium for the following reaction $3Ni + C \leftrightarrow Ni_3C$ where the continuous flux of carbon, generated by decomposition of C_2H_2, favours the formation of Ni_3C while the high temperature (>520 °C) favours its decomposition. It is not surprising that metal carbides form prior to the CNT growth as the high carbon affinity of 3d transition metals is reflected by their low enthalpy of carbide formation (Meschel and Kleppa, 1997). Confusion persists because lattice constants of pure metal and their carbide are sometimes very close. For example, the planes fcc Ni (111) or Ni_3C (113) have the same 'd' spacing and diffraction peaks may appear at the same angle. Moreover, for 'nano' particles, some deviation in the lattice constants from

33

that of the bulk crystal may be expected due to limited number of atoms in nanoparticles. Wirth et al. (Wirth et al, 2009), based on their in-situ electron microscopy and XPS analyses, argued that the catalyst exists in pure metallic form: right from the CNT nucleation to the growth termination. Takagi et al. (Takagi et al, 2006) have used non carbide forming catalysts like gold, silver and copper to grow SWCNT by CCVD. Thus, carbide formation may not be an essential step in the growth of CNS. With such a growth picture in mind, one can proceed to other important aspects of the different type of CNS growth.

It has been mentioned earlier that CNS may grow when nanoparticles of oxides of transition metals like Co, Ni or Fe etc are used as catalyst in CCVD. Since the environment during growth of CNS is highly reducing due to decomposition of carbon bearing gas, it may be questioned whether oxide as such acts as catalysts or the metal nanoparticles forming after its reduction. Baker et al. (Baker et al, 1982) claimed that FeO appears to be a much better catalyst than metallic iron for the formation of filamentary carbon, and thus claimed that there was no reduction before to growth. The oxide catalysts have often been subjected to pretreatment in reducing environment containing hydrogen, and this step may serve the purpose of reduction to metals (Amama et al, 2008). Hernadi et al. (Hernadi et al, 1996) also considered that prior reduction pretreatment of iron oxide is not necessary since the hydrocarbon atmosphere is able to reduce the catalyst to the required extent under prevailing conditions during growth of CNS.

2.3.2.1 Single Walled Carbon Nanotubes

The preferred conditions for the growth of SWCNT have been studied and it has been observed that the size of the catalyst is probably the most important parameter for the nucleation of SWCNT. The dependence of catalyst size on the formation of SWCNT has been reported by various researchers (Dai et al, 1996; Li et al, 2001a; Cheung et al, 2002). Li et al. (Li et al, 2001b) found the upper limit for SWCNT growth occurred at catalyst sizes between 4 and 8 nm. For catalyst size above 8.5 nm, no single walled structures were observed. Li et al. (Li et al, 2001a) also grew SWCNT from discrete catalytic nanoparticles of various sizes. Their TEM studies indicated that the nanotube diameters were closely related to the size of the catalytic nanoparticles. Cheung et al. (Cheung et al, 2002) prepared monodispersed nanoclusters of iron with diameters of 3, 9, and 13 nm. Single walled and double walled nanotubes were nucleated with nanoclusters having 3 and 9 nm diameters, whereas only MWCNT were observed with the 13 nm nanoclusters. These works clearly suggest that SWCNT are favoured when the catalyst particle is $\sim$ 5 nm or less. However, it is worth

mentioning that there are reports which suggest that SWCNT can be grown from larger catalyst particles. One hypothesis put forward was that bundles of nanotubes could be precipitated from a single metal particle, and that the bundle formation would be linked to the nature of the metal surface (Colomer et al, 1999). As mentioned earlier, binary catalyst mixtures have also been reported to increase the yield of SWCNT (Dupuis, 2005). Hafner et al. (Hafner et al, 1998) further suggested that the growth rate of SWCNT is limited by the carbon supply to the catalyst particles, whereas for MWCNT, the growth is limited by the diffusion of carbon through the catalyst particle. The authors demonstrated that SWCNT could in fact be grown from a highly diluted gas mixture of C_2H_4. A limited carbon supply will likely allow the structures to form more slowly, giving each carbon atom more time to anneal to its lowest energetic configuration as shown by energetics calculations.

2.3.2.2 Multi Walled Carbon Nanotubes

In comparison to SWCNT growth, MWCNT growth is usually observed on catalyst particles of relatively larger size. MWCNT arrays were synthesized by water assisted CVD using iron catalyst of size 15-50 nm at 750 $^{\circ}$C (Yun et al, 2006). The diameter of the tube, in terms of number of walls increases with growth time, and depends on the size of the catalysts. Vinciguerra et al. (Vinciguerra et al, 2003) have taken into account the diffusion of carbon into the catalyst particle and the consequent extrusion of the walls for the formation of MWCNT, with the coordinating action of transition metals and with a direct correlation of the tube diameter with that of the catalyst. Single or few-walled carbon nanotubes have been grown over Ni, Fe, Co catalyst of size less than 5 nm whereas the large MWCNT have been grown on the same respective catalyst of size greater than 15 nm at 700 $^{\circ}$C (Gohier et al, 2008). Jehng et al. (Jehng et al, 2008) found the optimum growth temperature for MWCNT was about 640-670 $^{\circ}$C, and concluded that, the particle size and structure of the catalyst controls the formation of MWCNT.

2.3.2.3 Double Walled Carbon Nanotubes

Hafner et al. (Hafner et al, 1998) produced a mixture of SWCNT and DWCNT (double walled carbon nanotube) by the catalytic decomposition of C_2H_4 at 700–850 $^{\circ}$C over Mo and Fe/Mo catalysts, and reported that the DWCNT proportion increases from 30 % at 700 $^{\circ}$C to 70 % at 850 $^{\circ}$C. Yamada et al. (Yamada et al, 2006) reported the fabrication of high-purity DWCNT forest by controlling the catalyst (Fe) film thickness via a water-assisted CVD technique. Unfortunately, according to these reports usually mixtures of DWCNT and SWCNT are

generated, in addition to metal particles, amorphous carbon and multilayered carbon nanotubes.

2.3.2.4 Carbon Nanofibers

The ability to control and tailor the structure of nanofibers (stacked or herringbone) has been demonstrated by Rodriquez et al. (Rodriguez et al, 1995). The general concept is the creation of a faceted catalyst particle so that carbon feedstock decomposition occurs at certain faces whereas carbon precipitation occurs at other faces. The alignment and crystalline perfection of the graphitic platelets is a parameter that is governed by the nature and shape of the catalyst particle and orientation of the precipitating faces as proposed by Boellard et al. (Boellaard et al, 1985). Under certain conditions of gas composition, temperature, and catalyst composition, the catalyst particles undergo surface reconstruction to form unique geometrical shapes which drive the formation of nanofibers (Chambers and Baker, 1997). For example, the herringbone structure was found to grow from Fe-Cu (7:3) particles in a C_2H_4–H_2 (4:1) gas mixture at 600 °C, whereas the stacked structure formed from Fe-based catalyst in a CO-H_2 (4:1) gas mixture at 600 °C (Rodriguez et al, 1995). The formation of herringbone structures is favoured when the catalyst particle is an alloy (Kim et al, 1992; Park et al, 2000). Nolan et al. (Nolan et al, 1998) have suggested that hydrogen plays a significant role in the formation of nanofibers. This is because the presence of hydrogen in abundance can cap the dangling bonds and allow free plane edges to be left behind, whereas without hydrogen termination, the more stable form of the carbon filament would be closed tubular graphene shells where there are no dangling bonds.

2.3.2.5 Other Nanostructures

The occurrence of defects (e.g., pentagons or heptagons) would cause the nanotube to bend during growth. When the temperature range in the CVD processes is about 428-1128 °C, "curly" and "coiled" nanotubes are common variations to the perfectly linear nanotube. The growth of various shapes of nanotubes, especially wavy and helical tubes, was investigated by Amelinckx et al. (Amelinckx et al, 1994). The concept of a spatial velocity was introduced to describe the extrusion of carbon from the catalyst particle to form the nanotube. Essentially, when the extruded carbon material was uniform, straight nanotubes are obtained, whereas mismatch between the extrusion velocity by the catalytic particle and the rate of carbon deposition caused the nanotube to deform elastically into complicated patterns such as the helical shape. Nanotubes containing bamboo compartments are also commonly observed. A growth model for bamboo-shaped carbon nanotubes was proposed by Lee and Park (Lee and

Park, 2000). They showed that the bamboo-shaped compartment layers were due to the surface geometry of the catalyst particle and the precipitation of carbon sheets from the bulk of the catalyst particle. Li et al. (Li et al, 2001c) found that when using a higher deposition pressure of carbon feedstock, the nanotubes became bamboo in structure. They argued that at high pressures, the carbon concentration was sufficiently high to cause bulk diffusion of carbon through the catalyst, forming the bamboo compartments behind the catalyst particle. In the literature, bamboo structures are sometimes called "nanofibers" though the bamboo structure actually contains graphene walls parallel to the filament axis, which suggest that these structures would inherit the physical properties of the "nanotube". Rana et al. (Rana et al, 2009) demonstrated synthesis of CNR (Carbon Nanoribbons) using $LiFePO_4$ as a catalyst by thermal CVD of acetylene at 650 °C. In another work the same group have shown modification in the structure of MWCNT by incorporating lithium in cobalt and nickel containing oxide based catalyst (Rana et al, 2010).

2.4 Application of Carbon Nanostructures

In the following sections several interesting applications of carbon nanostructures have been described.

2.4.1 Light Weight Materials

The automotive industry is under constant pressure to design vehicles capable of meeting increasingly demanding challenges such as improved fuel economy, enhanced safety and effective emission control, and is a material-intensive industry. A reduction in vehicle weight can lead to an impressive improvement in fuel usage. CNS have received much attention for their strength, each tube has the potential to inspire visions of a super-strong, super light weight material that could enable researchers to engineer the structures and fabrics of the future. The extraordinary mechanical, thermal and electrical properties of carbon nanotubes have prompted intense research into a wide range of applications in structural materials. Attempts have been made to develop advanced engineering materials with improved or novel properties through the incorporation of carbon nanotubes in matrices which includes polymers, metals and ceramics. Several articles have been published on CNS based composites and its different aspects in detail (Hu et al, 2006). In the case of metal matrix nanocomposites, incorporation of as little as volume percentage of CNS has led to a much greater increase in strength, hardness etc. (Li et al, 2009). Such potential improvements have great implications for the automotive, aerospace and in particular, the defense industries due to the drastic weight savings and exceptional properties that can be achieved. Potential

37

aerospace applications may include ventral fins for aircrafts, as well as fan exit guide vanes for commercial airline jet engines. Both components require high stiffness and strength, low weight as well as resistance to erosion from rain, airborne particulates and hail. In addition, exceptionally high thermal conductivities, possible in selected nanocomposites, will find applications in thermal management applications in computers. Metal matrix nanocomposites can lead to significant savings in materials and energy, and reduce pollution through the use of ultra-strong materials that exhibit low friction coefficients and greatly reduced wear rates (Rohatgi and Schultz, 2007). Dong et al. (Dong et al, 2001) have investigated the effect of CNT addition in Cu matrix and observed that CNT/Cu nanocomposite reduces the friction coefficient of Cu and also the wear loss. While with Al-CNT composite the wear data suggests that the presence of CNT in the matrix can reduce the direct contact between the Al matrix and the steel pin, and thereby decrease the friction coefficient due to the presence of carbon nanotubes (Zhou et al, 2007). By reducing the friction coefficient, the energy loss experienced by components in frictional contact will be reduced, improving efficiency of mechanical systems. In addition, the authors believe that the incorporation of CNS having relatively short lengths may allow them to slide and roll between the mating surfaces and result in a decrease of the friction coefficient. CNS have also been incorporated in different ceramic matrix to increase their toghness (Zhan et al, 2003). There have been signicant R & D activities involving CNS/polymer nanocomposites for automotive applications: major focuses were to enhance the prime structural properties and the robustness of new composite materials as well as their automation and large-scale production. Nanocomposites are an emerging class of polymeric materials exhibiting excellent mechanical properties, enhanced modulus, dimensional stability, flame retardancy, improved scratch and mar resistance, superior thermal and processing properties and enhanced impact resistance, making them suitable to replace metals in automotive and other applications. The commercialization of polymer nanocomposites started in 1991 when Toyota Motor Co. first introduced nylon-6/clay nanocomposites in the market to produce timing belt covers as a part of the engine for their Toyota Camry cars (Kojima et al, 1993). The real surge in the commercialization of nanocomposites production has occurred over the last ten years. Very recently Shin et al. (Shin et al, 2012) have demonstrated a new hybrid composite containing CNT with the gravimetric toughness approaches 1,000 Jg^{-1}, far exceeding spider dragline silk and Kevlar and this material is said to be the best that exceeds the toughness that of previously known materials. The realized structural components made from CNT/polymer nanocomposites are automobile bumpers (Breuer and Sundararaj, 2004). Andrews et al. (Andrews et al, 1999)

38

reported an increase in tensile strength by 90%, modulus by 150%, and electrical conductivity by 340% by incorporation of 5 wt.% of SWCNT.

Nanocomposites based on CNS are an emerging technology in the automotive industry and have attracted considerable attention worldwide. The commercial success of nano-enabled products for the automotive market has been slow and used currently only in niche applications such as external body parts, interior and under-bonnet parts, coating and fuel system components, etc., but is expected to be a major growth area in the coming era. According to a recent market report released by Frost and Sullivan, it is expected that carbon nanotubes will penetrate about 3.6% within automotive composites.

Polymer-based composites have been used also as critical components in aircraft and space shuttle. Organic polymers with uniformly dispersed CNS may enable polymer materials to withstand the harsh space environment and may be used for the purpose of critical weight-reduction on current and future space systems. Self-frigidizing and self-passivating nanocomposite materials could be used to construct space vehicle components that are both highly resistant to space-borne particles and resistant to degradation from electromagnetic radiation, while reducing the overall weight of the spacecraft (Njuguna and Pielichowski, 2003). All of these characteristics and advantages can be found in CNS/polymer nanocomposites. CNS/polymer nanocomposites also offer a unique opportunity for improved durability of physical and structural properties, such as the coefcient of thermal expansion and antielectromagnetic radiation, in an inter planetary environment, which would be especially useful in constructing large apparatus in human space exploration beyond the low-earth orbit. In summary, this type of analysis provides insight into the ultimate advantages of CNS/polymer nanocomposites for aerospace applications.

There are still many opportunities to employ CNS based nanocomposites for different structural applications such as materials used in civil engineering and public security. There have been numerous studies that have aimed at improving the low tensile strength, stiffness and toughness of cementitious materials by incorporating CNS (Konsta-Gdoutos et al, 2010). Recently a new approach has been initiated under which CNS are grown directly on the surface of matrix and matrix precursor particles. This novel cement hybrid material was synthesized in which CNS are attached to the cement particles, and said to increase the compressive strength by two times, and the electrical conductivity of the hardened paste by 40 times (Nasibulina et al, 2010). Hunashiyal et al. (Hunashyal et al, 2011) investigated the behaviour of cement beams reinforced with MWCNT. Compared with the plain cement

control beams, they have seen that the flexural strength of the cement composite can be increased by 43.75% due to MWCNT additions of only 0.75 wt.%.

2.4.2 Electrode Materials in Li-ion Batteries

2.4.2.1 Lithium-ion Batteries

Modern human life relies on a steady and continuous energy supply. However, the energy sources available in whatever forms it may require energy storage, and is one of the great challenges in this century. An elusive piece of the alternative energy puzzle is storage: how to save it for when it is needed or carry it around to use where it is needed. In both cases, energy density is the key parameter and in the later case, weight matters, too. A battery is kind of device that stores chemical energy and converts it to electrical energy efficiently without gaseous exhaust. Rechargeable lithium ion batteries are undergoing rapid expansion and providing power to many portable devices, in our information-rich and mobile society. Moreover, due to its high power and high energy, the lithium ion battery is the most promising candidate for next generation energy storage devices for hybrid or electrical vehicles (HEV and EV), which are expected to partially replace conventional vehicles, and help to relieve air pollution and prevent climate change (Broussely, 1999; Terada et al, 2001). Since early 1990's motor companies like Tesla, Chevrolet, Nissan, Renault, Mahindra, GM, Zenn, Tata started making car incorporating lithium ion battery technology. But still to compete with the petrol based cars in terms of price and fuel efficiency or battery life for each cycle, the charge density of the battery have to be increased. Accordingly, the development of the battery has been much slower and has not kept pace with the rate of progress in other electronics industries which fostering following Moore's law according to which the number of transistors on integrated circuits doubles approximately every two years. Millions of Li-ion cells are produced every year for portable applications, but this is not enough to take care of the present market demand. Meanwhile, safety is the most important issue for the batteries, as the cells contain combustible material and oxidizing agents and have a high risk of fires and explosions (Balakrishnan et al, 2006). The performance of these devices depends intimately on the properties of their materials. The first-generation lithium-ion battery consisted of electrodes with millimetre sized particles was used in only low-power devices at that time. When the size of materials is reduced to the nanoscale dimension, their properties can change dramatically. In addition, nanostructures also afford new exciting opportunities with a broad range of nanoscale properties including electrochemical, mechanical and interfacial properties (Bruce et al, 2008).

40

Table-2.3: Comparison of different types of rechargeable batteries (Tarascon and Armand, 2001).

Type of battery	Voltage (V)	Specific power (WKg^{-1})	Specific energy (WhKg^{-1})
Lead-acid	2.0	180	30-40
Ni-Cd	1.2	150	40-60
Ni-MH	1.2	250-1000	30-80
Li-ion	3.0-3.8	250-500	90-180

Table-2.3 compares the energy densities of the different types of rechargeable batteries. As shown, lithium-ion batteries deliver the highest energy density. Although the nickel-metal hydride and lithium ion battery are both excellent in terms of their volumetric energy density, the lithium ion battery is superior in weight energy density, as it provides 1.5 times as much energy as the nickel metal hydride battery does. The nominal voltage of a lithium ion battery is around 3.7 V, which is three times that of conventional nickel batteries (1.2 V) such as Ni–MH and Ni–Cd. Lithium-ion batteries have the highest energy density among all rechargeable battery systems. In order to compare the different battery types on the level of their performance, one can also make use of the so-called Ragone chart (Fig. 2.10), which plots specific power versus specific energy, where one can compare easily the different batteries suitable for use in either EV (which primarily need energy) or HEV (which primarily need power) (Bossche et al, 2006). Obviously, lithium-ion batteries offer a balanced combination of high power and energy density. However, the current technologies for producing rechargeable lithium-ion batteries do not completely satisfy all the requirements.
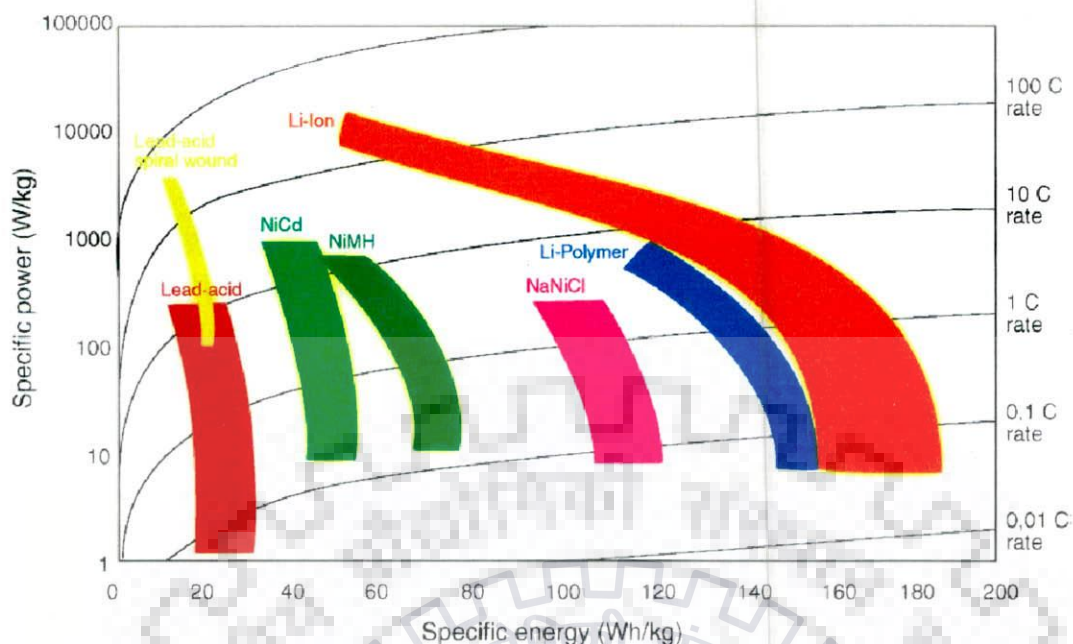
Fig. 2.10: Comparison of the different battery technologies in terms of specific power and specific energy density (Bossche et al, 2006).

The primary lithium batteries were developed in 1970 on the basis of pioneered research of Lewis using lithium metal as the anode (Robinson, 1974). The motivation to use lithium metal as the anode in a battery system was based on the fact that lithium is the most electronegative (-3.04 V versus the standard hydrogen electrode) and the lightest element (6.94 gmol^{-1} and 0.53 gcm^{-3}) (Tarascon and Armand, 2001). If lithium metal is used for anodes in batteries, a high energy density battery system could be obtained. The primary lithium batteries quickly found wide applications in electronic watches, calculators and implantable medical devices. Soon after research started on rechargeable lithium batteries using TiS$_2$ as the positive electrode and lithium metal as the negative electrode (Whittingham, 1977). TiS$_2$ is a very stable compound with a layered structure for repeated lithium intercalation and de-intercalation. But the problem associated with dendritic growth on the surface of the lithium metal electrode caused by the combination of lithium metal and liquid electrolyte during long-term cycling, which penetrate the porous separator causes short circuit, inducing a fire or even an explosion. Later, scientists attacked this problem by substituting lithium metal with lithium alloys (Li-Al) (Rao et al, 1977). However the energy densities of lithium alloys are normally low compared to pure lithium metal (Besenhard et al, 1986). Unfortunately, the volume changes related to the insertion/extraction of Li into/from alloy matrices are quite substantial. This causes a fast disintegration of the alloy anodes by cracking and thus using lithium alloys as the anode have a very short cycle life. In this regard graphitic carbon was found to be stable for lithium insertion and extraction. Lithium insertion in graphite host lattices from

42

conventional non-aqueous solvents was reported as early as 1976 (Besenhard, 1976). In 1977, demonstration of intercalation of lithium in graphite led to the development of a workable lithium intercalated graphite anode (LiC_6) (Zanini et al, 1978) to provide an alternative to the lithium metal battery. Intercalation of lithium ions corresponding to the composition LiC_6 results in only about a 10% increase in the layer distance (Yazami and Touzain, 1983). Therefore, graphite became the anode material of choice for the lithium-ion battery, replacing lithium metal and lithium alloys. Sony (Thackeray, 2002), first commercialized lithium-ion batteries in the early 1990. This technology is called Li-ion or rocking-chair batteries.

2.4.2.2 Electrochemical Principles

A lithium-ion battery consists of a positive electrode (cathode), a negative electrode (anode) and an electrolyte (solution or solid) containing dissociated salts separated by a micro-porous membrane (separator) between the electrodes. The lithium ions move between the two electrodes through the electrolyte system. Lithium metal free lithium batteries are usually termed as "rocking chair" batteries (Tarascon and Armand, 2001). Soon after, this concept was demonstrated using transition metal compound anodes and cathodes (Lazzari and Scrosati, 1980). The principles of operation of the lithium ion rechargeable battery are shown in Fig. 2.11. The $LiCoO_2$, which gives a high discharge voltage, is at present the major cathode-active material in commercial lithium ion rechargeable batteries. Graphite based material is used for the anode. The lithium battery couple could not function in an aqueous electrolyte, since its charge termination (cut-off) voltage (4.5 V) is high enough to provide a strongly oxidizing environment, resulting in electrolyte decomposition. However, organic liquids, such as PC (Propylene Carbonate), EC (Ethylene Carbonate), DEC (Diethyl Carbonate), and DMC (Dimethyl Carbonate), with a large potential window (stable potential domain) containing dissolved salts of lithium are stable to high voltage.
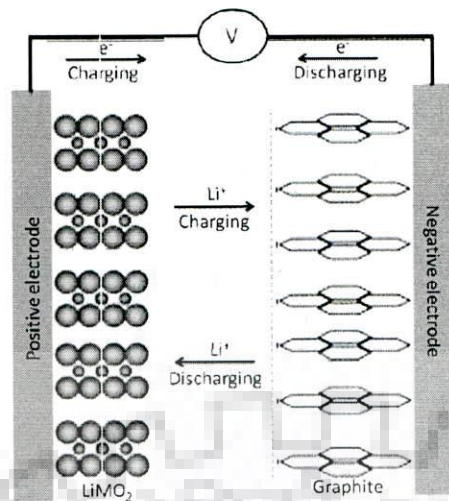
Fig. 2.11: Schematic diagram showing the principles of a Li-ion rechargeable cell (Manthiram, 2011).

During the charging process, lithium ions are extracted from the cathode usually comprised of a layered structure, go through the electrolyte and separator and intercalate into the anode. Simultaneously, electrons are liberated from the cathode, go through the external circuit and are accepted by anode materials. A reverse process occurs during the discharging process. A lithium ion rechargeable battery thus known as a swing battery or rocking chair battery since two-way movement of lithium ions between anode and cathode through the electrolyte occurs during the charge and discharge processes. Usually aluminum foil, which is easy to process and is resistant to an oxidizing potential, is used as the current collector for the cathode. Copper foil is used as the anode current collector since it does not react with lithium ions at low electrical potential. Fine, porous, thin films of polyethylene or polypropylene are used as separators and in order to minimize the internal resistance of the cell, securing sufficient current and energy density, the separator films are processed into thin sheets with large surface area. The materials selected for use should have excellent thermal and mechanical stability. The reactions involved in the charge and discharge process are described below (Nishi, 2001):

At positive electrode:

$$LiMO_2 \leftrightarrow Li_{1-x}MO_2 + xLi^+ + xe^- \qquad (2.12)$$

At negative electrode:

$$6C + xLi^+ + xe^- \leftrightarrow Li_xC_6 \qquad (2.13)$$

Overall reaction:

$$6C + LiMO_2 \leftrightarrow Li_{1-x}MO_2 + Li_xC_6 \qquad (2.14)$$

where, M = Fe, Co, Ni, Mn etc.

44

In order to achieve high cycling efficiency and long cycle life, the movement of Li ions in anode and cathode should not change or damage the host crystal structure. The design of a lithium-ion battery system requires careful selection of electrode pairs to obtain a high operating voltage (V_c). A high V_c can be realized with anode and cathode having smaller and larger work functions φ_a and φ_c respectively as the open-circuit voltage V_{oc} of the cell is related to the work functions of both the electrode:

$$V_{oc} = (\varphi_c - \varphi_a) / e \tag{2.15}$$

where e is the electronic charge.

Carbonaceous material with a potential of 0 - 0.8 V versus lithium metal is the major choice as the anode material for lithium ion batteries. The cathode materials can be chosen from the spinel $LiMn_2O_4$, layered $LiCoO_2$ and $LiNiO_2$, which have discharge potentials of around 4 V versus lithium metal. A battery with the combination of a high potential cathode material and a low potential anode material can deliver a voltage of 3.6 ~ 3.8 V.

2.4.2.3 Cathode Materials

In rechargeable lithium-ion batteries, the cathode provides the lithium ion for the intercalation reaction. So, the physical, structural and electrochemical properties of the cathode materials are critical to the performance of the whole battery. The principal properties required for cathode materials can be stated as (Bruce, 1997):

1. The discharge reaction should have a large negative Gibbs free energy i.e. high discharge voltage.

2. The material must have low molecular weight and the ability to intercalate large amount of lithium i.e. high energy capacity.

3. It must have high lithium chemical diffusion coefficient i.e. high power density.

4. The structural modifications during intercalation and de-intercalation should be as small as possible i.e. long cycle life, and

5. The materials should be chemically stable, non-toxic and inexpensive.

However, due to the criticality in the requirements there are a few compounds which are suitable as cathode for lithium-ion batteries and can be divided mainly into layered $LiMO_2$ compounds, manganese oxides (e.g. $LiMn_2O_4$ spinel) and other materials. Lithium ions reversibly intercalate into and de-intercalate from these compounds above 3 V versus Li/Li^+. Among these $LiCoO_2$ currently is the dominant cathode material in commercial lithium-ion batteries.

2.4.2.4 Anode Materials

Since the technological breakthrough on anode materials at the end of the 1980s and in the early 1990s, resulting in the birth and commercialization of the lithium ion battery, research on anode materials has been a focus of attention. As mentioned earlier that before the emergence of lithium-ion batteries, lithium metal was used for lithium primary batteries. However, rechargeable lithium batteries were unsuccessful in early trials. The main reason was the safety problem caused by using a lithium metal anode. During the charge/discharge cycle, lithium is often deposited as dendrite. These lithium dendrites are porous, have high surface area and are very reactive in organic electrolytes. Also, lithium dendrites gradually grow on cycling and penetrate the separator after a certain number of cycles resulting in short circuiting which lead to fire or explosion. The basic requirements for anode materials are (Huggins, 2007; Nazar and Crosnier, 2004):

1. The potential of lithium insertion and extraction in the anode versus lithium must be as low as possible.

2. The amount of lithium which can be accommodated by the anode material should be as high as possible to achieve a high specific capacity, and

3. It should endure repeated lithium insertion and extraction without any structural damage to obtain long cycle life.

However, carbonaceous-based materials are the most attractive and widely investigated materials for use as anode in lithium-ion batteries so far, and at present in lithium-ion battery industry, graphite is used as the anode material. Among the many types of carbon electrodes, well-ordered graphite is currently one of the representatives for the industrial standard because of their long plateau in voltage profiles and their low electrode potential relative to lithium metal. Carbon materials can reversibly accept and donate significant amounts of lithium without affecting their mechanical and electrical properties. Lithiated carbon also has Fermi energy only about 0.5 eV below that of lithium metal. Therefore, in the Li-ion cell, carbon is used for the anode instead of metallic lithium, and thus the electrochemical cell will have almost the same open-circuit voltage as one made with metallic lithium. In the history of lithium-ion battery development, the successful use of carbon anodes determined the success of commercialization of the lithium-ion battery. The situation changed with the feasibility of application of thermally decomposed carbons, which were less sensitive to electrolyte decomposition with modest capacities (Kanno et al, 1989). Sony was the first company to produce commercial lithium-ion batteries based on such a non-crystalline carbon anode. Since then various types of carbonaceous materials ranging from highly ordered graphites to

46

disordered carbons have been investigated experimentally and theoretically as potential anode materials. Investigations have focused on improving the specific capacity, cyclic efficiency and cyclic lifetime of the cell. It is known that the performance of lithium ion batteries depends strongly on the method of production and morphology of the carbon materials used (Endo et al, 1996). A great deal of effort has been devoted to the identification of the key parameters of the carbon used for the battery. Because carbon have large variations in their microstructure, texture, crystallinity and morphology, it has been important to design and choose the anode material from a wide variety in order to get better battery performance. There are hundreds of commercially available carbon types, including natural and synthetic graphites, carbon blacks, active carbons, carbon fibres, cokes and various other carbonaceous materials. Therefore, carbon materials have wide ranges of structure, texture and properties but the carbon anode materials are generally categorized into three classes (Flandrois and Simon, 1999) (1) graphitized carbon, (2) non-graphitized carbon (hard carbon) which cannot be graphitized even when heat treated at high temperature, and (3) soft carbon or graphitizable carbon, easily changeable with heat treatment.

Type one comprises the graphitic carbons, which are normally prepared by heating so-called soft carbon precursors to temperatures above ~ 2400 ^{o}C, where well graphitized materials result, and is a classic carbonaceous material that consists of hexagonal sheets of sp^2 carbon atoms (called graphene sheets), weakly bonded together by van der Waals forces. As mentioned earlier, intercalation/de-intercalation studies have been mainly carried out on natural graphite. An intercalation compound of lithium metal into graphite was demostrated (Besenhard, 1976) as a graphite intercalation compound (GIC) with a stage structure. Since then, extensive study has been performed to investigate the staging structure and charge transfer phenomena of the Li-GIC compounds (Zabel and Solin, 1992), which have the composition of Li$_x$C$_6$, where $0 \leq x \geq 1$, and $x = 3$ under high pressure, into ordered and disordered host materials. This intercalation process extends to the range of few mV versus lithium, i.e. well below the decomposition limit of the most common electrolytes. Electrolyte decomposition results in the formation of a surface protective film SEI (Solid Electrolyte Interphase), (Fig. 2.12) which offers an advantageous effect of allowing continuous operation of the carbonaceous anodes in terms of stability and cyclability of the carbon electrode, even if the electrochemical reactions occur at a voltage that is below the stability limit of the common electrolytes (Aurbach et al, 1995). The formation of SEI film is attributed to the exfoliation of graphite, inducing irreversible capacity in the first cycle (Wang et al, 2002a). The theoretical lithium storage capacity of a graphite anode for a Li ion secondary battery has

been considered to be 372 mAhg^{-1}, corresponding to the first stage LiC$_6$-GIC (Kambe et al, 1979; Henderson and White, 2011).
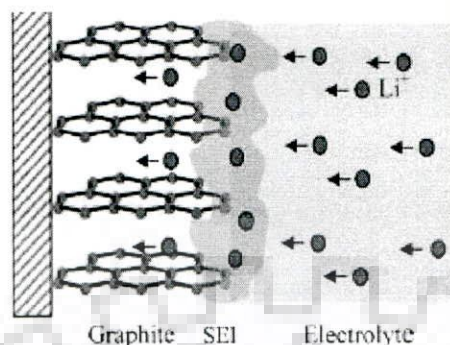
Fig. 2.12: Schematic representation of the formation of the SEI layer (Yazami, 1999).

Despite extensive basic studies, natural graphite flakes have not been employed in commercial carbon anodes. Many factors contribute to the limitations. Only the edge plane fraction of the natural graphite flakes contributes to the intercalation/de-intercalation process. A direct correlation is found between the basal plane fraction and irreversible capacity (Zaghib et al, 2001). Highly ordered pyrolytic graphite (HOPG) electrodes may indeed be considered as a better model of graphite material in this regard since the electrochemical process can be studied systematically on the basal plane or on the edge oriented plane by proper alignment of the working electrode. It is interesting to note that Basu (Basu, 1999) has employed HOPG as an anode material in one of the initial battery systems developed with LiC$_6$. By pyrolysed dipping of HOPG in molten lithium, a very high level of lithium insertion, up to LiC$_2$ can be achieved. It is well known that fluoride intercalation in HOPG only proceeds through the edge plane, and the influence of solvent-supporting electrolytes on HOPG is quite similar to that on natural graphite material. The main cause for the limited success of natural graphite material appears to be the large crystal size with substantially higher L$_c$ (crystalline size along c-axis: perpendicular to the layer) as well L$_a$ (crystalline size along the layer planes) values. The intercalation/de-intercalation requires movement of Li ions in a number of spatially packed graphene layers, travelling over longer distances. Obviously, the probability of irreversible surface damage becomes higher. A variety of strategies have been adopted to modify graphite materials in order to overcome this difficulty. The most successful of these attempts appear to be the use of MesoCarbon MicroBeads (MCMB) and graphite fibres. Simple reduction of particle-size by ball milling has also been attempted. A few other attempts at surface modification have been reported from time to time.

Recently, there has been tremendous interest in developing new graphite composites for potential application as anode materials for Li-ion batteries.

The second class of carbons are the hard carbons or non-graphitized carbons. Graphitization of carbon requires prolonged heat treatment which consumes a considerable amount of energy. Non-graphitic carbon materials require much lower heat treatment and hence, much less energy consumption. This, coupled with the general trend of higher charge–discharge capacity of hard carbon materials at least during the first few cycles has made hard carbon an attractive anode material for Li-ion batteries. The successful commercialisation of hard carbon has, thus, resulted in extensive research in different laboratories that is aimed at new and improved hard carbon materials. Non-graphitized carbons are derived from low temperature treatment of organic compounds. Typically, these carbons have a highly disordered structure, a large amount of porosity and heteroatoms remaining from the precursors (Sato et al, 1994). They deliver much higher capacities than graphite (e.g. 750 mAhg^{-1}) (Mabuchi et al, 1995), but have very high irreversible capacities in the first cycle with a large hysteresis in the potential profile.

The third one represents hydrogen containing carbons, which are prepared by pyrolyzed organic precursors and have a structure composed of misoriented crystallites (Flandrois and Simon, 1999). Pyrolytic carbon prepared by CVD of hydrocarbons was reported (Mohri et al, 1989) to have shown up to 99% Columbic efficiency. More detailed investigations have indicated, however, the limitations of these materials in terms of high discharge potentials and large hysteresis effects (Han et al, 1999). Their reversible capacities are normally lower than that of graphite because their maximum stoichiometric factor x in Li$_x$C$_6$ is typically about 0.5 to ~ 0.8 (for graphite, x = 1). The structure and chemistry of carbons strongly depend on the procedures for heating the organic precursors. The precursor materials include cokes, polymers, fibers and many others. Also, the insertion behaviour, and the mechanism behind it, of the lithium ions in various kinds of carbon and graphite hosts have been extensively studied both experimentally and theoretically (Mabuchi et al, 1995; Flandrois and Simon, 1999). In particular, the lithium insertion mechanism and electrochemical properties in low temperature carbons, unlike the case of well-ordered graphite, are not yet fully understood. The low temperature forms of carbon might be very promising for the next generation Li ion batteries because of their superior capacity. Also, the low temperature forms of carbon would be preferred in order to decrease the amount of energy used in anode production, since graphite

materials for anode application are heat-treated at around 3000 $^{\circ}$C and about 200 ton/month are consumed (Endo et al, 2000).

The latest progress in research on carbon anode materials mainly includes work on mild oxidation of graphite, formation of composites with metals and metal oxides, coating with polymers, other kinds of carbons and carbon nanotubes (Wu et al, 2003). It was first reported by Peled et al. (Peled et al, 1996) that mild oxidation of artificial graphite could modify its electrochemical performance as an anode material for lithium ion batteries. The main effect is ascribed to two processes: the production of nanochannels and/or micropores with the formation of a dense layer of oxides. The former enhances lithium intercalation and the later inhibits the decomposition of the electrolyte. As a result, reversible capacity and coulombic efficiency in the first cycle increase. Nevertheless, it should be borne in mind that the oxidation should not be drastic. If graphite is over-oxidized, an opposite effect will be observed. Other oxidative agents like metals or their oxides can be introduced to favour this oxidation process, and more nanochannels/micropores can be introduced. In addition, the metals may act as sites for lithium storage. As a result, reversible capacity is further enhanced (Wu et al, 2000). Oxidation can also be used to modify the electrochemical performance of high-temperature treated graphite (Spahr et al, 2002). Solvated lithium ions can co-intercalate, thereby causing significant exfoliation of the graphite sheets and, an increase in the irreversible capacity may result. In order to circumvent the exfoliation, an additional oxidation treatment of the heat-treated graphite in air has been tried. This oxidation produces a surface curing effect and increases the amount of disordered carbon atoms and the oxygen atom concentration, as well as the amount of prismatic surfaces, but keeps the number of low-energy defects unchanged. Due to these changes in surface structure, co-intercalation of solvated lithium ions vanishes at oxidation temperatures above 800 $^{\circ}$C (Spahr et al, 2002), and significant improvement in cycling behaviour will be achieved. In the case of practical applications this oxidation method has a shortcoming, i.e. the reproducibility and uniformity of products cannot be well controlled, since this oxidation happens at the interface between the solid and the gas phase. Consequently, liquid oxidants also have been explored (Ein-Eli and Koch, 1997). Researchers found that defects such as sp^3-hybridized carbon atoms, carbon chains and carbon radicals in common natural graphite could be removed by oxidation. As a result, the stability of the graphite structure is improved. As mentioned above, major processes during mild oxidation can be summarized as following: (i) removing some active sites and/or defects in graphitic materials resulting in the improvement of surface structure,

50

(ii) forming a dense layer of oxides acting as an efficient passivating film, and (iii) producing nanochannels/micropores for storage sites and passages for lithium.

Silver was first introduced onto the surface of graphite by composite formation (Momose et al, 1997). Due to the increase in conductivity and the incorporation of additional lithium storage sites the rate capability and cycling behaviour are much improved. In order to suppress co-intercalation of solvated lithium ions into graphite, graphite is encapsulated with nanosized Ni to form composite particles (Yu et al, 2000b). For example, a 10 wt.% Ni-coated composite increases the initial charge-discharge coulombic efficiency of graphite from 59 to 84% and the reversible capacity by 30-40 mAhg^{-1}. This coating effectively shields some of the edge surfaces from exposure to the electrolyte and minimizes co-intercalation of solvated lithium ions at these edge sites, with subsequent reduction of PC and exfoliation of the graphene layers. As a result, both the charge-discharge performance and the safety of the negative electrode in a rechargeable Li-ion cell are improved, and thus Ag, Au, Bi, In, Pb, Pd, Sn, Zn etc. can also form composites with graphite since it can be a host for lithium storage (Takamura et al, 1999). The composites increase the reversible capacity of graphite at some expense to the cyclability. However, Sn could also contribute to the irreversible capacity loss in the first cycle, probably through a mechanism similar to the formation of a SEI on a carbonaceous surface (Lee et al, 2000). When activated carbon fiber is coated with tin through impregnation and followed by heat-treatment, the composite shows enhanced capacity in comparison with the pure carbon (Egashira et al, 2002). When the amount of Sn is adequate, good cyclability is achieved. Nanosized particles of tin alloys such as SnSb, $Sn_{65}Sb_{18}Cu_{17}$ and $Sn_{62}Sb_{21}Cu_{17}$, can also form composites with carbon (Ulus et al, 2002). Composites of nanosized (<100 nm) particles with graphite show that lithium can be fully extracted from the host matrix only when the anode is cycled at low current densities. The kinetics of lithium insertion in and extraction from the composite anode materials slows gradually with the cycle number, since the deposited alloy becomes amorphous during cycling, although the graphite does not. Consequently, the active materials in the composites suffer from particle-to-particle disintegration, and the reversible capacity of the composites fades from the first cycle to the 34th, by less than 50% (Ulus et al, 2002). Coating of graphitic carbon have also been done with oxides such as SnO (Lee et al, 2000), SnO_2 (Lee et al, 2002), and M_xO (M = Cu, Ni, Fe, Pb) (Huang et al, 2001). A composite of MCMB with tin oxide gives higher capacity than uncoated MCMB, but the capacity decreases with cycling due to severe volume changes in the tin oxide. The reviewed results show that metals and metal oxides can act in several ways to improve the electrochemical performance of graphitic carbon: (i) covering active sites at

51
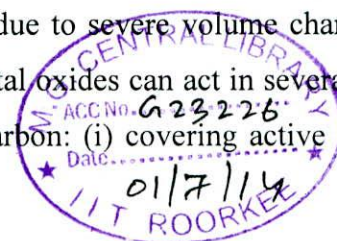
edge planes resulting in decreased electrolyte decomposition, gas evolution, exfoliation and absorption of water in the presence of high humidity, (ii) increasing conductivity leading to less charge-transfer resistance and improved high rate capability, and (iii) acting as a host for lithium storage, leading to enhancement of reversible capacity. It should also be remembered that metal oxides usually present some undesirable effects such as high irreversible capacity in the first cycle, which is an important factor that should be considered prior to practical application. Recently graphene materials have been used to form hybrid materials with metal oxides to improve electrode capacity and cycling stability. Zhu et al. (Zhu et al, 2011) used reduced graphene oxide/Fe_2O_3 composite as an anode material and observed discharge and charge capacities of 1693 and 1227 mAhg^{-1}, respectively. A positive synergistic effect on the improvement of electrochemical performance has been observed normalized to the mass of Fe_2O_3 in the composite and is higher than that of individuals. Likewise other form of oxides such as Co_3O_4, TiO_2, Mn_3O_4 etc. also have been incorporated in graphene for their superior performances in Li-ion batteries (Li et al, 2011; Wang et al, 2010; Paek et al, 2009).

In order to modify the surface structure of carbon based anode materials, besides mild oxidation and deposition of metals and their oxides, coating with polymers and other kinds of carbon have also explored to achieve improved performance as anode materials. At first, certain polymers were considered as coatings on the carbon surface to make composites with improved electrochemical performance. The polymers included conductive and electroactive ones, such as polythiophene (Kuwabata et al, 1998), polypyrrole (Veeraraghavan et al, 2002) and polyaniline (Gaberscek et al, 2001). Later, it was found that other kinds of polymers could also be used for effective coatings. The action of polythiophene is multiple when it forms coatings on the graphite surface (Kuwabata et al, 1998). First, it acts as a conductor since it is electronically conductive, and the resultant composite displays a good electrical network. Secondly, it can act as a binder, and additional insulating Fluorine-containing polymers are not necessary. As a result, the pressing step can be eliminated in the assembly line. Thirdly, lithium can also be doped into it, resulting in an increase in the reversible capacity. Finally, the polymer coating also decreases the contact of the graphite with the electrolyte, and thus the irreversible capacity of the electrode decreases. When PolyPyrrole (PPy) is polymerized onto commercial graphite by an in-situ polymerization technique, the initial irreversible capacity is also decreased due to the reduction in the thickness of the resultant SEI layer. A composite of PPy (7.8 wt.%) with graphite gives the optimum performance, based on irreversible and reversible capacity. It possesses good reversibility, higher coulombic efficiency, good rate capability and better cycle life than the bare graphite

(Veeraraghavan et al, 2002). Different polyanilines such as emeraldine base, emeraldine salt and protonated polyaniline have also been attempted (Gaberscek et al, 2001). It has been shown that they act as binder and decrease the thickness of the SEI film. As a result, capacity loss in the first cycle decreases. Ionically conductive co-polymers can also be coated onto the surface of graphite, where they act to reduce the irreversible capacity and enhance the cycle life of natural graphite anode materials (Pan et al, 2002). The improvement is due to the fact that encapsulation depresses the structural changes caused by the co-intercalation of solvated lithium ions and ensures stable electrode impedance during the cycling. Other polymers having no electro-activity have also been found to act to modify the electrochemical performances. In the case of graphitic carbon, PC is usually not regarded as an ideal electrolyte solvent because it decomposes at the graphite surface and an effective SEI film cannot be formed properly; it co-intercalates into graphite and results in exfoliation of graphene sheets. Therefore, EC-based electrolytes are commonly used. However, the melting point of PC (-49 °C) is lower than that of EC (38 °C). In order to broaden the application of liquid electrolyte-based lithium ion batteries, better performance at low temperature is a goal. Consequently, improving the electrochemical performance of graphitic carbon with PC-based electrolyte by coating with other kinds of carbons has become a focus of research. Meanwhile, other kinds of improvements can also be achieved by this type of coating. Carbon from thermal vapour decomposition at 1000 °C has been coated onto natural graphite (Wang and Yoshio, 2001; Yoshio et al, 2000). When the graphite surface was completely coated by a carbon shell, the PC content in the electrolyte with DMC can be increased without decomposition of PC and exfoliation of the graphite layers. The coated natural graphite shows much better electrochemical performance than bare natural graphite as an anode material in both PC- and EC-based electrolytes (Yoshio et al, 2000). However, high pressure in the process of rolling and pressing should be avoided since it will destroy the coated carbon shell and expose the graphite surface to the PC-based electrolyte again (Wang and Yoshio, 2001). As mentioned earlier there are two kinds of planes i.e. edge and basal on graphite crystallite surfaces. Edge planes show much higher activities towards chemical reactions than basal planes. The exfoliation and decomposition of the electrolyte mainly occur on edge planes rather than basal planes. The reduction in surface area of the coated graphite has also been tried by dispersing the artificial graphite in a tetrahydrofuran/acetone solution that contains coal tar pitch following heat-treatment at 1000 °C in argon atmosphere. Pores of less than 10 nm in the graphite are covered by the coke component resulting in a smaller surface-area than that of the pristine material. The reduction in the surface-area of the coke-coated graphite

53

leads to a decrease in the irreversible capacity in the first cycle, and also in the extent of electrolyte (EC/DEC) decomposition, gas evolution and surface film growth in comparison with the virgin graphite electrode (Yoon et al, 2001). Nevertheless, in general carbon coating greatly increases the specific surface area of the graphite particles (Lee et al, 2001a). In addition, compared with untreated graphite, reversible capacity and cycling behaviour along with coulombic efficiency in the first cycle are markedly improved, which is different from the situation with the coke-coated material.

There are several classifications of carbon nanostructures on the basis of configuration, degree of graphitization and structure which can be used individually or in a mixture to get the desired electrochemical performance. The uses of nanomaterials as a whole have some potential advantages and disadvantages associated with the development of electrodes for lithium batteries (Armand and Tarascon, 2008). Advantages include (i) better accommodation of the strain due to lithium insertion/removal thereby improving cycle life, (ii) new reactions not possible with bulk materials, (iii) higher electrode/electrolyte contact area leading to higher charge/discharge rates, (iv) short path lengths for electronic transport, and (v) short path lengths for Li^+ transport. With these advantages in mind, several efforts have been devoted to explore new carbon based negative electrode materials. Ordered nanoporous structure of carbon has shown faster charge-discharge superior to graphite due its larger graphitic spacing and its porous structure (Xing et al, 2006). CNT as nanostructures of carbon have also been examined as negative electrodes (Wang et al, 2002b; Wang et al, 2007). The typical charge discharge behaviour of MWCNT electrode is shown in Fig. 2.13.
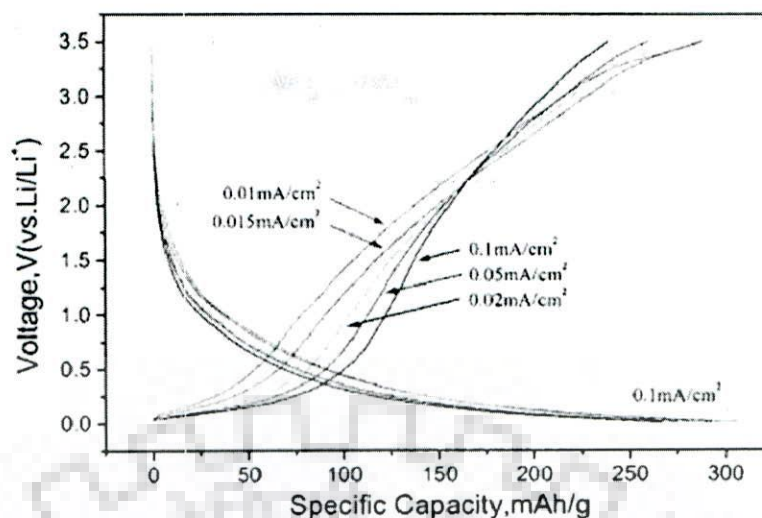
Fig. 2.13: Voltage vs. specific capacity profiles of MWCNT during insertion and extraction. The processes of lithium insertion were recorded at a current density of 0.1 mA cm^{-2}, and the extractions were carried out at different current values shown in figure (Wang et al, 2002b).

The electrochemical performance of MWCNT depends on the preparation process as the amount of impurities and defects depend on the preparation conditions. Most impurities, such as catalyst particles, graphite and disordered carbons, can be removed by purification. Defects such as dangling bonds, sidewall holes and open ends can be generally healed by annealing at high-temperature. Lithium intercalates between the graphene layers by formation of a stage compound. MWCNT prepared by catalytic decomposition without purification show high irreversible capacity. After purification and annealing, irreversible capacity decreases with annealing temperature (Leroux et al, 1999). Similar to the behaviour of amorphous and graphitic carbon, the structure of MWCNT also plays a major role in both specific capacity and cycle life. Slightly graphitized MWCNT exhibit a high specific capacity of 640 mAhg^{-1} during the first charge due to lithium doping into regions without any organized graphitic structure, micropores, edge sites and surfaces of graphitic layers. In contrast, well-graphitized MWCNT have been observed to show a lower capacity of 282 mAhg^{-1} during the first charge. After 20 charge/discharge cycles, the charge capacity of the slightly graphitized MWCNT fades to 65.3% of their original charge capacity, but the well-graphitized MWCNT maintain 91.5% of their original charge capacity due to their stable structure (Wu et al, 1999). Like the modification of other kinds of carbons by doping (Wu et al, 2002), carbon nanostructures also have been doped in that way (Mukhopadhyay et al, 2002). Boron-doped MWCNT consists of highly aligned nanotubes having 35-45 graphene layers with good 3D ordering features, but the boron doping destroys the local hexagonal symmetry. Reversible capacity after doping

increases from 156 to 180 mAhg^{-1} in the first cycle with almost equal coulombic efficiencies of 55-58%, which is from enhanced 3D ordering by B-doping. The coulombic efficiency increases to more than 92% after the second cycle. Highly reversible intercalation/de-intercalation of Li occurs with some undesirable reduction processes in the initial discharge process. Functionalization or oxidization of CNS also have been tried to improve the electrochemical properties (Yang et al, 2002). After oxidation with raw acid, the total discharge capacity (intercalation) during the first cycle is 660 mAhg^{-1}, but the reversible part is only 200 mAhg^{-1}. The nature of the SEI film formed by reaction of surface groups on the carbon nanostructures with lithium upon discharge determines to a large extent the reversible and irreversible capacity of the CNS. During oxidation in the acid mixture, the residual acids play an important role in this work and react with Li ions resulting in irreversible capacity. The H_2SO_4 and HNO_3 can easily make defects or pores in these sheets, causing increased reversible capacity. Vertically aligned MWCNT as the active anode material in lithium-ion batteries have shown high specific capacities up to 980 mAhg^{-1} which is better than the non aligned MWCNT (Welna et al, 2011).

Like MWCNT, SWCNT also contains impurities and defects. SWCNT has a high theoretical surface-area and the total specific surface-area of the outside plane. Lithium can reversibly intercalate into SWCNT, and the reversible capacities can range from 460 mAhg^{-1}, corresponding to a stoichiometry of $Li_{1.23}C_6$ (Claye et al, 2000), to 1000 mAhg^{-1} ($Li_{2.7}C_6$) after introduction of defects (Gao et al, 2000). However, irreversible capacity in the first cycle is very high, up to 1200 mAhg^{-1}, which is ascribed to the large specific surface-area. Shimoda et al. (Shimoda et al, 2002) used purified SWCNT bundles containing over 90% SWCNT. After chemical etching of CNT bundle of length 4 μm the stoitiometry turned out to be LiC_3. However, bundle with length 0.5 μm corresponded to $LiC_{2.8}$ whereas as purified SWCNT was reversibly intercalated to a saturation ratio of LiC_6. These results show that etching of CNT gives better results. Lithium can intercalate in the channels between nanotubes. This intercalation disrupts the inter tube binding, analogous to exfoliation in layered hosts and in a different way from the well-ordered staging of graphite. The disruption leads to an irreversible loss of crystallinity. Upon lithium intercalation, due to charge transfer from lithium to carbon, resistance decreases continuously contributing to high reversible capacity (Claye et al, 2000). Free standing SWCNT have shown a reversible capacity of ~ 400 mAhg^{-1} reduced from 1700 mAhg^{-1} during 1st discharge (Ng et al, 2005). Electrolytes have also been observed to affect the electrochemical performances besides their graphitization, and thus Landi et al. (Landi et al, 2008) have observed a reversible lithium ion capacity of 520 mAhg^{-1}

for high purity SWCNT with the addition of PC into the conventional EC:DMC cosolvent mixture which is greater than the capacity of 390 mAhg^{-1} or 485 mAhg^{-1} achieved using PC:DMC and EC:DMC electrolytes respectively. They have shown the importance of the SEI formation dependence on type of electrode-electrolyte reaction on SWCNT capacity. Binder free electrode has been proved to have better electrochemical properties (reversible capacity of 900 mAhg^{-1} at a rate of 1C or 767 mAhg^{-1} at a rate of 3C) as the capacity loss can be avoided as there will be no exothermic reaction between polymeric binder with graphite and metallic lithium (Lahiri et al, 2010). The SWCNT ball-milled with Si had a lithium-insertion capacity of up to ~ 2500 mAhg^{-1} in the first charge. Unfortunately, only less than half of this capacity was reversible during the first discharge. Such large irreversible capacity in the first cycle is unacceptable for any practical application (Wang et al, 1998b).

The CNF are easy to scale up and according to their degree of graphitization they can also be a prominent member of anode materials. The reversible specific capacity of the CNF at a 0.1 C rate was found to be 461 mAhg^{-1} where as the first-cycle discharge capacity was found to be 1261 mAhg^{-1} (Subramanian et al, 2006).

Pristine CNS have high surface area, and selective incorporation of foreign carbons into CNS can improve the spatial occupancy inside it and thus CNF grown inside CNT exhibited a reversible capacity of 410 mAhg^{-1} during 120 charge/discharge cycles, superior than pristine CNT (258 mAhg^{-1}) and irreversible capacity of about 700 mAhg^{-1}, when used as the anode in lithium-ion batteries as shown in Fig. 2.14 (Zhang et al, 2008).
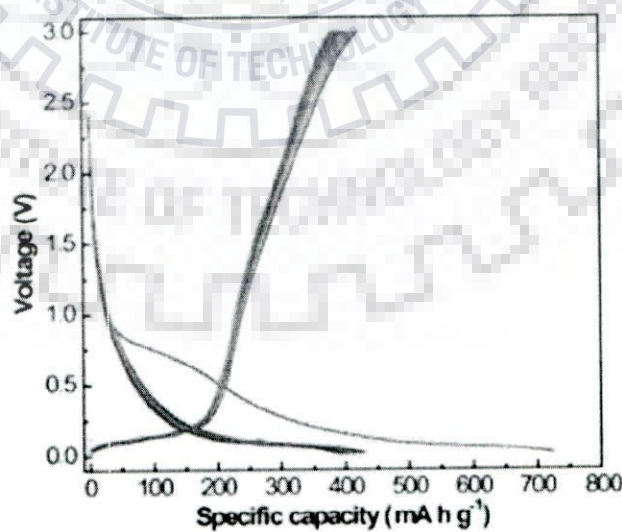
Fig. 2.14: Discharge/charge (Li insertion/extraction, voltage decrease/increase) curves of CNF inside CNT at a cycling rate of C/5 in 1 M LiPF$_6$ in 1:1 (v/v) EC/DMC (Zhang et al, 2008).

57

As mentioned earlier graphene based materials are emerging nanomaterials which have attracted much interest. The materials have shown the specific capacity of 540 mAhg^{-1} and were increased up to 730 mAhg^{-1} and 784 mAhg^{-1}, by the incorporation of macromolecules of CNT and C_{60} respectively (Yoo et al, 2008). In conclusion, carbon nanostructure with its interesting properties may be explored as anode materials.

Besides carbon based anode several other materials have been tested and being explored for application as anode material. The replacement of metallic lithium by lithium alloys has been under investigation since Dey (Dey, 1971) demonstrated the feasibility of electrochemical formation of lithium alloys in liquid organic electrolytes in 1971. However, the main problems associated with the use of lithium alloys instead of lithium in rechargeable batteries are caused by the huge changes in volume from the pure metals to the intermetallic compounds (Beaulieu et al, 2001). The molar volume increases by a factor of three in some cases, while the difference from graphite is below 10% for LiC_6. In consequence, successive charge-discharge cycles lead to mechanical stresses in the electrode and finally to fracture. The divided material loses the electrical contacts between the particles, which cause a sharp decrease in capacity. The volume change of alloy anodes has a detrimental effect on the performance of batteries. It usually causes a short cycle life. Materials based on tin oxide also have been proposed as another type of promising candidate, due to their high theoretical capacity, high packing density and safe thermodynamic potential compared to carbonaceous materials for lithium secondary batteries (Li et al, 2002). However, they also undergo severe structural and volume change during the process of Li uptake and removal, which results in mechanical disintegration of the electrode and consequently capacity fade, greatly limiting the potential for commercialization. Among the anode materials, silicon is one of the promising candidates, owing to its high natural abundance, low discharge potential and high theoretical capacity. However, the large volume changes (up to 270% for the $Li_{3.75}Si$ phase) and loss of electrical contact during lithium insertion and extraction result in capacity fading (Gomez-Camer et al, 2011). Many transition metals were also used as anodes for lithium-ion batteries. There are also other factors that affect the cycling performances, such as pulverization of the active particles during charge and discharge, and poor conductivity of the active materials, especially for transition metal oxides.

2.4.3 Other Applications

Since their discovery in 1991, carbon nanotubes - stronger than steel and lighter than a feather, have generated a huge potential of industrial and scientific applications. Some other possible applications are highlighted below.

Electron field emission materials have been investigated extensively for technological applications, such as flat panel displays, electron guns in electron microscopes, microwave amplifiers. Recently due to their excellent electron emission properties, CNT have a strong potential of applications to cold electron emission sources, which can be extended further to flat panel displays such as field emission displays (FED) (Lee et al, 2001b). Cathode ray lighting elements with carbon nanotube materials as the field emitters have also been fabricated (Saito et al, 1998).

The advantage of the electric double layer capacitor (EDLC) is considered to be its high discharge rate, thus making it applicable as a hybrid energy source for electric vehicles and portable electric devices. CNT have extraordinarily high surface area, and using them as the dielectric could increase the storage ability of capacitors to be on par with modern batteries. EDLC containing carbon nanotubes in the electrode exhibits relatively high capacitances resulting from the high surface area accessible to the electrolyte (An et al, 2001). CNS also finds application in Fuel cells. Carbon nanotubes decorated with metal nanoparticles as an electrode has doubled the fuel cell performance due to the increased catalytic activity of nanotube-based electrodes (Yoshitake et al, 2002). Materials with high hydrogen storage capacities are desirable for energy storage applications. Because of their cylindrical and hollow geometry, and nanometer-scale diameters, it has been found that the carbon nanotubes can store liquid and gas in the inner cores through a capillary effect. Extraordinarily high and reversible hydrogen adsorption in SWCNT and nanofibers (Chen et al, 1999) has been reported and attracted considerable interest among researchers and industry experts. Flywheels offer certain advantages over batteries and because of their strength, CNS could be used to make faster flywheels that store more energy without shattering.

The use of a MWCNT in scanning probe microscope tip for imaging has already been cited in the text. Since MWCNT tips are conducting, they can be used in STM (Scanning Tunneling Microscope), AFM (Atomic Force Microscope) instruments as well as other scanning probe instruments, such as an electrostatic force microscope with higher resolution (Wong et al, 1998). Recent research has also shown that nanotubes can be used as advanced miniaturized chemical sensors (Kong et al, 2000) where as bio sensing application has been observed by

several researchers (Xu et al, 2004). CNT may offer in future to target and destroy individual cancer cells without harming healthy tissues, a current drawback of treatments like chemotherapy. An array of CNT, which is excellent electron emitter, could be used in field emission displays to excite the phosphorous dots, creating bright, high resolution displays that are only millimeters thick, and consume less power than plasma and liquid crystal displays. The dream of fold-up TV and computer screens that can fit inside people's pockets has, up until now, been stifled by rigid silicon semiconductors. But CNS, in addition to being very flexible, compared favorably to silicon in terms of performance. Koziol et al. (Koziol et al, 2007) have figured out how to spin many tiny carbon nanotubes together to create fibers that have the strength of Kevlar, a composite material used in bullet-proof vests. As CNS prices drop, spun CNS could be the material of choice for better, lighter body armor. Other key applications of carbon nanostructures include bio imaging (Chandra et al, 2011), gas discharge tubes, electric and photo-electric elements, Nano-MEMs, catalytic support, schottky diodes, high-resolution printable conductor, solar cell etc.

2.5 Summary and Formulation of the Problem

Since the discovery, there has been significant number of investigations on the growth of CNS by CCVD process but often the experimental conditions varied to defy comparisons. Thus it is difficult to arrive at broad general conclusions regarding the steps involved in the process of growth. The experiments carried out under TEM or ETEM and the molecular dynamic simulations have thrown significant light on the steps involved in the growth of CNS but still we are far away from understanding the precise conditions differentiating the growth of different morphologies like SWCNT, MWCNT, CNF or carbon nanotapes. A number of relevant questions as outlined below have originated from the review of literature and these questions need to be addressed to gain better understanding of the growth mechanism of CNS.

- Do the oxide nanoparticles presumed to act as catalyst in the CCVD process, survive as oxides in the highly reducing environment prevailing during growth of CNS?
- Why does one observe significant shape change in the catalysts of metallic nanoparticles often observed inside nanotubes during growth?
- Why does one observe formation of nanobeads of carbon, sometimes alone or along with CNS?
- Which is the diffusion path of carbon in the catalyst delivering carbon atoms during growth of CNS?

- Is the formation of carbide on the metallic catalyst a necessary step for the process of growth, as observed sometimes, followed by their decomposition to provide carbon for the growth of CNS?

- What is the importance of size of catalyst or growth temperature in determining morphology of CNS?

- How does the flow rate of carbon bearing gas affect the growth of CNS?

The first phase of the present study has been formulated to address these questions, which have not yet been answered definitely. The study will begin with experiments to grow nanoparticles of cobalt and nickel oxide, which have been extensively used in CCVD process and there are results available in the literature to compare with. But a new idea of doping these oxides by copper oxide has been pursued to explore its effect on the growth of CNS. The nanoparticles of pure and doped oxides are expected to undergo physical and chemical changes under the conditions prevailing in the chamber of CCVD during the growth of CNS, particularly the reducing environment and the elevated temperature. These changes are dependent on the characteristics of the oxide particles like size and the level of doping. The present investigation attempts to understand these physical and chemical changes, and their role in the growth of CNS so as to be able to intervene in the CCVD process appropriately to attain the desired outcome.

Exploitation of nanomaterials for energy has become an important objective in research to meet the current challenges for sustainable energy. Rechargeable batteries are important source for providing mobile power to various types of devices, from consumer products to electric vehicles and satellites, and its area of application will extend if one could meet the challenge of packing more power for the same weight of the battery. Amongst the batteries, lithium ion battery has the highest power per unit weight but it is still not adequate for various purposes including next generation electric vehicles and wireless communications. Batteries are inherently simple in concept, while it is difficult to improve their performance and safety while reducing the cost. The performance of a battery is mostly related to the intrinsic properties of the materials employed. Carbon based anodes are still the main candidate for commercial use in spite its limit of charge capacity. Application of one dimensional carbon nanostructures may enhance the charge capacity further paving its use in the anode of high energy density batteries. This application will also necessitate commercial production of these materials at relatively lower cost on a large scale. The success of this approach will depend on the following issues:

- Enhancement of intercalation sites compared to graphite from where lithium ion may reversibly move in and out increasing reversible charge capacity and avoiding capacity fading.

- The ability of the electrode material to accommodate strain during lithium ion insertion/removal without disintegration, and thereby, not affecting the cycle life adversely.

- Ability to provide higher electrode/electrolyte contact area leading to higher charge/discharge rates.

- Ability to provide short path lengths for Li^+ transport to increase the power.

The second phase of the current investigation addresses the above issues by determining electrochemical performance of the different one dimensional nanostructures like SWCNT, DWCNT, MWCNT and CNF. The purpose is to finally assess the potential of the CNS for application in the anode of lithium ion battery.

Experimental Techniques
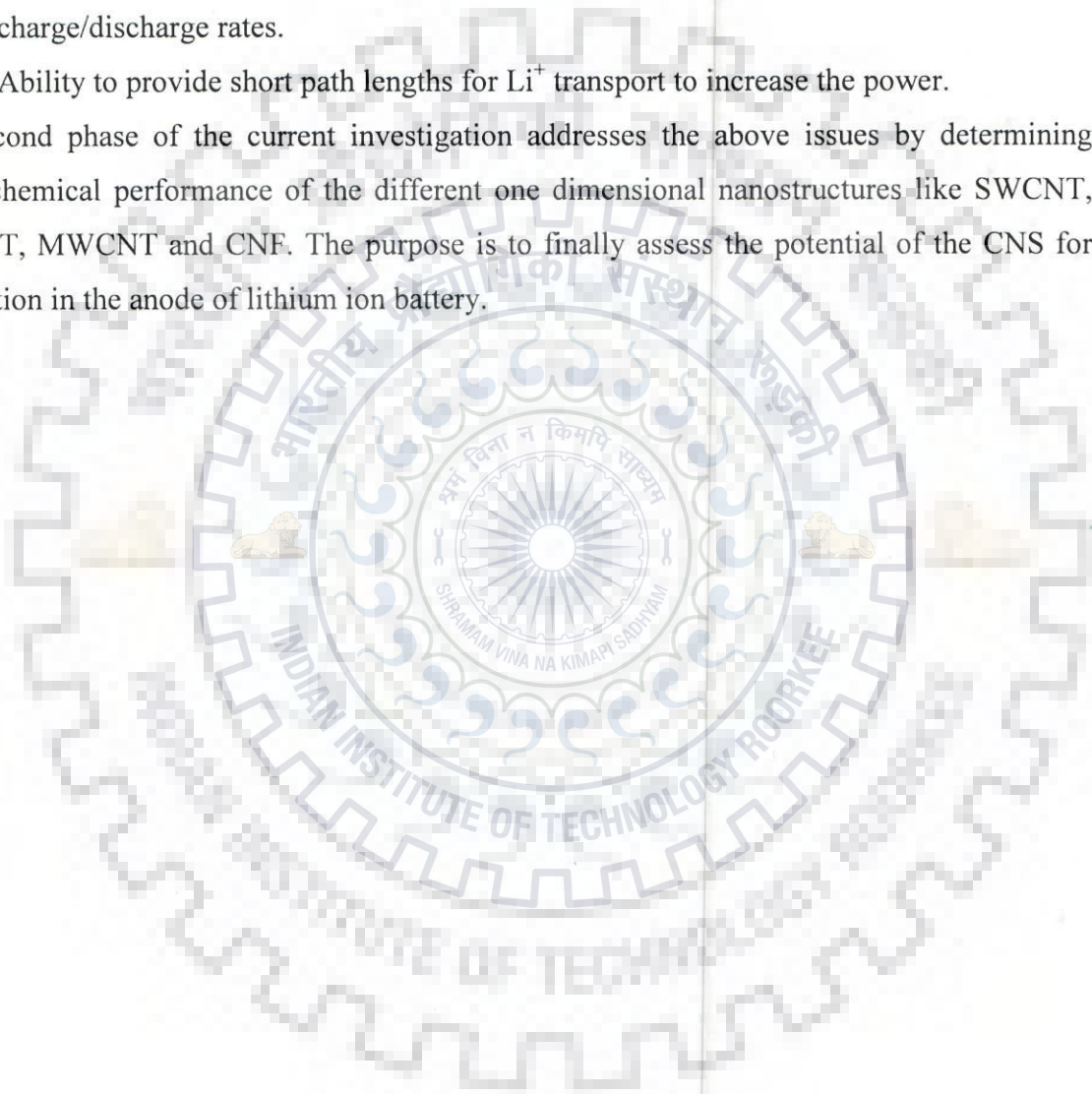
Chapter 3
Experimental Techniques

The main objectives of the present study are to develop nanostructured carbon materials with selective morphology, their structural and electrochemical characterizations. This chapter describes the preparations and characterizations of the catalysts, substrates, Carbon nanostructures (CNS). Preparation of the electrode using CNS and their electrochemical performance has also been described. The catalyst materials, substrate, CNS and the composite anode were synthesized in the laboratory. Fig. 3.1 outlines the procedure used for synthesis of CNS. Specific details of the instruments, experimental parameters and techniques used in the studies have been discussed.

This chapter describes (a) synthesis of catalyst nanoparticles based on cobalt and nickel doped with copper in the form of oxides by co-precipitation and or sol-gel technique, (b) preparation of anodized aluminium oxide (AAO) substrate by the method of anodization, (c) development of nanostructured carbon materials with different morphologies by catalytic chemical vapour deposition (CCVD), (d) the structural characterizations of the materials synthesized, and (e) electrochemical characterization of the carbon nanostructured materials for application in Li-ion battery.

The structural, elemental and compositional analyses have been carried out by X-ray diffraction (XRD), field emission scanning electron microscope (FESEM) and energy dispersive X-ray analysis (EDAX). Differential thermal analyses/differential scanning calorimetry (DTA/DSC) and high temperature XRD of the oxide nanoparticles have been carried out to study the effect of size and doping on melting behaviour to understand the role of melting if any, on the nucleation and growth of CNS. DTA has been employed further to estimate the quality and purity of the CNS based materials. The CNS based host anode materials have been characterized by Raman spectroscopy, as the carbon nanostructures have the presence of sp^2 hybridized carbons which can be correlated (by structure and Raman response of the materials) to an ideally perfect 2-D graphite (graphene). Raman spectroscopy has also been employed to investigate the reduction behaviour of oxide nanoparticles during or after the growth of nanostructures. The structural characterization of the carbon nanostructure samples has been carried out using transmission electron microscope (TEM)

and EDAX attached therein. Dynamic light scattering (DLS)/Zetasizer has been used to determine the particle size, and compared with the size determined using image-J software from FESEM micrographs. Brunauer, Emmett and Teller (BET) analyser has been employed to measure the surface area of the CNS samples.

Section A: Growth of CNS and characterizations
⇨ Part I: Synthesis of nanosized oxide particles by sol-gel process
⇨ Part II: Preparation of porous alumina substrate by the process of anodization
⇨ Part III: Growth of carbon nanostructures by catalytic chemical vapour deposition
⇨ Part IV: Characterizations by XRD, FESEM, TEM, SDT, Raman, BET, Zetasizer etc.

Section B: Cell fabrication and electrochemical characterizations
⇨ Part I: Cell fabrication for Li-ion battery
⇨ Part II: Electrochemical characterizations

Fig. 3.1: Schematic flow diagram of experimental work out.

3.1 Materials Synthesis

For preparing the carbon nanostructures by catalytic chemical vapour deposition method the required catalyst compounds were synthesized by co-precipitation/sol-gel process and the anodized aluminium oxide substrates were prepared by anodization. The details of these processes are described in the following subsections.

3.1.1 Preparation of Anodic Alumina Substrate

Carbon nanostructures have been grown by substrate-assisted route as well as without any substrate. Here anodized alumina has been used as a substrate, which has nanoporous structure with almost uniform diameter and length. Anodizing is an electrolytic passivation process used to increase the thickness of the natural oxide layer on the surface of metal parts. The process is called "anodizing" because the part to be treated forms the anode electrode of an electrical circuit. The flow chart of the two-step anodization process is shown in Fig. 3.2. For the formation of anodized alumina substrate, the anodization time and the voltage are the main factors in determining the uniformity and size of the nanopores for a particular electrolyte medium. For optimizing the process parameters viz. voltage (ranging from 40-80 V), time for anodization (15-50 min) and electrolyte medium (oxalic acid, phosphoric acid and sulfuric acid) were varied. Thin strips of aluminium were first electro-polished in a bath of ethyl alcohol and perchloric acid (in ratio of 5:1 by volume) by applying a voltage of 15 V

for 4 min at ~ 5 °C, and then electro-polished samples were anodized at a constant voltage of 80 V for 30 min in 5 wt.% concentration phosphoric acid electrolyte bath. The porous alumina film formed after the first anodization step was removed by chemical etching in a mixture of phosphoric (6 wt.%) and chromic acid (1.8 wt.%) at 80 °C. Subsequently, the Al sheet was further anodized for 30 min under identical conditions of the first step anodization process so as to obtain a regular array of pores.

Step: 1: Degreasing:
Cleaned with acetone and washed with deionized water

⇩

Step 2: Removing oxide layer:
Dipped in NaOH solution (30 gl^{-1}) for 10 mins, thereafter rinsed in distilled water, followed by immersing in HNO$_3$

⇩

Step 3: Electropolishing:
Electropolished using solution of Ethyl Alcohol and Perchloric acid in 5:1 ratio (v/v) at a current density of 1-2 A /cm^2 at 15 V for <4 minutes at 5 °C

⇩

Step 4: First-step anodization:
Anodized at 40-80 V for 30 min in 5 wt.% of phosphoric acid/oxalic acid/sulfuric acid electrolyte for 15-50 mins

⇩

Step 5: Two-step anodization:
Chemical etching in a mixture of phosphoric (6 wt. %) and chromic acid (1.8 wt. %) at 80 °C Subsequently, the Al sheet was anodized for 30 min under identical conditions of the first step anodization process

Fig. 3.2: Flow chart of anodization process.

Well-ordered nanoporous arrays can be obtained by etching of the oxide layer with irregular pores. As the anodization time was increased, a smoother pretexture was found to form which can increase the regularity of the pores. Therefore, the anodization time is one of the major factors for fabrication of ordered nanoporous arrays along with the applied voltage in determining the uniformity and size of the nanopore arrays.

3.1.2 Catalyst Preparation

The co-precipitation/sol-gel process is a wet-chemical technique starting from a colloidal solution (sol) that acts as the precursor for an integrated network (or gel) of either discrete particles or network polymers. Typical precursor is different types of metal salts viz. chlorides, nitrates and acetates, which undergo various forms of hydrolysis and polycondensation reactions. With further drying and heat treatment, the gel is converted into

dense particles. The sol-gel process over other traditional processing techniques also has other potential advantages such as better homogeneities, low processing temperature and improved material properties. The detailed steps for the synthesis of the materials by sol-gel method are shown in the Fig. 3.3.

```
┌─────────────────────────────────────────────────────────────┐
│                    Aqueous solution of                        │
│  Cobalt acetate/nickel acetate /copper sulphate in required   │
│                          amount                               │
│                            +                                  │
│  Chelating agent (citric acid) equivalent to the metal        │
│                   content in the salt                         │
│                            ⇩                                  │
│       Gel formation by slow stirring at ~ 72 to 84 °C         │
│                            ⇩                                  │
│              Drying at 120 °C for 12 hrs                      │
│                            ⇩                                  │
│          Calcined for 5 hrs at ~ 230 to 950 °C               │
│                            ⇩                                  │
│                  Ground to powders                            │
└─────────────────────────────────────────────────────────────┘
```
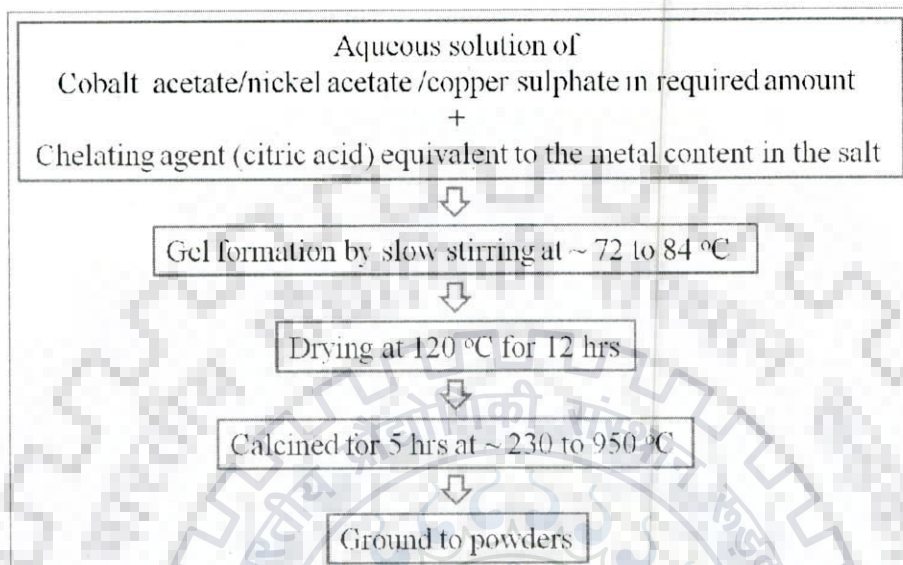
Fig. 3.3: The detailed steps for the synthesis of the oxide nanoparticles by sol-gel method.

Metal bearing oxide nanoparticles were prepared by aqueous sol-gel route using cobalt (II) acetate tetra-hydrate, nickel acetate tetra-hydrate (Merck) and copper (II) sulphate 5-hydrate (Merck) as source of cobalt, nickel and copper respectively. Chelating agent of citric acid monohydrate (Merck), having mole percentage equal to that of metal content in the salt was added to this solution for polymerization. The copper percentage was varied from 0 to 20 wt.% in all the catalyst as aqueous saturated solution and mixed with citric acid, followed by slow stirring at a gelation temperature ranging from 72 to 84 °C until the formation of gel takes place. The gels were dried at 120 °C for 12 hrs in an oven and then the dried samples were calcined in air for 5 hrs at a temperature varying from 230 to 950 °C and finally grounded to powder. The change in gelation temperature, time and the calcination temperature results in different average particle size.

3.1.3 Synthesis of CNS, using CCVD Method

Catalytic chemical vapour deposition (CCVD) is a versatile process suitable for the preparation of coatings, powders, fibers and monolithic components. Chemical vapour deposition may be defined as the deposition of a solid on a heated surface from a chemical reaction in the vapour or gas phase. By this method nanostructures can be build up from bottom up approach. CCVD has several important advantages in growing carbon

68

nanostructures, which make it the preferred over other processes in many cases. The synthesis of CNS by CCVD is achieved by decomposition of carbon source in the gas phase onto a catalyst over substrate, through a heated region. The energy is used to crack the molecule into reactive atomic carbon. Then carbon diffuses towards the substrate, which is heated and/or accompanied with a catalyst.
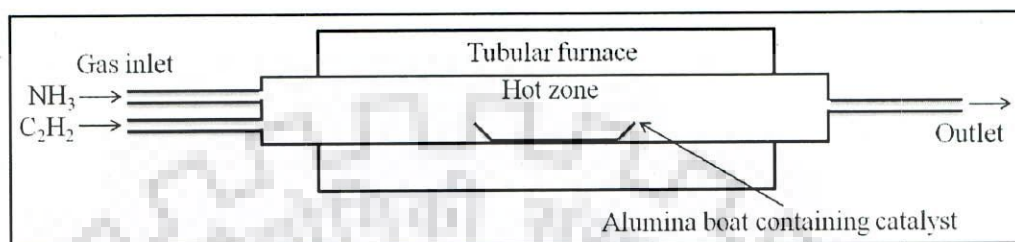
Fig. 3.4: Schematic of chemical vapour deposition setup.

The oxide nanoparticles used to grow CNS in this study have been used in two different processes. In the first process oxide nanoparticles were dispersed on the surface of AAO substrate and then these substrates were placed onto an alumina boat prior to the CCVD process, and in the second process the nanoparticles were loosely deposited onto the base of the alumina boat itself to make the process cost effective by increasing the yield without using the substrate. For dispersion the nanoparticles were dispersed in ethanol using ultrasonication (for 20 mins) to break the agglomeration between the nanoparticles and substrate was dipped into ethanol solution containing the oxide nanoparticles. The alumina boat loaded with the substrate containing nanoparticles was then placed inside a horizontal (quartz) tubular furnace (Fig. 3.4), and heated to a temperature of 600 $^{\circ}$C at a heating rate of 8 $^{\circ}$C/min. The temperature of the furnace was calibrated before introducing the catalyst in the hot chamber to assure a uniform temperature zone in the furnace. When the temperature in the furnace was reached at 600 $^{\circ}$C, ammonia gas (99.5 % Sigma) was introduced with a gas flow rate varying between 40 and 60 sccm at atmospheric pressure and under this condition, the temperature of the furnace was increased to 640 $^{\circ}$C. At this stage, acetylene gas was introduced along with ammonia gas both flowing for a time period varying between 2 and 15 minutes. The flow rate of acetylene gas (99.9 % Sigma) was varied from 10-40 sccm. The furnace was then allowed to cool down to room temperature, and CNS along with other forms of carbonaceous materials were removed from the substrate and treated in a solution of 6M HNO_3/HCl/HF or their mixture to remove primarily the catalyst particles. The CNS were then filtered and washed with deionised water until the filtrate has reached its pH of ~ 7. The CNS were then dried for about 10 hours in an oven at 120 $^{\circ}$C. The CNS were then heated in air to improve

their quality by way of having enhanced graphitization and removed the remaining amorphous carbon (Bera et al, 2006) present even after acid treatment above 400 °C depending upon their thermal stability determined by Thermogravimetric Analysis (TGA) (Joshi et al, 2009). Different types of CNS viz. MWCNT, nanofibers-straight and/or helical, tapes, chains of nanobeads have been grown by the decomposition of acetylene gas using oxide nanoparticles depending upon size of particles and other experimental conditions.

3.2 Material Characterisation Methods

3.2.1 X-Ray Diffraction (XRD) Analysis

X-ray diffraction (XRD) is a characterization technique based on the interaction of X-ray of wavelength λ comparable to the size of atoms, with the crystallographic planes of a material in accordance with Bragg's law,

$$n\lambda = 2d\mathrm{Sin}\theta \tag{3.1}$$

where n is an integer, d the spacing between successive planes in the atomic lattice and θ the diffraction angle. When the above equation is satisfied, diffraction occurs, and the diffraction pattern thus obtained allows determination of the phases in the material through its crystal structure and provides information on the orientation of the crystals in the sample. In wide angle X-ray scattering (WAXS) mode, diffraction occurs from interatomic planes separated by distances of the order of few angstroms and thus, it is related to the crystal structure of the material in terms of atomic positions. Small angle X-ray scattering (SAXS) occurs when larger entities diffract the X-rays and is associated with the degree of ordering in the structure typically in the range of 5-50 nm. The crystallographic structure of CNS is equivalent to that of graphite. The stack of graphene layers in a CNS and between layers of adjacent tubes give rise to the 002 reflection, corresponding to a d-spacing of around 0.34 nm similar to that observed between basal planes in turbostratic graphite. Other, lower intensity reflections from CNS correspond to the 100 and 101 planes of the graphitic structure. In the context of CNS, X-ray diffraction provides valuable information on the structure of samples. The main characteristics that can be observed by XRD are the crystallinity and the presence of the catalyst particles, if any. XRD was also used to determine the phase composition of the oxide nanoparticles before and after the CNS growth. Powder diffraction patterns were recorded on a Bruker AXS, D8 advance (operating at 40 kV and 30 mA) using a CuK_α radiation (1.5418 Å). The data were recorded using a step size of 0.02° and a 0.5 second dwell time. Measured diffraction patterns were compared to powder diffraction files from the JCPDS database. Quantitative estimations of phase composition were made using the semi-quantitative feature

70

present in the X'Pert Highscore Plus (PANalytical) software. For high temperature X-ray diffraction studies the sample powder was mixed with alcohol and a droplet of zapon lacquer (Anton Paar GmbH), and the resultant mixture was applied to the heating filament when operated in a vacuum chamber. Temperature was controlled using a Eurotherm 2604 controller.

3.2.2 Optical Microscopy

The surface morphology of aluminium strips was studied using an optical microscope as well as with FESEM as the resolution which is a limiting factor in optical microscope can be overcome by using FESEM. A Leica DMI5000 M microscope with Leica LAS software was used to study the surface finish of the samples.

3.2.3 Field Emission Scanning Electron Microscopy (FESEM)

Electron microscopy permits microstructure observation at very high magnification through the use of an electron beam focussed with magnetic lenses at the surface of the specimen. In scanning mode, the interaction of the electron beam with the sample produces scattering of secondary electrons from atoms in the sample and also causes electrons in the beam to be back-scattered from the sample after collision with atoms in the material, both events occurring mostly on the surface of the sample. These electrons can be detected separately and transformed into magnified images of the sample in secondary electron (SE) and backscattering (BS) modes, respectively. In SE mode, a detailed representation of the surface of a sample can be obtained. Therefore, most scanning electron microscopy (SEM) images showing the morphology of a material are taken in this mode. In BS mode, the intensity of back-scattered electrons is proportional to the atomic number of the element involved in the electron collision, therefore, this mode is usually employed to image compositional differences in a sample, observed as intensity variations in the image of the material. Further elemental analysis can be carried out using energy dispersive spectroscopy (EDS) by measuring the energy of photons emitted after scattering of atoms in the sample, which corresponds to energy transitions in the atoms of the material. After interacting with the sample, the electron beam is magnified and focused to provide an image of the structure of the material, in a manner which is conceptually similar to the acquisition of an optical image with an optical microscope in transmission mode. Samples were studied using FESEM to examine microstructural characteristics of the oxide nanoparticles, substrate, CNS, the composite electrode materials, and some qualitative elemental analysis. Samples were prepared by mounting on an aluminium stub with double sided tape and sputter coated with gold for 50

seconds with a deposition current of 30 mA in BAL-TEC sputter coater (SCD 005). A FEI QUANTA 200 F FE-SEM was used with an accelerating voltage of 20 kV and a working distance of about ~10 mm in most cases, and elemental analysis was also carried out using EDS. Catalyst size and CNS diameter were determined by image analysis of SEM micrographs using Image-J software application. Photoshop software was used to correct brightness and contrast in some SEM and TEM (discussed in next section) images.

3.2.4 Scanning Probe Microscopy (SPM)

Scanning probe microscopy (SPM) provides imaging, and measuring surfaces on a fine scale, down to the level of atoms. SPM technology shares the concept of scanning with an extremely sharp tip (3-50 nm radius of curvature) across the object surface. SPM techniques include a scanning probe microscope core with modules including AFM (atomic force microscopy). The AFM consists of a cantilever with a sharp tip (probe) at its end that is used to scan the specimen surface. The cantilever is typically silicon or silicon nitride with a tip radius of curvature of the order of nanometers. When the tip is brought into proximity of a sample surface, forces between the tip and the sample lead to a deflection of the cantilever according to Hooke's law. Depending on the situation, forces that are measured in AFM include mechanical contact forces, van der Waals forces, capillary forces, chemical bonding, electrostatic forces, magnetic forces, etc. Typically, the deflection is measured using a laser spot reflected from the top surface of the cantilever into an array of photodiodes. Other methods that are used include optical interferometry, capacitive sensing or piezoresistive AFM cantilevers. These cantilevers are fabricated with piezoresistive elements that act as a strain gauge, and the tip scans at a constant height. In most cases a feedback mechanism is employed to adjust the tip-to-sample distance to maintain a constant force between the tip and the sample. Traditionally, the sample is mounted on a piezoelectric tube that can move the sample in the z direction for maintaining a constant force, and the x and y directions for scanning the sample. The resulting map of the area f(x, y) represents the topography of the sample. The AFM can be operated in a number of modes, depending on the application. In general, possible imaging modes are divided into static (also called contact) modes and a variety of dynamic (non-contact or "tapping") modes where the cantilever is vibrated. In static mode, the cantilever is "dragged" across the surface of the sample and the contours of the surface are measured directly using the deflection of the cantilever. However, close to the surface of the sample, attractive forces can be quite strong, causing the tip to "snap-in" to the surface. Thus static mode AFM is almost always done in contact where the overall force is

repulsive. In this contact mode, the force between the tip and the surface is kept constant during scanning by maintaining a constant deflection. In the dynamic (non-contact) mode, the cantilever is externally oscillated at or close to its fundamental resonance frequency or a harmonic. In this mode, the tip of the cantilever does not contact the sample surface. The cantilever is instead oscillated at a frequency slightly above its resonant frequency where the amplitude of oscillation is typically a few nanometers. The van der Waals forces, which are strongest from 1 to 10 nm above the surface, or any other long range force which extends above the surface acts to decrease the resonance frequency of the cantilever. This decrease in resonant frequency combined with the feedback loop system maintains a constant oscillation amplitude or frequency by adjusting the average tip-to-sample distance. Measuring the tip-to-sample distance at each (x, y) data point allows the scanning software to construct a topographic image of the sample surface. Non-contact mode AFM does not suffer from tip or sample degradation effects that are sometimes observed after taking numerous scans with contact AFM. This makes non-contact AFM preferable for measuring soft samples. In the case of rigid samples, contact and non-contact images may look the same. In this study topographic image of the samples have been taken using a NT-MDT NTEGRA scanning probe microscope having Si_3N_4 probe with a tip height of 10-15 μm and radius of curvature 10 nm.

3.2.5 Transmission Electron Microscopy (TEM)

Transmission electron microscopy (TEM) is a technique whereby a beam of high energy electrons is transmitted through an ultra thin specimen, interacting with the specimen as it passes through it. An image is formed from the interaction of the electrons transmitted through the specimen; the image is magnified and focused with electromagnetic lenses onto an imaging device, such as a fluorescent screen, on a layer of photographic film, or to be detected by a sensor such as a CCD camera. The electrons are accelerated at ~ 200 kV, giving wavelengths much smaller than that of light. An accelerating voltage of 200 kV gives rise to electron wavelength of 0.025 Å. Whereas the resolution of the optical microscope is limited by the wavelength of light, that of the electron microscope is limited by aberrations inherent in electromagnetic lenses, to about 1-2 Å. Even for very thin samples one is looking through many atoms, one does not usually see individual atoms. Rather the high resolution imaging mode of the microscope, images the crystal lattice of a material as an interference pattern between the transmitted and diffracted beams. This allows one to observe planar and line defects, grain boundaries, interfaces, etc. with atomic scale resolution. The bright field/dark

field imaging modes of the microscope, which operate at intermediate magnification, combined with electron diffraction, are also invaluable for giving information about the morphology, crystal phases and defects in a material. At lower magnifications TEM image contrast is due to absorption of electrons in the material, thickness and composition of the material. At higher magnifications complex wave interactions modulate the intensity of the image, requiring intense analysis of observed images. Alternate modes of use allow for the TEM to observe modulations in chemical identity, crystal orientation, electronic structure and sample induced electron phase shift as well as the regular absorption based imaging. By adjusting the magnetic lenses such that the back focal plane of the lens rather than the imaging plane is placed on the imaging apparatus, a diffraction pattern can be generated. For thin crystalline samples, this produces an image that consists of a pattern of dots in the case of a single crystal, or a series of rings in the case of a polycrystalline or amorphous solid material. For the single crystal case the diffraction pattern is dependent upon the orientation of the specimen and the structure of the sample illuminated by the electron beam. This is typically done without utilising any information but the position at which the diffraction spots appear and the observed image symmetries. Structure of CNS, the morphology and elemental analysis of catalyst particles inside the CNS were observed with TEM using a FEI Tecnai G^2 20, JEOL-2100 HRTEM, FEI Tecnai F20-G2 FEGTEM and JEOL 200CX TEM with an acceleration voltage of 200 kV. Samples were prepared for TEM by dispersing a small amount of powdered (or ground) material in ethanol/isopropanol/acetone, placing a few drops of the suspension on a holey carbon-coated copper grid, and allowing it to dry.

3.2.6 Simultaneous DTA and TGA (SDT) Analyses

Thermal analysis provides information on structural and phase change as well as energy of transformation involved in the materials with increasing temperature. Several methods are commonly used and these are distinguished from one another by the property, which is measured. The methods are thermogravimetric analysis (TGA) for weight loss, differential thermal analysis (DTA) for temperature difference etc. However, in the present study both DTA and TGA have been used. The thermal stability of CNS and their impurities were studied. Typically, the measurements were carried out in air, so as to identify the different carbonaceous species in the sample by recording the mass-loss associated with the temperature at which they oxidize. In most cases, several decomposition peaks are readily separable, and the fraction of CNS, amorphous carbon and catalyst can therefore be determined. Thermal analysis (DTA/DSC) is also carried out on oxide nanoparticles to

determine further oxidation, decomposition or melting that may occur along with weight loss over the temperature range of interest. Measurements were made in a variety of atmospheres (Ar/N$_2$/air) using a Perkin Elmer (Pyris Diamond) and Exstar TG/DTA 6300 (SII Nanotechnology Inc.) (for samples up to 1500 $^\circ$C), and a TA Instruments SDT Q600 (for samples up to 1000 $^\circ$C from -150 $^\circ$C) at a heating rate of 10 $^\circ$C min^{-1} by using alumina as the reference material and aluminium as the reference material in case of low temperature analysis.

3.2.7 Raman Spectroscopy

Raman spectroscopy is a characterisation technique based on inelastic scattering of light from materials and related to different vibrational modes of their atoms. Since it involves light in the visible range, only atoms on or near the surface of the material is excited and therefore, in most cases, Raman spectroscopy is only a surface characterization technique. As Raman modes originate from scattering caused by atomic vibrational modes of oscillation, they are susceptible to frequency changes due to thermal variations, pressure and stress in the molecule, all of which translate as shifts in the position of the Raman peaks. The main Raman-active vibrational modes in CNS in general give rise to peaks at ~ 1320 cm^{-1}, ~ 1580 cm^{-1} and ~ 2635 cm^{-1}, labelled as D, G and 2D, respectively; although each effectively consists of a superposition of several peaks related to specific characteristics of the material. The first peak is associated with impurities in the form of sp^3 bonds and poor graphitization, and is referred to as the 'disorder or defect' peak (D). The G (Graphitic) peak originates from the tangential vibration of C atoms in a hexagonal lattice, and is indicative of the degree of graphitization in the material. It is common practice to evaluate the purity of a graphitic material as the ratio of the intensities of these peaks (I_D/I_G). The 2D peak, sometimes also referred to G', is a second order peak related to the D peak, although not directly related to poor graphitisation in the material in the same way. It is, however, affected by the interaction between stacked graphene layers and by the termination of the layers. SWCNT and tubes with few walls show an additional Raman active mode associated with the radial expansion/contraction of the nanotube, referred to as radial breathing mode (RBM) and, typically, found in the range 70-400 cm^{-1}. It holds a special relation with the electronic band structure of the tubes, which allows estimation of the tube diameter from the Raman shift of the RBM peak (ω). For nanotubes with diameters greater than 1 nm the diameter is obtained as,

$$\Phi = \frac{234}{\omega - 10}$$

(3.2)

The lack of RBM peaks was another confirmation of the existence of MWCNT with rather large diameter inner tubes. The spectrum from carbon nanobeads show D and a single G peak with no clear G' or D'. The spectrum is sensitive to the change in lengths, strengths and arrangement of bonds in a material than it is to the change in chemical composition. Therefore the Raman spectrum of oxide nanoparticles before and after growth was also studied. In this context, the possibility of values relating to the shift and the intensity ratio (I_D/I_G or $I_D/I_{G'}$) in Raman spectrum are proposed: assuming that all structures posses their individual morphology. A Renishaw 1000 Ramascope spectrometer and Renishaw inVia with a 514 nm wavelength (green visible light) excitation laser was used, and several spectra were taken from different samples. Raman spectra were processed using the Renishaw WIRE 2.0 software application and also with Origin 8.0 software, using a multi-peak Gaussian fit.

3.2.8 Surface Area (BET) Analysis

BET theory aims to explain the physical adsorption of gas molecules on a solid surface and serves as the basis for an important analysis technique for the measurement of the specific surface area of a material. In 1938, Stephen Brunauer, Paul Hugh Emmett and Edward Teller published an article about the BET theory in a journal (Brunauer, et al, 1938) for the first time. The concept of the theory is an extension of the Langmuir theory, which is a theory for monolayer molecular adsorption, to multilayer adsorption with the following hypotheses: (a) gas molecules physically get adsorbed on a solid in layers infinitely, (b) there is no interaction between each adsorption layer, and (c) the Langmuir theory can be applied to each layer. The resulting BET equation is expressed as:

$$\frac{1}{v\left[\left(\frac{P_0}{P}\right)-1\right]} = \frac{C-1}{v_m C}\left(\frac{P}{P_0}\right) + \frac{1}{v_m C} \tag{3.3}$$

P and P_0 are the equilibrium and the saturation pressure of adsorbates at the temperature of adsorption, v is the adsorbed gas quantity (for example, in volume units) and v_m is the monolayer adsorbed gas quantity. C is the BET constant. A total surface area S_{total} and a specific surface area S are evaluated by the following equations:

$$S_{total} = \frac{(v_m N s)}{V} \tag{3.4}$$

where v_m is in units of volume which are also the units of the molar volume of the adsorbate gas

$$S_{BET} = \frac{S_{total}}{a} \tag{3.5}$$

N: Avogadro's number,

s: adsorption cross section of the adsorbing species,

76

V: molar volume of adsorbate gas,

a: mass of adsorbent (gm)

The equation 3.3 is an adsorption isotherm and from the plot, v_m and *C* can be calculated, which will be needed to calculate the specific surface area. The BET specific surface area and the pore volume of the CNS were determined using a Micromeritics Chemisorb 2720. Samples were prepared by out gassing in N_2 at 150 °C for at least two hours.

3.2.9 Particle Size Distribution

In dynamic light scattering (DLS) when light hits small particles the light scatters in all directions (Rayleigh scattering) as long as the particles are small compared to the wavelength of light (below 250 nm). If the light source is a laser, and thus is monochromatic and coherent, then one observes a time-dependent fluctuation in the scattering intensity. These fluctuations are due to the fact that the small molecules in solutions are undergoing Brownian motion and so the distance between the scatterers in the solution is constantly changing with time. This scattered light then undergoes either constructive or destructive interference by the surrounding particles and within this intensity fluctuation, information is contained about the time scale of movement of the scatterers. Zetasizer works on the principle of DLS, which is used to measure particle size and molecule size. This technique measures the diffusion of particles moving under Brownian motion, and converts this to size and a size distribution using the Stokes-Einstein relationship. Non-invasive back scatter technology is incorporated to give the highest sensitivity simultaneously with the highest dynamic size and concentration range. The distribution of powder particle sizes was measured using a Zetasizer Nano-ZS90 (MALVERN Instrument). To prepare samples for measurement, approximately 50 mg of powder was ultrasonicated in 100 mL of water for 8 mins. Measurements were made over the size range of 10-600 nm. Reported values are the averages of three measurements taken for each sample. The particle sizes measured using the software 'Image-J' on FESEM micrographs were then compared with the particle size identified from 'Zetasizer'.

3.3 Electrochemical Study

The electrochemical measurements of the Li-ion cell carried out in different steps are discussed below.

3.3.1 Preparation of CNS based Electrode

Preparation of the electrodes involves mixing the synthesized sample (70 wt.%) with small amounts of carbon black (CB) (15 wt.%), a binder material and an organic solvent for the binder (15 wt.%). The mixture is then subsequently spread over a copper foil, which acts as a current collector to form the electrode. The carbon black additive is used to increase the conductivity of the electrode. The binder used in this study was Polyvinylidene Fluoride (PVDF) diluted in N-Methyl-2-Pyrrolidinone (NMP) as an organic solvent. NMP is also added to thin out the slurry so that it can be spread homogeneously onto the electrode. The electrode material consisting of active material (CNS), carbon black and PVDF binder in NMP solvent. The mixing was carried out using mortar and pestle to form viscous slurry. Electrodes were prepared by coating of slurries on copper foil and initially the copper foil was thoroughly cleaned by degreasing it with acetone. Then the coated sample was dried in a vacuum oven for 12 hrs and then the coated copper foil was pressed between steel rollers. The particular area of electrode has been cut with an area of $\sim 1 \text{ cm}^2$, which has been used as anode of the cell.

3.3.2 Cell Fabrication

Teflon made cylindrical cells were fabricated for all electrochemical testings. A micro porous sheet (Celgard 2400) was used as separator. The main steps used in fabrication of cell are shown in Fig. 3.5. However, the detailed schematic of the cell is shown in Fig. 3.6, which shows the positions of electrodes and a separator inside a cell. The electrolyte used was 1M LiPF_6 in a 1:1 volume ratio of ethylene carbonate (EC) and diethyl carbonate (DEC) (Mitsubishi Chemical Corp.). These cells were assembled in an argon-filled MBRAUN glove box (MB 200G) having both oxygen and moisture contents less than 0.1 ppm.

Developed CNS + acetylene black + PVDF (70:15:15 wt.%) + N-Methyl-2-pyrrolidone (NMP)
⇩
Coated onto Cu foil and dried in vacuum oven at 120 °C for 12 hrs and cut into 1cm²
⇩
Thin strip of Li foil as reference electrode
⇩
Celgard (2400) as separator
⇩
Electrolyte: 1M LiPF_6 in ethylene carbonate (EC) and diethyl carbonate (DEC) in 1:1 v/v
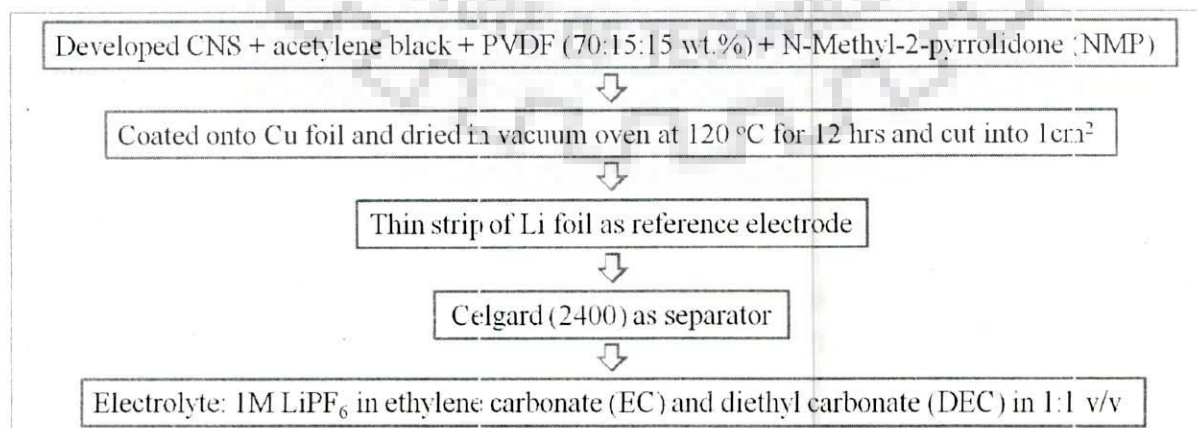
Fig. 3.5: Steps used for cell-fabrication.
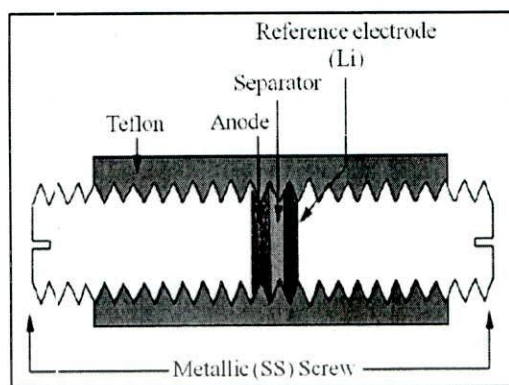
Fig. 3.6: Schematic of the cell used for electrochemical testing.

3.3.4 Electrochemical Testing

Five different types of CNS viz. SWCNT, DWCNT, MWCNT with two different diameters and CNF have been tested electrochemically, and among which the MWCNT with larger diameter and CNF have been prepared by the process of CCVD mentioned earlier in this Chapter. The other three types of CNS were purchased from Chengdu Organic Chemicals Co., Ltd. Chinese Academy of Sciences, China. Electrochemical testing of active electrode materials is done using lithium metal as the reference electrode. Li-metal used can provide infinite number of Li-ions with constant chemical potential. The voltage of a real cell, depends on the chemical potential of both the electrodes and thus, if two intercalation compounds were used, one could not ascertain the voltage profile of individual electrode. In a real lithium ion cell, carbon based material would be used as the anode, however, in the test cells the carbon based material is the cathode as the tests have been conducted with respect to lithium metal as counter electrode. The discharge cycle for this half-cell corresponds to the insertion of lithium into the carbon-based material. This is opposite to the real cell situation where the discharge process corresponds to the transfer of lithium from the carbonaceous material to the transition metal oxide cathode. The test cells were charged and discharged in the potential window of 0.01-3.00 V vs. Li/Li$^+$, at a rate of 0.1C assuming 1C is equivalent to 372 mA for pure graphite based electrode using the electrochemical analyzer (ARBIN: BT-2000). In constant current cycling, a constant current is applied to the battery and the resulting change in the cell potential as a function of time is monitored. From one complete charge-discharge cycle, the gravimetric capacity is derived from the total charge passed per unit mass of the active electrode material, following the equation

$$\text{Charge capacity} = \frac{I(mA) \times t(hrs)}{W\ (gm)} \tag{3.6}$$

where I is the current in mA at which cell has been cycled, t is the time in hours and w is weight of active materials in gram.

Results and Discussion: Growth of Carbon Nanostructures

Chapter 4

Results and Discussion: Growth of Carbon Nanostructures

Carbon nanostructures (CNS) have been synthesized by catalytic chemical vapour deposition (CCVD) method following the procedure described in the previous chapter (Chapter 3) on experimental procedure. For the synthesis of carbon nanostructure by the method of CCVD there are two essential steps to be followed prior to the synthesis of CNS, which are (i) preparation of the substrate for the catalyst support, on which the nanoparticles will be dispersed, and (ii) preparation of the oxide nanoparticles on which the CNS will grow. In this chapter, the results on synthesis and characterization of substrate (porous anodized alumina), oxide nanoparticle and CNS have been described in the following sections and the results are discussed at the end in the context of results reported in the literature.

4.1 Characterization of the Substrate

The substrates of porous anodic aluminium oxide (PAAO) were prepared by anodizing the thin foil of aluminum strip (thickness about 0.3 mm) as described in chapter-3. The anodized porous alumina has been used as a support of catalyst in some experiments to grow CNS. Prior to anodizing, pretreatment of the aluminum strip is an important step for obtaining ordered porous structure in the anodized alumina, and the process consists of mechanical polishing, degreasing and finally electro polishing as mentioned in the section on experimental procedure in chapter-3. The good quality of surface finish of the aluminum strip can be seen from the optical micrograph as shown in Fig. 4.1(a) and hence no mechanical polishing has been carried out for these samples for anodizing. The optical and FESEM micrographs (inset of Fig. 4.1(b)) of aluminum sample with visible rolling marks are shown in Fig. 4.1(b) at two different magnifications.
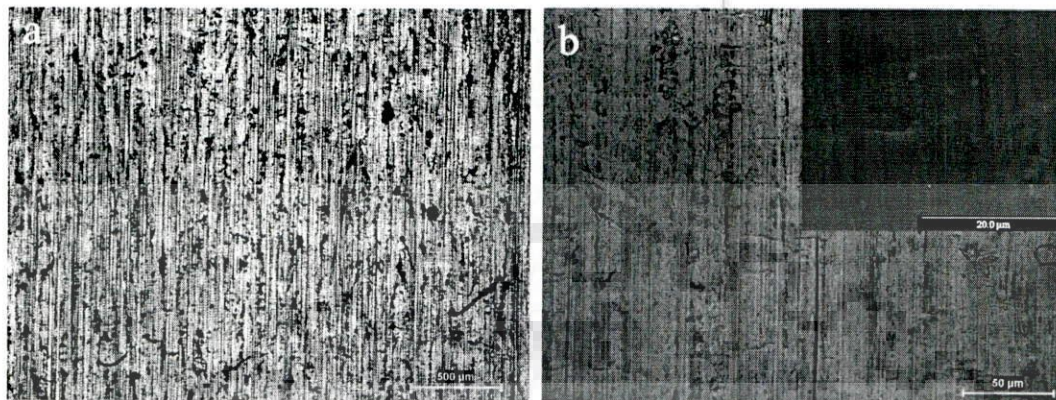
Fig. 4.1: Optical micrograph of as received pure aluminum sample at two different magnifications at (a), and (b) along with FESEM micrograph of the same (inset of 'b').

The electro polishing was carried out in the solution of ethyl alcohol and perchloric acid in the ratio of 5:1 by volume. The typical FESEM image of an electro-polished sample is shown in Fig. 4.2(a). The anodizing has been carried out in the electro-polished area using three different electrolyte baths, namely, of phosphoric, oxalic and sulfuric acid, in order to obtain appropriate condition to obtain the pores of different sizes. On the basis of these results, the electrolyte bath of phosphoric acid has been chosen for anodizing the electro-polished samples of pure aluminum for use as substrate in this study. The first anodizing results in very irregular pore structure when the pores are nucleated inhomogeneously on the surface of the sample as shown in Fig. 4.2(b).
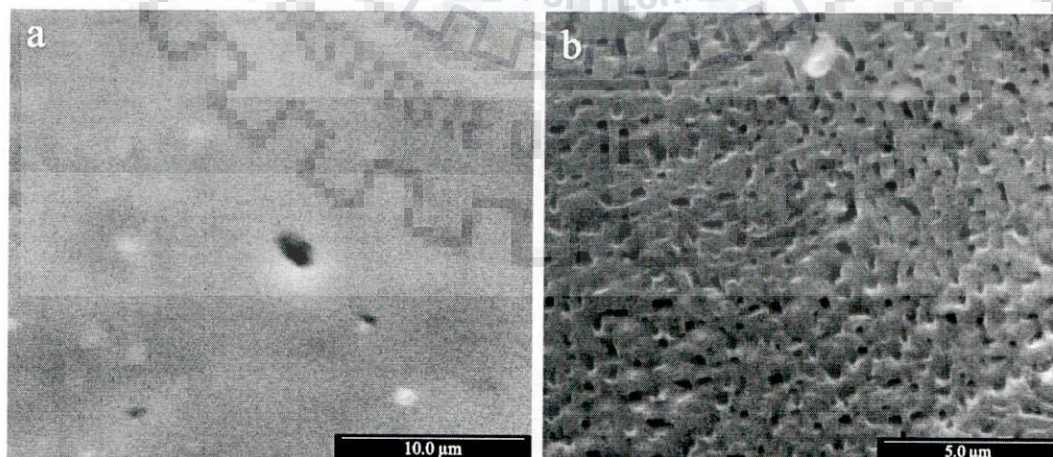
Fig. 4.2: Typical FESEM micrograph of aluminum strip after (a) electro-polishing, and (b) anodizing for the first time.

When these irregularly distributed pores are etched out and second anodization is carried out for long anodizing time, the repulsive forces between neighboring pores lead to self-organization of nano-sized pores resulting in a new nanoporous anodized layer. Fig. 4.3 shows the top view of anodized aluminum strip anodized second time at 80 V for 30 min to get a regular array of pores. The FESEM micrographs of anodized aluminum are shown at two different magnifications in Fig. 4.3(a) and (b). The extent of ordering in the pore structure can be clearly observed.
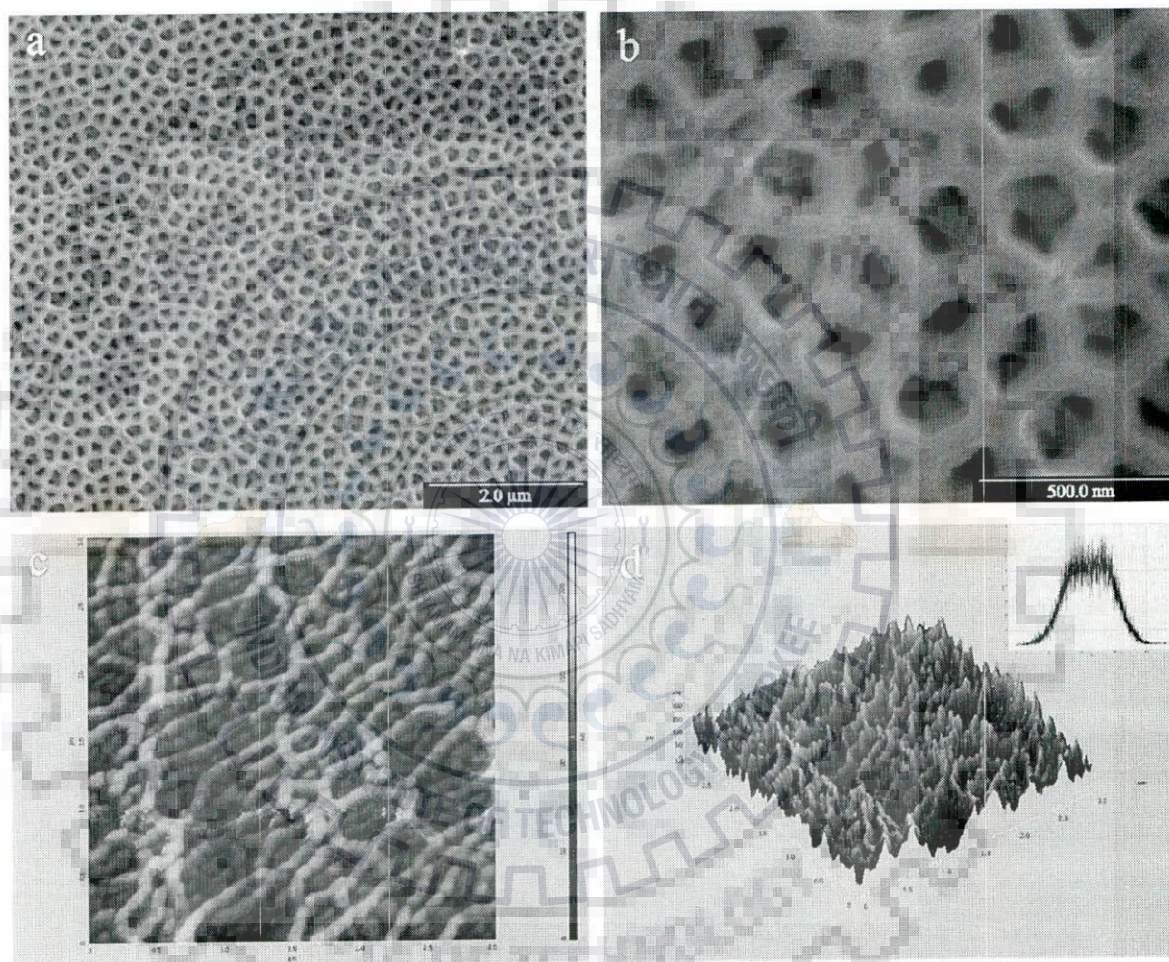
Fig. 4.3: Typical FESEM micrograph of nanoporous alumina substrate at magnifications: (a) 20K, and (b) 1000K; Typical AFM image of the same substrate (c) two-dimensional image, and (d) three-dimensional image; Histogram inset in (d) shows the size distribution of pores.

The average size of pore as determined by FESEM is ~ 128 nm whereas the range of pore diameter obtained is 55 to 275 nm whereas from AFM images (Fig. 4.3(c) and (d)), one obtains the average pore size of ~ 120 nm and roughness value (H) of 33 nm. This variation in pore diameter may have been enhanced by the presence of pits and scratches on the surface of

85

as received samples, as the pores in these reactive locations could grow faster. The nanoporous alumina obtained by two step anodization has been used as a substrate to support nano-sized particles to catalyze growth of CNS.

4.2 Characterization of the Oxide Nanoparticles

The oxide nanoparticles were prepared by sol-gel route following the procedure given in chapter-3. Table-4.1 gives the different sizes of oxide nanoparticles resulting from varying composition of salt mixture and use of different processing conditions in respect of gelation time, temperature, firing conditions etc. For each and every composition of salt mixture, two different sizes of oxide particles have been prepared. The temperature and the time of the gel formation have been maintained as chosen and the dried gels have been calcined at 800 ^{o}C for 5 hrs to get relatively larger oxide particles. Smaller oxide particles in the desired size range have been obtained by lowering the calcination temperature by 230-500 ^{o}C from 800 ^{o}C used for growing the larger particles. Lower limit of the calcination temperature is limited by the decomposition temperature so that volatile matters are removed. The size of the oxide particles could thus be varied in a limited range by suitably choosing calcination temperature as reported in Table-4.1. The table also presents the variation of copper oxide doping levels used in particles of cobalt and nickel oxide, the designation of oxides used in the text and their size distribution. The designation contains the chemical symbol of the corresponding metallic elements of the primary oxide and that of the dopant, if present, followed by the doping level expressed in wt.% of metallic element of the dopant replacing the metallic element of primary oxide. Further 'C' and 'F' present with bracket in the designation indicates 'coarse' for relatively larger particles and 'fine' for relatively smaller particles. The particle sizes obtained by "Image-J" software have been compared with those obtained through zetasizer and the results are reported in Table-4.1.

86

Table-4.1: Details of doping and size distribution of oxide nanoparticles.

Sample designation	Doping level of copper (wt.%)	Time for gel formation (hrs)	Temperature (^{o}C) for gel formation	Temperature (^{o}C) of calcination	Size range (nm)	Average size (nm)	
						Image-J	Zetasizer
Co(C)	0	4	75	800	167-691	581	583.4
Co(F)		4	75	400	19-50	40	35
CoCu01(C)	1	2	75	800	88-424	350	327.3
CoCu01(F)		2	75	310	19-45	33	29.5
CoCu10(C)	10	1	84	800	71-391	225	251
CoCu10(F)		1	84	310	58-117	71	84
CoCu20(C)	20	6	76	800	137-663	500	531.9
CoCu20(F)		6	76	350	20-54	41	34
Ni(C)	0	5	72	800	134-295	204	190.1
Ni(F)		5	72	360	23-82	53	48
NiCu10(C)	10	4	71.5	800	137-319	248	267.2
NiCu10(F)		4	71.5	450	27-57	41	37.5
NiCu15(C)	15	4	75	800	45-165	97	91.2
NiCu15(F)		4	75	500	42-78	66	59
NiCu20(C)	20	3	76	800	70-173	130	141.8
NiCu20(F)		3	76	360	28-60	46	41.6
Cu(C)	0	2	72	800	531-1281	1129	805.6
Cu(F)		2	72	230	15-29	19	22

4.2.1 Structure and Morphology of Oxide Nanoparticles

This subsection contains the results on the structure and morphology of copper doped (0-20 wt.%) oxide nanoparticles of cobalt and nickel, which have been used in CCVD for CNS growth. At higher calcination temperature of 800 ^{o}C, the resulting nanoparticles of cobalt oxide without doping are of larger size (average size ~ 581 nm) but with a low level of doping such as in CoCu01(C), the average particle size decreases to ~ 350 nm, as given in Table-4.1. However, with lower calcination temperature the average particle size becomes 40 nm and the effect of doping on size reduction is relatively small. The average size of the coarse particles of nickel oxide is relatively smaller (average size ~ 204 nm) than that of coarse cobalt oxide particles (average size ~ 581 nm), calcined at the same temperature of 800 ^{o}C. For fine particles of nickel based oxide, the average particle size decreases from 53 nm in Ni(F) to 41 nm in NiCu10(F) due to doping but with the same level of doping in CoCu10(F) results in an increase in the average size of particles to 71 nm, though the average size is found to decrease with 1 wt.% of copper doping as given in Table-4.1.
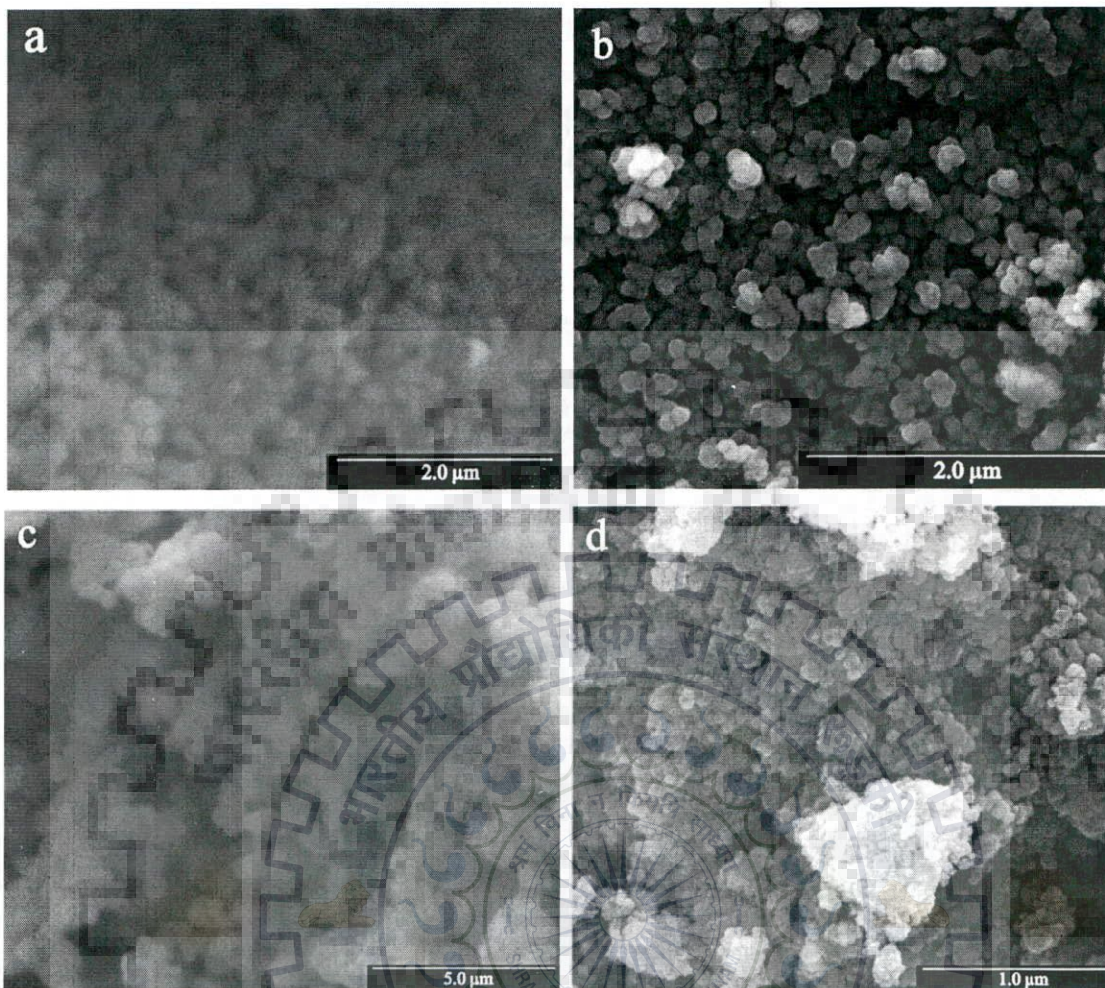
Fig. 4.4: Typical FESEM micrographs of doped cobalt oxide based nanoparticles: (a) CoCu10(C), (b) CoCu10(F), (c) CoCu20(C), and (d) CoCu20(F).

Fig. 4.4(a) shows polydispersity (71-391 nm) of the coarse nanoparticles, designated CoCu10(C), obtained by calcination at relatively higher temperature of 800 ^{o}C while the fine particles having the same composition obtained by calcination at lower temperature of 310 ^{o}C, as shown in Fig. 4.4(b), have better uniformity in size although some particles are agglomerated. FESEM micrographs of relatively coarser cobalt oxide nanoparticles doped to 20 wt.% copper, designated CoCu20(C), shows elongated shape with aspect ratio lying in the range of ~ 1.5 to 2.5 besides being polydisperse as can be seen in Fig. 4.4(c). But the shape remains by and large rounded for finer particles of the same composition as shown in Fig. 4.4(d).
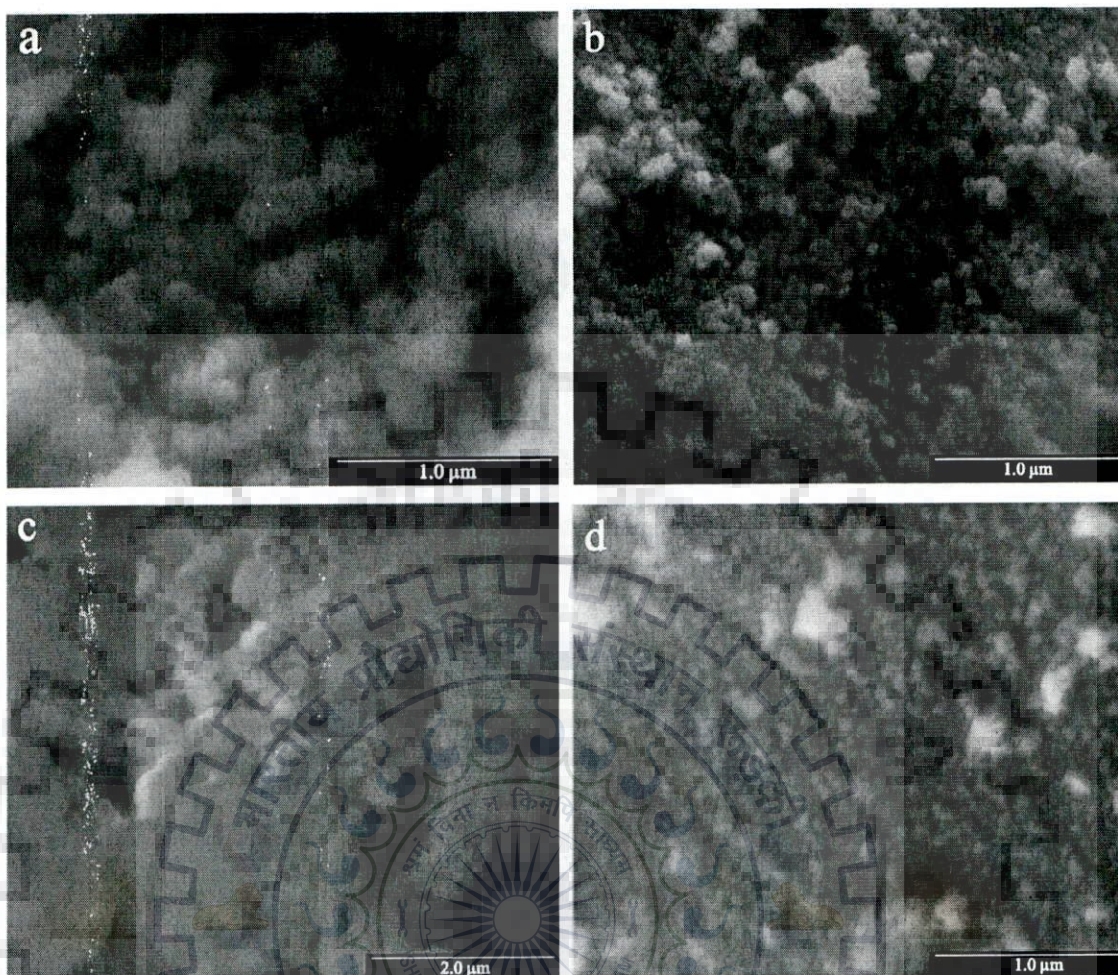
Fig. 4.5: Typical FESEM micrographs of doped nickel based oxide nanoparticles: (a) NiCu10(C), (b) NiCu10(F), (c) NiCu20(C), and (d) NiCu20(F).

Fig. 4.5(a) shows that relatively larger nanoparticles of doped nickel oxide, NiCu10(C), calcined at 800 °C reveal polydispersity as it was observed in doped cobalt oxide in Fig. 4.4(a). But for the same level of copper doping, the particle size range of doped nickel oxide is relatively narrower as given in Table-4.1. But for the same level of doping fine particles of nickel oxide system are smaller than cobalt oxide system (Fig. 4.5(b)) though calcination temperature (450 °C) is higher for nickel oxide based system compared to cobalt oxide based system. The smaller particles of nickel oxide have a smaller degree of dispersity compared to the larger particles of the same composition as given in Table-4.1. It is interesting to observe that with an increased doping level as in NiCu20(C), the shape of the larger particles as shown in Fig. 4.5(c) is not elongated, unlike that observed in similarly doped larger cobalt oxide particles shown in Fig. 4.4(c). The average size of larger particles is considerably smaller than cobalt oxide based particles for the same level of copper doping and calcination temperature, as given in Table-4.1. The smaller nanoparticles of NiCu20(F) obtained by calcination at 360

°C as shown in Fig. 4.5(d), have sizes similar to CoCu20(F) calcined at similar temperature of 350 °C shown in Fig. 4.4(d) and the particles are nearly rounded shape.
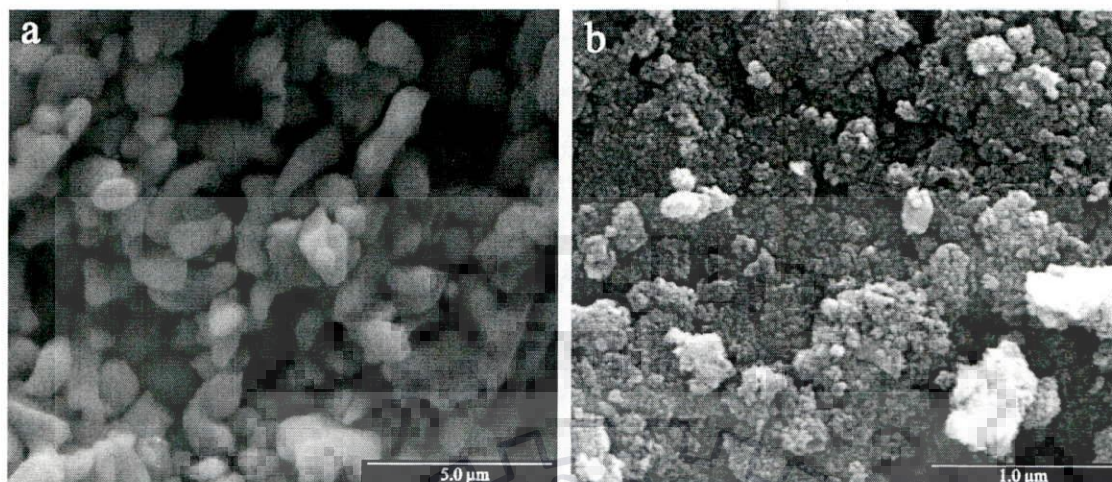
Fig. 4.6: Typical FESEM micrographs of pure copper oxide with two different sizes (a) Cu(C), and (b) Cu(F).

Pure copper oxide based nanoparticles have also been prepared for use as catalyst in the synthesis of CNS as reported in Table-4.1. At higher calcination temperature of 800 °C, the particles are elongated and are also significantly coarser with an average size of about 1 μm as shown in Fig. 4.6(a) while the smaller particles obtained after calcination at 230 °C has an average size of 19 nm as shown in Fig. 4.6(b).

X-ray diffraction (XRD) pattern of pure cobalt oxide nanoparticles shown in Fig. 4.7, reveals only cubic phase of spinel Co_3O_4 exists. This phase contains Co^{2+} and Co^{3+} located at tetrahedral and octahedral positions respectively in face centered cubic oxygen lattice structure. The positions of the diffraction peaks and their relative intensities for pure and doped cobalt oxides are given in Table-4.2. The doping has resulted in replacement of divalent cobalt by copper resulting in $Co_{3-x}Cu_xO_4$. The crystal structure remains cubic on doping as observed from XRD patterns of doped oxides in Fig. 4.7 and the structure has a space group (*Fd3m*; 227). There is nominal reduction in the lattice parameter from 8.11 to 8.074 Å due to doping, which may be taken as an indication of copper ions entering into the lattice of Co_3O_4.
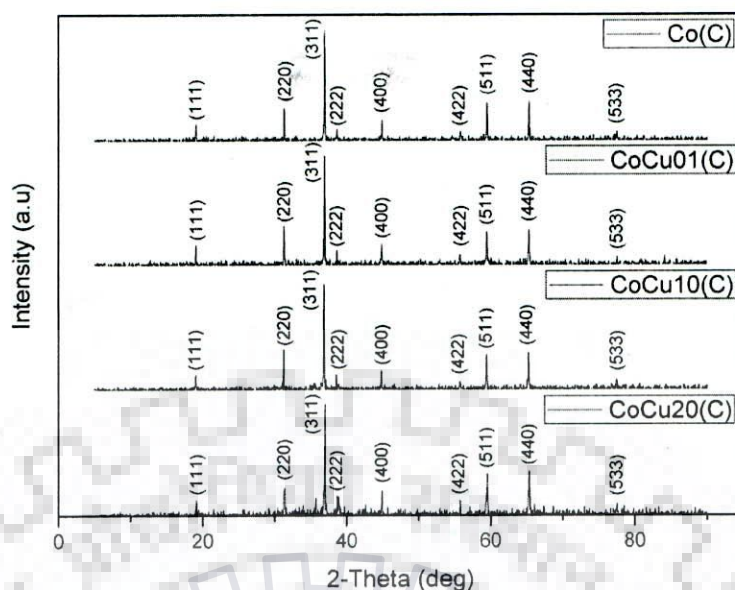
Fig. 4.7: Typical XRD pattern of pure and doped cobalt oxide nanoparticles indexed respectively to Co_3O_4 (top), and $Co_{3-x}Cu_xO_4$.

Table-4.2: Positions of X-ray diffraction peaks and the corresponding relative intensities for pure and doped cobalt oxides.

No. of peaks	Co(C)		CoCu01(C)		CoCu10(C)		CoCu20(C)	
	2θ (degree)	Rel. Intensity (%)	2θ (degree)	Rel. Intensity (%)	2θ (degree)	Rel. Intensity (%)	2θ (degree)	Rel. Intensity (%)
1	18.8894	11.35	18.9745	21.08	18.9564	12.16	19.1014	16.54
2	31.3469	27.17	31.3409	45.59	31.4288	25.28	31.2683	28.17
3	36.976	100	36.9524	100	36.8883	100	36.977	100
4	38.682	11.2	38.7453	15.99	38.863	12.11	38.801	10.14
5	44.9452	17.97	44.8814	30.74	44.8224	16.96	45.0257	22.43
6	55.7974	10.12	55.7609	14.53	55.8266	5.1	55.9309	9.38
7	59.4454	36.59	59.4617	56.52	59.4682	40.92	59.4624	43.76
8	65.401	39.88	65.3838	55.92	65.4138	41.43	65.3046	44.24
9	77.3291	8.09	77.3342	8.39	77.1424	6.58	77.4189	4.35

Fig. 4.8 shows XRD patterns of the pure and doped nickel oxide nanoparticles and only cubic phase of nickel oxide (NiO) has been identified in the sample of pure nickel oxide. The positions of the diffraction peaks and their relative intensities for pure and doped nickel oxides are given in Table-4.3. Doping has resulted in replacement of divalent nickel by copper resulting in $Ni_{1-x}Cu_xO$. The structure remains cubic on doping, belongs to the space group (*Fm3m;* 225). A nominal increase in lattice parameter from 4.168 to 4.188 Å takes place on doping and it may be indicative of copper entering into the lattice of NiO.

91
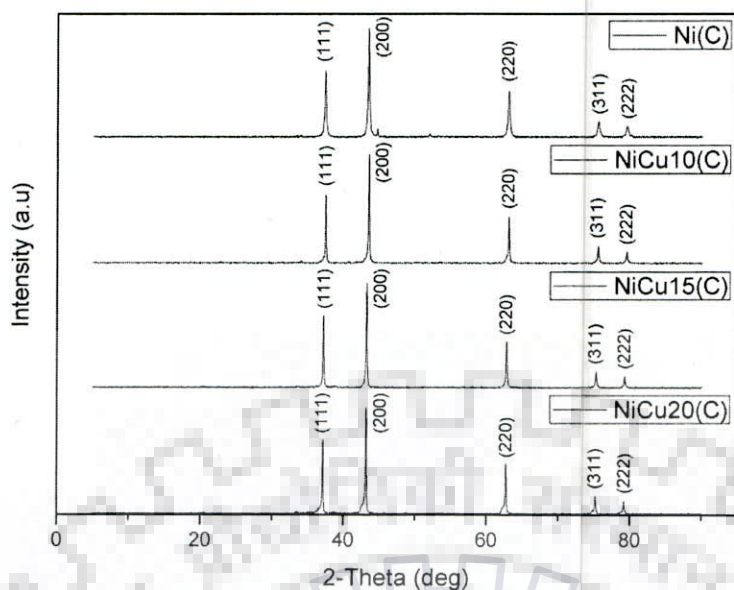
Fig. 4.8: Typical XRD pattern of pure and doped nickel oxide nanoparticles indexed to NiO (top), and $Ni_{1-x}Cu_xO$ respectively.

Table-4.3: Positions of X-ray diffraction peaks and the corresponding relative intensities for pure and doped nickel oxides.

No. of peaks	Ni(C)		NiCu10(C)		NiCu15(C)		NiCu20(C)	
	2θ (degree)	Rel. Intensity (%)	2θ (degree)	Rel. Intensity (%)	2θ (degree)	Rel. Intensity (%)	2θ (degree)	Rel. Intensity (%)
1	37.3838	61.89	37.4252	61.83	37.1959	63.16	37.0584	57.45
2	43.4163	100	43.4623	100	43.2284	100	43.0904	100
3	63.0377	46.41	63.0411	54.18	62.8193	52.18	62.6835	58.62
4	75.5924	17.21	75.5703	20.07	75.3457	18.39	75.2228	22.79
5	79.6041	12.44	79.5837	14.5	79.3626	13.83	79.1995	15.9

Fig. 4.9 shows XRD pattern of the pure copper oxide which has been used as dopant as well as oxide used for the growth of CNS in the present study. The positions of the diffraction peaks and their relative intensities are given in Table-4.4. The indexing of the pattern reveals the material is of CuO phase having monoclinic phase belonging to the space group (*C2/c; 15*) with lattice parameters as $a = 4.685$ Å, $b = 3.423$ Å and $c = 5.132$ Å.
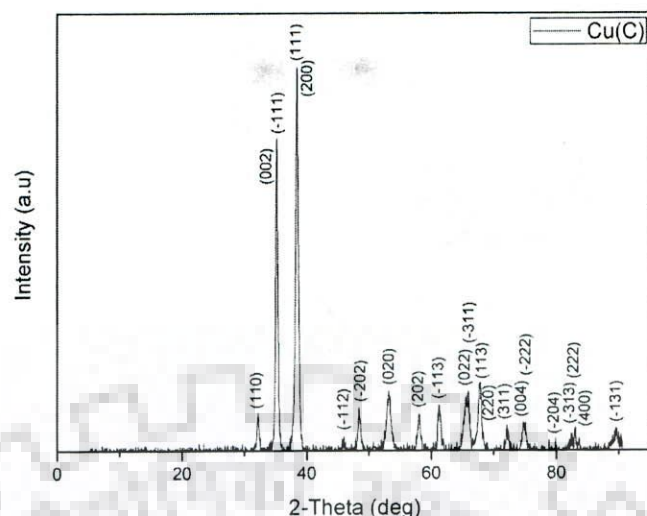
Fig. 4.9: Typical XRD pattern of pure copper oxide nanoparticles indexed to CuO.

Table-4.4: Positions of X-ray diffraction peaks and the corresponding relative intensities for pure copper oxide.

No. of peaks	Cu(C)	
	2θ (degree)	Rel. Intensity (%)
1	32.4735	7.66
2	35.4818	82.26
3	38.7386	100
4	46.458	3.46
5	48.7973	8.77
6	53.5177	15.74
7	58.3796	7.52
8	61.6352	10.42
9	66.2199	14.97
10	68.1122	18.18
11	72.5236	5.71
12	75.2352	6.51
13	80.3234	1.76
14	83.3486	3.99
15	89.9327	4.17

4.2.2 Melting/Surface Melting of the Oxide Nanoparticles

In order to understand the role of the oxide nanoparticles in the growth of CNS it is necessary to understand the state of the nanoparticles in which they are present at the temperature of CNS growth in the CCVD process. Differential thermal analysis (DTA) and high temperature XRD studies have been carried out to track the changes taking place in the oxide nanoparticles. Due to large number of surface atoms in nanoparticles, their thermal behaviour is expected to be different from that of the bulk material.

93
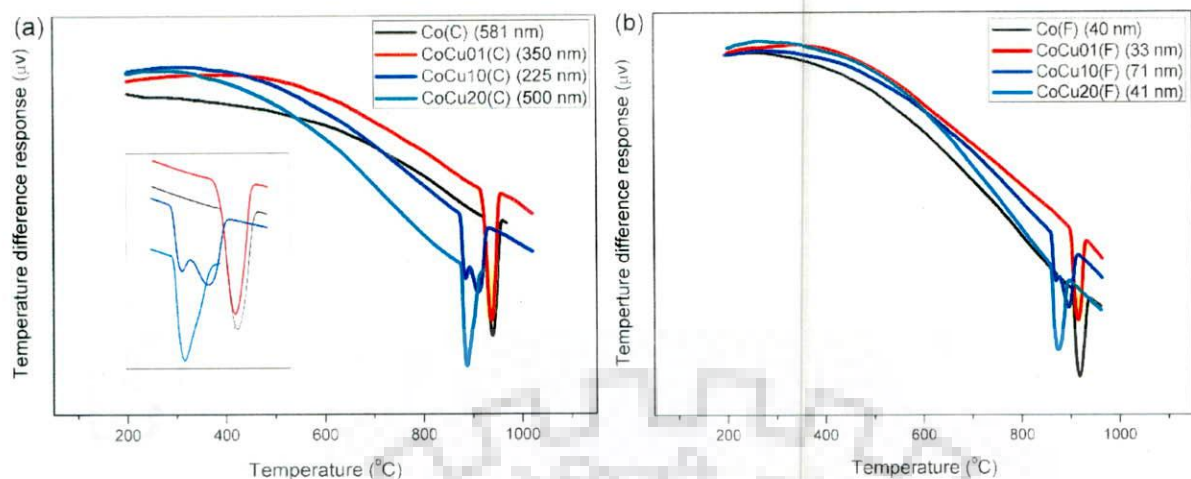
Fig. 4.10: Typical DTA curves of cobalt oxide based nanoparticles with (a) different levels of doping and size (the inset showing magnified view of sharp endothermic peak), and (b) limited range of average particle sizes.

Fig. 4.10 shows the DTA response of pure and doped nanoparticles of cobalt oxides having different composition and particle size distribution as given in Table-4.1. The results show a broad endothermic peak, within which a sharp endothermic peak is embedded. The position of the sharp peak is around the melting point of Co_3O_4 of 895 °C and the peak therefore may be attributed to bulk melting. Increase in level of doping decreases the temperature at start of the broad peak as well as the sharp peak temperature. The broad endothermic peak for oxide of a given average size could be overlap of several peaks corresponding to melting/surface melting of different sizes of nanoparticles. The start of the broad endothermic peak could therefore be attributed to the melting/surface melting of smallest size of nanoparticles. Increased level of doping has also resulted in relatively rapid fall in the broad peak. When the average size of particles are different, the contours of the broad peak of different samples are away from each other as shown in Fig. 4.10(a) while these contours are relatively close to each other when the average size of the particles are in a close range, as shown in Fig. 4.10(b). The temperature at the start of the broad endothermic peak has been taken as a characteristic relevant for the growth of CNS and it has been noted in Table-4.5 for different oxide nanoparticles used in this study.
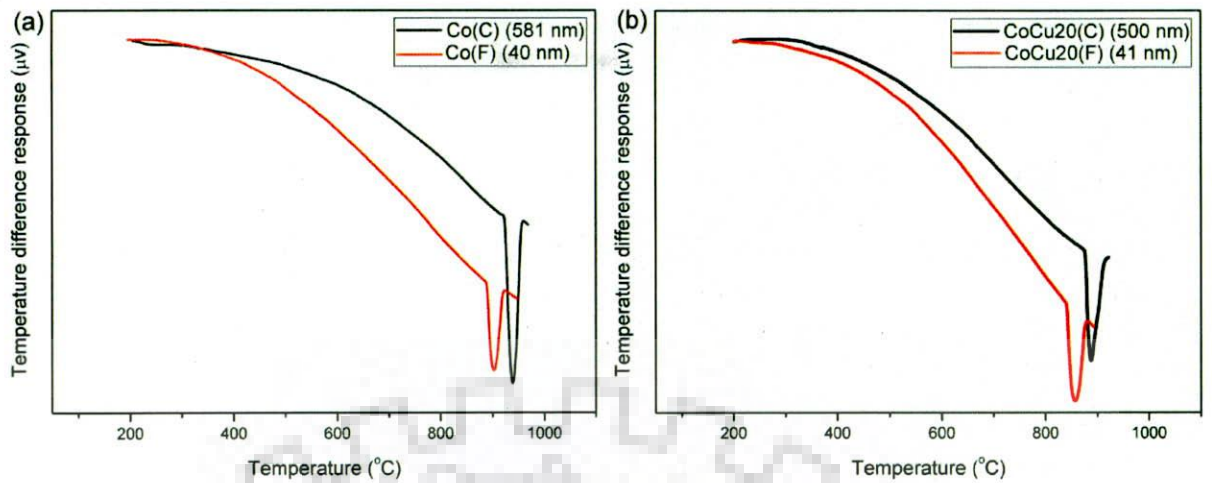
Fig. 4.11: Typical DTA curves of cobalt oxide based nanoparticles of two different sizes: (a) pure, and (b) doped with 20 wt.% of copper.

In order to understand the effect of particle size, the DTA responses of pure cobalt oxide nanoparticles of relatively small and large average particle sizes have been compared in Fig. 4.11(a). For undoped particles broad endothermic peak of the larger particles has relatively lower slope compared to that of smaller particles as in the later there are more number of smaller particles melting at relatively lower temperatures. The same effect of average particle size is observed even with high level of doping as shown in Fig. 4.11(b). It may be noted that for undoped material the DTA curve is relatively flatter than the case with higher level of doping as in CoCu20, which enhances the process of melting resulting in larger and continuous slope in the curve.
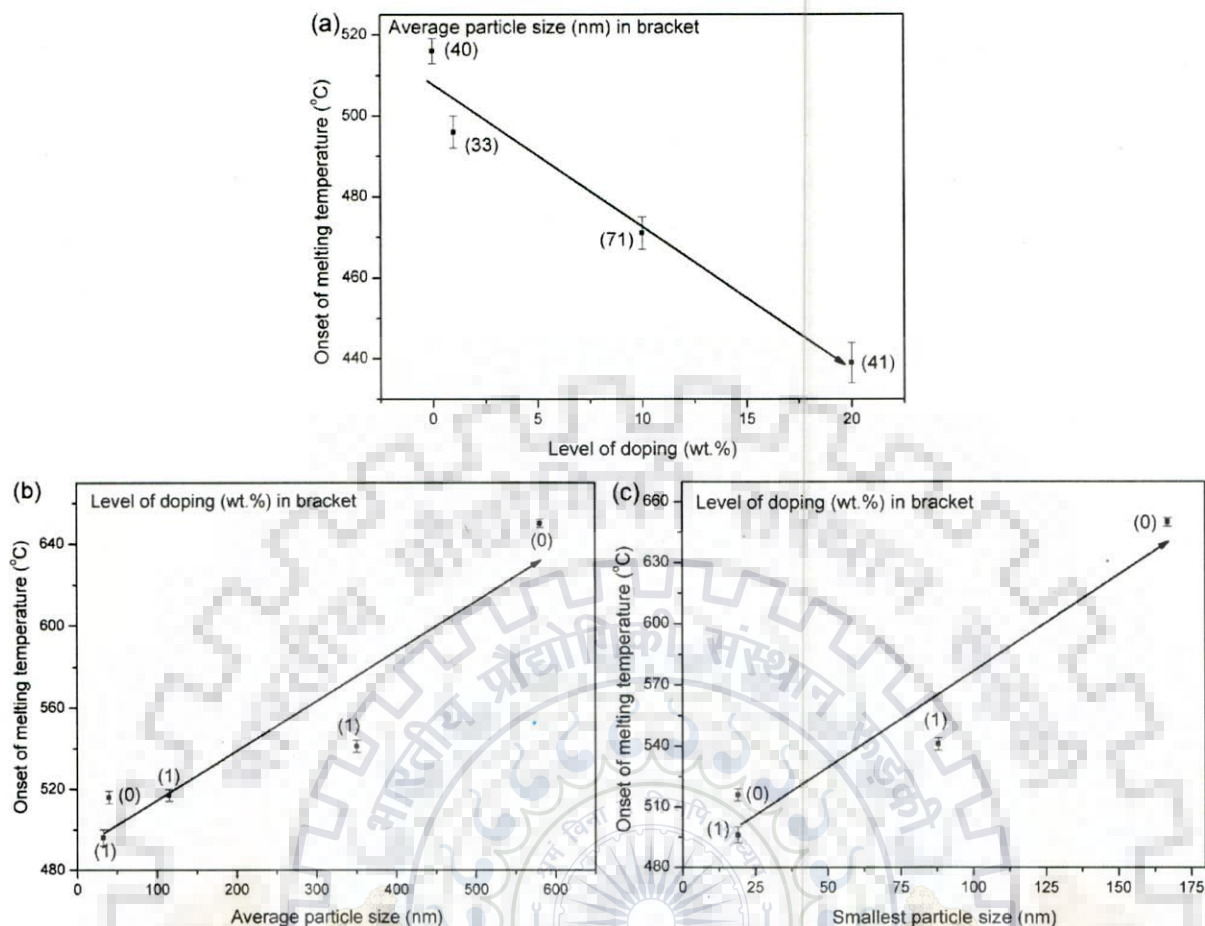
Fig. 4.12: Variation of onset of melting temperature for cobalt based oxide nanoparticles with (a) level of doping, (b) average particle size, and (c) smallest particle size in the sample.

The temperature at the start of melting as noted in Table-4.5, decreases with increasing level of doping in cobalt oxide based nanoparticles as indicated by an arrow in Fig. 4.12(a) where the particles lie in a narrow size range of about 33-71 nm, so as to limit the effect of its variation. Solid solution between cobalt oxide and copper oxide is expected to lower the temperature of melting or surface melting. It is even possible that there is segregation of the dopant on the surface, which may further reduce the temperature for the surface melting. The effect of size on the onset of melting temperature has been shown in Figs. 4.12(b) and (c) where doping has been limited to either to zero or low level. It may also be noted that at low doping as in oxide particles CoCu01, the variation of average particle size from 33 to 115 or 350 nm has increased the start of melting temperature and size has a significant influence. Without doping or with lower level of doping, one observes considerable influence of minimum particle size on the start of melting, particularly over the higher end of the size range, as shown in Fig. 4.12(c). The limit of variability (standard deviation) for determination of onset melting temperature has been found to be ~ 2.5.

96
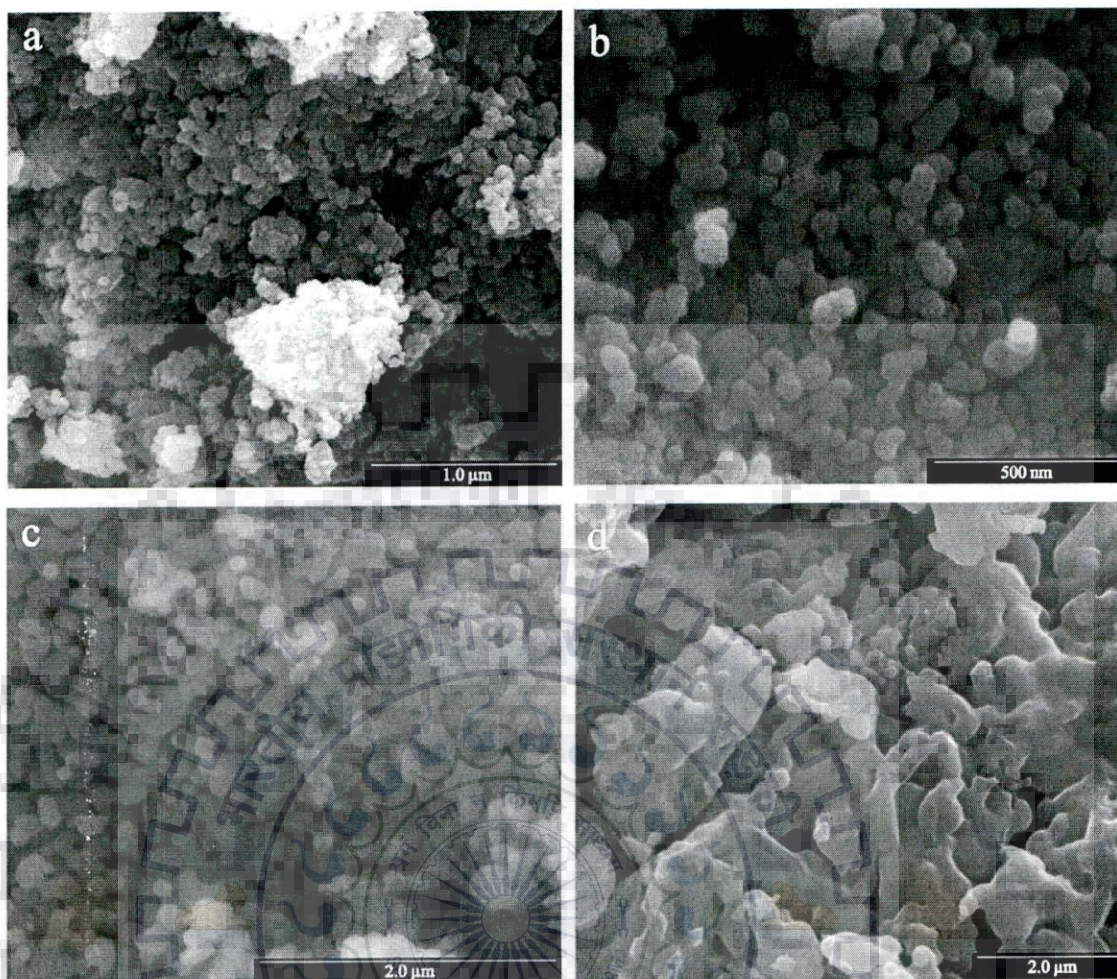
Fig. 4.13: FESEM micrographs of CoCu20(F): (a) as prepared, and after heating during DTA to (b) 540 $^{\circ}$C, (c) 640 $^{\circ}$C, and (d) 1000 $^{\circ}$C.

The melting/surface melting of nanoparticles could also be inferred from the FESEM micrograph of some typical doped cobalt oxide nanoparticles (CoCu20(F)) after DTA when compared with the micrograph of the same particles before DTA as shown in Fig. 4.13. The particles and their aggregates could be observed clearly in Fig. 4.13(a) showing the nanoparticles before DTA. While heating, the particles are becoming distinctly spherical and often with merged boundary with the surrounding particles as observed in Figs. 4.13 (b) and (c) heated respectively below the sharp peak temperature to 540 $^{\circ}$C and 640 $^{\circ}$C. After DTA there is clear evidence of widespread fusion of the particles when one crosses the sharp peak temperature as shown in Fig. 4.13(d) indicating widespread surface melting/melting of particles, re-solidified during cooling to result in fused mass.

Table-4.5: The temperature at the start of melting/surface melting of oxide nanoparticles of different size and level of doping.

Designation of oxide	Level of doping of copper (wt.%)	Average size (nm)	Onset of melting temperature (^{o}C)
Co(C)	0	581	650
Co(F)		40	516
CoCu01(C)	1	350	541
CoCu01(F)		33	496
CoCu10(C)	10	225	500
CoCu10(F)		71	471
CoCu20(C)	20	500	455
CoCu20(F)		41	439
Ni(C)	0	204	638
Ni(F)		53	523
NiCu10(C)	10	248	635
NiCu10(F)		41	505
NiCu15(C)	15	97	494
NiCu15(F)		66	478
NiCu20(C)	20	130	476
NiCu20(F)		46	453
Cu(C)	0	1129	625
Cu(F)		19	389

The melting has been further explored by taking XRD pattern of a typical doped oxide (CoCu10(C)) at 640 ^{o}C, the temperature at which growth of nanostructure has been carried out in the present study, and the peaks have been compared by superimposing those over the corresponding peaks of XRD pattern obtained at room temperature, as shown in Fig. 4.14.
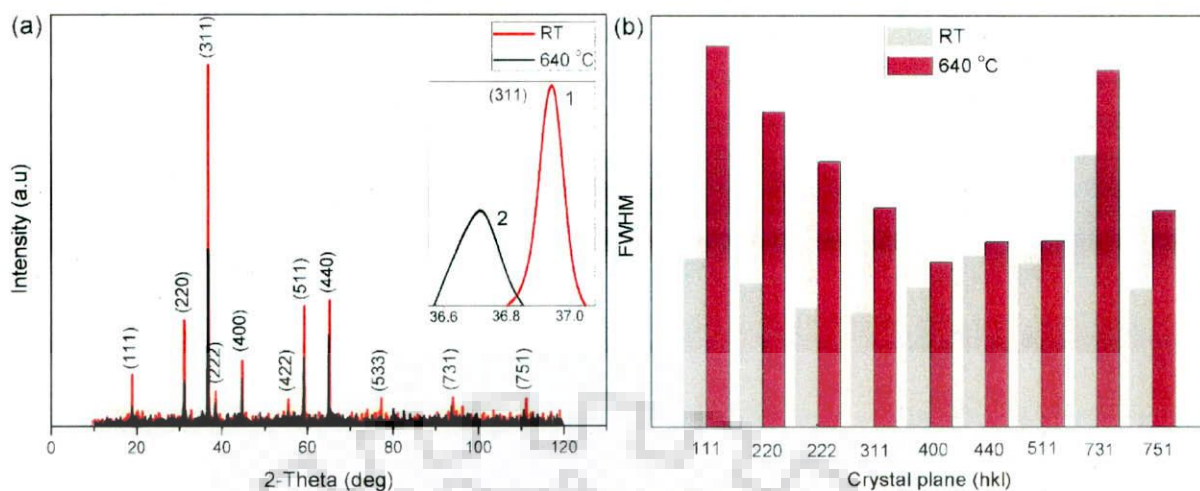
Fig. 4.14: (a) Comparison of XRD pattern of doped cobalt oxide nanoparticles (CoCu10(C)) at 640 °C with that obtained at room temperature (RT) (the inset showing magnified view of comparison of a typical peak (311) for RT and 640 °C marked 1 and 2 respectively), and (b) comparison of intensity in terms of FWHM.

There has been significant decrease in intensity at elevated temperature, particularly for certain peaks, which have broadened more as indicated by increased full width at half maximum (FWHM) of intensity, as shown in Fig. 4.14(b). The crystal bounded by planes (111), (220) and (311) appears to be more prone to melting compared to other planes like (400), (440) or (511) and it may be attributed to surface melting of the oxide nanoparticles. Further it can be seen that there is a shift in the XRD peak towards lower angle as shown in the inset of Fig. 4.14(a). Near the melting temperature there would be significant increase in vacancy concentration, which explains the observed shifts of XRD peaks towards lower angles (Gondi et al, 2002).
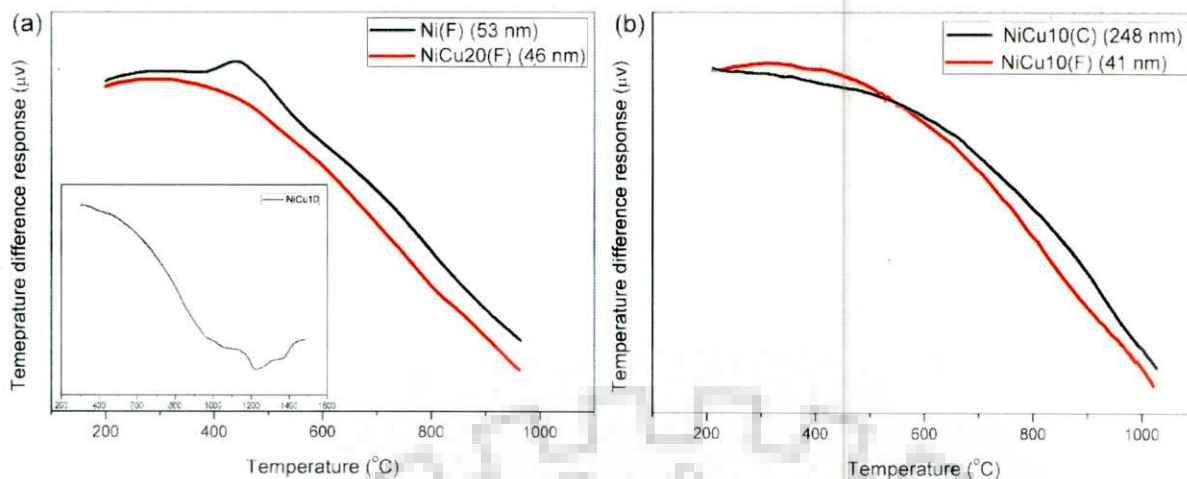
Fig. 4.15: Typical DTA curves for nickel oxide based nanoparticles: (a) undoped and doped (20 wt.%) but with the same average size (inset showing DTA curves of NiCu10 up to 1500 °C), and (b) of two different particle sizes but with the same level of doping.

Nickel oxide based catalyst in its DTA response shown in Fig. 4.15 also has a broad endothermic peak as observed in the DTA response of cobalt oxide based nanoparticles but there is no sharp endothermic peak until the end temperature of DTA showing bulk melting does not take place within 1000 °C. The bulk melting temperature of nickel oxide (NiO) is 1955 °C. Nickel oxide based catalyst, thus, shows surface melting or melting of very small nanoparticles and the core may remain solid in case of surface melting. The sharp peak in the DTA response of these oxide nanoparticles as shown in the inset of Fig. 4.15(a), has been observed at higher temperature of ~ 1200 °C, which is significantly lower than bulk melting point of NiO. The comparison of the contour of DTA curves in the broad peak region in Fig. 4.15(a) shows that higher doping by 20 wt.% of copper results in a lower start of melting but with almost similar slope in the entire region. Fig. 4.15(b) shows that the DTA curves for nickel oxide based nanoparticles (NiCu10) of different average size of particles but having the same level of doping. For smaller sized oxide nanoparticles, the endothermic peak develops more rapidly crossing the curve for the larger size particles possibly due to increased number of surface atom in relatively smaller particles. The temperature corresponding to the start of melting of different nickel oxide based nanoparticles is given in Table-4.5.
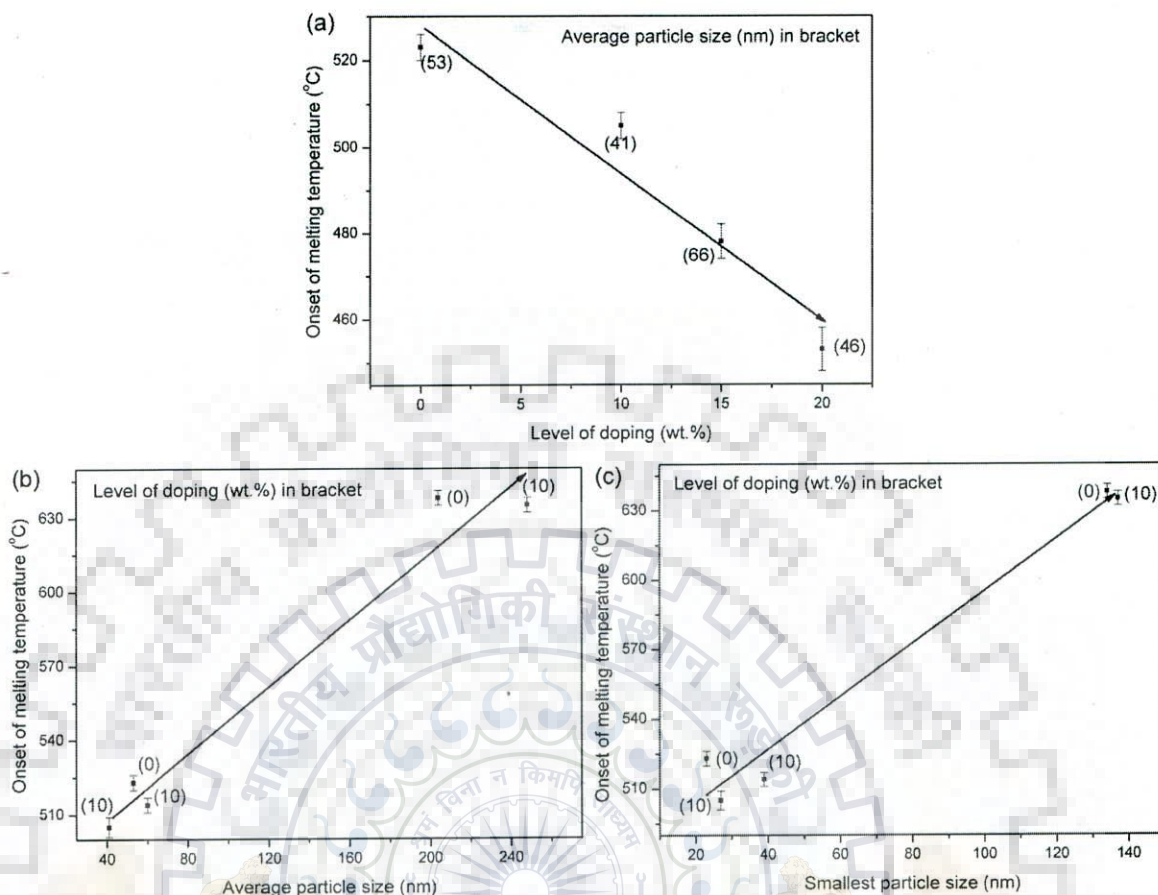
Fig. 4.16: Variation of onset of melting temperature of nickel based oxide nanoparticles with (a) level of doping, (b) average particle size, and (c) smallest particle size in the sample.

Fig. 4.16(a) shows that when the effect of size is restricted by limiting the range of average particle size, the temperature at the start of melting decreases with increasing level of doping, indicated by the amount of copper relative to total metal content in the oxide catalyst. Doping of nickel oxide by copper oxide of lower melting point is expected to decrease bulk melting temperature of the doped solid and so is the temperature of melting or surface melting of nanoparticles. Even possibility of segregation of the dopant to the surface may also reduce the melting temperature further. The size of the particle also has an influence on the start of melting/surface melting as shown in Figs. 4.16(b) and (c) and the smaller the minimum particle size, the lower is the start of melting/surface melting temperature for nickel oxide when the effect of doping is limited in a narrow range as shown in Fig. 4.16(c).
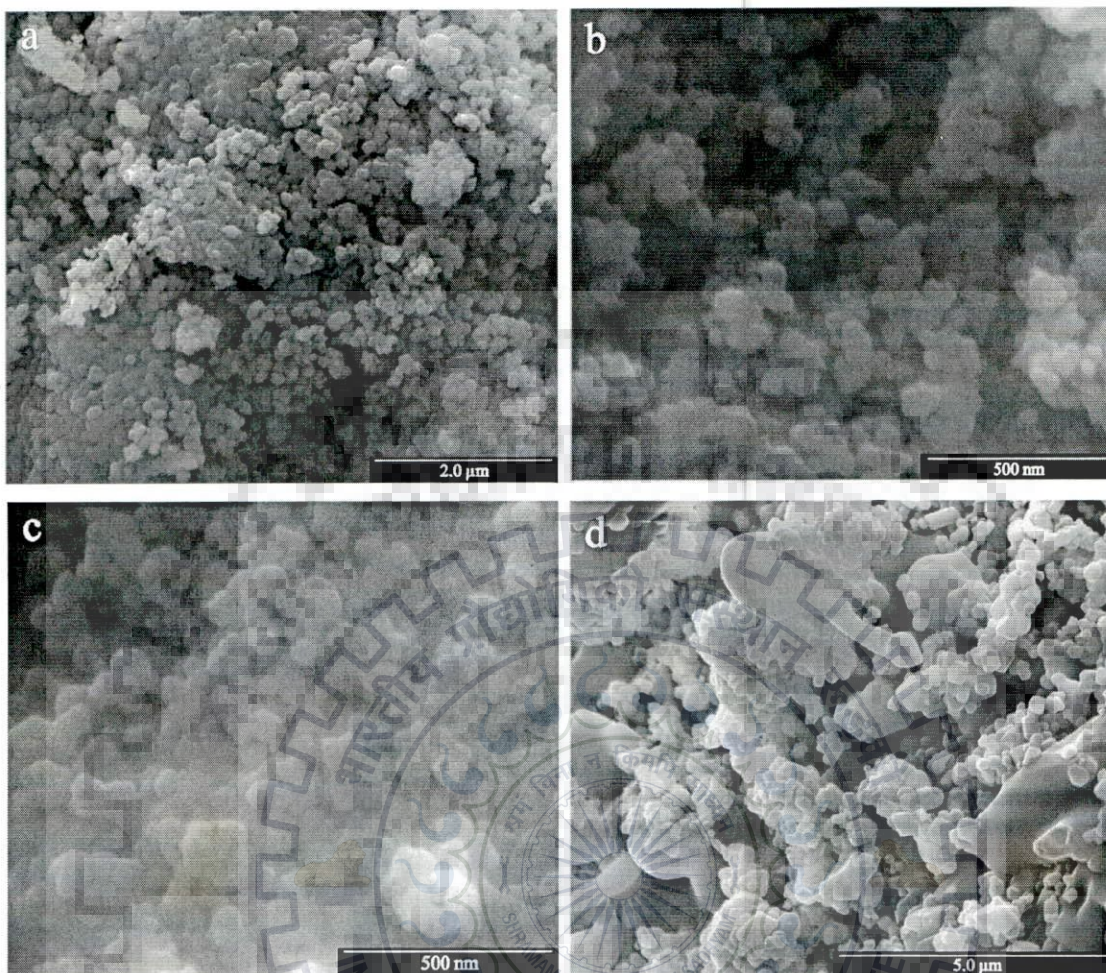
Fig. 4.17: FESEM micrographs of NiCu10(F): (a) as prepared, and after heating during DTA to (b) 540 °C, (c) 640 °C, and (d) 1000 °C.

The effect of heating during DTA has also been determined by comparing the morphology of particles before and after DTA as shown by typical FESEM micrographs of doped nickel oxide, NiCu10(F), in Fig. 4.17. Before DTA, the nanoparticles have distinct surface contour showing clear particle size distribution in Fig. 4.17(a). After heating to 540 °C and 640 °C during DTA, the particles appear to become more spherical and merged boundary with surrounding particles as shown respectively in Figs. 4.17(b) and (c) but the shape of the particles are clearly retained. Heating to higher temperatures, the particles are appeared to have been fused in certain places, which is a clear evidence of melting/surface melting and re-solidified particles fused together as revealed by Fig. 4.17(d). The retention of shapes of particles even after heating to a higher temperature strongly indicates the possibility that there is surface melting only. The surface melting of nanoparticles may be driven by lowering of free energy due to entropy term overcoming lower enthalpy term of the surface atoms

compared to that in the bulk and obviously the number of such surface atoms depends on the size of the nanoparticles.
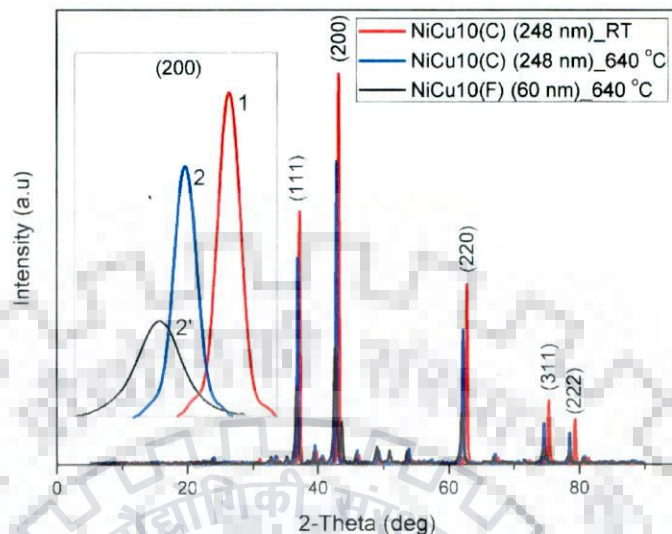
Fig. 4.18: Comparison of XRD pattern of doped nickel oxide nanoparticles (NiCu10(C)) of average size 248 nm at 640 °C with that obtained at room temperature (RT); XRD pattern at 640 °C of the smaller particles but of the same composition also included (the inset showing magnified view of comparison of a typical peak (200).

The melting of nickel oxide based nanoparticles (NiCu10(C)) has also been further investigated by taking XRD pattern at the temperature of 640 °C, at which growth of CNS has been carried out in this study and the peaks have been compared in Fig. 4.18 by superimposing it over the XRD pattern obtained at ambient temperature. It is observed that there has been significant decrease in intensity at elevated temperature, particularly for certain peaks like (111), (311), which have broadened more and possibly, it is an indication of surface melting. Melting of the entire particle in smaller size class would produce identical intensity reduction for all the peaks, however the existence of peaks is attributed to the presence of larger particles, which are yet to melt. It has been further observed that for smaller particles the intensity decreases further compared to larger particles of the same composition of the catalyst as revealed in Fig. 4.18. The shift in peak positions indicated by 1 and 2 or 2′ shown in inset of Fig. 4.18 could be attributed to higher concentration of vacancies in the nanoparticles at elevated temperatures resulting in peak shift towards lower angles as it has been observed in case of cobalt oxide based nanoparticles.
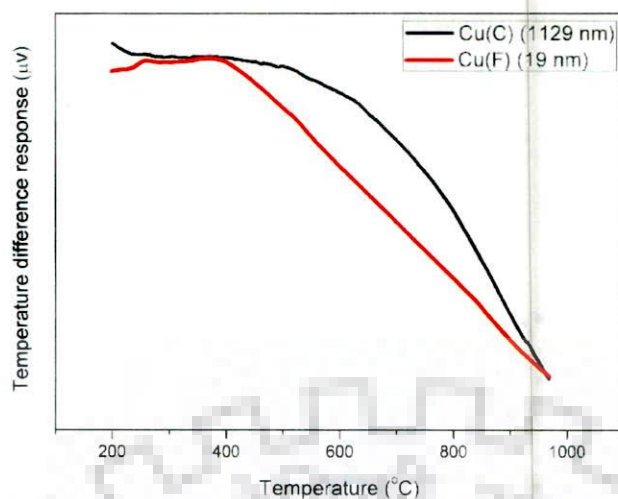
Fig. 4.19: Typical DTA curves for copper oxide nanoparticles showing effect of different average sizes.

Pure copper oxide nanoparticles have also been investigated by DTA to understand their melting behaviour and to compare it with the melting of much larger particles of average size of ~ 1 µm, as shown in Fig. 4.19. The smaller particles of copper oxide of average size 19 nm shows broad endothermic peak similar to that observed in nanoparticles based on cobalt oxide and nickel oxide. But the larger particles of copper oxide contain particles with wide variation in sizes from 531 to 1281 nm and so, the endothermic peak starts at relatively higher temperature.
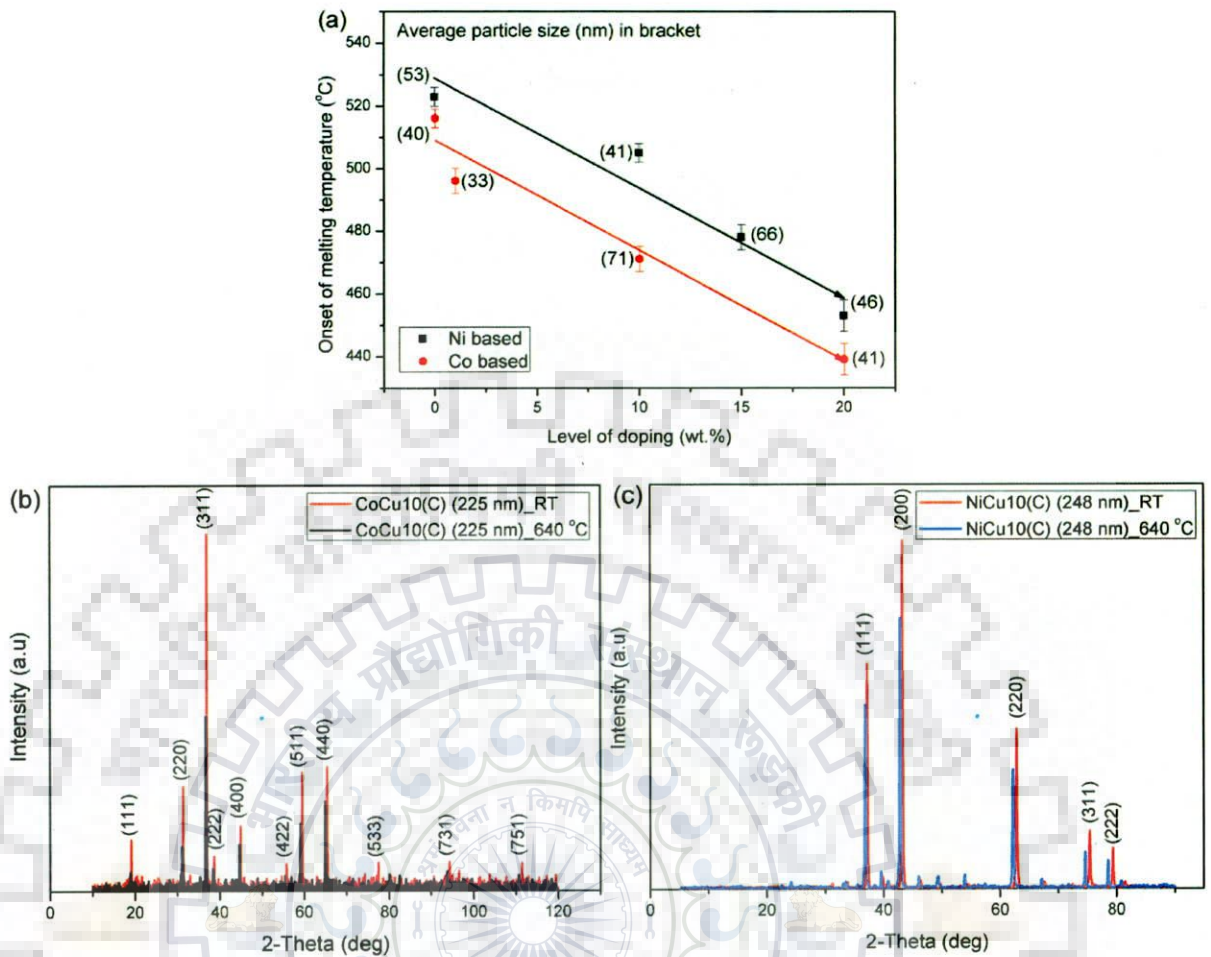
Fig. 4.20: (a) Variation of the onset melting/surface melting temperature with the level of doping for a limited range of average particle size, and comparison of XRD pattern at 640 °C with those obtained at room temperature (RT) for similar average size of particles of (b) cobalt oxide, and (c) nickel oxide based nanoparticles.

For similar doping, the melting starts at relatively lower temperature in cobalt oxide than that observed in nickel oxide as shown in Fig. 4.20(a). However, with increase in doping level, the start of melting/surface melting decreases similarly as indicated by almost parallel curve. Thus, the melting or surface melting of oxide nanoparticles depends on the level of doping as well as on the nature of base oxide. On comparison of the XRD patterns of cobalt and nickel based oxide nanoparticles taken at the same growth temperature, it can be seen that there is a larger reduction in height of the peaks in cobalt oxide based nanoparticles compared to the cases of nickel oxide based nanoparticles as shown in Fig. 4.20(b) which is due to the fact that the bulk melting point of nickel oxide (NiO) is higher than that of cobalt oxide (Co_3O_4).

105

4.3 Growth of Carbon Nanostructures by Catalytic Decomposition

In this section, the results have been reported on the growth of carbon nanostructure (CNS) on oxide nanoparticles dispersed on anodized alumina substrate at 640 °C in the chamber following CCVD method using acetylene gas as the source of carbon. A few experiments have also been carried out without using substrate in order to avoid the melting of metallic aluminum below the anodized layer when growth temperature more than 660 °C has been employed to investigate the effect of temperature and obtain higher yield. Thus, the catalyst particles are either loosely dispersed on an alumina boat or dispersed in iso-propanol and spread over the anodized alumina substrate. The details of the process have been described in the previous chapter on experimental procedure (Chapter-3).
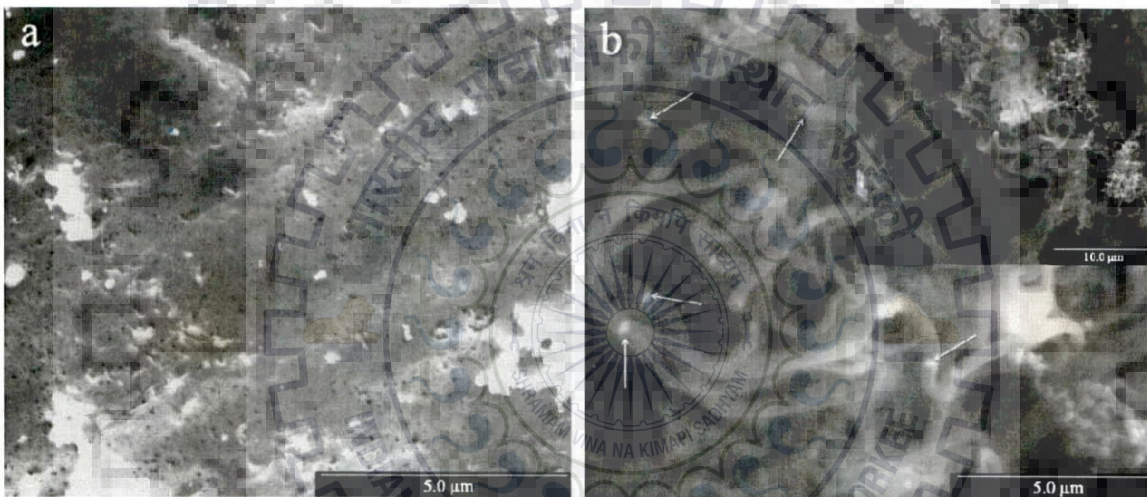
Fig. 4.21: (a) Top view of anodized alumina substrate containing dispersed nanoparticles of oxide over the surface and inside some pores, and (b) carbon nanostructures, often showing catalyst nanoparticles inside CNS indicated by arrow.

The oxide nanoparticles, when dispersed on the anodized alumina substrate, are often observed on the surface although some particles are embedded in pores as shown in Fig. 4.21(a). A Few clusters (bright spots) of oxide nanoparticles are also present on the surface of the substrate even after ultrasonication of the oxide nanoparticles. Fig. 4.21(b) shows typical growth of CNS over the oxide nanoparticles dispersed onto the anodized alumina substrate and the magnified image is shown as inset in the figure. The catalyst nanoparticles generally appear as bright spots inside CNS as indicated by arrows in Fig. 4.21(b).

4.3.1 Chemical Nature of Catalysts during Growth of Carbon Nanostructures

It is important to understand the role of oxide nanoparticles during the growth process of carbon nanostructure (CNS) in the reaction chamber of CCVD. The chemical changes taking place in the oxide nanoparticles during growth of CNS have been examined by (i) XRD analysis of the particles held in the same reducing environment prevailing during growth of CNS but at a lower temperature of 575 ^{o}C (to avoid significant formation of CNS), (ii) direct examination of the catalyst particles observed inside CNS as shown in Fig. 4.21(b), under TEM/STEM (Scanning TEM) along with energy dispersive spectrum (EDS) as well as selected area diffraction (SAD) pattern, and (iii) Raman spectroscopy of the oxide nanoparticles before and after reduction. Table-4.6 contains the details of oxide based nanoparticles used and the phases detected after exposure to the reducing environment prevailing during growth of CNS.

Table-4.6: Details of oxide based nanoparticles and the phases detected after exposure to reducing environment prevailing during the growth of CNS.

Designation of oxide particles	Doping level (wt.%)	Size distribution (nm)	Avg. size (nm)	Reduced phases and their crystal structure
Co(F)	0	19-50	40	Cobalt (fcc)
CoCu01(F)	01	19-45	33	Cobalt (fcc) Co_2C (Orthorhombic)
CoCu10(F)	10	58-117	71	Cobalt (fcc) Co_2C (Orthorhombic)
CoCu20	20	20-54	41	Cobalt (fcc) Copper (fcc)
		137-663	500	Cobalt (fcc) Copper (fcc)
Ni(F)	0	23-82	53	Nickel (fcc) Nickel (hcp)
NiCu10	10	27-57	41	Nickel/NiCu (fcc) Nickel (hcp)
		39-84	60	Nickel/NiCu (fcc) Nickel (hcp)
NiCu15(F)	15	42-78	66	Nickel/NiCu (fcc) Nickel (hcp) Ni_4N (fcc)
NiCu20(F)	20	28-60	46	Nickel/NiCu (fcc) Nickel (hcp) Ni_4N (fcc)
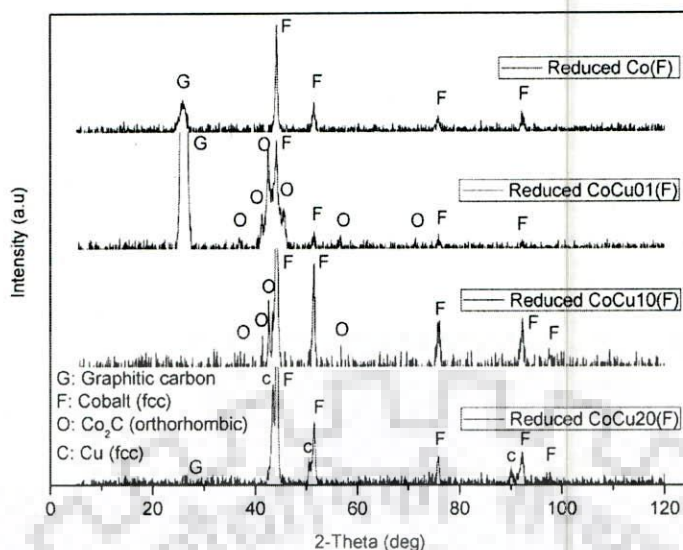
Fig. 4.22: XRD patterns showing the phases obtained due to exposure of cobalt oxide based nanoparticles to reducing environment prevailing during the growth of CNS.

The XRD patterns of cobalt based oxide nanoparticles after exposure to reducing environment shows that the oxides get completely reduced to fcc phase of cobalt (*Fm-3m; 225*) with lattice parameter of 3.545 Å and there is no significant presence of reduced copper oxide up to 10 wt.% of copper as revealed in Fig. 4.22. It may be noted that cobalt is stable in its hexagonal phase at room temperature but fcc phase appears in stacking faults indicating small difference in energy of these two phases (Strauss et al, 1996). Therefore it is not surprising that fcc cobalt is observed in nano-size. The presence of orthorhombic Co_2C phase formed due to limited doping up to 10 wt.%., is evident from the XRD pattern. The reduced copper in doped oxide perhaps remains in solid solution in the reduced cobalt even when the level of doping reaches as high as 20 wt.% of copper. At 20 wt.% doping, it is likely that copper has come out separately and orthorhombic Co_2C has disappeared. Although cobalt has a very low bulk solubility (<0.48 wt.%) in copper (Nishizawa and Ishida, 1984) but in nano-sizes, the solubility limit may extend as it has been observed for Pb-Sn, Co-ZnO or C-Cu systems (Ouyang et al, 2006; Straumal et al, 2008; Homma et al, 2009). It is interesting to observe that doping promotes formation of carbide, which is absent in reduced pure cobalt oxide and that with 20 wt.% doping as shown in Fig. 4.22.
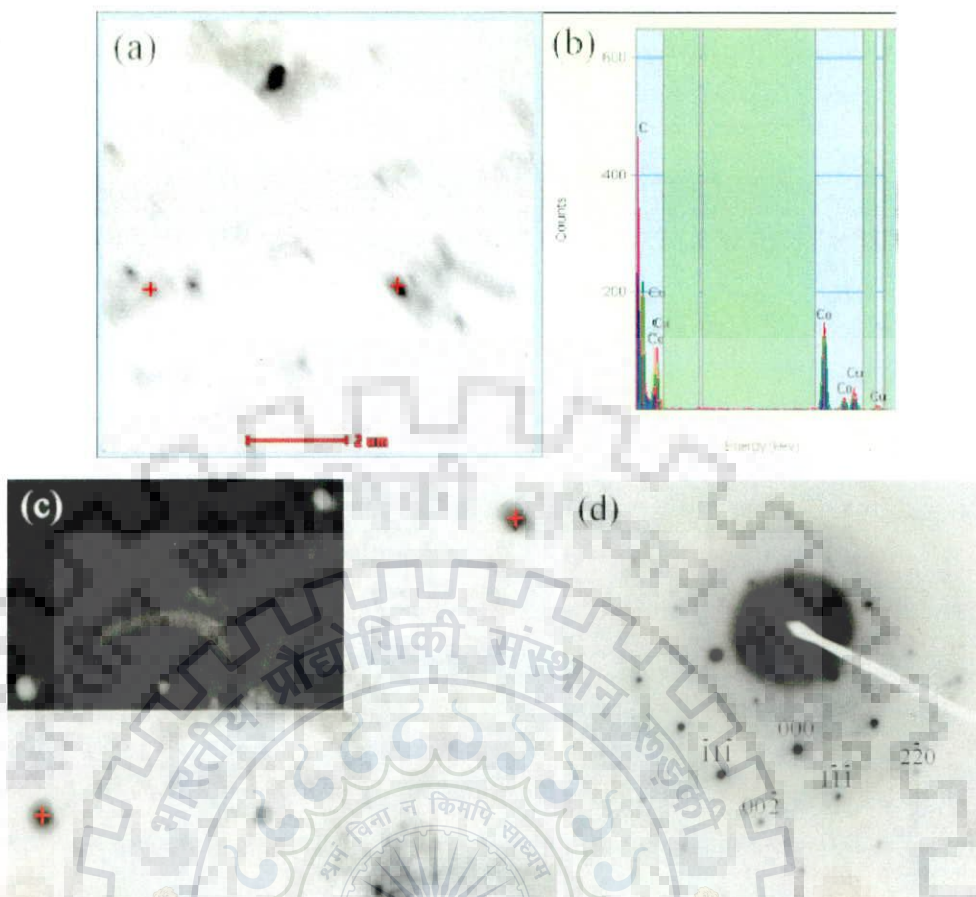
Fig. 4.23: (a) STEM image of nanoparticles inside CNS, (b) EDS spectrum taken on the cross points indicated in (a), (c) bright and dark (inset) field TEM image of CNS containing catalyst nanoparticles, and (d) selected area diffraction (SAD) of catalyst nanoparticle inside CNS as shown by cross point in (c), with spots belonging to fcc cobalt and rings to the graphitic carbon.

The nanoparticles located inside CNS synthesized using pure cobalt oxide (Co_3O_4) have been examined under TEM and the results are shown in Fig. 4.23. It has been observed that the oxide nanoparticles of cobalt has been reduced to pure metallic fcc cobalt as detected by SAD pattern (Fig. 4.23(d)). Here it is worth mentioning that the copper peaks observed in EDS spectrum of Fig. 4.23(b) is due to the grid used as sample holder in TEM study. The dark field image inset in Fig. 4.23(c) confirmed that the point used to get the SAD pattern is from the catalyst nanoparticle inside CNS.
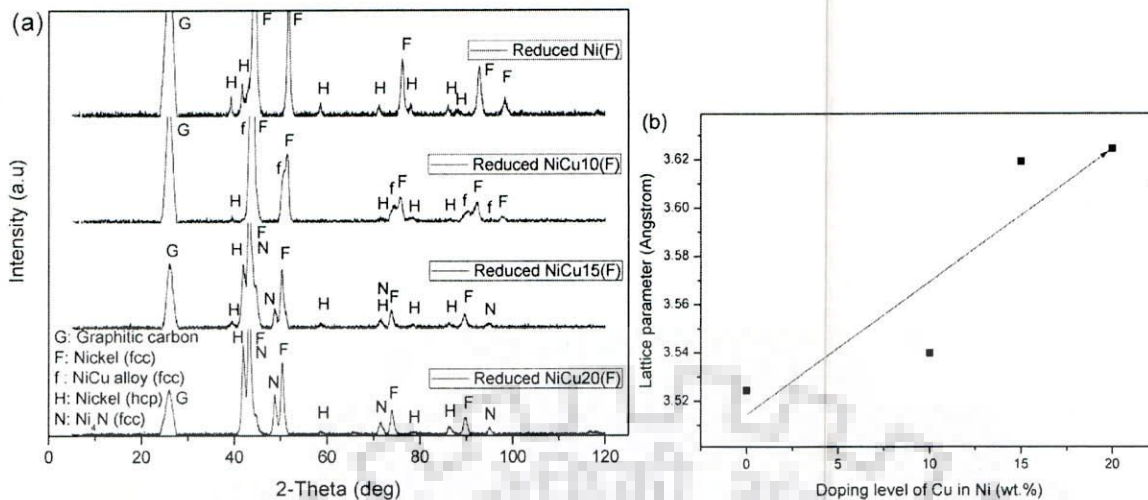
Fig. 4.24: (a) XRD patterns of nanoparticles obtained after exposure of nickel oxide based particles to similar reducing environment prevailing during the growth of CNS, and (b) variation of lattice parameter of fcc nickel (solid solution) obtained by reduction.

Fig. 4.24(a) shows XRD patterns of the reduced nanoparticles of pure nickel oxide and those with doping up to 20 wt.%. Pure NiO nanoparticles reduce into both cubic (*Fm-3m; 225*) and hexagonal (*P63/mmc; 194*) phases of metallic nickel. It may be noted that at room temperature cubic nickel is the stable state of nickel and not the hcp phase of nickel. But NiO doped with CuO as in NiCu10(F) gets reduced to more of fcc phase and less of hcp phase compared to pure NiO. Interestingly, increasing doping up to 15 or 20 wt.% when copper is expected to enter into the lattice of nickel, there is increasing amount of hcp phase of the solid solution of nickel along with some cubic nitride of nickel. However, there appears to be split in peaks of fcc nickel solid solution marked 'f' in XRD of NiCu10, which could be due to different copper contents in different locations leading to these additional peaks. Fig. 4.24(b) shows the variation of lattice parameter of fcc phase of nickel with the extent of doping. Increasing lattice parameter of the fcc phase is an indication of copper being in the lattice of fcc nickel, forming NiCu alloy upon reduction. Some contribution to the change in lattice parameter may also be due to deviation from bulk equilibrium positions towards the surface of nanocrystallites depending on size. Doping to a still higher level of 20 wt.% results mainly in fcc phase. There is also significant presence of nitride. If there is any carbide it could not be distinctly identified as all the peaks corresponding to the carbide of nickel (Ni_3C) overlap with the peaks corresponding to nickel. It is reported that hcp nickel formation involves the formation of Ni_3C via martensitic transformation (Tian et al, 2005). Pearson (Pearson, 1958) has observed that although nickel with an fcc structure is more stable than hcp nickel under

ambient conditions, hcp nickel could be induced by hydride, nitride and carbide formation. There is presence of hydrogen, nitrogen and carbon in the reaction chamber of CCVD derived from ammonia and a carbon bearing gas introduced there.
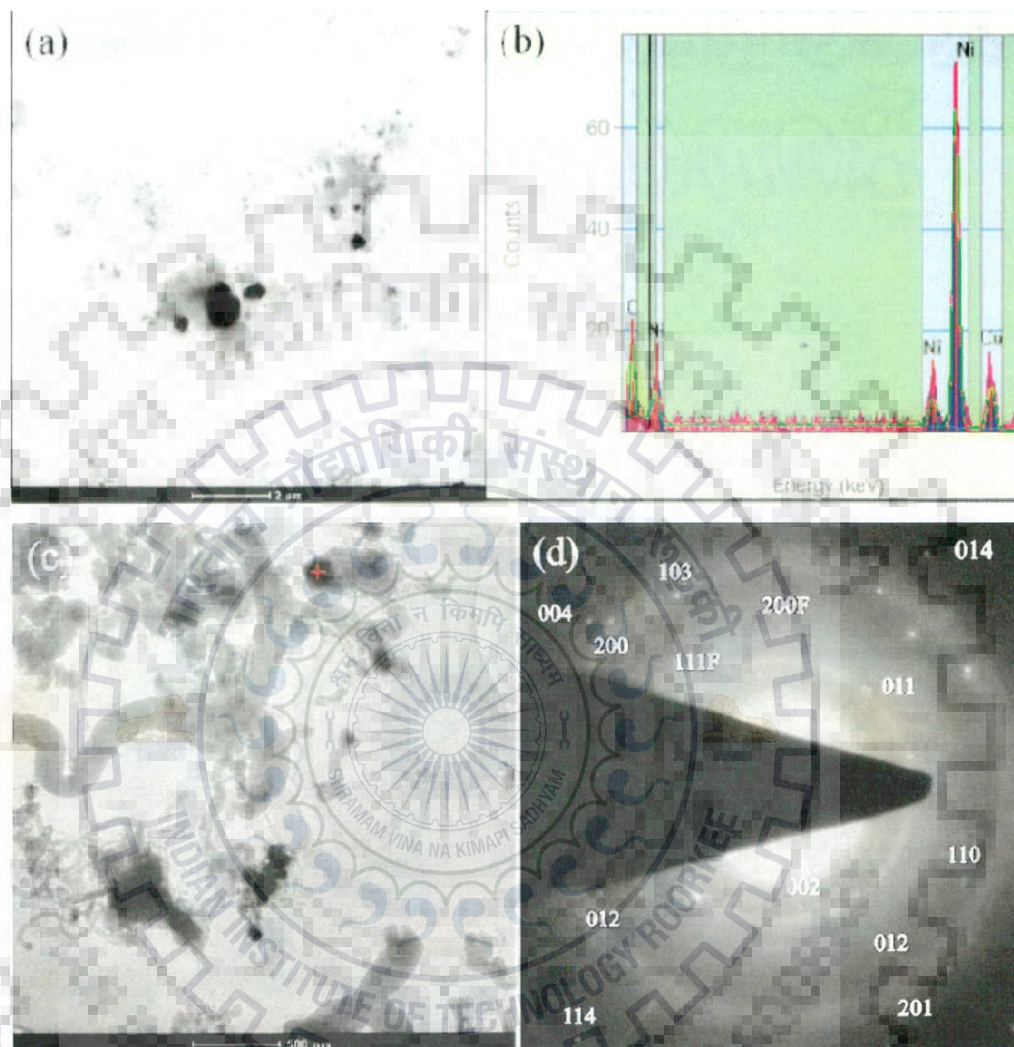
Fig. 4.25: (a) STEM image of nanoparticles inside CNS, (b) EDS spectrum of dark spots in (a), and (c) bright field TEM image of CNS containing catalyst particles, and (d) selected area diffraction (SAD) of nanoparticle inside CNS as shown by cross point in (c), with spots belonging to hcp nickel (unmarked) and fcc nickel (marked F), and rings belonging to graphitic carbon.

The nanoparticles observed inside CNS grown using pure nickel oxide have been examined using TEM and the results are shown in Fig. 4.25. The EDS spectrum taken on the nanoparticle inside CNS, as shown in Fig. 4.25 (a), demonstrates the reduction of NiO into nickel as shown in Fig. 4.25(b). The particles inside CNS have also been observed under TEM as shown in Fig. 4.25(c) and selected area electron diffraction shows the presence of hcp nickel and fcc nickel as revealed in Fig. 4.25(d).

111
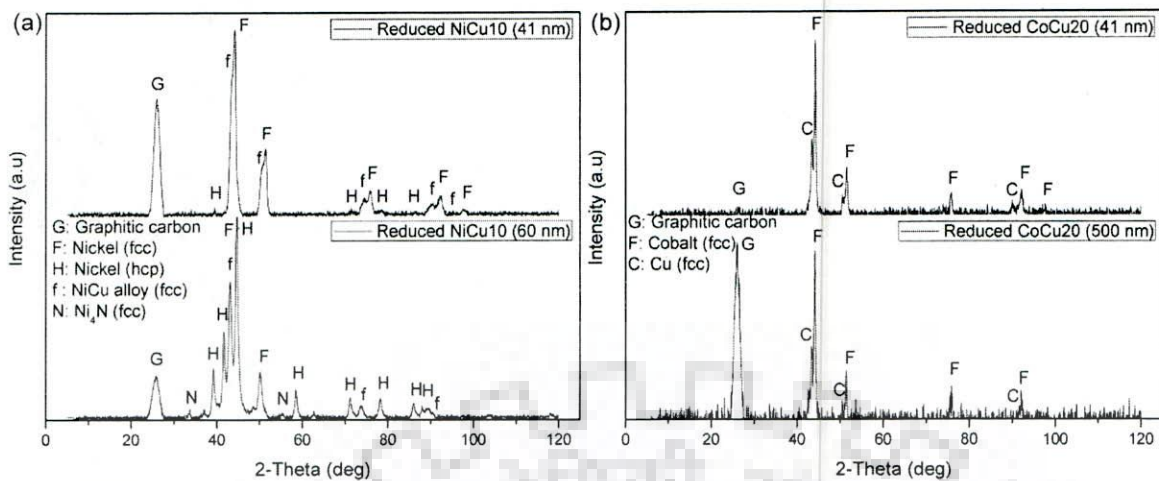
Fig. 4.26: XRD patterns of doped nanoparticles of (a) nickel (NiCu10), and (b) cobalt (CoCu20) with two different average sizes of particles for each.

In order to study if there is any effect of size on the nature of the phases obtained after reduction of the nanoparticles of oxide, two different sizes of oxides designated as NiCu10 and CoCu20 have been subjected to the same reducing environment used earlier for this purpose. For relatively bigger size particles (60 nm) of nickel oxide doped with 10 wt.% copper, the hcp phase of nickel is relatively more compared to the smaller particles of oxide (41 nm), which reduces mostly to fcc phase of nickel, as shown in Fig. 4.26(a). This observation is contrary to the results of Tian et al. (Tian et al, 2005). When the size change from 41 to 500 nm for cobalt oxide doped with 20 wt.% copper, there is no significant change in the phase constituents as shown in Fig. 4.26(b).
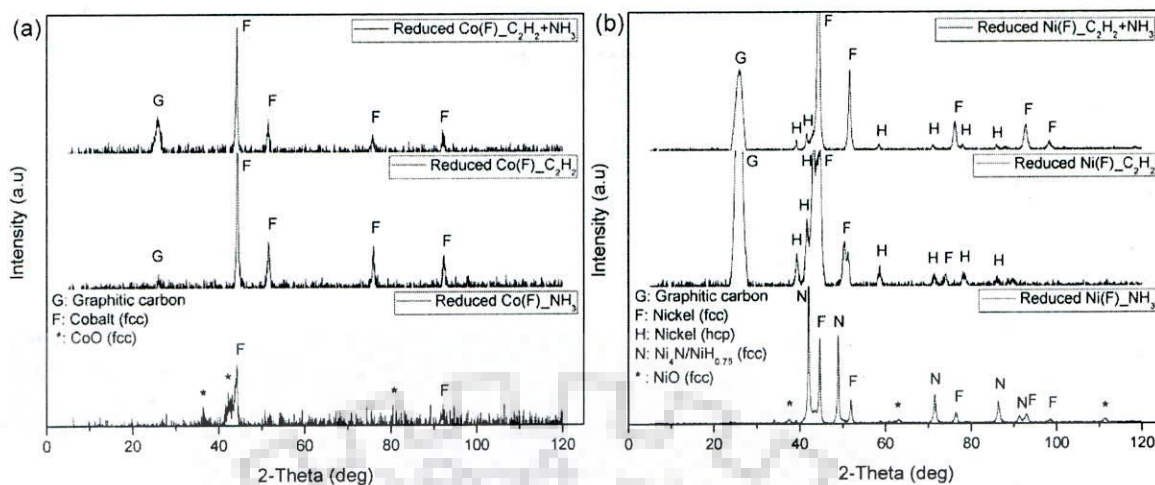
Fig. 4.27: XRD pattern of (a) cobalt, and (b) nickel nanoparticles reduced from their respective oxides in three different atmospheres.

A few experiments have been carried out at similar temperature but at different chemical environment to show their effect in the phase if any. Fig. 4.27(a) shows the effect of different environment on the reduction behaviour of pure cobalt oxide (Co_3O_4) on which the reduction reaction has been tested. In C_2H_2 as a reducing environment there is formation of some carbonaceous material which is obvious, though it has been tried and chosen a temperature and flow rate by which one can avoid an extensive formation of CNS, so as to get X-ray intensities coming mostly from the reduced oxide. It has been observed from Fig. 4.27 that ammonia (NH_3) alone can also reduce the oxide nanoparticles though a few weak traces of oxides are also present showing that the reduction is not yet complete at a temperature of 575 ^{o}C. It has been observed that with both the gases the growth of graphitized carbon is more favourable onto these nanoparticles which help to catalyze the growth of CNS at a temperature of 640 ^{o}C. In all three cases of reducing environment, it may be noted that the cobalt nanoparticles are in cubic phase which is a metastable phase at room temperature regardless of their sizes. When pure NiO undergoes both C_2H_2 and NH_3 treatment it produces mainly fcc phase of nickel with some hcp phase and some graphitic carbon as can be seen from Fig. 4.27(b), while the same material under only C_2H_2 atmosphere gives rise to strong hcp phase of nickel with fcc phase as well and it may be due to the fact that carbon has been able to enter into the nickel. Under NH_3 gas environment, the reduction is only by hydrogen resulting in fcc nickel and some nickel nitride and there is no participation of carbon.
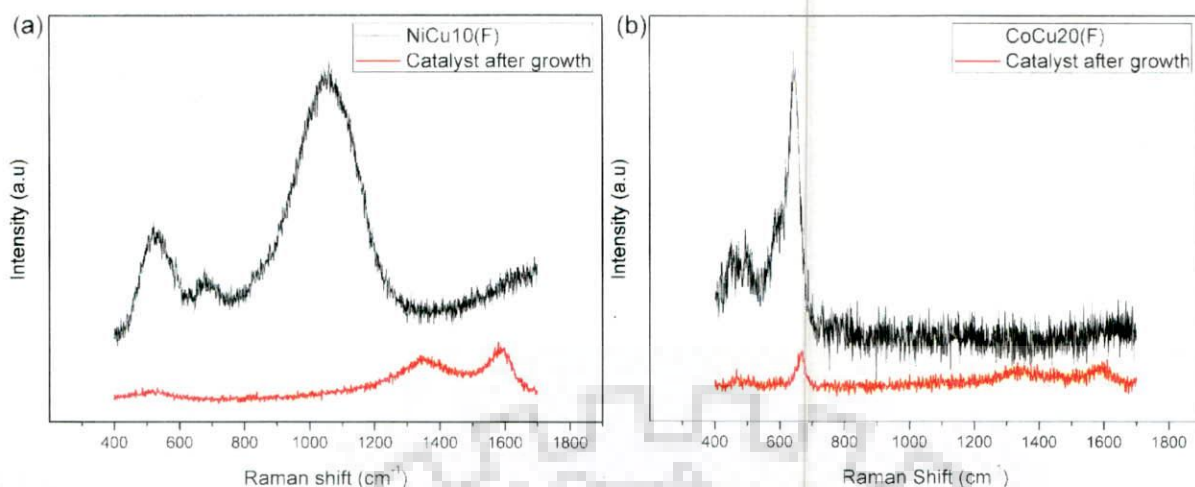
Fig. 4.28: Typical Raman spectrum showing changes in oxide nanoparticles of (a) NiCu10(F), and (b) CoCu20(F) after exposure to similar reducing environment prevailing during the growth of CNS.

Raman spectroscopy has been used as a tool to detect the extent of reduction of the oxide phases. The Raman spectrum has been taken for two oxides designated as NiCu10(F) and CoCu20(F) having smaller size of particles before and after reduction and the results are presented in Fig. 4.28. The nickel oxide based nanoparticles exhibit multiple peaks at 521.809, 678.513, 1054.383 cm^{-1}. It may be noted that CuO phase has the characteristic peaks at 500 and 634 cm^{-1}, and NiO phase has peaks at 550 and 1100 cm^{-1} in their respective Raman spectrum (Chen et al, 2011). In the present case, the doped oxide shows the characteristic peaks of both NiO and CuO merged because of their presence in the same lattice shifted the peaks to lower frequency compared to NiO and higher frequency compared to CuO. After exposure to similar reducing environment prevailing during growth of CNS but at 575 $^{\circ}$C, the reduced nanoparticles do not show the characteristic peaks of doped oxide although there are some graphitic materials present and the peaks corresponding to the graphitic (G) and defect (D) bands respectively at 1591.706 and 1345.144 cm^{-1} may be observed in Fig. 4.28(a). Thus, it is evident that the oxide nanoparticles have undergone significant reduction when exposed to reducing atmosphere prevailing during growth of CNS as inferred from XRD pattern of these reduced nanoparticles earlier in this section.

The Raman spectrum of doped cobalt oxide designated as CoCu20(F) is shown in Fig. 4.28(b) and the peaks are at 453.502, 491.491 and 642.351 cm^{-1}. It has been reported that pure nanocrystalline Co_3O_4 has peaks at 483, 523, 621 and 694 cm^{-1} corresponding to E_g, F^1_{2g}, F^2_{2g} and A_{1g} modes respectively (Yu et al, 2005). Doping by CuO to replace 20 wt.% cobalt in Co_3O_4 has resulted in shift of Co_3O_4 peak positions towards lower wave number and shift of

CuO peaks to higher wave number. After exposure to similar reducing environment prevailing during growth of CNS but at 575 $^{\circ}$C, the resulting nanoparticles do not show the peaks corresponding to doped cobalt oxide, CoCu20(F), oxide material almost vanishes except the peak at 642.351 cm^{-1} considerably weakened and shifted to ~ 630.297 cm^{-1} apart from two other peaks at 1342.222 and 1584.401 cm^{-1} corresponding to the D and G bands of graphitic carbon. Pure cobalt has no characteristic Raman peak in the said region (400-1700 cm^{-1}) of wave numbers as it has been observed by Cheng et al. (Cheng et al, 1998) attributed to absence of covalent bonding in cobalt which may contribute a peak as in the case of oxides.
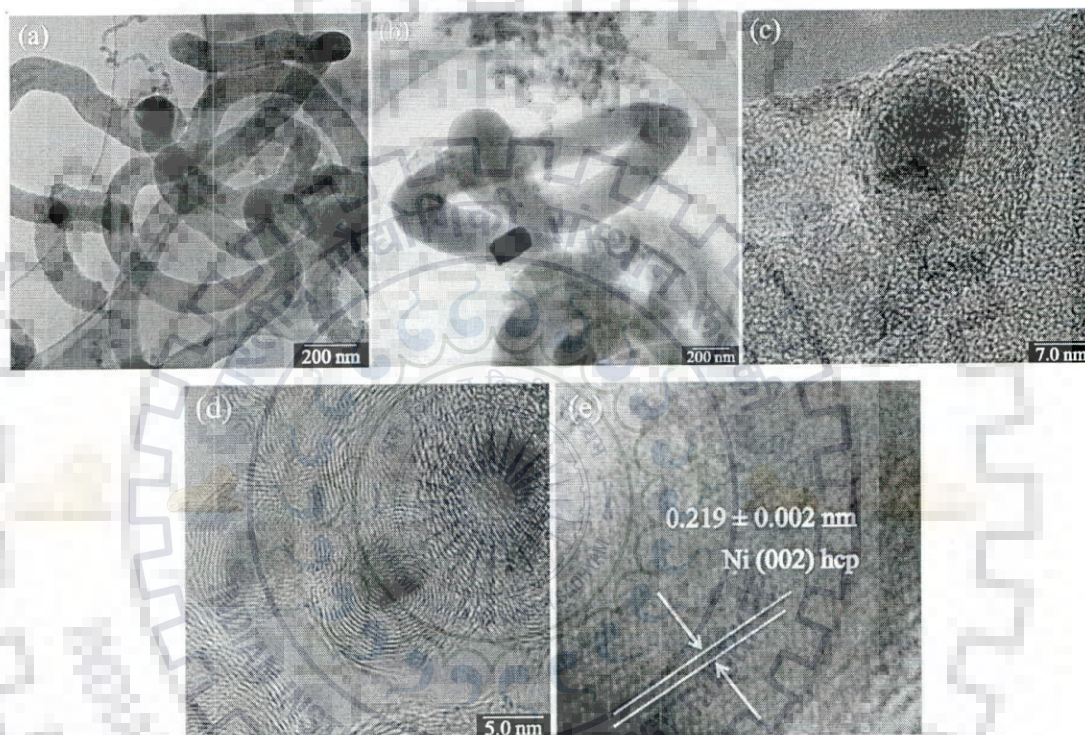
Fig. 4.29: (a-e) Typical TEM and HRTEM images of the nanoparticles inside CNS grown using nanoparticles of oxide (NiCu10).

The nanoparticles inside CNS grown using oxide NiCu10 have been examined by TEM and HRTEM and the results are shown in Fig. 4.29. Although the average size of the particles of the material designated as NiCu10 is in the range of few tens of nm, the reduced particles observed inside CNS have large variation of size from about 3 to 200 nm as shown in Figs. 4.29(a) and (b) under TEM and Figs. 4.29(c) and (d) under HRTEM. The solubility of copper and the resulting structure of the phases present in the reduced oxide nanoparticles may depend on the size. The structure of reduced nanoparticles of smaller size and of larger size are different as observed earlier when the oxide nanoparticles are exposed to reducing

115

environment as revealed by XRD in Fig. 4.26. The HRTEM image in Fig. 4.29(e) reveals that the lattice spacing (~ 0.219 nm) of the nanoparticle examined matches with (002) planes of hcp nickel.
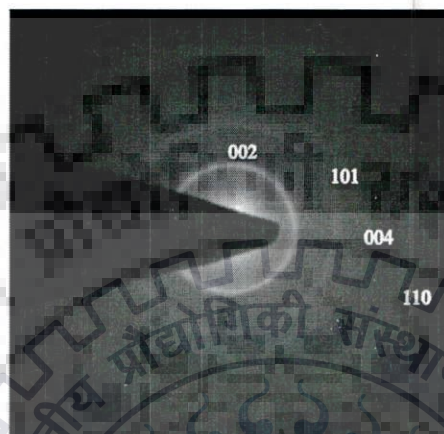
Fig. 4.30: Typical selected area diffraction (SAD) pattern of the graphitic CNS.

Fig. 4.30 gives the SAD pattern of CNS containing circular rings corresponding to different planes indicated and these rings have been observed earlier in the Figs. 4.23(d) and 4.25(d) along with diffraction spots attributed to the presence of the reduced oxide nanoparticles inside CNS.
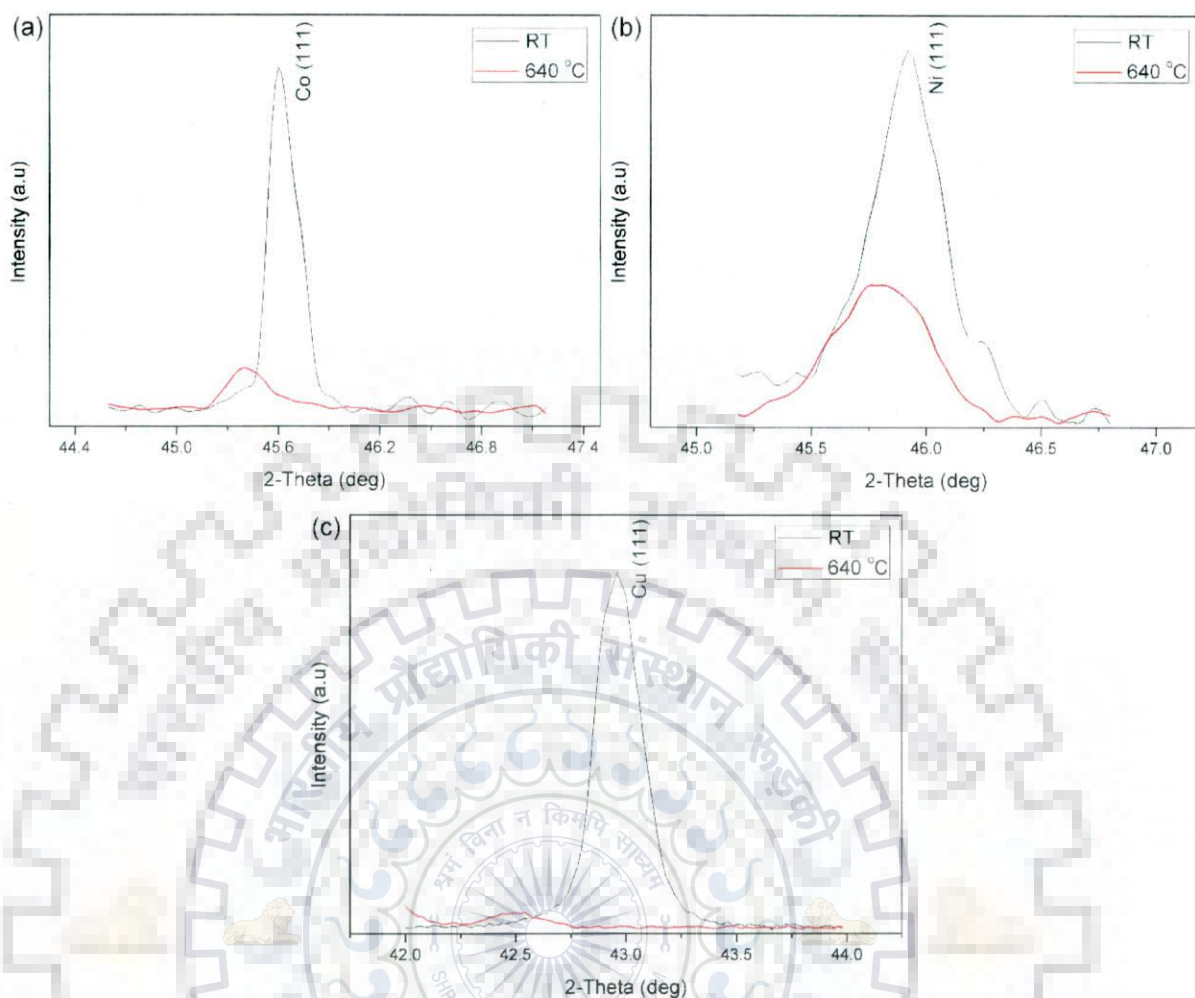
Fig. 4.31: Comparison of the intensity of (111) peak in XRD patterns of reduced nanoparticles at 640 °C with that at room temperature (RT): (a) Co(F), (b) Ni(F), and (c) Cu(F).

The status of metallic nanoparticles reduced from oxides of cobalt, nickel and copper without doping have been investigated by taking XRD pattern at room temperature and at elevated temperature of 640 °C, the temperature at which growth of nanostructure has been carried out in the present study. The intensity of a typical peak (111) has been compared by superimposing that over the corresponding peak at room temperature, as shown in Fig. 4.31. For all the reduced metallic particles it has been observed that there is a significant decrease in intensity at elevated temperature. The decrease in intensity has been attributed to melting and surface melting of particles. The drastic reduction in intensity observed with copper nanoparticles (Fig. 4.31(c)) may be attributed to its relatively lower bulk melting point.

4.3.2 Growth and Morphology of Carbon Nanostructures

Carbon nanostructures have been grown by CCVD method at a temperature of 640 $^{\circ}$C using oxide based nanoparticles. In the earlier subsection the results presented clearly demonstrate complete reduction of oxide nanoparticles under reducing conditions prevailing during growth of CNS. Table-4.7 summarizes the results on the type of CNS growing on the resulting catalyst particles originating from oxide based particles dispersed on porous alumina substrate. There has been formation of nanobeads of carbon even when there is no SWCNT, MWCNT, CNF or nanotape observed to form. In the present report, carbon nanobeads (CNB) have been excluded from the term CNS as such structure is not desirable in the present study.

Table-4.7: Size and type of nanostructures formed using nanoparticles of oxide having different size and doping levels.

Designation of oxide	Size distribution (nm)	Average size (nm)	Onset of melting temperature ($^{\circ}$C)	Type of CNS formed	Diameter distribution of CNS
Co(C)	167-691	581	650	CNB	-
Co(F)	19-50	40	516	MWCNT	41-315
CoCu01(C)	88-424	350	541	MWCNT	134-256
CoCu01(F)	19-45	33	496	CNF, MWCNT	25-156
CoCu10(C)	71-391	225	500	CNF-straight/helical	131-147
CoCu10(F)	58-117	71	471	CNF	37-218
CoCu20(C)	137-663	500	455	Nanotape, CNF	210-590
CoCu20(F)	20-54	41	439	CNF	46-172
Ni(C)**	134-295	204	638	CNB	-
Ni(F)	23-82	53	523	MWCNT	32-121
NiCu10(C)	137-319	248	635	CNB	-
NiCu10(F)	27-57	41	505	MWCNT, CNF	48-146
NiCu15(C)	45-165	97	494	MWCNT, CNF	48-179
NiCu15(F)	42-78	66	478	CNF	63-167
NiCu20(C)	70-173	130	476	CNF	56-166
NiCu20(F)	28-60	46	453	CNF	42-132
Cu(C)	531-1281	1129	625	CNB	-
Cu(F)	15-29	19	389	SWCNT/MWCNT	5-31

** Ni(C) has been used to grow CNS at 600 $^{\circ}$C besides the usual growth temperature i.e. 640 $^{\circ}$C and formation of only nanobeads was observed.

118

4.3.2.1 Growth of CNS using Cobalt Oxide Based Nanoparticles

When cobalt oxide has relatively larger average size of 581 nm, there is formation of carbon nanobeads (CNB) and no growth of CNS has been observed at 640 ^{o}C as shown in Figs. 4.32(a, b). But decreasing the average size of cobalt oxide based catalyst to 40 nm one could observe an extensive formation of MWCNT as shown in Figs. 4.32(c, d).
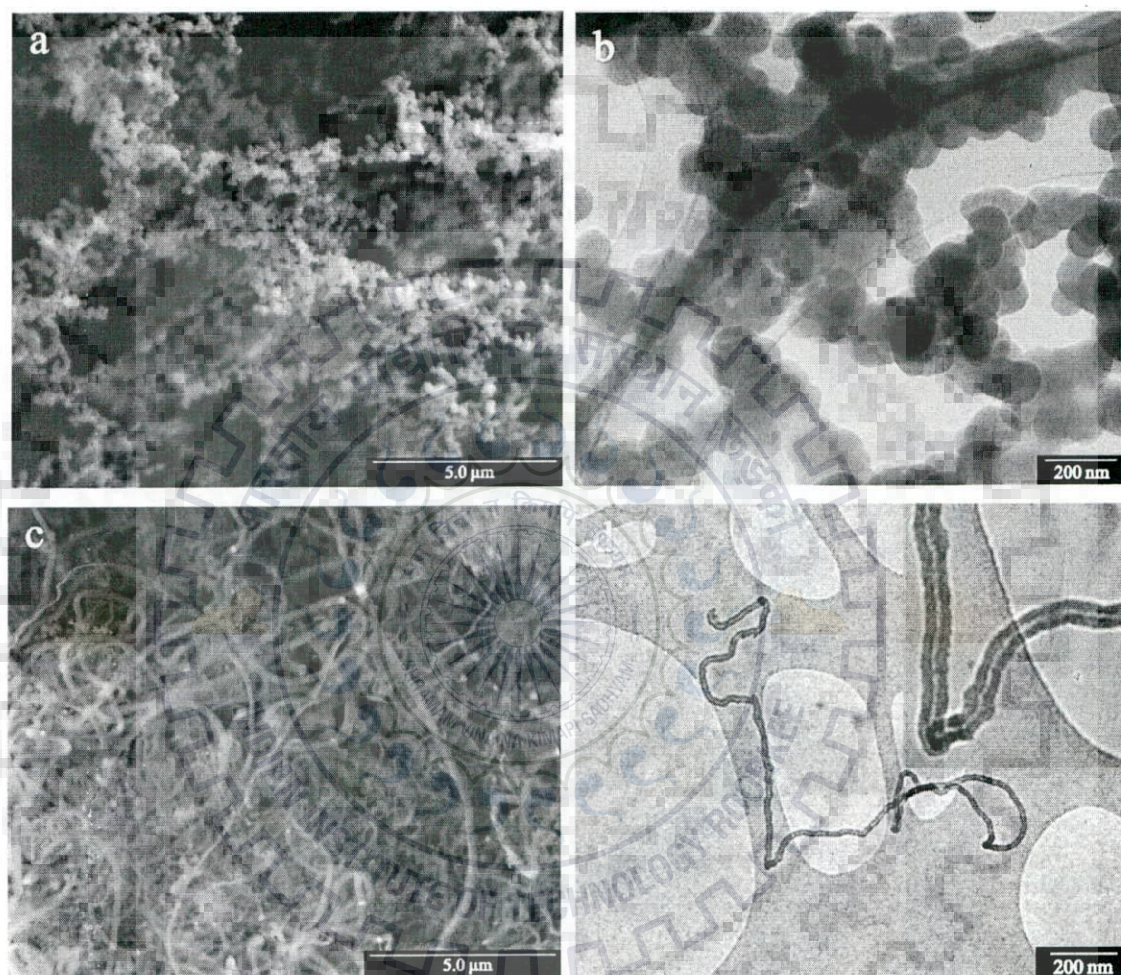
Fig. 4.32: FESEM and TEM images of CNS grown using cobalt oxide based catalyst: (a and b) average size 581 nm, showing CNB but no CNS, and (c and d) average size 40 nm showing MWCNT.

It has been noted that the melting or surface melting of the cobalt oxide based catalyst of larger average size of 581 nm starts at 650 ^{o}C, which is higher than the temperature used in CCVD and there was no melting and only nanobeads formed. But a lower average size of 40 nm of cobalt oxide particles decreases the start of melting to 516 ^{o}C, which is lower than 640 ^{o}C, the temperature used in CCVD and one could observe growth of MWCNT and thus melting or surface melting appears to be important for the growth of CNS like MWCNT.

119

When the extent of doping in oxide increases to 1 wt.% of copper replacing cobalt, as in CoCu01(C) and the average size of nanoparticles decreases to 350 nm, the melting/surface melting starts at temperature 541 $^{\circ}$C. At this relatively lower average size of particles and lower level of doping, the oxide particles are rounded in shape. Since the XRD pattern of oxides taken at 640 $^{\circ}$C shows only reduction of peak heights as revealed in Fig. 4.14 and 4.18, it is likely that at least for particles of some size there would be surface melting at the temperature used in CCVD, which is higher than the temperature at the start of melting but lower than the bulk melting temperature of cobalt oxide, Co_3O_4. The thin molten layer at the surface of the oxide nanoparticle leads to the formation of MWCNT as indicated in Table-4.7. At this level of doping (1 wt.%) decreasing the average size from 350 nm to 33 nm decreases the start of melting temperature to 496 $^{\circ}$C and for which there has been formation of nanofiber also, along with MWCNT.
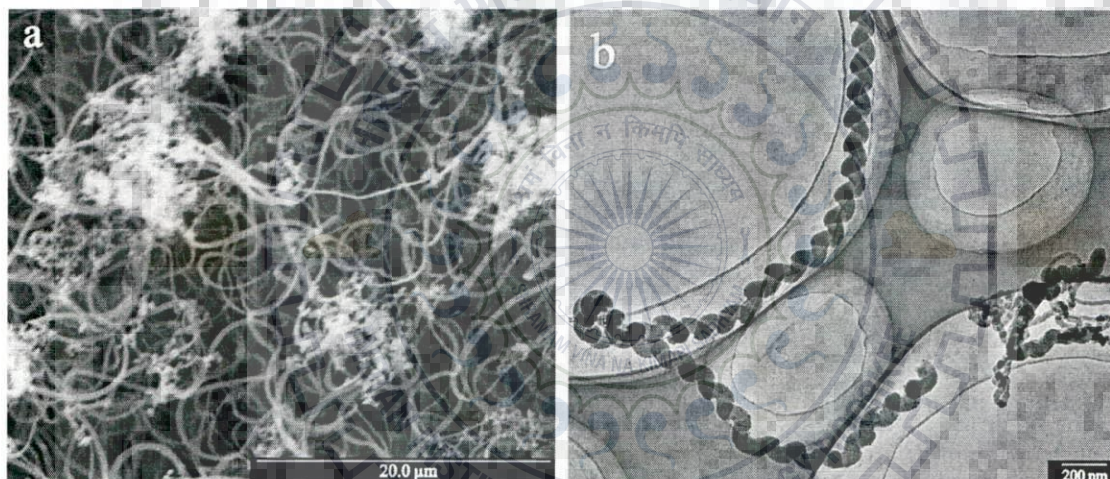
Fig. 4.33: (a) FESEM image of the CNS grown using CoCu10(C), and (b) TEM image of the same showing some helical nanofiber.

If the extent of doping increases to 10 wt.% as in CoCu10(C) and the particles have relatively higher average size of 225 nm, the melting starts at 500 $^{\circ}$C and there is formation of nanofiber either straight or helical in shape as shown in Fig. 4.33. Larger particles may lead to periodic collapse resulting in helical structure and mechanism of formation of helical or coiled CNS may be due to localized stresses and anisotropic rates of carbon deposition on catalytic particles. For the same level of doping of oxide when the average size of particles becomes 71 nm, the melting starts at 471 $^{\circ}$C and one could get CNS in the form of fiber.
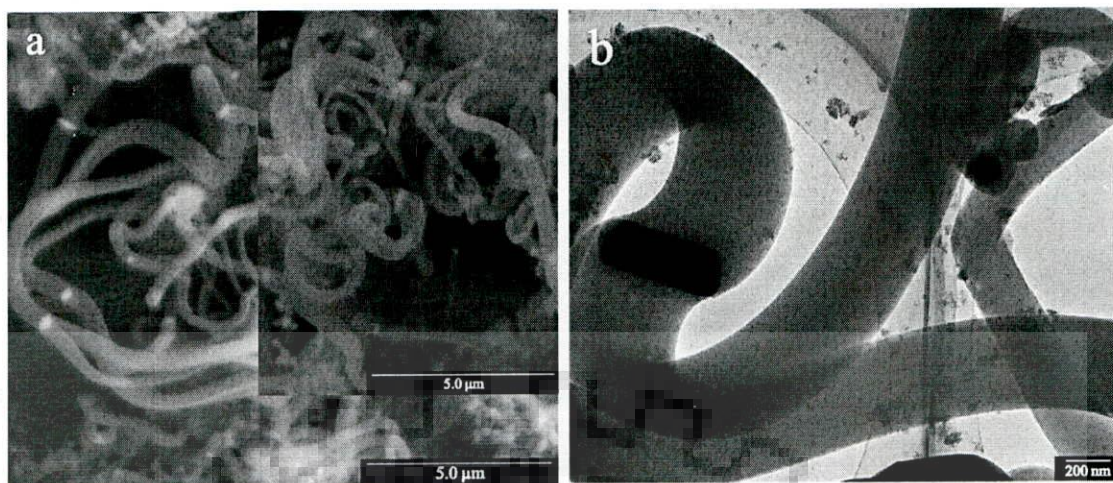
Fig. 4.34: (a) FESEM image of the CNS grown over catalyst of CoCu20(C), and (b) TEM image of the same showing extended shape of the catalyst particle inside a nanotape.

When the average size of particles is similar to cobalt oxide particles of larger size but the level of doping is higher as in CoCu20(C), there has been extensive formation of CNS at 640 °C in the form of fibers and tapes apart from some nanobeads as shown in Fig. 4.34. This has been attributed to the decrease in the temperature at the start of melting of the oxide nanoparticles. The oxide based particles have 20 wt.% of copper replacing cobalt in their oxides, which decreases the temperature at the start of melting to 455 °C. In some of the tapes one may observe extended catalyst particles as revealed in the TEM micrograph shown in Fig. 4.34(b). It may be recalled that the oxide based catalyst CoCu20(C) has more extended particles as shown in Fig. 4.4(c). Now maintaining the level of doping if the particle size decreases as in CuCo20(F), one could observe formation of CNF only as the particles are round and melting of these oxide nanoparticles starts at 439 °C.

4.3.2.2 Growth of CNS using Nickel Oxide Based Nanoparticles

When there is no doping and the nickel oxide nanoparticles have relatively larger average size of 204 nm, the start of melting takes place at a temperature only 2° below 640 °C, at which CCVD has been carried out and only nanobead forms as reported in Table-4.7. With the same particles, an effort has also been made to grow CNS at 600 °C, 38° below the start of melting of these particles and there is formation of nanobeads only. Similar growth of nanobead is observed when doped oxide particles, NiCu10(C), of average size 248 nm is used at the growth temperature of 640 °C, higher than the start of melting by 5°. Thus, when a number of particles are not affected by melting/surface melting at the growth temperature, only chains of carbon nanobeads could form similar to that shown in Fig. 4.35(a) for nickel oxide and in Fig.

121

4.32(a) for cobalt oxide. But by decreasing the particle size of both these oxides one could observe formation of MWCNT. However, decrease in size of doped nickel oxide, NiCu10(F), one could observe formation of nanofiber along with MWCNT as melting of this doped oxide starts well below the growth temperature as reported in Table-4.7.
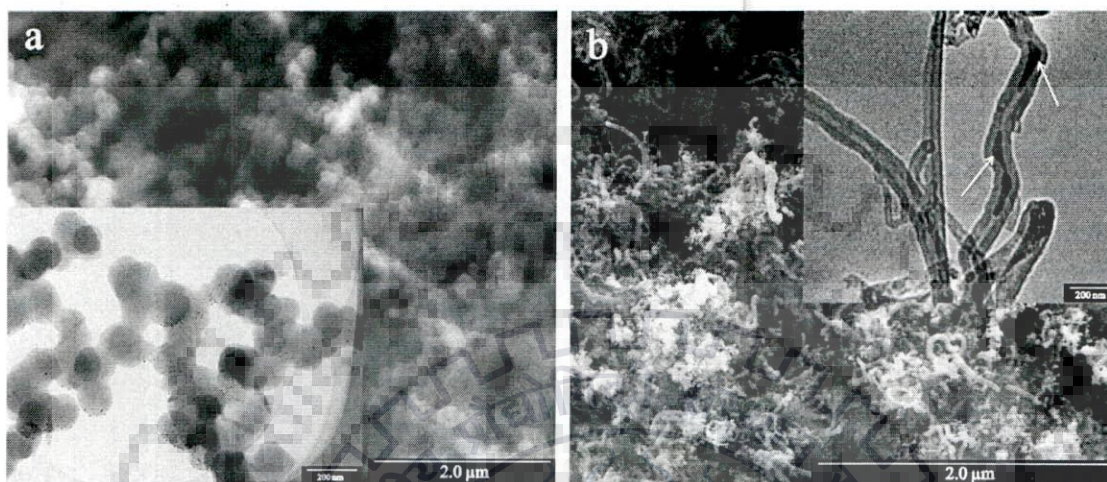
Fig. 4.35: FESEM image of the (a) nanobeads grown using Ni(C) nanoparticles, and (b) CNS grown using the same oxide of smaller size, designated as Ni(F). Inset showing the TEM images and arrows indicate the reshaping of the catalyst particle inside MWCNT as shown in inset of (b).

When the extent of doping increases to 15 wt.% of copper replacing nickel in nickel oxide as in NiCu15(C) and the average particle size is 97 nm, the start of melting is at 494 °C while for the same level of doping but with relatively smaller size, as in NiCu15(F), the melting starts at 478 °C which is about 16 °C lower than that of NiCu15(C) of 97 nm average size. Apart from nanobeads, there is formation of CNF at 640 °C when NiCu15(F) is used but using NiCu15(C), one gets MWCNT along with CNF as indicated in Table-4.7.
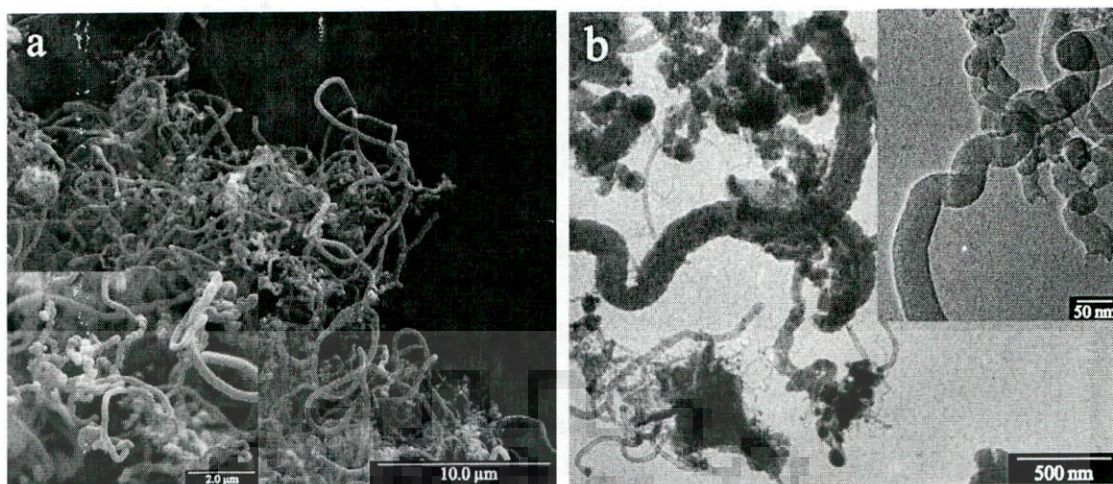
Fig. 4.36: Image of the CNS grown using NiCu20(F) nanoparticles: (a) under FESEM, and (b) under TEM, showing formation of nanofiber; inset showing magnified images in (a) and (b).

When doping increases to 20 wt.%, the melting of nickel oxide based nanoparticles starts at 476 °C even when the average size of the particles is 130 nm. There is hardly any formation of MWCNT and mostly fibers form at 640 °C apart from some nanobeads. Maintaining the level of doping but decreasing the size of the particles to 46 nm, one observes further decrease of the start of melting temperature to 453 °C, which is still 14 °C higher than the start of melting temperature for CoCu20(F) with almost the same sized particles and use of both these nanoparticles results in the formation of nanofibers as reported in Table-4.7.

4.3.2.3 Growth of CNS using Copper Oxide Nanoparticles

It has been reported that the copper oxide particles of very small size have the ability to grow CNS but with a low yield (Zhou et al, 2006; Takagi et al, 2006). In the present study, there have been efforts to grow CNS (Fig. 4.37) using nanoparticles of copper oxide and the results are reported in Table-4.7. Use of very large copper oxide particles having average size of 1129 nm, designated as Cu(C), has not resulted in formation of CNS although that the melting of these particles starts below the growth temperature. Decreasing the size to an average size of 19 nm, as in Cu(F), where even some very tiny particles exist as shown in Fig. 4.37(a) one may observe formation of CNS from these tiny particles as observed in Fig. 4.37(b). Here it may be pertinent to point out that bulk copper has very little solubility of carbon but very tiny nanoparticles may show relatively higher solubility of carbon to enable growth of CNS on it but relatively larger particles are not be able to support any growth of CNS.

123
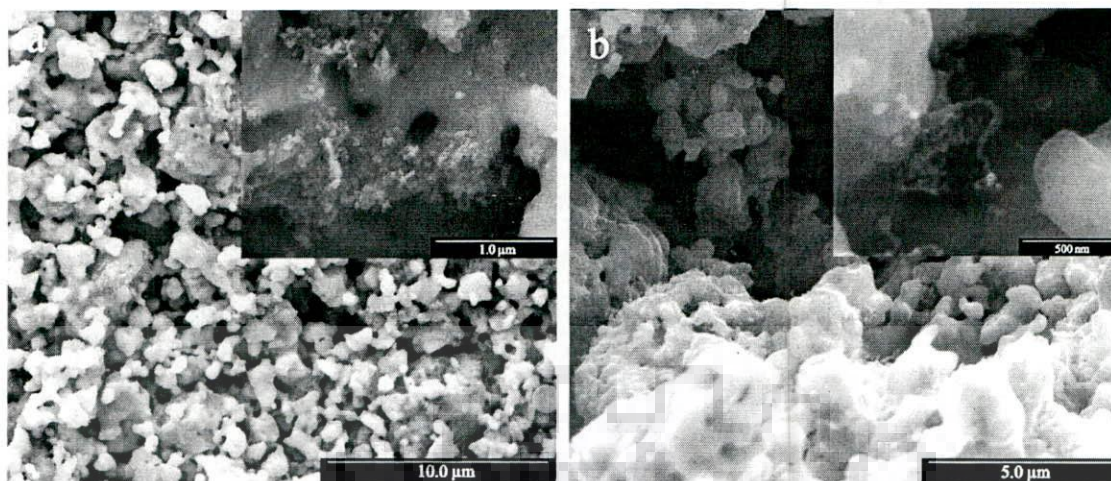
Fig. 4.37: FESEM image of the (a) pure copper oxide after CCVD and the inset showing very fine particles at higher magnification, inside the agglomerates embedded on fused mass, and (b) SWCNT grown over tiny catalyst particles (inset showing magnified image of an isolated SWCNT).

4.4 Discussion

In the present study on the growth of carbon nanostructures (CNS) by CCVD method, the porous alumina shown in Fig. 4.3 has been made by two step anodization of pure aluminium sheet shown in Fig. 4.1. The porous alumina has been used as the substrate for dispersion of the oxide nanoparticles (Fig. 4.21(a)) in order to grow CNS by CCVD process.

Number of studies have been reported earlier using primarily transition metal oxides of cobalt, nickel and iron (Dupuis, 2005; Helveg et al, 2004; Hofmann et al; 2007). In the present study, cobalt and nickel oxide nanoparticles with and without copper oxide doping have been used. It is to mention that copper oxide doped systems have been used for the first time and it is believed that copper oxide is not an effective promoter of CNS growth. This study has also established (in subsection 4.3.1) that the oxide nanoparticles are first reduced to metallic state in the reducing environment inside the reaction chamber used for CCVD at the temperature employed during the growth of CNS. Thus, it is possible that oxides nanoparticles by themselves are not acting as catalyst but the metallic nanoparticles resulting from reduction of oxides act as the catalyst. The present study has demonstrated for the first time a correlation between melting of oxide particles and the growth of CNS and the extent of melting has an influence on the type of CNS growing as it is evident from the results presented in Table-4.7.

The melting of oxide nanoparticles has been investigated by DTA which shows a broad endothermic peak beginning at well below the bulk melting point and it is followed by sharp

124

endothermic peak around the bulk melting temperature as shown in Fig. 4.10 for cobalt oxide based particles. Since nanoparticles have relatively larger proportion of surface atoms having significantly higher energy per atom compared to those in the bulk, it is logical to think that these atoms will satisfy the thermodynamic condition for melting in the surface layer at a temperature lower than the bulk melting temperature (Dash, 2002; Yeshchenko et al, 2007). This surface melting temperature will depend on the internal energy of the surface atoms, which vary with size (Qi et al, 2001). Thus, one may expect size dependent surface melting resulting in a broad peak corresponding to surface melting when the size of the nanoparticles varies over a wide range. The core atoms in the nanoparticles may have energy per atom similar to that of the bulk solid and will attain thermodynamic condition for melting at a temperature similar to bulk melting temperature, where the particles of very large size will melt. If for some smaller size of particles, core atoms may have significantly higher energy than that of atoms in bulk solid, the entire nanoparticles may melt at a temperature lower than the bulk melting temperature. Thus, the observed behaviour of melting in Fig. 4.10 is indicative of possibly either surface melting or bulk melting of the smaller nanoparticles followed by core melting or bulk melting of the larger nanoparticles in cobalt oxide based nanoparticles. But nickel oxide based nanoparticles do not show the sharp peak in DTA response as these particles have been heated to a temperature much below the bulk melting point of nickel oxide as shown in Fig. 4.15. However when the heating was carried out up to 1500 °C, the relatively sharp core/bulk melting peak was observed at a higher temperature but lower than the bulk melting temperature of nickel oxide as shown in Fig. 4.15(a). The DTA response of copper oxide nanoparticles shown in Fig. 4.19 is similar to those observed for cobalt and nickel oxides. After heating at different stages of the entire temperature range while carrying out DTA, the nanoparticles have been examined under FESEM and it could be observed that cobalt oxide based nanoparticles are all fused together as the core melting temperature has been exceeded while heating for DTA response but shape contour of some smaller particles could be clearly observed in Fig. 4.13(d), possibly due to high viscosity and surface tension of oxide melt at these temperatures. But for nickel oxide based nanoparticles, the core melting temperature has not been exceeded during DTA and one could see fused particles in certain locations only where there are smaller nanoparticles but one may observe aggregates of particles resulting from fusion of surfaces as shown in Fig. 4.17. The DTA response has, therefore, been identified with melting as discussed previously. The XRD pattern of oxide nanoparticles registered at 640 °C, which is the growth temperature of CNS, shows presence of crystalline peaks. However the peaks are shifted, broadened and have

reduced intensity, as shown in Fig. 4.14 and Fig. 4.18 for cobalt oxide and nickel oxide based nanoparticles respectively. It is interesting to observe an appreciable change has been occurred for a few peaks, which gives an indication of surface melting of the corresponding planes and not the total melting of the smaller particles, which would have affected all the peaks and planes similarly. The melting behaviour of the nanoparticles is also influenced by the extent of doping, which increases the entropy, thereby lowering the melting point if the effect is not counterbalanced by internal energy change. Thus, both doping and particle size strongly influence the melting behaviour as well as the start of melting, which has been taken as a characteristic relevant for the growth of CNS, as evident from Figs. 4.11 and 4.12 for cobalt oxide based nanoparticles and Figs. 4.15 and 4.16 for nickel oxide based particles.

When these oxide nanoparticles having different level of doping and size are dispersed on the nanoporous alumina substrate and put in the highly reducing environment of the CCVD chamber, the oxides get reduced. The studies on the chemical evolution of the oxide nanoparticles have been carried out by examining the nanoparticles inside CNS using STEM, EDS, TEM and SAD as shown in Fig. 4.23, for CNS grown using cobalt oxide based nanoparticles and in Fig. 4.25 for nickel oxide based nanoparticles. Apart from presence of graphitic CNS, EDS and SAD both indicate presence of the corresponding metallic phases containing either cobalt and copper or nickel and copper reduced from the corresponding oxides. The presence of copper in the reduced particles could not be confirmed by EDS because of use of copper grid to hold the particles. The oxide nanoparticles have also been subjected to similar reducing environment as prevailing during the growth of CNS but at a relatively lower temperature so as to reduce the extent of formation of CNS and these particles have been examined by XRD as shown in Fig. 4.22 for cobalt oxide based nanoparticles and Fig. 4.24 for nickel oxide based nanoparticles. The observed metallic phases after exposure of different oxide nanoparticles to reducing environment are given in Table-4.6. It is well known that bulk metallic nickel and cobalt occurring in fcc and hcp structures respectively show stacking faults in their microstructure and the faulted region has respectively hcp and fcc structures. In these two metals fcc and hcp structures have very similar energy and so stacking fault is observed. Thus, it is only natural to expect that in small nanoparticles having higher energy per atom of fcc cobalt or of hcp nickel may result. Doping by copper, which has stable fcc phase, may enhance the stability of fcc nickel and drive cobalt from hcp to fcc. However, copper also has small difference in energy between fcc and hcp structures as indicated by commonly occurring stacking faults. Both nickel and copper whether in fcc or hcp structures have stacked hexagonal close packed planes which may

126

provide template for the heterogeneous nucleation of graphene layer and effectively act as catalyst for the growth of CNS. The comparison of typical Raman spectra of the oxide nanoparticles and those exposed to reducing environment shows that the reduction is almost complete for both cobalt and nickel oxide based nanoparticles as shown in Fig. 4.28. Thus, there is ample confirmation that it is not the oxide nanoparticles but the reduced metallic nanoparticles, which are possibly acting as the catalyst for the growth of CNS.

On the basis of the results discussed so far it is apparent that in the reaction chamber of CCVD, there are two processes taking place during growth of CNS using nanoparticles of oxide – (a) reduction of the oxide nanoparticles, and (b) growth of CNS. Before one embarks on a discussion of these processes, it is necessary to have a clear idea as to how the growth is taking place vis-à-vis a nanoparticle. The catalyst particles are often inside CNS as observed in the TEM micrographs of CNS presented earlier. The diameter (y in nm) of CNS is plotted againstthe size (x in nm) of catalyst particle inside, in Fig. 4.38(a) for cobalt oxide based nanoparticles yielding a linear least square fit equation, $y = 0.997x + 27.231$, with correlation coefficient better than 0.98.
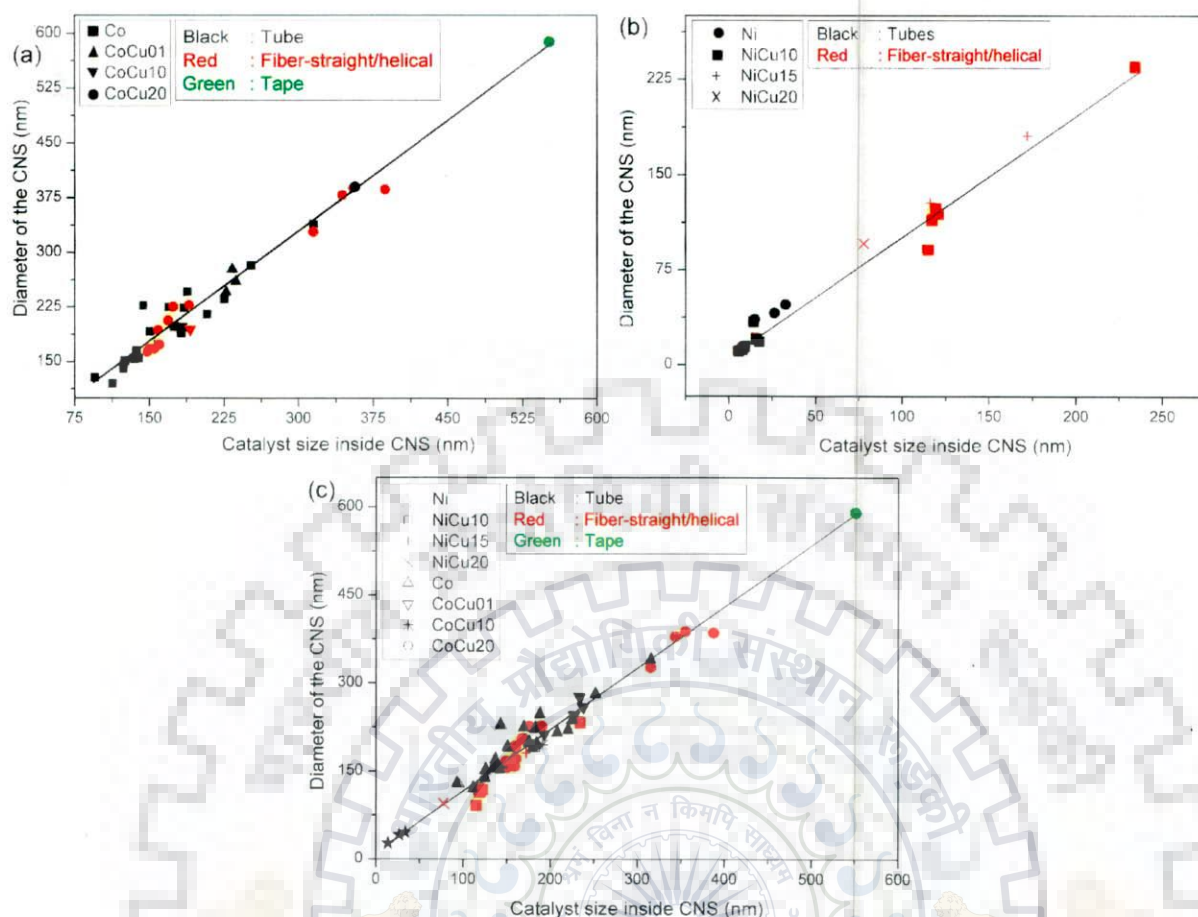
Fig. 4.38: Variation of diameter of CNS with the size of catalyst generating it using (a) cobalt oxide based particles, (b) nickel oxide based particles, and (c) combined for both cobalt and nickel oxide based particles.

The same linear trend has been observed to follow for the CNS grown using nickel oxide based nanoparticles as shown in Fig. 4.38(b), showing a linear variation given by equation, $y = 0.944x + 11.234$, with correlation coefficient ~ 0.98. When the results of both cobalt and nickel oxide based nanoparticles are plotted together in Fig. 4.38(c) showing a linear variation given by $y = 1.028x + 17.085$, with correlation coefficient of 0.99, similar to their separate plots. Thus, it may be presumed that CNS is growing around the catalyst particles in a large number of cases as evident from the linear trend of the results. Further, it may be observed that in the same size range of catalyst particles, MWCNT forms at lower level of doping while fibres form at higher level of doping, which implies increased melting of the originating oxide nanoparticles.

The picture emerging from this study so far indicates that one may consider a nanoparticle of oxide with molten surface layer exposed to the reducing environment having ammonia and a carbon bearing gas in the chamber of CCVD. These gases decompose into two powerful

reducing agents of hydrogen and carbon, which start reducing the molten metallic oxide layer to metal from the surface, progressing radially inside the nanoparticle with diffusion of these species in the molten layer. Hydrogen is of very small size and has high diffusion coefficient in solid oxide. Thus, solid state reduction of oxide nanoparticles by hydrogen is possible and melting is not prerequisite for this purpose. However, melting will accelerate reduction. Since carbon bearing gas is decomposed on the surface of the oxide nanoparticle, it may insulate the nanoparticle from further reduction unless the carbon is dissolved by the molten surface layer allowing the access of hydrogen and carbon inside the particle radially by diffusion. Melting is, thus, a prerequisite for dissolution of the deposited carbon and ingress of high flux of carbon inside. Suppose a given temperature profile within an oxide nanoparticle results in surface melting, then it may be safely presumed that the surface layer will also remain molten after reduction as it has been observed by high temperature XRD studies in Fig. 4.31, as metal generally has a lower melting point than its oxide. Thus, the thickness of the molten surface layer of metal is expected to be more than that originally existed in the oxide. However, cobalt oxide, Co_3O_4, has a lower melting point than cobalt and the thickness of the molten layer may be less. One may, therefore, perceive a situation when the solid oxide core may start melting with the progress of reduction. Graphene prefers to nucleate on hexagonal close packed plane of fcc/hcp metals like cobalt or nickel etc. It may take place when the reduction has proceeded to the surface of solid oxide core and in the reduced area of the solid oxide the graphene layer may nucleate. Once graphene has nucleated, there is growth of the layer around the particle to a cylinder. The flux of carbon entering the particle through the molten layer at the surface has two roles - one is reduction of oxide (along with hydrogen) and the other is the formation of CNS involving nucleation and growth. The cylinder of graphene sheet may grow in two directions - radially in the thickness direction by addition of more graphene layers and axially along the length on the graphene planes. If the growth around the particle or axial growth is slow, there could be growth over top surface of the catalyst creating a cap. The growth in the thickness direction by addition of parallel layers over the graphene layer at similar distance as in graphite could be termed graphitic growth and this growth may take place both outside and inside of the initial graphene cylinder. On the outside, this growth will take place provided there is molten layer or else there will be no graphitic growth and only loose carbon deposit may form as it has been commonly observed. The possibility of growing inside will depend on: (i) flux of carbon inside the graphene tube possibly through partial dissolution of the graphene layer, which will be repaired/reformed by flux arriving from outside, and (ii) progress of reduction and melting. Melting inside is required not only

for part dissolution of graphene and high flux of carbon inside but also for squeezing out the melt along the axial hole of the tube to make place for the graphitic growth inside. This could be the explanation for the shape change inside CNS as it has been observed in Fig. 4.35(b). If the progress of melting is through the entire core it is likely that that graphitic growth will progress inside to fill up the space creating a nanofiber. This may be the reason for observing fibers growing in oxides having higher level of doping as noted in Fig. 4.36. When the oxide particle is very small and it does not have enough thickness in the liquid layer for radial graphitic growth either inside or outside, SWCNT is expected to grow only by axial growth as observed for copper oxide based nanoparticles shown in the image inset in Fig. 4.37(b) but the larger particle in the same sample of oxide, Cu(F), has given rise to MWCNT as reported in Table-4.7.

In case of solid catalyst without any melting, decomposition of the carbon bearing gas, results in rapid build-up of carbon around catalyst particles leading to the formation of carbon nanobeads. The flow rate of carbon bearing gas controls the rate of decomposition and higher flow rate may favour the formation of nanobeads even when the start of melting is slightly lower than the growth temperature and there is very less surface melting, which could dissolve only a very small amount of carbon compared to that deposited on the surface. When the flow rate of carbon bearing gas was decreased, the decomposition rate of the carbon bearing gas and the consequently, the deposition rate of carbon decreases and one could observe growth of MWCNT as shown in Fig. 4.39(a) for the catalyst particles of pure cobalt oxide of larger average size 581 nm and in Figs. 4.39(b) and (c) for nickel oxide particles of average size 204 nm and NiCu10(C) of average size 248 nm, which have grown nanobeads at higher flow rates as shown in Figs. 4.32(a, b) and 4.35(a).
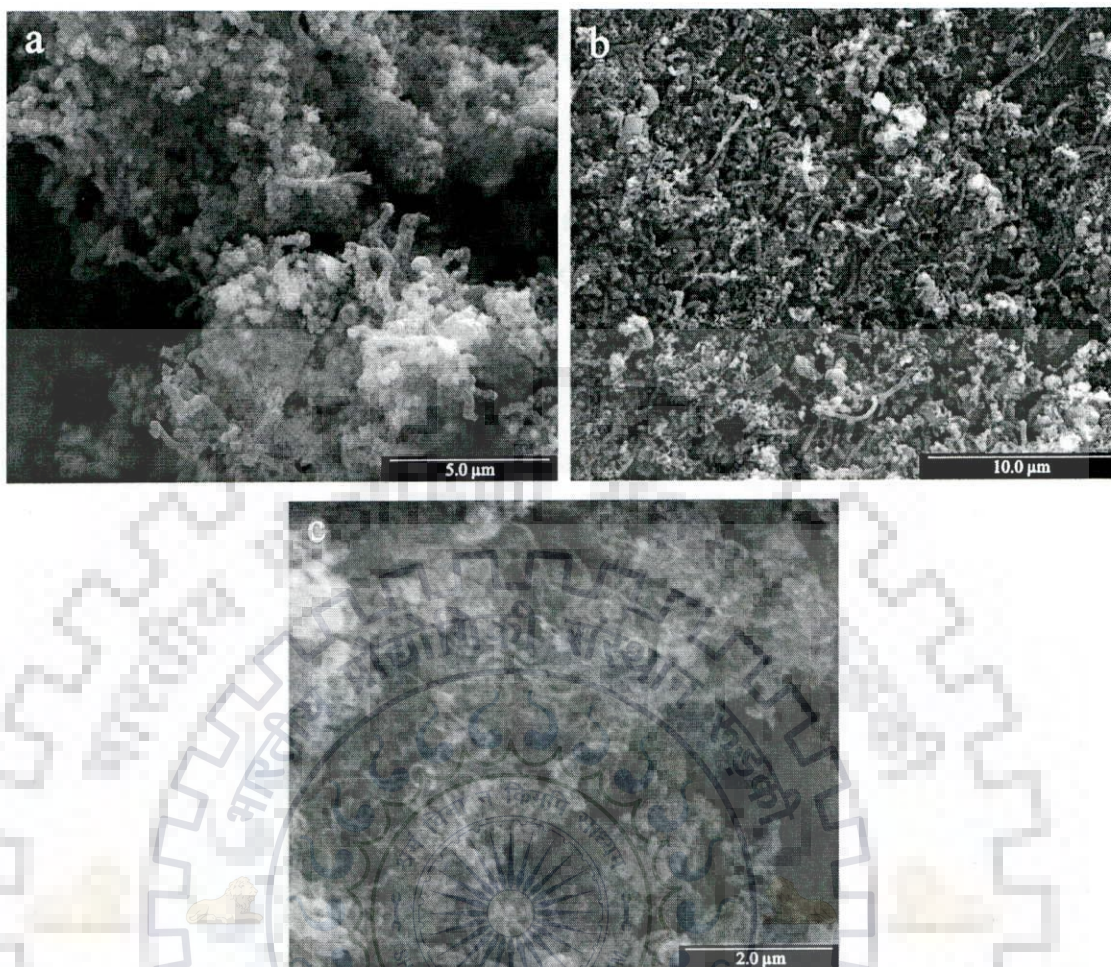
Fig. 4.39: FESEM image of the CNS synthesized using the catalyst designated as (a) Co(C), (b) Ni(C), and (c) NiCu10(C) grown at lower flow rate of C_2H_2.

Thus, it appears that the growth of CNS requires higher flux of carbon through diffusion, which is possible in molten state as it results in higher diffusion coefficient (*D*) of carbon to support a high flux compared to that in solid catalyst particle. So, melting appears to be necessary and without melting or surface melting there is no growth of CNS below the temperature at the start of melting as observed in Table-4.7.

For the oxides designated as Co(F), Ni(F) or CoCu01(C), the smallest particle sizes are respectively 19, 23 and 88 nm, the entire core may not have melted even on reduction to metals since the level of doping is either zero or less and so, the growth of MWCNT is favoured. When the particle size lies between 19 and 45 nm as in the case of CoCu01(F), similar to that in Co(F), the temperature at the start of melting is relatively lower compared to CoCu01(C) and consequently, for some of the smaller particles, the entire core may melt and one observes mixture of MWCNT and CNF. Similar mixture of MWCNT and CNF is also observed for oxide particles in NiCu10(F) where the particle size is between 27 and 57 nm,

131

and also for NiCu15(C) where the size is between 45 and 165nm i.e. relatively larger but the extent of doping is also relatively higher. In all these cases of mixed MWCNT and CNF, the temperature at the start of melting is between 494° and 505 °C and the average particle size is nearly below 100 nm. When the average particle size (225 nm) is relatively larger, lying in the range of 71 and 391 nm, and the temperature at the start of melting is 500 °C for CoCu10(C), one does not observe mixture of MWCNT and CNF. However, both helical and straight CNF are found to develop. Larger particle size requires higher flux of carbon to grow axially and lack of steady supply of this flux may lead to periodic collapse of size. When the temperature at the start of melting falls below 478 °C as in case of CoCu10(F), CoCu20(F), NiCu15(F), NiCu20(C) and NiCu20(F), one can observe the formation of CNF with average size of the oxide particles below 100 nm and only in case of NiCu20(C) it is 130 nm. For elongated larger particles of average size 500 nm, one observes nanotape and CNF as in CoCu20(C) and both these growth are presumed to indicate melting of the entire core during reduction. The core melting at the temperature prevailing in the reaction chamber of CCVD, may explain the difference between growth of MWCNT and CNF, depending both on the melting characteristics of the oxide particle, indicated by the temperature at the start of surface melting, T_s, and the size of the oxide particle. When the temperature at the start of melting is normalized with respect to the growth temperature, T_g, prevailing during growth of CNS as $\Delta = (T_s-T_g)/T_s$ and is plotted with the minimum size of the oxide nanoparticle used in an experiment for the growth of CNS as shown in Fig. 4.40, it is observed that similar morphology clusters in a region irrespective of the catalyst used in the present study.
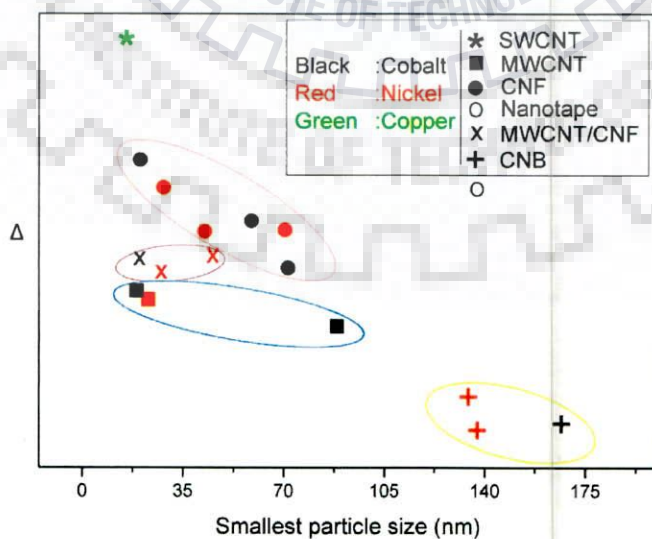
Fig. 4.40: Morphology map of carbon nanostructures grown by catalytic chemical vapour deposition using cobalt, nickel and copper based oxide nanoparticles.

For the smallest size of oxide particles, when Δ increases, one may observe morphology change from MWCNT to CNF with mixed morphology around the transition region. The observation of the growth of SWCNT at high Δ at smaller particle size is possibly due to lack of space for graphitic growth. On increasing minimum particle size up to around 100 nm, the transition from MWCNT to CNF is still observed with increasing Δ. When the minimum size of nanoparticles increases further to around 150 nm, the oxide growth is anisotropic leading to formation of tape at similar values of Δ where smaller particle sizes lead to CNF. Higher particle size and lower Δ, lead to the formation of nanobeads. If one could create a condition of limited space for graphitic growth by limiting Δ, there should be growth for SWCNT around larger size of particles. However, the condition for the growth of SWCNT could not be attained at higher particle sizes and the search for a region of SWCNT in this region requires further study.

Results and Discussion: Carbon Nanostructures and their Electrochemical Performances

Chapter 5

Results and Discussion: Carbon Nanostructures and their Electrochemical Performances

There is continuing global effort to develop lithium ion batteries with higher capacity and better stability in order to extend their application, particularly to mobile tools and automobiles. The battery performance solely depends upon the capacity of electrode materials to hold active species of lithium and discharge/charge reversibly. The currently used commercial anode of graphite has excellent stability and low cost but could be intercalated to a maximum level corresponding to chemical formula LiC_6 i.e., one lithium for every six carbon atoms leading to a theoretical limit of its specific charge capacity 372 mAhg^{-1} (Henderson and White, 2011). Carbon nanostructures (CNS) have been used in electrodes, with the aim to obtain higher lithiation capability and better overall performance as they have high electrical conductivity, strength and chemical stability. Several types of carbon materials exhibiting different morphologies and textures have been investigated for use as anode of lithium ion batteries. The electrochemical behaviour of carbon-based materials depends on their morphology and microstructures. In this context different types of CNS having different morphologies like single walled, double walled, multi walled carbon nanotubes (with two different range of diameters) and carbon nanofibers have been tested as an efficient electrode material as they have large amount of intercalated sites within them in order to understand the role of morphological features and defects in the context of their application in the anode of lithium ion batteries.

5.1 Physical Characterization of the Different Types of CNS

High surface area of CNS is attractive for application in anode of lithium ion battery. The structural characterization of different CNS samples is important to develop structural correlation with their performances. The size (OD: outer diameter, L: length) and the surface area (BET) of the samples are reported in Table-5.1.
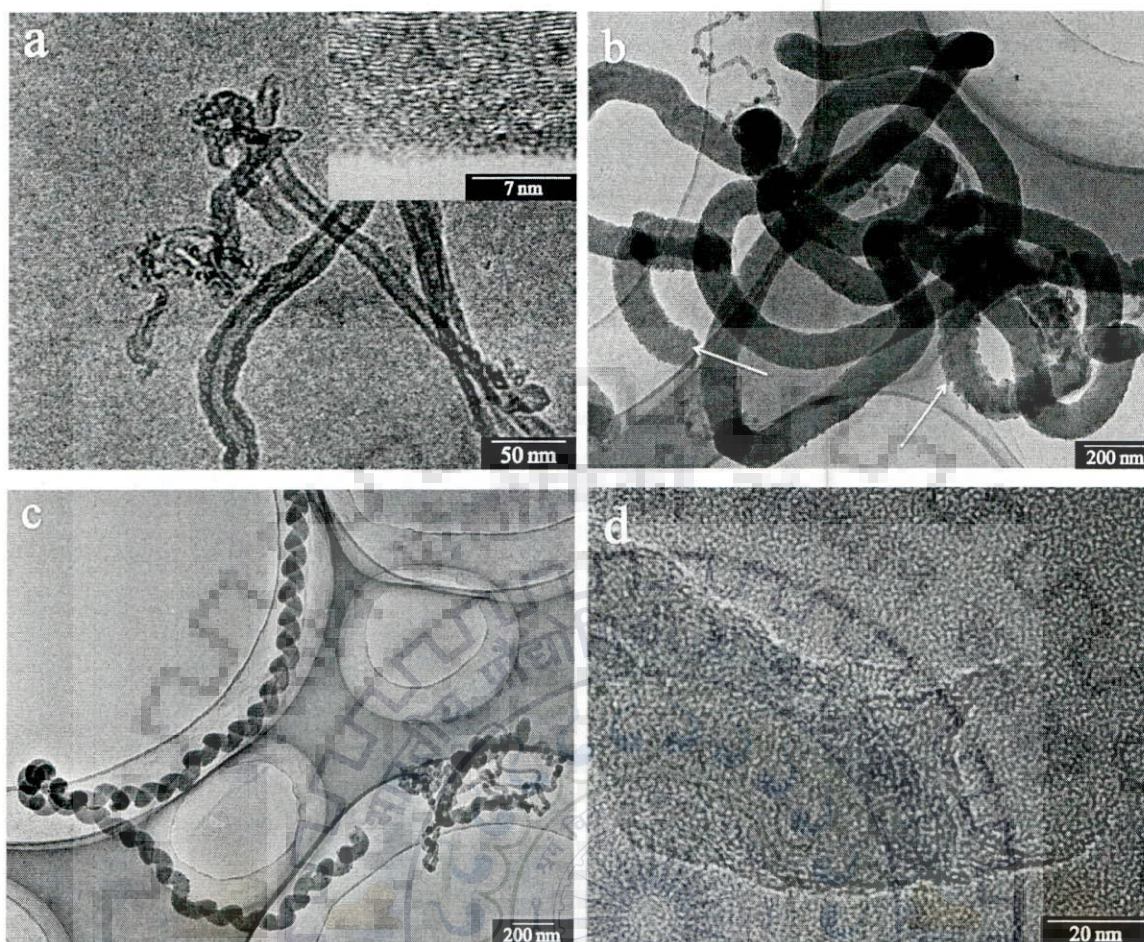
Fig. 5.1: Structure of the CNS as revealed under TEM showing (a) graphitized areas (inset) in MWCNT, (b) defective spring like structures (marked by arrow) in CNF, (c) twisted type of CNF, and (d) open end of MWCNT.

The structural arrangement of the CNS, however, cannot be categorized as purely graphitic because there are disordered regions between graphitic regions observed from the HRTEM image (inset) in Fig. 5.1(a). The defects due to twisting and turning of CNS sometimes with open ends, as shown in Fig. 5.1, may provide the sites for enhanced lithiation but it may not be easy to extract lithium from all the sites during the delithiation step. This difficulty results in high specific capacity during initial charging-discharging, however, with low reversible capacity. But enhanced sites for easy lithiation and delithiation similar to those between well graphitized planes will result in high specific capacity as well as high coulombic efficiency.
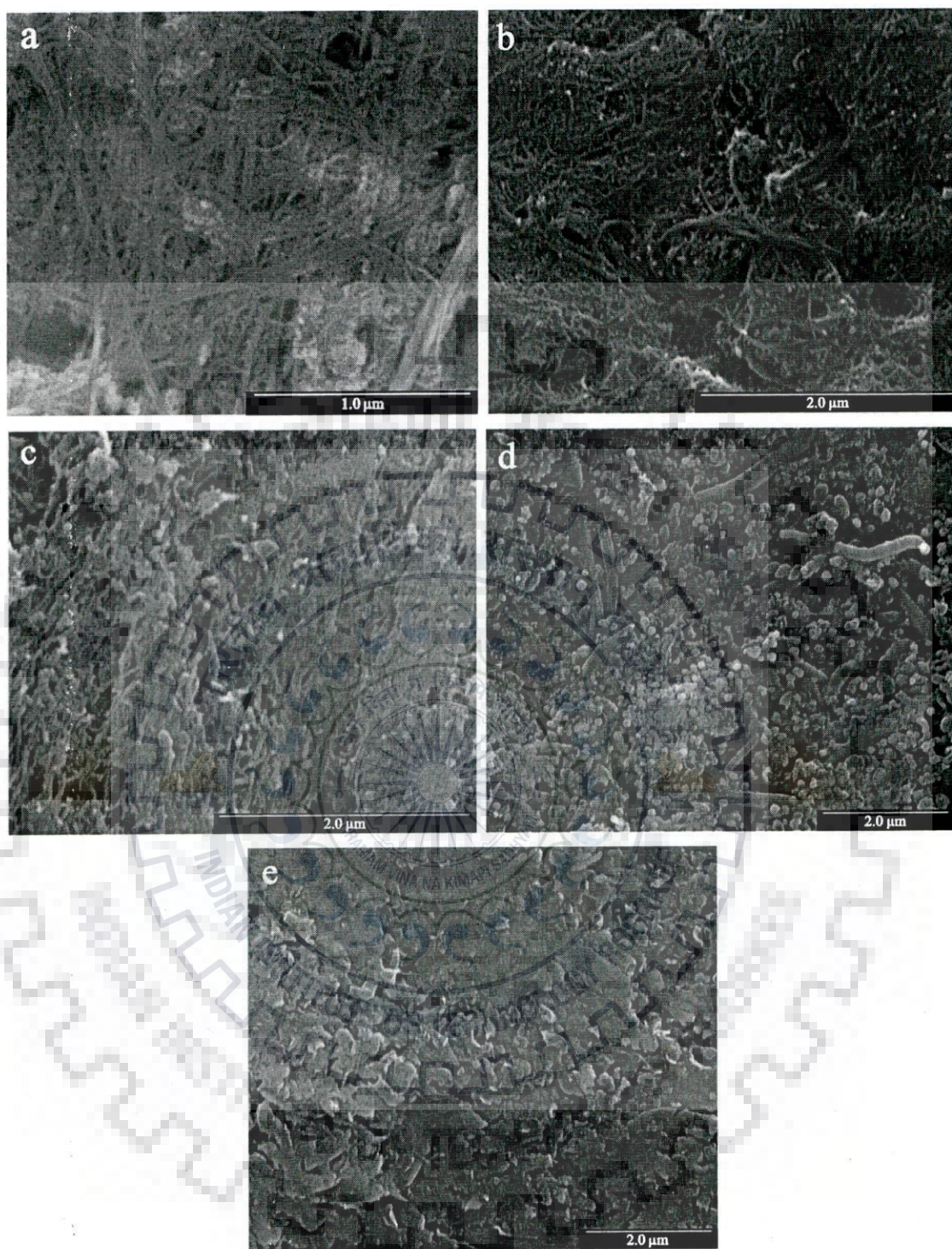
Fig. 5.2: FESEM images of the CNS electrodes before cycling: (a) SWCNT, (b) DWCNT, (c) MWCNT with small diameter, (d) MWCNT with large diameter, and (e) CNF.

In the anode preparation the current collector i.e. copper foil is coated with thin layer of CNS based materials. Fig. 5.2 shows FESEM images of the anode materials with different CNS morphology. From the morphological characterizations, the active electrodes materials are appeared as inter-twined entanglements of nanostructures forming a forest-like porous

structure of ~ 20 μm thickness on the copper current collector as shown in Fig. 5.2, and thereby, making large surface area of CNS accessible for enhanced lithiation.

Table-5.1: Dimension and other physical characteristics of CNS as obtained from FESEM, TEM, BET and XRD.

Type of CNS	Physical properties			XRD	
	OD (nm)	L (μm)	BET (m^2g^{-1})	FWHM	Lattice spacing d_{002} (Å)
SWCNT	1-2	5-30	380	2.404	-
DWCNT	2-4	50	350	3.887	3.437
MWCNT(S)	10-20	10-30	212	2.14	3.447
MWCNT(L)	100-200	1-10	165	5.513	3.479
CNF	200-600	5-50	57	1.934	3.493

The phases and purity of different CNS were checked by XRD and the diffraction patterns are shown in Fig. 5.3. The presence of (002) graphitic reflection in the XRD pattern of SWCNT indicates the presence of turbostratic graphite, MWCNT, ordered graphite or their combination. The XRD pattern for DWCNT is similar to SWCNT and similar inference may be drawn about the presence of other carbon based structures. The diffraction peaks corresponding to (002) graphitic plane are observed in MWCNT and CNF and it belongs to hexagonal phase (*P63/mmc*; 194) of graphitic carbon. The peak at ~ 44° corresponds to (101) graphitic plane for MWCNT and CNF though it also overlaps with the catalyst peaks. It may be noted that for larger diameter MWCNT designated as MWCNT(L) prepared in the laboratory, the (101) peak is sharper due to the presence of more catalyst nanoparticles located inside the tubes.
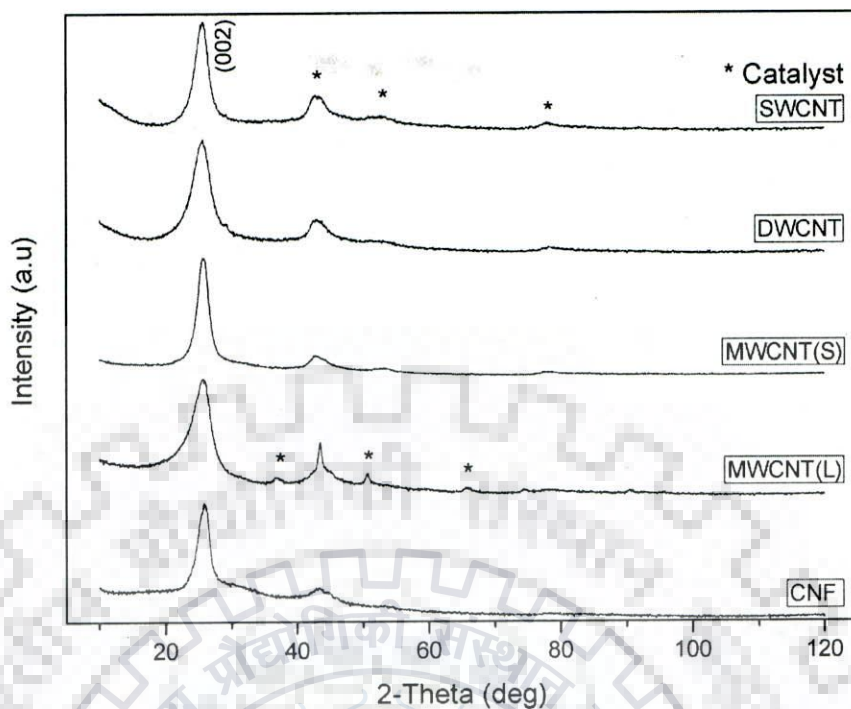
Fig. 5.3: Typical XRD patterns of CNS: SWCNT, DWCNT, MWCNT (small (S) or large (L) diameters), and CNF.

The line shape of the (002) peak is related to the variation of the interlayer spacing and orientation of the tube with respect to the X-ray incident beam (Cao et al, 2001) and the full width at half maximum (FWHM) of each type of CNS is given in Table-5.1. Based on the Bragg's equation, it is confirmed that between (002) planes, the interplanar spacing (d_{002}) is approximately ~ 0.34 nm similar to that in graphite, but varies slightly in different types of CNS as given also in Table-5.1 and shown in Fig. 5.4. In graphitic carbon or MWCNT/CNF, the spacing of (002) increases slightly with increasing tube diameter as shown in Fig. 5.4.
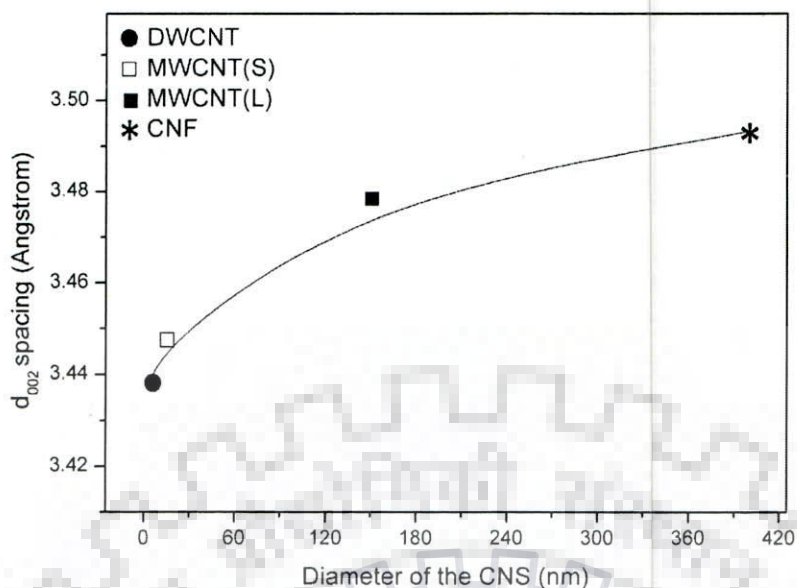
Fig. 5.4: Variation of d spacing for (002) planes in different CNS samples with tube diameter.

Typical Raman spectrum of different CNS used in the present study as obtained with green laser is shown in Fig. 5.5. A small peak corresponding to radial breathing mode could be observed in SWCNT and DWCNT respectively at $\omega_{RBM} = 270$ cm^{-1} and $\omega_{RBM} = 300$ cm^{-1} and the corresponding diameter of the nanotube resonating at these frequencies are 0.9 nm and 0.8 nm. It appears that the inner tube of DWCNT is smaller in diameter than SWCNT. The Raman spectrum of the DWCNT is similar to that of the SWCNT, due to the small diameters of both materials. The single resonance G-band peak involving optical phonon mode (both longitudinal and transverse) is observed at ~ 1573 cm^{-1} for SWCNT, DWCNT and MWCNT(S) but the line width of MWCNT(S), which has relatively larger diameter of 10-20 nm compared to those of SWCNT or DWCNT, is significantly more. But for a still larger diameter of 100-200 nm in MWCNT(L) the G-band peak shifts to ~ 1589 cm^{-1} with a broader line width whereas this peak for graphite is at 1582 cm^{-1}, close to that observed for CNF.

142
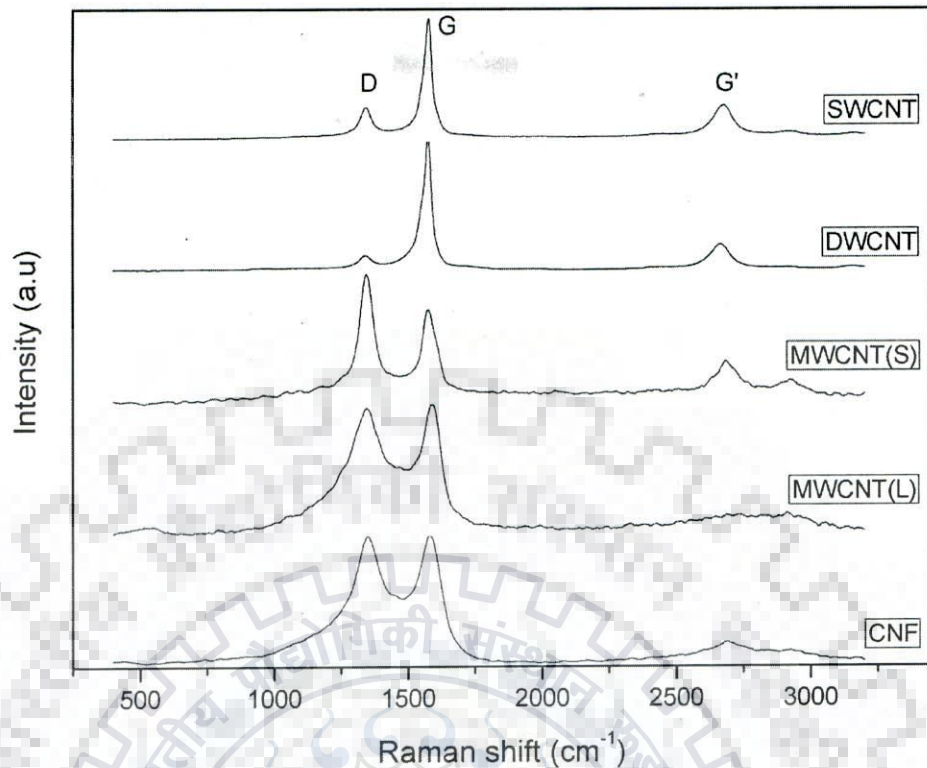
Fig. 5.5: Raman spectra of SWCNT, DWCNT, MWCNT of small (S) as well as large (L) diameters, and CNF.

The details of the Raman spectra of the samples including the peak broadening and intensity ratio between D- and G'-band are given in Table-5.2. The value in bracket in Table-5.2 indicates the shift with reference to the peaks corresponding to graphite. G-band frequency is usually affected by the interlayer bonds (Gupta et al, 2006), which also increases with the diameter of CNS as revealed by XRD. It is interesting to observe that for SWCNT and DWCNT of relatively smaller diameter, the intensity of double resonance D-band peak is relatively much smaller compared to G-band peak and it is more so for DWCNT. But for MWCNT and CNF of relatively larger diameters, the intensity of D-band peak is considerably stronger and as good as the strength of G-band peak. It can be seen from the Fig. 5.5 that the D- and G- band peaks for MWCNT are broader compared to those of SWCNT and DWCNT. The peak corresponding to D-band is observed at around ω_D = 1341 cm^{-1} for SWCNT, DWCNT and MWCNT(S) while the second harmonic G' occurs at around $\omega_{G'}$ = 2674 cm^{-1} (~ $2\omega_D$) for SWCNT but it is at $\omega_{G'}$ = 2666 cm^{-1} and $\omega_{G'}$ = 2682 cm^{-1} for DWCNT and MWCNT(S) respectively. MWCNT(L) having still larger diameter lying between 100 and 200 nm has ω_D at 1341 cm^{-1} while $\omega_{G'}$ = 2690 cm^{-1}, which is also the same for CNF but higher than that observed for MWCNT(S). D-band originates from in-plane transverse optical phonon branch close to K-point in Brillouin Zone of graphite and the double resonance could

143

involve one elastic scattering from defects and one inelastic scattering or both inelastic scattering involving phonons. Thus, defects like dangling bonds at the edges and other lattice defects will significantly influence D-band while G'-band is less sensitive to defects (Dresselhaus et al, 2005). Broad and intense D-band may be indicative of disordered and low graphitized carbon in between ordered region as shown in Fig. 5.1(a) (inset) under HRTEM. If one compares the peak positions with those of graphite, positions of the D-band are similarly shifted in all the CNS examined except CNF, for which it is close to graphite. The shift in G-band is also similar to those in D-band except for MWCNT(L) for which it is negative. For G' peaks, the shift is 2-4 times that of D-bands, largest for DWCNT, then in decreasing order for SWCNT and MWCNT(S). For MWCNT(L) and CNF, the shift is lower and similar. The precision of the spectrometer measurement is < 1 cm^{-1} whereas, the significant digit of the results could be ascertained by the standard deviation of the results, which is ~ 1.1.

Table-5.2: Details of the observed peaks in Raman spectra - their position, FWHM and intensity ratio R.

Type of CNS	$R=I_D/I_{G'}$	Raman peak position (cm^{-1}) Shift compared to those of graphite are indicated in brackets*					
		~ D		~ G		~ G'	
		Position	FWHM	Position	FWHM	Position	FWHM
SWCNT	0.97	1341 (9)	64	1573 (7)	39	2674 (26)	82
DWCNT	0.62	1341 (9)	244	1573 (7)	39	2666 (34)	85
MWCNT(S)	2.23	1341 (9)	391	1573 (7)	273	2682 (18)	102
MWCNT(L)	2.43	1341 (9)	333	1589 (-9)	337	2690 (10)	47
CNF	3.19	1350 (0)	200	1582 (-2)	87	2690 (10)	218

* The positions of G-band and G'-band peaks of graphite crystals are at ~ 1580 and ~ 2700 cm^{-1} respectively. D-band due to defects and finite size of graphite appears at ~ 1350 cm^{-1}.

5.2. Electrochemical Properties

The electrochemical properties of electrodes developed with the five different types of CNS have been investigated. The lithium insertion in SWCNT shows the signature of typical solvent decomposition or co-insertion and further side reactions in the formation of the solid electrolyte interphase (SEI) (Chen et al, 2002) below ~ 1 V as shown in Fig. 5.6(a). Such plateau is typical of all CNS-based electrodes with a slight change in the voltage. The plateau becomes more distinct with relatively increased SEI formation observed in electrodes with SWCNT presumably because of its high surface area (refer to the BET results shown in Table-5.1) as compared to that observed in MWCNT with larger diameter. However, the formation

144

of SEI appears to take place over an extended voltage region from 0.6 - 1.1 V for CNF based electrode in the 1st cycle, indicating possibly relatively slower kinetics for the formation of SEI (Fig. 5.6(c)). After the formation of SEI in the 1st cycle the plateau region vanishes for the next successive cycles which clearly indicate that the irreversible process of formation of SEI has been completed, leading to a stable electrolyte-electrode interface.
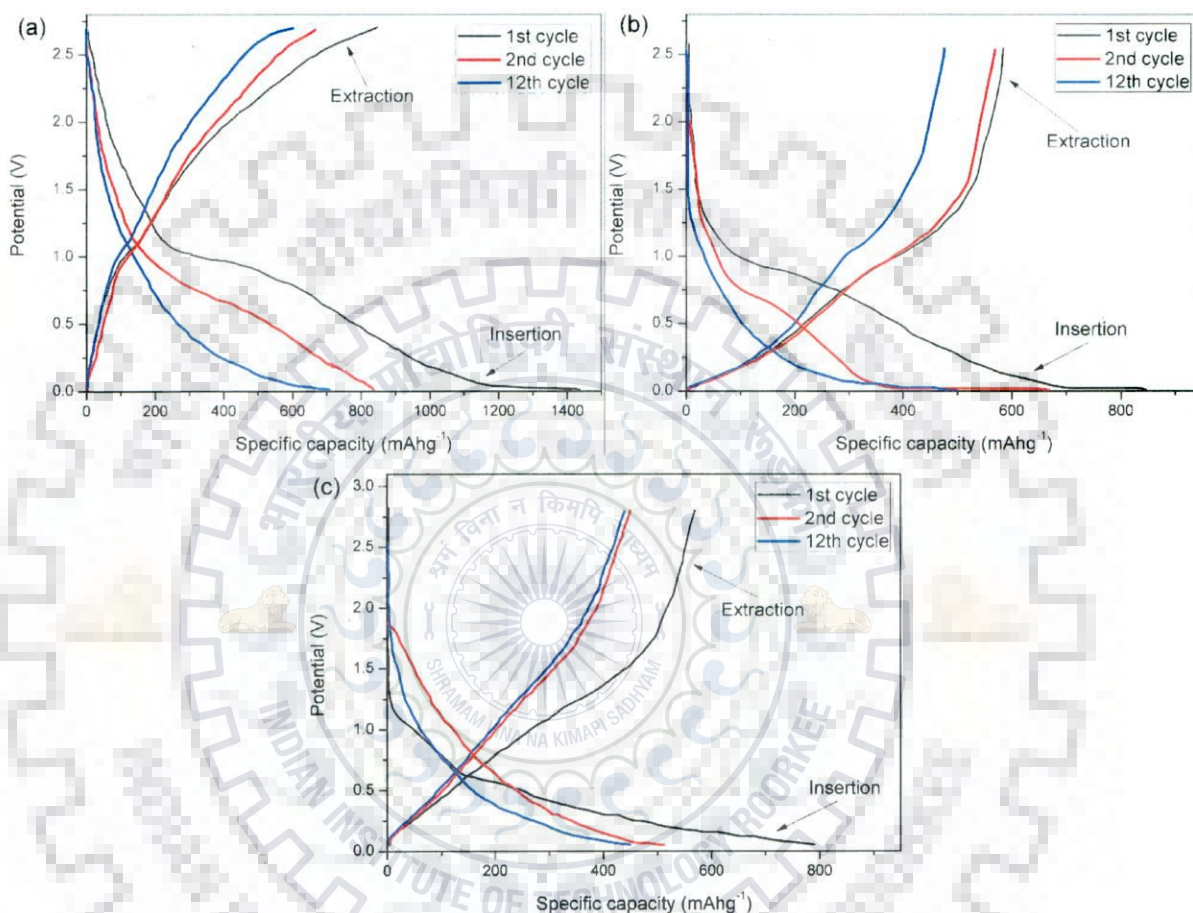
Fig. 5.6: Typical charge–discharge profiles (a) SWCNT, (b) MWCNT(L), and (c) CNF based electrodes.

The 1st insertion capacity of the SWCNT based electrode is 1435 mAhg[-1] but the capacity decreases with change in structure as given in Table -5.3 and amongst the CNS investigated, CNF based electrode shows the lowest capacity of 790 mAhg[-1]. Table-5.3 presents the charge and discharge capacities of each electrode type. The presence of voltage plateaus accounts for the major loss in specific capacity and irreversibility, which are due to the electrolytic degradation of DEC and EC, leading to the formation of a SEI layer as mentioned earlier. Thus, the insertion and extraction capacities for SWCNT electrodes leading progressively to the observed reversible capacity of 603 mAhg[-1]. The coulombic efficiency after 1st cycle is 59%. The electrode based on DWCNT shows almost similar trend as SWCNT but with a

lower reversible capacity of 544 mAhg^{-1}. The lithium insertion capacity of the MWCNT(S) with lower diameter is characterized by very high initial insertion capacity of 904 mAhg^{-1} compared to that in the MWCNT(L) with larger diameter showing a capacity of 846 mAhg^{-1}. The 1st cycle showed a extraction capacity of 601 and 584 mAhg^{-1}, respectively for smaller and larger diameter of MWCNT and hence, an irreversible capacity loss of 302 and 262 mAhg^{-1} have been observed with corresponding coulombic efficiency of 66% and 69% respectively. CNF based electrode apart from their structural arrangement, has also a large number of lattice and surface defects along their length and open ends and these defects may have led to higher intercalation and accessibility of the lithium ions to the interior of the CNF, resulting in both higher irreversible and reversible capacities than that of pure graphite electrode. In the 1st cycle one observes a large insertion capacity of 790 mAhg^{-1}, while, during extraction, the capacity reaches only up to 569 mAhg^{-1} with a coulombic efficiency of 72% as shown in Table-5.3.

Table-5.3: Electrochemical properties of the CNS based electrodes.

Type of CNS	Electrochemical performances				
	Extraction capacity (mAhg^{-1}) (1st cycle)	Insertion capacity (mAhg^{-1}) (1st cycle)	Reversible capacity (mAhg^{-1}) (12th cycle)	Coulombic efficiency (%) after	
				1st cycle	3rd cycle
SWCNT	847	1435	603	59	85
DWCNT	773	1238	544	62	87
MWCNT(S)	601	904	497	66	92
MWCNT(L)	584	846	476	69	96
CNF	569	790	444	72	98
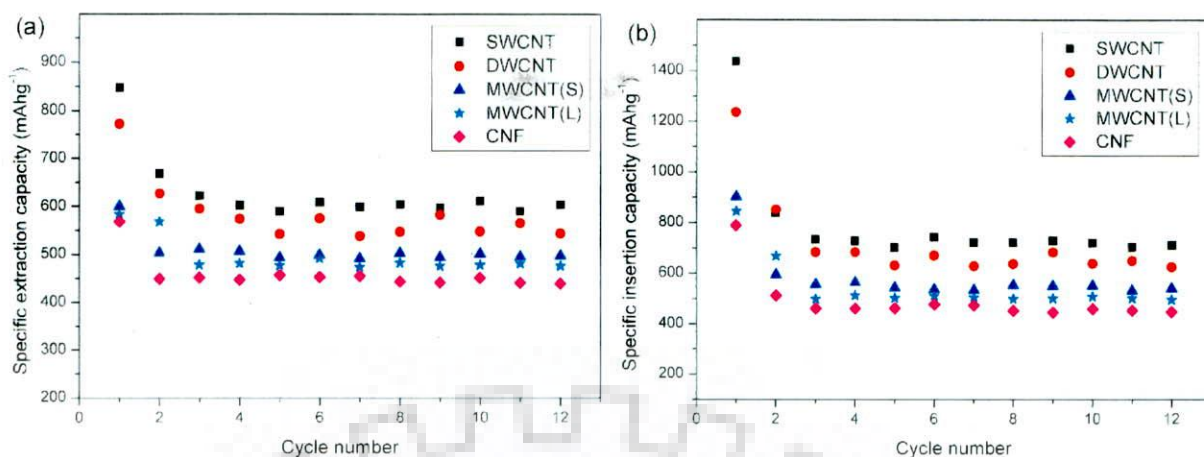
Fig. 5.7: Cyclic behaviour of the different types of CNS with (a) extraction, and (b) insertion capacity.

To understand the stability of the capacity, the electrode was subjected to 12 charge-discharge cycles. The specific capacity of the electrodes during extraction and insertion can be seen from Figs. 5.7(a) and (b) respectively and it reveals that the electrodes approach towards a stable capacity after a few initial cycles of operation both for charging and discharging. After about 3 - 4 initial cycles, both the SWCNT and DWCNT based electrodes show very good stability with very little capacity degradation and attain coulombic efficiency of 85 and 87% respectively. However, MWCNT(S) and MWCNT(L) attain coulombic efficiency of 92% and 96% from 3rd cycle onwards as the plateau region is almost absent from the second cycle resulting in a very high reversible capacity of the electrode ($\sim$ 500 mAhg^{-1}) and excellent stability of the capacity after 12th cycle. In fact, there was no capacity degradation during these cycles (96% of coulumbic efficiency). For the electrode based on MWCNT(L), the reversible capacity after 12th cycle has been found to be 476 mAhg^{-1}, which is still higher than that of graphite. For CNF based electrode the coulombic efficiency reaches up to 98% after 3rd cycle and after 12th cycle the reversible capacity was found to be 444 mAhg^{-1} with almost no capacity fading. The intercalated CNS appears to have a stoichiometry of LiC$_x$, where x may vary from 2-6, as reported previously (Zhao et al, 2000). The stoichiometry achieved in comparison to graphitic anode is significantly more in respect of the active species of lithium.

5.3 Post Cyclic Material Characterization

The volume change during intercalation and deintercalation in the anode materials is an important issue limiting the application of a material in anode. The FESEM micrographs in Fig. 5.8, before and after cycling, show that there is no damage to the mechanical integrity of the electrode.
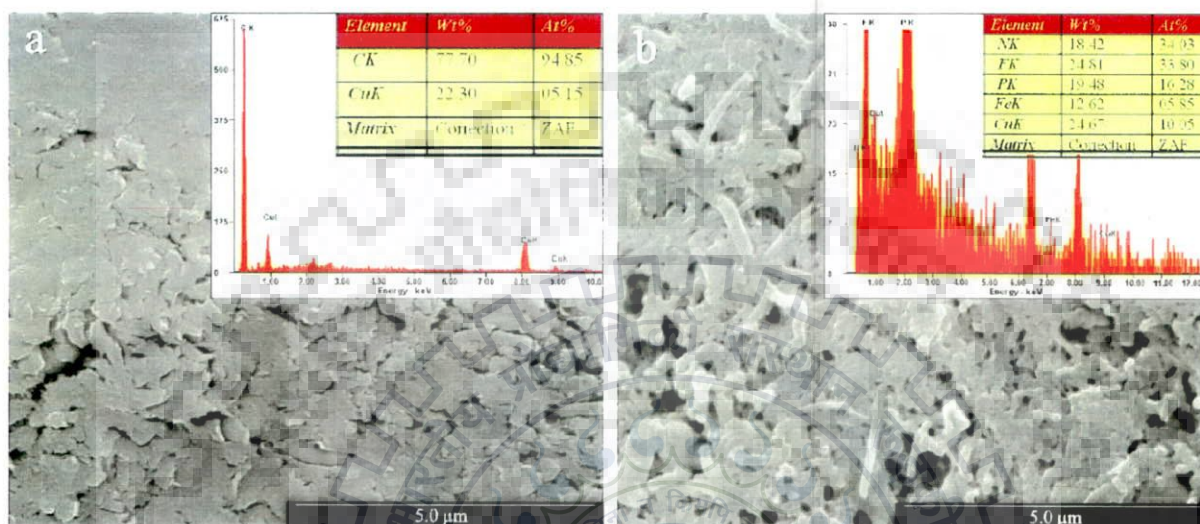
Fig. 5.8: Typical FESEM images and EDS (inset) over the scanned area of the CNS electrodes at an identical magnification: (a) before cycling for CNF, and (b) after 12 cycles showing bright areas of SEI formation.

High coulombic efficiency could not be obtained from a material without having its good mechanical integrity. Nanosized constituent in the electrode may also have contributed to its improved mechanical integrity. The anode, after recycling as shown in Fig. 5.8(b), reveals relatively bright SEI layers as confirmed by the comparison of the EDS with that of Fig. 5.8(a). There are some spurious signals of elements like iron, which could have been picked up from some component of the cell.

5.4 Discussion

The present chapter explores the possibility of attaining higher charge capacity in different CNS based electrode. Apart from MWCNT(L) and CNF grown in our laboratory, the study uses commercially available SWCNT, DWCNT and MWCNT(S) in order to correlate the structure of CNS with the possibility of enhanced lithiation and reversible charge capacity. It has been broadly claimed earlier by the researchers that increased surface and defects result in more sites for lithium ions but these sites contribute to increased irreversible capacity (Winter et al, 1998) but this may not be totally correct. Different CNS used for this study have been characterized for surface area and the results are given in Table-5.1. It has been observed that

SWCNT has surface area of 380 m^2g^{-1}, exceeding 350 m^2g^{-1} observed in DWCNT. MWCNT(L) has surface area of 165 m^2g^{-1}, less than 212 m^2g^{-1} observed in MWCNT(S). CNF has the lowest surface area of 57 m^2g^{-1}. The ratio of surface areas of (SWCNT/DWCNT):MWCNT:CNF may be taken approximately as 365:188:57. The diameter of SWCNT and DWCNT are the smallest. MWCNT(L) has a much larger diameter of around 100-200 nm, which is more than that of MWCNT(S) by a factor of 10 but of lower length. CNF has the largest diameter of 200-600 nm.

The D-band in the Raman spectra originates from in-plane transverse optical phonon branch of CNS close to K-point in Brillouin Zone and the double resonance could involve one elastic scattering from defects and one inelastic scattering or both inelastic scattering involving phonons. Thus, defects are expected to influence D-band, which is broad and intense indicating contribution of defect regions, while G'-band is relatively sensitive to defects (Dresselhaus et al, 2005). The ratio of intensities of D-band to G'-band (= $I_D/I_{G'}$) has been taken as an indicator of the extent of defects in the structure of CNS and in order of increasing defects the CNS under investigation may be arranged as DWCNT < SWCNT < MWCNT(S) < MWCNT(L) < CNF.

The electrochemical performance of these CNS under investigation shows significantly increased insertion and extraction of lithium in the first cycle and according to increased capacity, the materials may be arranged as CNF < MWCNT(L) < MWCNT(S) < DWCNT < SWCNT, which is also in the sequence of increasing reversible capacity and capacity fading as shown in Figs. 5.9 (a) and (b) respectively. The significant increase in irreversible capacity in the first cycle indicates considerable increase of defect sites, from which de-intercalation may not take place leading to capacity fading, which, however, has trend reverse of the extent of defects in the structures, presumed on the basis Raman spectra. There could be two possibilities: (i) the indicator for defect estimated on the basis of Raman spectra is not good or (ii) there could be existence of sites other than defect sites which lead to irreversibility. The enhancement of reversible electrode capacity over that of graphite clearly indicates occurrence of additional sites, from which charging and discharging may take place reversibly.
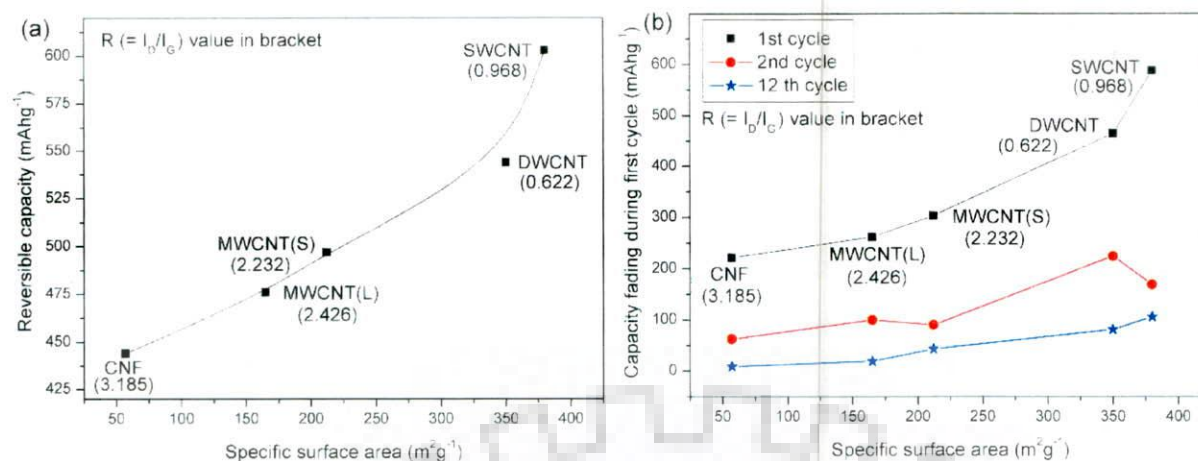
Fig. 5.9: Variation of (a) reversible capacity for different CNS anodes, and (b) capacity fading with specific surface area. The corresponding R (= $I_D/I_{G'}$) is indicated in bracket.

The lithium intercalated graphite has graphene layers in AA stacking and this is equivalent to simple hexagonal cell stacked in three dimensional space and lithium ion occupies the centre of hexagonal cells, midway between the hexagonal faces. But once a cell is occupied by lithium ion, it is not energetically favourable for other lithium ions to occupy the surrounding hexagonal cells and thereby, fully intercalated graphite has chemical formula LiC_6. The lithium ions in such occupied positions will be able to reversibly de-intercalate and intercalate to qualify as active species in a rechargeable battery. Apart from the regular sites of occupation as mentioned, if there are any defect sites like dangling bond etc., which are occupied by the lithium ions during intercalation, there will be no de-intercalation from these sites and thereby, contributing only to irreversible capacity. If there is SEI formation it will also contribute to irreversible capacity leading to capacity fading.

Carbon nanostructures also involve graphene layers and so, one may try to understand their intercalation behaviour in the context of that in graphite as described above. If one considers SWCNT, which has only one graphene layer folded into a tube, it is pertinent to know the possible sites for intercalation by lithium ions. Is it possible to have intercalation sites above and below the hexagons in the graphene layer as observed in intercalated graphite? Udomvech and coworkers (Udomvech et al, 2005) in their density functional calculation of potential surface have demonstrated that lithium atoms or ions may be adsorbed on both the interior and exterior to the sidewall of the SWCNT instead of being located at the tube center of high potential. Therefore, larger diameter of CNT will contain useless empty space inside and is at a disadvantage compared with the small-diameter ones when used in batteries. This may explain lower irreversible and reversible capacity of MWCNT(L) compared to MWCNT(S) as shown in Fig. 5.9(a) and Table 5.3. Kar et al. (Kar et al, 2001) have shown that as Li^+ moves

150

toward the center of the ring, the energy rises creating a barrier and lithium ion would have to cross this barrier to enter the tube through the hexagons of the side-wall or cap-region of the tube and this barrier has been estimated to lie in the range between 11 and 15 eV. Structural defects like 5-ring or 7-ring in the graphene wall still provides intercalation sites near the wall as in the case of 6-ring but the intercalation energy decreases from 24 eV to about 2 eV with increasing ring size from 5 to 8. However, the distance of intercalated ion from the centre of the ring is independent of the size of the ring. However, diffusion through the ends of the tube along the inside surface of the tube is relatively much easier. So, open ended tubes are more suitable for application in batteries.

Now, the sites near the wall inside and outside SWCNT may intercalate lithium ions but these are also sites which may adsorb lithium atoms. If we assume that all these sites are fully intercalated in SWCNT, it should be possible to intercalate it to LiC_3. The charge capacity should be nearly double of graphite but the observed capacity is lower and it may indicate that some of the near wall sites may be occupied by adsorbed lithium. SEI formation may destroy some of the surface sites. The graphitized region in the SWCNT sample will reduce charge capacity and the dangling bonds at the ends may contribute sites from where de-intercalation may not be possible contributing to irreversible capacity and increased capacity fading observed in SWCNT. The extent of capacity fading decreases with increasing cycles as the sites from where de-intercalation does not take place gets filled up progressively during successive cycles. If, in the present study, the assumption about occupation of sites by intercalated Li^+ is valid, then graphene layers in MWCNT should have similar intercalation as in graphite but there will be additional sites near the outside of the outer graphene layer and inside of the inner graphene layer to make its charge capacity between that of graphite and SWCNT and the charge capacity should increase with decreasing number of graphene layers. CNF does not have any inner hollow space to locate sites inside but the near wall sites outside the outer layer will still be there and the charge capacity should only be a little higher than that of graphite. In all these different CNS, SEI will destroy some intercalation sites and thereby, adversely affect the charge capacity, which will also be reduced by graphitized region. The observed order of charge capacity, CNF < MWCNT(L) < MWCNT(S) < DWCNT < SWCNT, may thus be clearly understood in the context of the above discussion. The cost of SWCNT is relatively higher than MWCNT. Therefore, from the standpoint of application in the anode of lithium ion battery, MWCNT may provide a good compromise between cost and charge capacity as it has the reversible charge capacity of 500 mAhg^{-1}, which is significantly more than that in graphite intercalated to LiC_6.

151

Conclusions

Chapter 6
Conclusions

The present investigation has focused on growth of carbon nanostructures by catalytic chemical vapour deposition (CCVD) method using cobalt and nickel oxide undoped and doped with copper oxide. Thereafter, different nanostructures of carbon have been investigated for their electrochemical performance in order to explore their potentiality for application in the anode of lithium ion battery in place of graphite in order to enhance charge capacity. The results on CNS growth and their electrochemical behaviour are presented in chapter-4 and chapter-5 respectively. The results have been discussed. The major conclusions are the following:

A. Growth of Carbon Nanostructures

1. The nanoparticles of cobalt and nickel oxide doped with copper oxide and supported on a substrate of nanoporous alumina in CCVD reactor at 640 °C leads to the formation of carbon nanostructures (CNS) of SWCNT, MWCNT, CNF/nano-tape or their mixture under appropriate conditions of doping and particle size. When the conditions are not proper, there is extensive formation of nanobeads with little or without formation of CNS.

2. The nanoparticles of copper did not show extensive growth of CNS under the experimental conditions used in the present study excepting on very small particles of a few nanometer size, from where SWCNT has grown.

3. The nanoparticles of oxides prepared by sol-gel method have particle size variation over a range and the surface melting or melting of these particles depends on the size and the extent of doping.

4. Melting of oxide nanoparticles appears to play a significant role in the growth of CNS and it is observed that when there is no melting of nanoparticles under the conditions existing in CCVD chamber, there is no or very little formation of CNS.

5. The melting behaviour of nanoparticles prepared by sol-gel method and having a range of sizes could be observed by DTA, which shows a broad endothermic peak, presumed to be overlapping of many melting peaks of nanoparticles of increasing sizes followed by a sharp peak near but below the bulk melting point.

6. XRD studies of oxide nanoparticles at temperature similar to that existing in CCVD chamber shows only reduction in intensity of peaks and the extent of reduction is different for different peaks leading one to infer that there is surface melting of the oxide nanoparticles during the growth of CNS and the core of many particles may still remain solid.

7. Use of oxide particles of larger size and smaller level of doping, which pushes the start of melting above the temperature of growth, leads to the formation of nanobeads, particularly when the rate of flow of carbon bearing gas in the CCVD chamber is high.

8. The surface melting of nanoparticles may help to dissolve the decomposed carbon on the oxide particles in CCVD chamber to allow fast and continuing access of reducing agents like carbon and hydrogen to inside the particles leading to their reduction to metals. Fast diffusion of carbon through molten layer also facilitates nucleation and growth of CNS.

9. The oxide nanoparticles are reduced under the conditions prevailing in the chamber of CCVD during growth of CNS and the close packed plane of the reduced metallic particles of fcc cobalt and of fcc and hcp nickel with or without copper in solid solution, act as template for the nucleation and growth of graphene layers. The appearance of structures other than that of bulk cobalt or nickel is due to the nano-size of the particles.

10. MWCNT generally forms when oxide nanoparticles with lower level of doping is at a growth temperature in CCVD, which is more than the start of melting temperature by a relatively small extent but for oxide nanoparticles with higher level of doping at a growth temperature significantly more than the start of melting temperature, there is formation of fibers. For flat oxide nanaoparticles with high aspect ratio, the condition favouring the growth of fibers, results in nanotapes.

11. For very large oxide nanoparticles, the start of melting is high and there is generally formation of nanobeads while very small nanoparticles with relatively lower temperature at the start of melting favour formation of SWCNT.

B. Electrochemical Performances

1. The CNS samples of different morphologies investigated has surface area decreasing in the order CNF < MWCNT(L) < MWCNT(S) < DWCNT < SWCNT. MCWNT(L) has larger diameter compared to MWCNT(S) while SWCNT and DWCNT have

relatively smaller diameters compared to MWCNT investigated while CNF has the largest diameter. MWCNT(L) and CNF synthesized have relatively smaller length.

2. The extent of defects in the structure of CNS as indicated by the ratio of intensities of D-band to G'-band (= $I_D/I_{G'}$) increases in the following order: DWCNT < SWCNT < MWCNT(S) < MWCNT(L) < CNF.

3. The insertion and extraction of lithium in the first cycle is very high and increases in the CNS materials as CNF < MWCNT(L) < MWCNT(S) < DWCNT < SWCNT. The capacity fading indicating the lithium sites from where it is not extracted, also follows the same order.

4. In spite of high capacity fading SWCNT retains a capacity of 603 mAhg^{-1} after twelfth cycle, where there is almost no capacity fading and so, this capacity is reported as the reversible capacity. The reversible capacity of SWCNT is significantly more than a charge capacity of 372 mAhg^{-1} obtainable at maximum intercalation of graphite.

5. The reversible capacity decreases in the following order CNF < MWCNT(L) < MWCNT(S) < DWCNT < SWCNT, to the lowest capacity of 444 mAhg^{-1} obtained in CNF, which is still higher than the maximum obtainable capacity in graphite.

6. From the standpoint of application in the anode of lithium ion battery, MWCNT may provide a good compromise between cost and charge capacity as one could obtain a reversible charge capacity of ~ 500 mAhg^{-1}, which is significantly more than that in graphite intercalated to LiC_6.

References

[1]   Abdi, Y., Koohsorkhi, J., Derakhshandeh J., Mohajerzadeh, S., Hoseinzadegan, H., Robertson, M. D., Bennett, J. C., Wu, X. and Radamson, H., PECVD-grown carbon nanotubes on silicon substrates with a nickel-seeded tip-growth structure, Mater. Sc. Engg. C, 26 (2006) 1219.

[2]   Ajayan, P. M. and Iijima, S., Smallest carbon nanotube, Nature, 358 (1992) 23.

[3]   Alvarez, L., Guillard, T., Olalde, G., Rivoire, B., Robert, J. F., Bernier, P., Flamant, G. and Laplaze, D., Large scale solar production of fullerenes and carbon nanotubes, Synth. Met., 103 (1999) 2476.

[4]   Amama, P. B., Zemlyanov, D., Sundarakannan, B., Katiyar, R. S. and Fisher, T. S., XPS and Raman characterization of single-walled carbon nanotubes grown from pretreated Fe_2O_3 nanoparticles, J. Phys. D: Appl. Phys., 41 (2008) 165306.

[5]   Amelinckx, S., Zhang, X. B., Bernaerts, D., Zhang, Z. F., Ivanov, V. and Nagy, J. B., A formation mechanism for catalytically grown helix shaped graphite nanotubes, Science, 265 (1994) 635.

[6]   An, K. H., Kim, W. S., Park, Y. S., Moon, J. M., Lim, S. C., Lee, Y. S. and Lee, Y. H., Electrochemical properties of high-power supercapacitors using single-walled carbon nanotube electrodes, Adv. Mater., 11 (2001) 387.

[7]   Andrews, R., Jacques, D., Rao, A. M., Rantell, T., Derbyshire, F., Chen, Y., Chen, J. and Haddon, R. C., Nanotube composite carbon fibers, Appl. Phys. Lett., 75 (1999) 1329.

[8]   Armand, M. and Tarascon, J.-M., Building better batteries, Nature, 451 (2008) 652.

[9]   Aurbach, D., Ein-Eli, Y., Markovshy, B., Zaban, A., Lusky, S., Carmeli, Y. and Yamin, H., The study of electrolyte solutions based on ethylene and diethyl carbonates for rechargeable Li batteries, J. Electrochem. Soc., 142 (1995) 2882.

[10] Avouris, Ph., Carbon nanotube electronics, Chem. Phys., 281 (2002) 429.

[11] Bachtold, A., Strunk, C., Salvetat, J-P., Bonard, J-M., Forro, L., Nussbaumer T. and Schoenenberger, C., Aharonov-Bohm oscillations in carbon nanotubes, Nature, 397 (1999) 673.

[12] Bacon, R., Growth, structure and properties of graphite whiskers, J. Appl. Phys., 31 (1960) 283.

[13] Baker, R. T. K., Barber, M. A., Harris, P. S., Feates F. S. and Waite, R. J., Nucleation and growth of carbon deposits from the nickel catalyzed decomposition of acetylene, J. Catal., 26 (1972) 51.

[14] Baker, R. T. K., Harris, P. S., Thomas, R. B. and Waite, R. J., Formation of filamentous carbon from iron, cobalt and chromium catalyzed decomposition of acetylene, J. Catal., 30 (1973) 86.

[15] Baker, R. T. K. and Harris, P. S., Chemistry and physics of carbon, Marcel Dekker, NY, 14 (1978) 83.

[16] Baker, R. T. K., Alonzo, J. R., Dumesic, J. A. and Yates, D. J. C., Effect of the surface state of iron on filamentous carbon formation, J. Catal., 77 (1982) 74.

[17] Balakrishnan, P. G., Ramesh, R. and Kumar, T. P., Safety mechanisms in lithium-ion batteries, J. Power Sources, 155 (2006) 401.

[18] Basu, S., Early studies on anodic properties of lithium intercalated graphite, J. Power Sources, 82 (1999) 200.

[19] Beaulieu, L. Y., Eberman, K. W., Turner, R. L., Krause, L. J. and Dahn, J. R., Colossal reversible volume changes in lithium alloys, Electrochem. Solid State Lett., 4 (2001) A137.

[20] Bera, D., Johnston, G., Heinrich, H. and Seal, S., A parametric study on the synthesis of carbon nanotubes through arc-discharge in water, Nanotech., 17 (2006) 1722.

[21] Bernier, P. and Lefrant, S., Le carbone dans tous sesetats, Gordon and Breach Sc. (1997).

[22] Besenhard, J. O., The electrochemical preparation and properties of ionic alkali metal- and NR_4- graphite intercalation compounds in organic electrolytes, Carbon, 14 (1976) 111.

[23] Besenhard, J. O., Komenda, P., Paxines, A., Wudy, E. and Josowics, M., Binary and ternary Li-alloys as anode materials in rechargeable organic electrolyte Li-batteries, Solid State Ionics, 18 & 19 (1986) 823.

[24] Bethune, D. S., Kiang, C. H., de Vries, M. S., Gorman, G., Savoy, R., Vazquez, J. and Beyers, R., Cobalt-catalysed growth of carbon nanotubes with single-atomic-layer walls, Nature, 363 (1993) 605.

[25] Boellaard, E., Debokx, P. K., Kock, A. and Geus, J. W., The formation of filamentous carbon on iron and nickel catalysts, J. Catal., 96 (1985) 481.

[26] Bossche, P. V., Vergels, F., Mierlo, J. V., Matheys, J. and Autenboer, W. V., SUBAT: An assessment of sustainable battery technology, J. Power Sources, 162 (2006) 913.

[27] Bourgoin, J.-P., Loiseau, A. and Nierengarten, J.-F., Fullerenes and carbon nanotubes, in: nanoscience: nanotechnologies and nanophysics, Springer (2007).

[28] Breuer, O. and Sundararaj, U., Big returns from small fibers: a review of polymer/carbon nanotube composites, Poly. Comp., 25 (2004) 630.

[29] Broussely, M., Recent developments on lithium ion batteries at SAFT, J. Power Sources, 82 (1999) 140.

[30] Bruce, P. G., Solid-state chemistry of lithium power sources, Chem. Comm., 2 (1997) 1817.

[31] Bruce, P. G., Scrosati, B. and Tarascon, J-M., Nanomaterials for rechargeable lithium batteries, Angew Chem. Int. Ed., 47 (2008) 2930.

[32] Brunauer, S., Emmett, P. H. and Teller, E., Adsorption of gases in multimolecular layers, J. Am. Chem. Soc., 60 (1938) 309.

[33] Buffat, Ph. and Borel, J-P., Size effect on the melting temperature of gold particles, Phys. Rev. A, 13 (1976) 2287.

[34] Cao, A., Xu, C., Liang, J., Wu, D. and Wei, B., X-ray diffraction characterization on the alignment degree of carbon nanotube, Chem. Phys. Lett., 344 (2001) 13.

[35] Cassell, A. M., Raymakers, J. A., Kong, J. and Dai, H., Large scale CVD synthesis of single-walled carbon nanotubes, J. Phys. Chem. B, 103 (1999) 6484.

[36] Chambers, A. and Baker, R. T. K., Influence of chlorine on the decomposition of ethylene over iron and cobalt particles, J. Phys. Chem. B, 101 (1997) 1621.

[37] Chandra, S., Das, P., Bag, S., Laha, D. and Pramanik, P., Synthesis, functionalization and bioimaging applications of highly fluorescent carbon nanoparticles, Nanoscale, 3 (2011) 1533.

[38] Charlier, J.-C., Vita, A. D., Blase, X. and Car, R., Microscopic growth mechanisms for carbon nanotubes, Science, 275 (1997) 646.

[39] Charlier, J.-C., Amara, H. and Lambin, Ph., Catalytically assisted tip growth mechanism for single-wall carbon nanotubes, ACS Nano, 1 (2007) 202.

[40] Chen, P., Wu, X., Lin, J. and Tan, K., High H_2 uptake by alkali-doped carbon nanotubes under ambient pressure and moderate temperatures, Science, 285 (1999) 91.

[41] Chen, S., Brown, L., Levendorf, M., Cai, W., Ju, S-Y., Edgeworth, J., Li, X., Magnuson, C. W., Velamakanni, A., Piner, R. D., Kang, J., Park, J. and Ruoff, R. S., Oxidation resistance of graphene-coated Cu and Cu/Ni alloy, ACS Nano, 5 (2011) 1321.

[42] Chen, W. X., Lee, J. Y. and Liu, Z., Electrochemical lithiation and de-lithiation of carbon nanotube-Sn_2Sb nanocomposites, Electrochem. Comm., 4 (2002) 260.

[43] Cheng, G., Sang, H., Ni, G., Chen, H., Du, Y. and Gong. X., Low frequency Raman spectra of granular Co_xAg_{1-x} films, NanoStructured Mater., 10 (1998) 1153.

[44] Cheung, C. L., Kurtz, A., Park, H. and Lieber, C. M., Diameter-controlled synthesis of carbon nanotubes, J. Phys. Chem. B, 106 (2002) 2429.

[45] Claye, A., Fischer, J. E., Huffman, C. B., Rinzler, A. G. and Smalley, R. E., Solid-state electrochemistry of the Li single wall carbon nanotube system, J. Electrochem. Soc., 147 (2000) 2845.

[46] Collins, P. G. and Avouris, Ph., Nanotubes for electronics, Sc. American, (2000) 62.

[47] Collins, P. G. and Avouris, Ph., Multishell conduction in multiwalled carbon nanotubes, Appl. Phys. A, 74, (2002) 329.

[48] Colomer, J. F., Bister, G., Willems, I., Konya, Z., Fonseca, A., Tendeloo, G. V. and Nagy, J. B., Synthesis of single-wall carbon nanotubes by catalytic decomposition of hydrocarbons, Chem. Commun., (1999) 1343.

[49] Couteau, E., Hernadi, K., Seo, J. W., Nga, L. T., Miko, C., Gaal, R. and Forro, L., CVD synthesis of high-purity multiwalled carbon nanotubes using $CaCO_3$ catalyst support for large-scale production, Chem. Phys. Lett., 378 (2003) 9.

[50] Cui, H., Eres, G., Howe, J. Y., Puretkzy, A., Varela, M., Geohegan, D. B. and Lowndes, D. H., Growth behavior of carbon nanotubes on multilayered metal catalyst film in chemical vapor deposition, Chem. Phys. Lett., 374 (2003) 222.

[51] Dai, H. J., Rinzler, A. G., Nikolaev, P., Thess, A., Colbert, D. T. and Smalley, R. E., Single-wall nanotubes produced by metal-catalyzed disproportionation of carbon monoxide, Chem. Phys. Lett., 260 (1996) 471.

[52] Dai, H. J., Kong, J., Zhou, C. W., Franklin, N., Tombler, T., Cassell, A., Fan, S. S. and Chapline, M., Controlled chemical routes to nanotube architectures, physics, and devices, J. Phys. Chem. B, 103 (1999) 11246.

[53] Dash, J. G., Melting from one to two to three dimensions, Contemp. Phys., 43 (2002) 427.

[54] Davis, W. R., Slawson, R. J. and Rigby, G. R., An unusual form of carbon, Nature, 171 (1953) 756.

[55] Demczyk, B. G., Wang, Y. M., Cumings, J., Hetamn, M., Han, W., Zettl, A. and Ritchie, R. O., Direct mechanical measurement of the tensile strength and elastic modulus of multiwalled carbon nanotubes, Mater. Sci. Eng. A, 334 (2002) 173.

162

[56] Dey, A. N., Electrochemical alloying of lithium in organic electrolytes, J. Electrochem. Soc., 118 (1971) 1547.

[57] Dillon, C., Parilla, P. A., Alleman, J. L., Perkins, J. D. and Heben, M. J., Controlling single-wall nanotube diameters with variation in laser pulse power, Chem. Phys. Lett., 316 (2000) 13.

[58] Ding, D., Wang, J., Cao, Z. and Dai, J., Synthesis of carbon nanostructures on nanocrystalline Ni-Ni$_3$P catalyst supported by SiC whiskers, Carbon, 41 (2003) 579.

[59] Dong, S. R., Tu, J. P. and Zhang, X. B., An investigation of the sliding wear behavior of Cu-matrix composite reinforced by carbon nanotubes, Mater. Sci. Eng. A, 313 (2001) 83.

[60] Dragoman, M. and Dragoman, D., Graphene-based quantum electronics, Prog. Quant. Elect., 33 (2009) 165.

[61] Dresselhaus, M. S., Dresselhaus, G. and Saito, R., Physics of carbon nanotubes, Carbon, 33 (1995) 883.

[62] Dresselhaus, M. S. and Avouris, Ph., Introduction to carbon material research, in: carbon nanotubes, Springer, 80 (2001) (Topics in Applied Physics).

[63] Dresselhaus, M. S., Dresselhaus, G., Charlier, J. C. and Hernandez, E., Electronic, thermal and mechanical properties of carbon nanotubes, Phil. Trans. R. Soc. Lond. A, 362 (2004) 2065.

[64] Dresselhaus, M. S., Dresselhaus, G., Saito, R. and Jorio, A., Raman spectroscopy of carbon nanotubes, Phys. Reports., 409 (2005) 47.

[65] Dupuis, A. C., The catalyst in the CCVD of carbon nanotubes-a review, Prog. Mater. Sc., 50 (2005) 929.

[66] Ebbesen, T. W. and Ajayan, P. M., Large-scale synthesis of carbon nanotubes, Nature, 358 (1992) 220.

[67] Egashira, M., Takatsuji, H., Okada, S. and Yamaki, J., Properties of containing Sn nanoparticles activated carbon fiber for a negative electrode in lithium batteries, J. Power Sources, 107 (2002) 56.

[68] Ein-Eli, Y. and Koch, V. R., Chemical oxidation: a route to enhanced capacity in Li-ion graphite anodes, J. Electrochem. Soc., 144 (1997) 2968.

[69] Endo, M., Takeuchi, K., Igarashi, S., Kobori, K., Shiraishi, M. and Kroto, H. W., The production and structure of pyrolytic carbon nanotubes (PCNTs), J. Phys. Chem. Solids, 54 (1993) 1841.

[70] Endo, M., Nishimura, Y., Takahashi, T., Takeuchi, K. and Dreselhaus, M. S., Lithium storage behavior for various kinds of carbon anodes in Li ion secondary battery, J. Phys. Chem. Solids, 57 (1996) 725.

[71] Endo, M., Kim, C., Nishimura, K., Fujino, T. and Miyashita, K., Recent development of carbon materials for Li ion batteries, Carbon, 38 (2000) 183.

[72] Fan, S., Chapline, M., Frankline, N., Tombler, T., Cassel, A. M. and Dai, H., Self-oriented regular arrays of carbon nanotubes and their field emission properties, Science, 283 (1999) 512.

[73] Filleter, T., Bernal, R., Li, S. and Espinosa, H. D., Ultrahigh strength and stiffness in cross-linked hierarchical carbon nanotube bundles, Adv. Mater., 23 (2011) 2855.

[74] Fischer, J. E., Dai, H., Thess, A., Lee, R., Hanjani, N. M., Dehaas, D. L. and Smalley, R. E., Metallic resistivity in crystalline ropes of single-wall carbon nanotubes, Phys. Rev. B, 55 (1997) R4921.

[75] Flandrois, S. and Simon, B., Carbon materials for lithium-ion rechargeable batteries, Carbon, 37 (1999) 165.

[76] Fujiwara, Y., Maehashi, K., Ohno, Y., Inoue, K. and Matsumoto, K., Jpn. J. Appl. Phys., 44 (2005) 1581.

[77] Gaberscek, M., Bele, M., Drofenik, J., Dominko, R. and Pejovnik, S., Improved carbon anode properties: pretreatment of particles in polyelectrolyte solutions, J. Power Sources, 97/98 (2001) 67.

[78] Gao, B., Bower, C., Lorentzen, J. D., Fleming, L., Kleinhammes, A., Tang, X. P., McNeil, L. E., Wu, Y. and Zhou, O., Enhanced saturation lithium composition in ball-milled single-walled carbon nanotubes, Chem. Phys. Lett., 327 (2000) 69.

[79] Geim, A. K. and Novoselov, K. S., Rise of graphene, Nat. Mater., 6 (2007) 183.

[80] Gibson, J. A. E., Early nanotubes?, Nature, 359 (1992) 369.

[81] Gohier, A., Ewels, C. P., Minea, T. M. and Djouadi, M. A., Carbon nanotube growth mechanism switches from tip- to base-growth with decreasing catalyst particle size, Carbon, 46 (2008) 1331.

[82] Gomez-Camer, J. L., Morales, J. and Sanchez, L., Anchoring Si nanoparticles to carbon nanofibers: an efficient procedure for improving Si performance in Li batteries, J. Mater. Chem., 21 (2011) 811.

[83] Gomez-Gualdron, D. A., McKenzie, G. D., Alvarado, J. F. J. and Balbuena, P. B., Dynamic evolution of supported metal nanocatalyst/carbon structure during single-walled carbon nanotube growth, ACS Nano, 6 (2012) 720.

[84] Gondi, P., Montanari, R. and Costanza, G., X-ray characterization of indium during melting, Adv. Space Res., 29 (2002) 521.

[85] Guillard, T., Flamant, G., Robert, J. F., Rivoire, B., Olalde, G., Laplaze, D. and Alvarez, L., A large scale fullerenes synthesis solar reactor modelling and first experimental results, J. Phys. IV France, 9 (1999) 59.

[86] Guo, T., Nikoleav, P., Rinzler, A. G., Tomanek, D., Colbert, D. T. and Smalley, R. E., Self-assembly of tubular fullerenes, J. Phys. Chem., 99 (1995) 10694.

[87] Gupta, A., Chen, G., Joshi, P., Tadigadapa, S. and Eklund, P. C., Raman scattering from high-frequency phonons in supported n-graphene layer films, Nano Lett., 6 (2006) 2667.

[88] Hafner, J. H., Bronikowski, M. J., Azamian B. R., Nikolaev, P., Rinzler, A. G., Colbert, D. T., Smith, K. A. and Smalley, R. E., Catalytic growth of single-wall carbon nanotubes from metal particles, Chem. Phys. Lett., 296 (1998) 195.

[89] Hamada, N., Sawada, S. and Oshiyama, A., New one-dimensional conductors: graphitic microtubules, Phys. Rev. Lett., 68 (1992) 1579.

[90] Han, Y.-S., Yu, J.-S., Park, G.-S. and Lee, J.-Y., Effects of synthesis temperature on the electrochemical characteristics of pyrolytic carbon for anodes of lithium-ion secondary batteries, J. Electrochem. Soc., 146 (1999) 3999.

[91] Hata, K., Futaba, D. N., Mizuno, K., Namai, T., Yumura, M. and Iijima, S., Water-assisted highly efficient synthesis of impurity-free single-walled carbon nanotubes, Science, 306 (2004) 1362.

[92] Helveg, S., Lopez-Cartes, C., Sehested, J., Hansen, P. L., Clausen, B. S., Rostrup-Nielsen, J. R., Abild-Pedersen, F. and Norskov, J. K., Atomic-scale imaging of carbon nanofibre growth, Nature, 427 (2004) 426.

[93] Henderson, M. J. and White, J. W., An X-ray diffraction and small angle X-ray scattering study of solvated Li-graphite intercalation compounds, Int. J. Energy Eng., 1 (2011) 19.

[94] Hernadi, A., anFonseca, K., Nagy, J. B., Bernaerts, D. and Lucay, A. A., Fe-catalyzed carbon nanotube formation, Carbon, 34 (1996) 1249.

[95] Hofmann, S., Sharma, R., Ducati, C., Du, G., Mattevi, C., Cepek, C., Cantoro, M., Pisana, S., Parvez, A., Cervantes-Sodi, F., Ferrari, A. C., Dunin-Borkowski, R., Lizzit, S., Petaccia, L., Goldoni, A. and Robertson, J., In situ observations of catalyst dynamics during surface-bound carbon nanotube nucleation, Nano Lett., 7 (2007) 602.

[96] Homma, Y., Liu, H., Takagi, D. and Kobayashi, Y., Single-walled carbon nanotube growth with non-iron-group "catalysts" by chemical vapor deposition, Nano Res., 2 (2009) 793.

[97] Hong, S. and Myung, S., Nanotube electronics: A flexible approach to mobility, Nature Nanotech., 2 (2007) 207.

[98] Hongo, H., Yudasaka, M., Ichihashi, T., Nihey, F. and Iijima, S., Chemical vapor deposition of single-wall carbon nanotubes on iron-film-coated sapphire substrates, Chem. Phys. Lett., 361 (2002) 349.

[99] Horibe, M., Nihei, M., Kondo, D., Kawabata, A. and Awano, Y., Influence of growth mode of carbon nanotubes on physical properties for multiwalled carbon nanotube films grown by catalystic chemical vapor deposition, Jpn. J. Appl. Phys., 43 (2004) 7337.

[100] Hsu, W. K., Hare, J. P., Terrones, M., Kroto, H. W. and Walton, D. R. M., Electrolytic formation of carbon nanostructures, Chem. Phys. Lett., 262 (1996) 161.

[101] Hu, W., Gong, D., Chen, Z., Yuan, L., Saito, K., Grimes, C. A. and Kichambare, P., Growth of well-aligned carbon nanotube arrays on silicon substrates using porous alumina film as a nanotemplate, Appl. Phys. Lett., 79 (2001) 3083.

[102] Hu, Y., Shenderova, O. A., Hu, Z., Padgett, C. W. and Brenner, D. W., Carbon nanostructures for advanced composites, Rep. Prog. Phys., 69 (2006) 1847.

[103] Huang, H., Kelder, E. M. and Schoonman, J., Graphite-metal oxide composites as anode for Li-ion batteries, J. Power Sources, 97/98 (2001) 114.

[104] Huggins, R. A., Handbook of battery materials, Wiley (2007).

[105] Hughes, T. V. and Chambers, C. R., Manufacture of carbon filaments, US Patent No. 405,480 (1889).

[106] Huh, Y., Lee, J. Y., Cheon, J., Hong, Y. K., Koo, J. Y., Lee, T. J. and Lee, C. J., Controlled growth of carbon nanotubes over cobalt nanoparticles by thermal chemical vapor deposition, J. Mater. Chem. 13 (2003) 2297.

[107] Hunashyal, A. M., Sundeep, G. V., Quadri, S. S. and Banapurmath, N. R., Experimental investigations to study the effect of carbon nanotubes reinforced in cement-based matrix composite beams, Proc. Inst. Mech. Engg., Part N: J. Nanoeng. Nanosyst., 225 (2011) 17.

[108] Iijima, S., Helical microtubules of graphitic carbon, Nature, 354 (1991) 56.

[109] Iijima, S. and Ichihashi, T., Single-shell carbon nanotubes of 1-nm diameter, Nature, 363 (1993) 603.

[110] Iyuke, S. E., Mamvura, T. A., Liu, K., Sibanda, V., Meyyappan, M. and Varadan, V. K., Process synthesis and optimization for the production of carbon nanostructures, Nanotech., 20 (2009) 375602-1.

[111] Jang, Y. T., Ahn, J. H., Lee, Y. H. and Ju, B. K., Effect of NH_3 and thickness of catalyst on growth of carbon nanotubes using thermal chemical vapor deposition, Chem. Phys. Lett., 372 (2003) 745.

[112] Jehng, J-M., Tung, W-C. and Kuo, C-H., The formation mechanisms of multi-wall carbon nanotubes over the Ni modified MCM-41 catalysts, J. Porous Mater., 15 (2008) 43.

[113] Jeong, G. H., Suzuki, S., Kobayashi, Y., Yamazaki, A., Yoshimura, H. and Homma, Y., Effect of nanoparticle density on narrow diameter distribution of carbon nanotubes and particle evolution during chemical vapor deposition growth, J. Appl. Phys., 98 (2005) 124311.

[114] Joshi, R., Engstler, J., Haridoss, P. and Schneider, J. J., Formation of carbon nanotubes from a silicon carbide/carbon composite, Solid State Sc., 11 (2009) 422.

[115] Kambe, N., Dresselhaus, M. S., Dresselhaus, G., Basu, S., Mcghie, A. R. and Fischer, J. E., Intercalate ordering in first stage graphite-lithium, Mater. Sc. Engg., 40 (1979) 1.

[116] Kanno, R., Takeda, Y., Ichikawa, T., Nakamishi, K. and Yamamoto, O., Carbon as negative electrodes in lithium secondary cells, J. Power Sources, 26 (1989) 534.

[117] Kar, T., Pattanayak, J. and Scheiner, S., Insertion of lithium ions into carbon nanotubes: an ab initio study, J. Phys. Chem. A., 105 (2001) 10397.

[118] Kim, M. S., Rodriguez, N. M. and Baker, R. T. K., The role of interfacial phenomena in the structure of carbon deposits, J. Catal., 134 (1992) 253.

[119] Kim, P., Shi, L., Majumdar, A. and McEuen, P. L., Thermal transport measurements of individual multiwalled nanotubes, Phys. Rev. Lett., 87 (2001) 215502.

[120] Kitiyanan, B., Alvarez, W. E., Harwell, J. H. and Resasco, D. E., Controlled production of single-wall carbon nanotubes by catalytic decomposition of CO on bimetallic Co–Mo catalysts, Chem. Phys. Lett., 317 (2000) 497.

[121] Kojima, Y., Usuki, A., Kawasumi, M., Okada, A., Kurauchi, T. and Kamigaito, O., Sorption of water in nylon 6-clay hybrid, J. Appl. Pol. Sc., 4 (1993) 1259.

[122] Kong, J., Cassell, A. M. and Dai, H. J., Chemical vapor deposition of methane for single-walled carbon nanotubes, Chem. Phys. Lett., 292 (1998a) 567.

[123] Kong, J., Soh, H. T., Cassell, A. M., Quate, C. F. and Dai, H., Synthesis of individual single-walled carbon nanotubes on patterned silicon wafers, Nature, 395 (1998b) 878.

[124] Kong, J., Franklin, N. R., Zhou, C., Chapline, M. C., Peng, S., Cho, K. and Dai, H., Nanotube molecular wires as chemical sensors, Science, 287 (2000) 622.

[125] Konsta-Gdoutos, M. S., Metaxa, Z. S. and Shah, S. P., Highly dispersed carbon nanotube reinforced cement based materials, Cement Conc. Res., 40 (2010) 1052.

[126] Koziol, K., Vilatela, J., Moisala, A., Motta, M., Cunniff, P., Sennett, M. and Windle, A. H., High-performance carbon nanotube fiber, Science, 318 (2007) 1892.

[127] Kroto, H. W., Heath, J. R., O'Brien, S. C., Curl, R. F. and Smalley, R. E., C60: Buckminsterfullerene, Nature, 318 (1985) 162.

[128] Kumar, M. and Ando, Y., A simple method of producing aligned carbon nanotubes from an unconventional precursor – camphor, Chem. Phys. Lett., 374 (2003) 521.

[129] Kumar, M. and Ando, Y., Controlling the diameter distribution of carbon nanotubes grown from camphor on a zeolite support, Carbon, 43 (2005) 533.

[130] Kuwabata, S., Tshumura, N., Goda, S., Martin, C. R. and Yoneyama, H., Charge-discharge properties of composite of synthetic graphite and poly(3-n-hexylthiophene) as an anode active material in rechargeable lithium-ion batteries, J. Electrochem. Soc., 145 (1998) 1415.

[131] Kvande, I., Yu, Z., Zhao, T., Ronning, M., Holmen, A. and Chen, D., Towards large scale production of CNF for catalytic applications, Chem. Sust. Dev., 14 (2006) 583.

[132] Lahiri, I., Oh, S-W., Hwang, J. Y., Cho, S., Sun, Y-K., Banerjee, R. and Choi, W., High capacity and excellent stability of lithium ion battery anode using interface-controlled binder-free multiwall carbon nanotubes grown on copper, ACS Nano, 4 (2010) 3440.

[133] Lai, S. L., Guo, J. Y., Petrova, V., Ramanath, G. and Allen, L. H., Size-dependent melting properties of small tin particles: nanocalorimetric measurements, Phys. Rev. Lett., 77 (1996) 99.

[134] Landi, B. J., Ganter, M. J., Schauerman, C. M., Cress, C. D. and Raffaelle, R. P., Lithium ion capacity of single wall carbon nanotube paper electrodes, J. Phys. Chem. C, 112 (2008) 7509.

[135] Laplaze, D., Bernier, P., Maser, W. K., Flamant, G., Guillard, T. and Loiseau, A., Carbon nanotubes: the solar approach, Carbon, 36 (1998) 685.

[136] Lazzari, M. and Scrosati, B., A cyclable lithium organic electrolyte cell based on two intercalation electrodes, J. Electrochem. Soc., 127 (1980) 773.

[137] Lee, C. J. and Park, J., Growth model of bamboo-shaped carbon nanotubes by thermal chemical vapor deposition, Appl. Phys. Lett., 77 (2000) 3397.

[138] Lee, C. J. and Park, J., Growth model for bamboo like structured carbon nanotubes synthesized using thermal chemical vapor deposition, J. Phys. Chem. B, 105 (2001a) 2365.

[139] Lee, C. J. and Park, J., Growth and structure of carbon nanotubes produced by thermal chemical vapor deposition, Carbon, 39 (2001b) 1891.

[140] Lee, H-Y., Baek, J-K., Jang, S-W., Lee, S-M., Hong, S-T., Lee, K-Y. and Kim, M-H., Characteristics of carbon-coated graphite prepared from mixture of graphite and polyvinylcholride as anode materials for lithium ion batteries, J. Power Sources, 101 (2001a) 206.

[141] Lee, J. K., Ryu, D. H., Ju, J. B., Shul, Y. G., Cho, B. W. and Park, D., Electrochemical characteristics of graphite coated with tin-oxide and copper by fluidised-bed chemical vapour deposition, J. Power Sources, 107 (2002) 90.

[142] Lee, J. Y., Zhang, R. F. and Liu, Z. L., Dispersion of Sn and SnO on carbon anodes, J. Power Sources, 90 (2000) 70.

[143] Lee, N. S., Chung, D. S., Han, I. T., Kang, J. H., Choi, Y. S., Kim, H. Y., Park, S. H., Jin, Y. W., Yi, W. K., Yun, M. J., Jung, J. E., Lee, C. J., You, J. H., Jo, S. H., Lee, C. G. and Kim, J. M., Application of carbon nanotubes to field emission displays, Diam. Rel. Mater., 10 (2001b) 265.

[144] Leroux, F., Metenier, K., Gautier, S., Frackowiak, E., Bonnamy, S. and Beguin, F., Electrochemical insertion of lithium in catalytic multi-walled carbon nanotubes, J. Power Sources, 81/82 (1999) 317.

[145] Li, B., Cao, H., Shao, J., Li, G., Qu, M. and Yin, G., Co_3O_4@graphene composites as anode materials for high-performance lithium ion batteries, Inorg. Chem., 50 (2011) 1628.

[146] Li, H., Shi, L., Wang, Q., Chen, L. and Huang, X., Nano-alloy anode for lithium ion batteries, Solid State Ionics, 148 (2002) 247.

[147] Li, H., Misra, A., Horita, Z., Koch, C. C., Mara, N. A., Dickerson, P. O. and Zhu, Y., Strong and ductile nanostructured Cu-carbon nanotube composite, Appl. Phys Lett., 95 (2009) 071907.

[148] Li, W. Z., Xie, S. S., Qian, L. X., Chang, B. H., Zou, B. S., Zhou, W. Y., Zhao, R. A. and Wang, G., Large-scale synthesis of aligned carbon nanotubes, Science, 274 (1996) 1701.

[149] Li, W. Z., Wen, J. G., Tu, Y. and Ren, Z. F., Effect of gas pressure on the growth and structure of carbon nanotubes by chemical vapor deposition, Appl. Phys. A, 73 (2001c) 259.

[150] Li, Y., Kim, W., Zhang, Y., Rolandi, M., Wang, D. and Dai, H., Growth of single-walled carbon nanotubes from discrete catalytic nanoparticles of various sizes, J. Phys. Chem. B, 105 (2001a) 11424.

[151] Li, Y., Liu, J., Wang, Y. Q. and Wang, Z. L., Preparation of monodispersed Fe-Mo nanoparticles as the catalyst for CVD synthesis of carbon nanotubes, Chem. Mater., 13 (2001b) 1008.

[152] Lin, M., Tan, J. P. Y., Boothroyd, C., Loh, K. P., Tok, E. S. and Foo, Y-L., Dynamical observation of bamboo-like carbon nanotube growth, Nano Lett., 7 (2007) 2234.

[153] Liu, B., Ren, W., Gao, L., Li, S., Pei, S., Liu, C., Jiang, C. and Cheng, H-M., Metal-catalyst-free growth of single-walled carbon nanotubes, J. Am. Chem. Soc., 131 (2009) 2082.

[154] Lu, J. P., Novel magnetic properties of carbon nanotubes, Phys. Rev. Lett., 74 (1995) 1123.

[155] Lu, X. and Chen, Z., Curved Pi-conjugation, aromaticity, and the related chemistry of small fullerenes (C_{60}) and single-walled carbon nanotubes, Chem. Rev., 105 (2005) 3643.

[156] Mabuchi, A., Fujimoto, H., Tokumitsu, K. and Kasuh, T., Charge-discharge characteristics of the mesocarbon miocrobeads heat-treated at different temperatures, J. Electrochem. Soc., 142 (1995) 1041.

[157] Manafi, S. A. and Badiee, S. H., Production of carbon nanofibers using a CVD method with lithium fluoride as a supported cobalt catalyst, Res. Lett. Mater. Sc., 2008 (2007) 1.

[158] Maniwa, Y., Fujiwara, R., Kira, H., Kataura, H., Suzuki, S., Achiba, Y., Nishibori, E., Takata, M., Sakata, M., Fujiwara, A. and Suematsu, H., Thermal expansion of SWNT bundles: X-ray diffraction studies, Phys. Rev. B, 64 (2001) 241402.

[159] Manthiram, A., Materials challenges and opportunities of lithium ion batteries, J. Phys. Chem. Lett., 2 (2011) 176.

[160] Matthews, K. D., Lemaitre, M. G., Kim, T., Chen, H., Shim, M. and Zuo, J-M., Growth modes of carbon nanotubes on metal substrates, J. App. Phys., 100 (2006) 044309-1.

[161] Megahed, S. and Scrosati, B., Lithium-ion rechargeable batteries, J. Power Sources, 51 (1994) 79.

170

[162] Meschel, S. V. and Kleppa, O. J., Standard enthalpies of formation of some 3d transition metal carbides by high temperature calorimetry, J. Alloys Compd., 257 (1997) 227.

[163] Mohri, M., Yanagiasawa, N., Tajima, T., Tanaka, H., Mitate, T., Nakajima, S., Yoshida, M., Yoshimoto, Y., Suzuki, T. and Wada, H., Rechargeable lithium battery based on pyrolytic carbon as a negative electrode, J. Power Sources, 26 (1989) 545.

[164] Momose, H., Honbo, H., Takeuchi, S., Nishimura, K., Horiba, T., Muranaka, Y., Kozono, Y. and Miyadaera, H., X-ray photoelectron spectroscopy analyses of lithium intercalation and alloying reactions on graphite electrodes, J. Power Sources, 68 (1997) 208.

[165] Mukherjee, P. K., Chatterjee, K. and Chakravorty, D., Semiconductor to metal transition in PbS nanowires grown in mica channels, Phys. Rev. B, 73 (2006) 035414.

[166] Mukhopadhyay, I., Hoshino, N., Kawasaki, S., Okino, F., Hsu, W. K. and Touhara, H., Electrochemical Li insertion in B-doped multiwall carbon nanotubes, J. Electrochem. Soc., 149 (2002) A39.

[167] Nanda, K. K., Size-dependent melting of nanoparticles: Hundred years of thermodynamic model, Pramana-J. Phys., 72 (2009) 617.

[168] Nasibulina, L. I., Anoshkin, I. V., Shandakov, S. D., Nasibulin, A. G., Cwirzen, A., Mudimela, P. R., Habermehl-Cwirzen, K., Malm, J. E. M., Koltsova, T. S., Tian, Y., Vasilieva, E. S., Penttala, V., Tolochko, O. V., Karppinen, M. J. and Kauppinen, E. I., Direct synthesis of carbon nanofibers on cement particles, J. Transport. Res. Board, 2142 (2010) 96.

[169] Nazar, L. F. and Crosnier, O., Lithium batteries science and technology, Kluwer Acad., (2004).

[170] Ng, S. H., Wang, J., Guo, Z. P., Chen, J., Wang, G. X. and Liu, H. K., Single wall carbon nanotube paper as anode for lithium-ion battery, Electrochim. Acta, 51 (2005) 23.

[171] Ni, L., Kuroda, K., Zhou, L-P., Ohta, K., Matsuishi, K. and Nakamura, J., Decomposition of metal carbides as an elementary step of carbon nanotube synthesis, Carbon, 47 (2009) 3054.

[172] Nikolaev, P., Bronikowski, M. J., Bradley, R. K., Rohmund, F., Colbert, D. T., Smith, K. A. and Smalley, R. E., Gas-phase catalytic growth of single-walled carbon nanotubes from carbon monoxide, Chem. Phys. Lett., 313 (1999) 91.

[173] Nishi, Y., Lithium ion secondary batteries; past 10 years and the future, J. Power Sources, 100 (2001) 101.

[174] Nishizawa, T. and Ishida, K., The Co-Cu (Cobalt-Copper) System, J. Phase Equilibria, 5 (1984) 161.

[175] Njuguna, J. and Pielichowski, K., Polymer nanocomposites for aerospace applications: properties, Adv. Eng. Mater., 5 (2003) 769.

[176] Nolan, P. E., Lynch, D. C. and Cutler, A. H., Carbon deposition and hydrocarbon formation on group VIII metal catalysts, J. Phys. Chem. B, 102 (1998) 4165.

[177] Oberlin, A., Endo, M. and Koyama, T., Filamentous growth of carbon through benzene decomposition, J. Cryst. Growth, 32 (1976) 335.

[178] Oncel, C. and Yurum, Y., Carbon nanotube synthesis via the catalytic CVD method: A review on the effect of reaction parameters, Fullerenes, Nanotubes, and Carbon Nanostruct., 14 (2006) 17.

[179] Ouyang, G., Tan, X., Wang, C. X. and Yang, G. W., Solid solubility limit in alloying nanoparticles, Nanotech., 17 (2006) 4257.

[180] Ouyang, M., Huang, J-L., Cheung, C. L. and Lieber, C. M., Energy gaps in "metallic" single-walled carbon nanotubes, Science, 292 (2001) 702.

[181] Paek, S. M., Yoo, E. and Honma, I., Enhanced cyclic performance and lithium storage capacity of SnO_2/graphene nanoporous electrodes with three-dimensionally delaminated flexible structure, Nano Lett., 9 (2009) 72.

[182] Pan, Q., Guo, K. K., Wang, L. Z. and Fang, S. B., Ionic conductive copolymer encapsulated graphite as an anode material for lithium ion batteries, Solid State Ionics, 149 (2002) 193.

[183] Park, C., Engel, E. S., Crowe, A., Gilbert, T. R. and Rodriguez, N. M., Use of carbon nanofibers in the removal of organic solvents from water, Langmuir, 16 (2000) 8050.

[184] Pearson, W. B., A Handbook of lattice spacings and structures of metal and alloys, Pergamon Press, (1958) 871.

[185] Peigney, A., Laurent, Ch., Flahaut, E., Bacsa, R. R. and Rousset, A., Specific surface area of carbon nanotubes and bundles of carbon nanotubes, Carbon, 39 (2001) 507.

[186] Peled, E., Menachem, C. and Melman, A., Improved graphite anode for lithium-ion batteries, J. Electrochem. Soc., 143 (1996) L4.

[187] Peng, B., Locascio M., Zapol, P., Li, S., Mielke, S. L., Schatz, G. C. and Espinosa, H. D., Measurements of near-ultimate strength for multiwalled carbon nanotubes and irradiation-induced crosslinking improvements, Nat. Nanotech., 3 (2008) 626.

172

[188] Peters, K. F., Chung, Y-W. and Cohen J. B., Surface melting on small particles, Appl. Phys. Lett., 71 (1997) 2391.

[189] Piedigrosso, P., Konya, Z., Colomer, J. F., Fonseca, A., Tendeloo, G. V. and Nagy, J. B., Production of differently shaped multi-wall carbon nanotubes using various cobalt supported catalysts, Phys. Chem. Chem. Phys., 2 (2000) 163.

[190] Pop, E., Mann, D., Wang, Q., Goodson, K. and Dai, H., Thermal conductance of an individual single-wall carbon nanotube above room temperature, Nano Lett., 6 (2006) 96.

[191] Popov, M., Kyotani, M., Nemanich, R. J. and Koga, Y., Superhard phase composed of single-wall carbon nanotubes, Phys. Rev. B, 65 (2002) 033408.

[192] Qi, W. H., Size effect on melting temperature of nanosolids, Phys. B: Cond. Matter., 368 (2005) 46.

[193] Qi, Y., Cain, T. and Johnson, W. L., Melting and crystallization in Ni nanoclusters: The mesoscale regime, J. Chem. Phys., 115 (2001) 385.

[194] Radushkevich, L. V. and Lukyanovich, V. M., O cnpyrnype yukepola, o,papyoeuocz gpb nepybxecrov kapkoeybb orbcb yukepola yaekepyov roynarne, J. Phys. Chem., 26 (1952) 88 [in Russian].

[195] Rana, K., Sil, A., Ray, S., Synthesis of ribbon type carbon nanostructure using LiFePO$_4$ catalyst and their electrochemical performance, Mater. Res. Bull., 44 (2009) 2155.

[196] Rana, K., Sil, A. and Ray, S., Modification of the structure of multi-walled carbon nanotubes by choice of catalyst and their electro-chemical behavior, Mater. Chem. Phys., 120 (2010) 484.

[197] Rao, B. M. L., Francis, R. W. and Christopher, H. A., Lithium-aluminum electrode, J. Electrochem. Soc., 124 (1977) 1490.

[198] Raty, J-Y., Gygi, F. and Galli, G., Growth of carbon nanotubes on metal nanoparticles: a microscopic mechanism from ab initio molecular dynamics simulations, Phys. Rev. Lett., 95 (2005) 096103-1.

[199] Reibold, M., Paufler, P., Levin, A. A., Kochmann, W., Patzke, N. and Meyer, D. C., Materials: Carbon nanotubes in an ancient Damascus sabre, Nature, 444 (2006) 286.

[200] Robinson, A. L., Lithium primary cells: serendipitous search for a new laser leads to an advanced battery, Science, 184 (1974) 554.

[201] Rodriguez, N. M., Chambers, A. and Baker, R. T. K., Catalytic engineering of carbon nanostructures, Langmuir, 11 (1995) 3862.

[202] Rohatgi, P. K. and Schultz, B., Lightweight metal matrix nanocomposites-stretching the boundaries of metals, Mater. Matters, 2.4 (2007) 16.

[203] Rummeli, M. H., Schaffel, F., Kramberger, C., Gemming, T., Bachmatiuk, A., Kalenczuk, R. J., Rellinghaus, Buchner, B. and Pichler, T., Oxide-driven carbon nanotube growth in supported catalyst CVD, J. Am. Chem. Soc., 129 (2007) 15772.

[204] Saavedra, M. S., Sims, G. D., McCartney, L. N., Stolojan, V., Anguita, J. V., Tan, Y. Y., Ogin, S. L., Smith, P. A. and Silva, S. R. P., Catalysing the production of multiple arm carbon octopi nanostructures, Carbon, 50 (2012) 2141.

[205] Saito, Y., Uemura, S. and Hamaguchi, K., Cathode ray tube lighting elements with carbon nanotube field emitters, Jpn. J. Appl. Phys., 37 (1998) L346.

[206] Sarkar, J., Khan, G. G., Basumallick, A., Bandyopadhyay, N. R., Samudrala, S. K., Bandyopadhyay, S., Synthesis of ordered nano porous alumina template for quasi one – dimensional nanostructures fabrication, J. Inst. of Engg. (I), 88 (2007) 27.

[207] Sato, K., Nogchi, M., Demachi, A., Oki, N. and Endo, M., A mechanism of lithium storage in disordered carbons, Science, 264 (1994) 556.

[208] Schonenberger, C., Bachtold, A., Strunk, C., Salvetat, J.-P. and Forro, L., Interference and interaction in multi-wall carbon nanotubes, Appl. Phys. A, 69 (1999) 283.

[209] Schultzenberger, P. and Schultzenberger, L., Sur quelques faits relatifs à l'histoire du carbone, C. R. Acad. Sci. Paris, 111 (1890) 774.

[210] Schunemann, C., Schaffel, F., Bachmatiuk, A., Queitsch, U., Sparing, M., Rellinghaus, B., Lafdi, K., Schultz, L., Buchner, B. and Rummeli, M. H., Catalyst poisoning by amorphous carbon during carbon nanotube growth: fact or fiction?, ACS Nano, 5 (2011) 8928.

[211] Sen, R., Govindaraj, A. and Rao, C. N. R., Carbon nanotubes by the metallocene route, Chem. Phys. Lett., 267 (1997) 276.

[212] Shaikjee, A. and Coville, N. J., The role of the hydrocarbon source on the growth of carbon materials, Carbon, 50 (2012) 3376.

[213] Sharma, R., Moore, E. S. and Rez, P., Site-specific fabrication of Fe particles for carbon nanotube growth, Nano Lett., 9 (2009) 689.

[214] Sharma, R., Chee, S-W., Herzing, A., Miranda, R. and Rez, P., Evaluation of the role of Au in improving catalytic activity of Ni nanoparticles for the formation of one-dimensional carbon nanostructures, Nano Lett., 11 (2011) 2464.

[215] Shimoda, H., Gao, B., Tang, X. P., Kleinhammes, A., Fleming, L., Wu, Y. and Zhou, O., Lithium intercalation into opened single-wall carbon nanotubes: Storage capacity and electronic properties, Phys. Rev. Lett., 88 (2002) 015502-1.

[216] Shin, H. S., Yu, J. and Song, J. Y., Size-dependent thermal instability and melting behavior of Sn nanowires, Appl. Phys. Lett., 91 (2007) 173106-1.

[217] Shin, M. K., Lee, B., Kim, S. H., Lee, J. A., Spinks, G. M., Gambhir, S., Wallace, G. G., Kozlov, M. E., Baughman, R. H. and Kim, S. J., Synergistic toughening of composite fibres by self-alignment of reduced graphene oxide and carbon nanotubes, Nat. Comm., 3:650 (2012) 1.

[218] Singh, V., Sengupta, S., Solanki, H. S., Dhall, R., Allain, A., Dhara, S., Pant, P. and Deshmukh, M. M., Probing thermal expansion of graphene and modal dispersion at low-temperature using graphene nanoelectromechanical systems resonators, Nanotech., 21 (2010) 165204.

[219] Sinha, S., Barjami, S, Iannacchione, G., Schwab, A. and Muench, G., Off-axis thermal properties of carbon nanotube films, J. Nanopart. Res., 7 (2005) 651.

[220] Smalley, R. E. and Yakobson, B. I., The future of the fullerenes, Solid State Comm., 107 (1998) 597.

[221] Spahr, M. E., Wilhelm, H., Joho, F., Panitz, J., Wambach, J., Novak, P. and Dupont-Pavlovsky, N., Purely hexagonal graphite and the influence of surface modifications on its electrochemical lithium insertion properties, J. Electrochem. Soc., 149 (2002) A960.

[222] Straumal, B. B., Mazilkin, A. A., Protasova, S. G., Myatiev, A. A., Straumal, P. B. and Baretzky, B., Increase of Co solubility with decreasing grain size in ZnO, Acta Materialia, 56 (2008) 6246.

[223] Strauss, B., Frey, F., Petry, W., Trampenau, J., Nicolaus, K., Shapiro, S. M. and Bossy, J., Martensitic phase transformation and lattice dynamics of fcc cobalt, Phys. Rev. B, 54 (1996) 6035.

[224] Subramanian, V., Zhu, H. and Wei. B., High rate reversibility anode materials of lithium batteries from vapor-grown carbon nanofibers, J. Phys. Chem. B, 110 (2006) 7178.

[225] Takagi, D., Homma, Y., Hibino, H., Suzuki, S. and Kobayashi, Y., Single-walled carbon nanotube growth from highly activated metal nanoparticles, Nano Lett. 6 (2006) 2642.

[226] Takagi, M., Electron-diffraction study of liquid-solid transition of thin metal films, J. Phys. Soc. Jpn., 9 (1954) 359.

[227] Takamura, T., Sumiya, K., Suzuki, J., Yamada, C. and Sekine, K., Enhancement of Li doping/undoping reaction rate of carbonaceous materials by coating with an evaporated metal film, J. Power Sources, 81/82 (1999) 368.

[228] Tarascon, J.-M. and Armand, M., Issues and challenges facing rechargeable batteries, Nature, 414 (2001) 359.

[229] Terada, N., Yanagi, T., Arai, S., Yoshikawa, M., Ohta, K., Nakajima, N., Yanai, A. and Arai, N., Development of lithium ion batteries for energy storage and EV applications, J. Power Sources, 100 (2001) 80.

[230] Terrones, M., Grobert, N., Olivares, J., Zhang, J. P., Terrones, H., Kordatos, K., Hsu, W. K., Hare, J. P., Townsend, P. D., Prassides, K., Cheetham, A. K., Kroto, H. W. and Walton, D. R. M., Controlled production of aligned-nanotube bundles, Nature, 388 (1997) 52-55.

[231] Thackeray, M., Lithium-ion batteries: an unexpected conductor, Nat. Mater., 1 (2002) 81.

[232] Thess, A., Lee, R., Nikolaev, P., Dai, H., Petit, P., Robert, J., Xu, C., Lee, Y. H., Kim, S. G., Rinzler, A. G., Colbert, D. T., Scuseria, G. E., Tomanek, D., Fischer, J. E. and Smalley, R. E., Crystalline ropes of metallic carbon nanotubes, Science, 273 (1996) 483.

[233] Thostenson, E. T., Li, C. and Chou, T-W., Nanocomposites in context, Comp. Sc. and Tech. 65 (2005) 491.

[234] Tian, W., Sun, H. P., Pan, X. Q., Yu, J. H., Yeadon, M., Boothroyd, C. B., Feng, Y. P., Lukaszew, R. A. and Clarke, R., Hexagonal close-packed Ni nanostructures grown on the (001) surface of MgO, Appl. Phys. Lett., 86 (2005) 131915.

[235] Tibbetts, G. G., Why are carbon filaments tubular?, J. Crystl. Growth, 66 (1984) 632.

[236] Udomvech, A., Kerdcharoen, T. and Osotchan, T., First principles study of Li and Li^+ adsorbed on carbon nanotube: variation of tubule diameter and length, Chem. Phys. Lett., 406 (2005) 161.

[237] Ulus, A., Rosenberg, Y., Burstein, L. and Peled, E., Tin alloy-graphite composite anode for lithium-ion batteries, J. Electrochem. Soc., 149 (2002) A635.

[238] Veeraraghavan, B., Paul, J., Haran, B. and Popov, B., Study of polypyrrole graphite composite as anode material for secondary lithium-ion batteries, J. Power Sources, 109 (2002) 377.

[239] Vinciguerra, V., Buonocore, F., Panzera, G. and Occhipinti, L., Growth mechanisms in chemical vapour deposited carbon nanotubes, Nanotech., 14 (2003) 655.

176

[240] Wang, C., Appleby, A. J. and Little, F. E., Irreversible capacities of graphite anode for lithium-ion batteries, J. Electroanal. Chem., 519 (2002a) 9.

[241] Wang, C. S., Wu, G. T., Zhang, X. B., Qi, Z. F. and Li, W. Z., Lithium insertion in carbon-silicon composite materials produced by mechanical milling, J. Electrochem. Soc., 145 (1998b) 2751.

[242] Wang, H. and Yoshio, M., Carbon-coated natural graphite prepared by thermal vapor decomposition process, a candidate anode material for lithium-ion battery, J. Power Sources, 93 (2001) 123.

[243] Wang, H., Cui, L-F., Yang, Y., Casalongue, H. S., Robinson, J. T., Liang, Y., Cui, Y. and Dai, H., Mn_3O_4–graphene hybrid as a high-capacity anode material for lithium ion batteries, J. Am. Chem. Soc., 132 (2010) 13978.

[244] Wang, Q., Chen, L. and Huang, X., Anomalous electrochemical behavior of multiwalled carbon nanotubes as host material for lithium insertion/extraction, Electrochem. Solid State Lett., 37 (2002b) A188.

[245] Wang, X. X., Wang, J. N., Chany, H. and Zhang, Y. F., Preparation of short carbon nanotubes and application as an electrode material in Li-ion batteries, Adv. Funct. Mater., 17 (2007) 3613.

[246] Wang, Z. L., Petroski, J. M., Green, T. C. and El-Sayed M. A., Shape transformation and surface melting of cubic and tetrahedral platinum nanocrystals, J. Phys. Chem. B, 102 (1998a) 6145.

[247] Ward, J., Wei, B. Q. and Ajayan, P. M., Substrate effects on the growth of carbon nanotubes by thermal decomposition of methane, Chem. Phys. Lett., 376 (2003) 717.

[248] Wei, B. Q., Vajtai, R., Jung, Y., Ward, J., Zhang, R., Ramanath, G. and Ajayan, P. M., Organized assembly of carbon nanotubes, Nature, 416 (2002) 495.

[249] Welna, D. T., Qu, L., Taylor, B. E., Dai, L. and Durstock, M. F., Vertically aligned carbon nanotube electrodes for lithium-ion batteries, J. Power Sources, 196 (2011) 1455.

[250] Whittingham, M. S., Chalcogenide battery, US Patent 4009052 (1977).

[251] Winter, M., Novak, P. and Monnier, A., Graphites for lithium-ion cells: the correlation of the first-cycle charge loss with the Brunauer-Emmett-Teller surface area, J. Electrochem. Soc., 145 (1998) 428.

[252] Wirth, C. T., Hofmann, S. and Robertson, J., State of the catalyst during carbon nanotube growth, Diamond Rel. Mater., 18 (2009) 940.

177

[253] Wong, S. S., Harper, J. D., Lansbury, Jr. P. T. and Lieber, C. M., Carbon nanotube tips: high-resolution probes for imaging biological systems, J. Am. Chem. Soc., 120 (1998) 603.

[254] Wu, G. T., Wang, C. S., Zhang, X. B., Yang, H. S., Qi, Z. F., He, P. M. and Li, W. Z., Structure and lithium insertion properties of carbon nanotubes, J. Electrochem. Soc., 146 (1999) 1696.

[255] Wu, Y. P., Wan, C., Jiang, C. and Tsuchida, E., Composite anode material for lithium ion battery with low sensitivity to water, Electrochem. Comm., 2 (2000) 626.

[256] Wu, Y. P., Rahm, E. and Holze, R., Effects of heteroatoms on electrochemical performance of electrode materials for lithium ion batteries, Electrochim. Acta., 47 (2002) 3491.

[257] Wu, Y. P., Rahm, E. and Holze, R., Carbon anode materials for lithium ion batteries, J. Power Sources, 114 (2003) 228.

[258] Xing, W., Bai, P., Li, Z. F., Yu, R. J., Yan, Z. F., Lu, G. Q. and Lu, L. M., Synthesis of ordered nanoporous carbon and its application in Li-ion battery, Electrochim. Acta, 51 (2006) 4626.

[259] Xu, Z., Chen, X., Qu, X., Jia, J. and Dong, S., Single-wall carbon nanotube-based voltammetric sensor and biosensor, Biosensors and Bioelect., 20 (2004) 579.

[260] Yamada, T., Namai, T., Hata, K., Futaba, D. N., Mizuno, K., Fan, J., Yudasaka, M., Yumura, M. and Iijima, S., Size-selective growth of double-walled carbon nanotube forests from engineered iron catalysts, Nat. Nanotech., 1 (2006) 131.

[261] Yang, Q-H., Hou, P-X., Bai, S., Wang, M-Z. and Cheng, H-M., Adsorption and capillarity of nitrogen in aggregated multi-walled carbon nanotubes, Chem. Phys. Lett., 345 (2001) 18.

[262] Yang, Z., Wu, H. and Simard, B., Charge–discharge characteristics of raw acid-oxidized carbon nanotubes, Electrochem. Comm., 4 (2002) 574.

[263] Yazami, R. and Touzain, Ph., A reversible graphite-lithium negative electrode for electrochemical generators, J. Power Sources, 9 (1983) 365.

[264] Yazami, R., Surface chemistry and lithium storage capability of the graphite-lithium electrode, Electrochim. Acta, 45 (1999) 87.

[265] Yeshchenko, O. A., Dmitruk, I. M., Alexeenko, A. A., Dmytruk, A. M., Size-dependent melting of spherical copper nanoparticles embedded in a silica matrix, Phys. Rev. B, 75 (2007) 085434-1.

[266] Yoo, E., Kim, J., Hosono, E., Zhou, H-S. Kudo, T. and Honma, I., Large reversible Li storage of graphene nanosheet families for use in rechargeable lithium ion batteries, Nano Lett., 8 (2008) 2277.

[267] Yoon, S., Kim, H. and Oh, S. M., Surface modification of graphite by coke coating for reduction of initial irreversible capacity in lithium secondary batteries, J. Power Sources, 94 (2001) 68.

[268] Yoshida, H., Takeda, S., Uchiyama, T., Kohno, H. and Homma, Y., Atomic-scale in-situ observation of carbon nanotube growth from solid state iron carbide nanoparticles, Nano Lett., 8 (2008) 2082.

[269] Yoshio, M., Wang, H., Fukuda, K., Hara, Y. and Adachi, Y., Effect of carbon coating on electrochemical performance of treated natural graphite as lithium-ion battery anode material, J. Electrochem. Soc., 147 (2000) 1245.

[270] Yoshitake, T., Shimakawa, Y., Kuroshima, S., Kimura, H., Ichihashi, T., Kubo, Y., Kasuya, D., Takahashi, K., Kohai, F., Yudasaka, M. and Iijima, S., Preparation of fine platinum catalyst supported on single-wall carbon nanohorns for fuel cell application, Phys. B, 323 (2002) 124.

[271] Yu, M-F., Lourie, O., Dyer, M. J., Moloni, K., Kelly, T. F. and Ruoff, R. S., Strength and breaking mechanism of multiwalled carbon nanotubes under tensile load, Science, 287 (2000a) 637.

[272] Yu, P., Ritter, J. A., White, R. E. and Popov, B. N., Ni-composite microencapsulated graphite as the negative electrode in lithium-ion batteries, J. Electrochem. Soc., 147 (2000b) 1280.

[273] Yu, T., Zhu, Y., Xu, X., Shen, Z., Chen, P. and Lim, C. T., Controlled growth and field emission properties of cobalt oxide nanowalls, Adv. Mater., 17 (2005) 1595.

[274] Yu, X. and Duxbury. P. M., Kinetics of nonequilibrium shape change in gold clusters, Phys. Rev. B, 52 (1995) 2102.

[275] Yun, Y. H., Shanov, V., Tu, Y., Subramaniam, S. and Schulz, M. J., Growth mechanism of long aligned multiwall carbon nanotube arrays by water-assisted chemical vapor deposition, J. Phys. Chem. B, 110 (2006) 23920.

[276] Zabel, H. and Solin, S. A., Graphite intercalation compounds, Springer (1992).

[277] Zaghib, K., Nadeau, G. and Kinoshita, K., Influence of edge and basal plane sites on the electrochemical behavior of flake-like natural graphite for Li-ion batteries, J. Power Sources, 97/98 (2001) 97.

[278] Zanini, M., Basu, S. and Fischer, J. E., Alternate synthesis and reflectivity spectrum of stage 1 lithium-graphite intercalation compound, Carbon, 16 (1978) 211.

[279] Zhan, G-D., Kuntz, J. D., Wan, J. and Mukherjee, A. K., Single-wall carbon nanotubes as attractive toughening agents in alumina-based nanocomposites, Nat. Mater., 2 (2003) 38.

[280] Zhang, J., Hu, Y-S., Tessonnier, J-P., Weinberg, G., Maier, J., Schlogl, R. and Su, D. S., CNFs@CNTs: superior carbon for electrochemical energy storage, Adv. Mater., 20 (2008) 1450.

[281] Zhao, J., Buldum, A. and Han, J., First-principles study of Li-intercalated carbon nanotube ropes, Phys. Rev. Lett., 85 (2000) 1706.

[282] Zhou, S-M., Zhang, X-B., Ding, Z-P., Min, C-Y., Xu, G-L. and Zhu, W-M., Fabrication and tribological properties of carbon nanotubes reinforced Al composites prepared by pressure less infiltration technique, Comp.: Part A, 38 (2007) 301.

[283] Zhou, W., Han, Z., Wang, J., Zhang, Y., Jin, Z., Sun, X., Zhang, Y., Yan, C. and Li, Y., Copper catalyzing growth of single-walled carbon nanotubes on substrates, Nano Lett., 6 (2006) 2987.

[284] Zhu, H., Suenaga, K., Wei, J., Wang, K. and Wu, D., A strategy to control the chirality of single-walled carbon nanotubes, J. Cryst. Growth, 310 (2008) 5473.

[285] Zhu, X., Zhu, Y., Murali, S., Stoller, M. D. and Ruoff, R. S., Nanostructured reduced graphene oxide/Fe_2O_3 composite as a high-performance anode material for lithium ion batteries, ACS Nano, 5 (2011) 3333.

[286] Zhu, Y. A., Sui, Zh. J., Zhao, T. J., Dai, Y. Ch., Cheng, Zh. M. and Yuan, W. K., Modeling of fishbone-type carbon nanofibers: A theoretical study, Carbon, 43 (2005) 1694.